Paulo Jorge Pereira Gomes

Graduated in Physics and Chemistry Teaching

Characterization of Molecular Damage Induced by UV Photons and Carbon Ions on Biomimetic Heterostructures

Dissertation to obtain the PhD Degree in Physics

Speciality Condensed Matter Physics

Supervisor: Maria de Fátima Guerreiro da Silva Campos Raposo,
Assistant Professor, Universidade Nova de Lisboa

Co-supervisor: Paulo António Martins Ferreira Ribeiro,
Assistant Professor, Universidade Nova de Lisboa

Jury:

President:	Prof. Doutor António M. D. de Sá Nunes dos Santos
Examiners:	Prof. Doutora Ana Margarida M. V. de Barros Timmons Doutora Octávia Gabriela da S. V. Nené Monteiro Gil
Vowels:	Prof. Doutora Maria Luísa Dias de Carvalho S. Leonardo Prof. Doutor Henrique Leonel Gomes Prof. Doutor Paulo Manuel Assis Loureiro Limão Vieira Prof. Doutora Amélia Maria P. S. Gonçalves da Silva Prof. Doutora Maria de Fátima G. S. Campos Raposo

FACULDADE DE CIÊNCIAS E TECNOLOGIA
UNIVERSIDADE NOVA DE LISBOA

December 2014

To My Mother, Júlia

In Memory of My Father, José

In Memory of My Aunt, Helena

ACKNOWLEDGEMENTS

Prof. Dr. Maria Raposo for the first insights into condensed matter physics during my undergraduate years and for her commitment in supporting me throughout the years developing the PhD work. My eternal gratitude for the opportunities created since the time of graduation, when I was invited to join the research group, up to today, having always placed enormous confidence in me as an individual, and in my scientific and pedagogical capabilities, allowing my development over the years. Thanks Maria by your friendship.

Prof. Dr. Paulo Ribeiro for the guidance given throughout this work, for is support during the hard weeks working in external institutions and is willingness and camaraderie, important for good moments of relaxation.

Prof. Dr. Amélia Gonçalves da Silva for accepting to join the committee for monitoring this PhD thesis, for giving me the opportunity to have access the laboratory over her direction, for the support and accompaniment provided, and transmitted by learning which greatly contributed to my development in achieving scientific and pedagogical maturity.

Prof. Dr. Maria de Lourdes Costa for inviting me during graduation to develop research in her laboratory. Without this opportunity, certainly, I would not delve into the area of scientific research.

Prof. Dr. Nigel J. Mason from the Centre of Molecular and Optical Sciences, The Open University, UK, for financial and institutional conditions created, that enabled the development of a large part of the work of this PhD.

Doctor Søren Vrønning Hoffmann and *Doctor Nykola Jones* from Institute for Storage Ring Facilities, University of Aarhus, Denmark, for their supervision, discussion and assistance while working on the synchrotron radiation facility.

Prof. Dr. Robert Mc. Cullough from Center of Plasma Physics, School of Mathematics and Physics, Queen's University of Belfast, for their supervision, discussion and assistance while working on the ion beam facility.

Prof. Dr. Madalena Dionísio from Chemistry Department, Universidade nova de Lisboa, for her supervision, discussion and assistance while working on the impedance spectroscopy facility.

Prof. Dr. Ana Botelho do Rego from Centro de Química Física Molecular, Instituto Superior Técnico, Universidade de Lisboa, for their collaboration and discussion with the measurements done on the x-ray photoelectron spectroscopy facility.

Doctor David Shaw from Daresbury Laboratory, Daresbury Science & Innovation Campus, UK, for their supervision, discussion and assistance while working on the synchrotron radiation facility.

Prof. Dr. Paulo Limão-Vieira by the opportunities to visit and meet other international research groups and to participate in several international projects.

Prof. Dr. Laura Ilharco from Centro de Química Física Molecular, Instituto Superior Técnico, Universidade de Lisboa for the supervision, discussion and assistance while working on the infrared spectroscopy facility.

Dr. Andreia Duarte, Mestre Margarida Coelho, Mestre Gonçalo Martins e Mestre Luís Abegão for their great friendship, and discussions and collaboration in the development of the work over several stages of this PhD.

Doctor João Lourenço, Doctor Carla Madruga, Doctor Quirina Ferreira, Eng. Jorge Ribeiro and remaining elements that went through the Grupo de Sistemas Moleculares Funcionais, for the opportunities over the years, the support provided and developed.

Prof. Dr. Osvaldo Novaes Jr., Doctor Marli Moraes and other elements of the Grupo de Física de Polímeros do Instituto de Física São Carlos, for collaborating on several projects developed.

Mrs. Helena Rodrigues for their support since the time of graduation, for her friendship and encouragement in the most troubled times of my career in the Physics Department of Universidade Nova de Lisboa.

The Department of Physics and CeFiTec Staff for technical and bureaucratic support throughout these years.

Dr. Ana Ramos by upholding me in the final phase of this work and for their important contribution to their conclusion.

Dr. Glória Pires for early learning with physical and chemical, through its teachings, and its assertive words in my vocational guidance, which led me to reach this ambitious academic goal.

My friends Ana Duarte, Célia Pereira, Daniel Duarte and Miguel Cunha for the relentless friendship, encouragement and unconditional support in all these years, in most important and memorable moments.

My friends Filipe Romão and José Carlos Martins for their encouragement and support on thesis graphic edition.

My aunt Helena by awakening the dazzle for knowledge and learning who developed the strength to achieve ambitious goals.

My parents Júlia and José. Thanks for the education and knowledge they transmitted to me through all these years that made me who I am and that greatly contributed to the achievement of these professional goals. To you father, that are no longer among us, special thanks for having been present and for everything you did so I could reach this goal. To you mother, thank you for being always present in my life and for your support at all times…

All other collaborators, friends and familiars not referenced who have contributed directly or indirectly, positively or negatively for the developed of these works, thanks for your contribution.

Departamento de Física, Universidade Nova de Lisboa, for the provided working conditions.

Fundação para a Ciência e Tecnologia - Portugal for the SFRH/BD/35954/2007 doctoral Grant.

ABSTRACT

The study of the effect of radiation on living tissues is a rather complex task to address mainly because they are made of a set of complex functional biological structures and interfaces. Particularly if one is looking for where damage is taking place in a first stage and what are the underlying reaction mechanisms. In this work a new approach is addressed to study the effect of radiation by making use of well identified molecular hetero-structures samples which mimic the biological environment. These were obtained by assembling onto a solid support deoxyribonucleic acid (DNA) and phospholipids together with a soft water-containing polyelectrolyte precursor in layered structures and by producing lipid layers at liquid/air interface with DNA as subphase. The effects of both ultraviolet (UV) radiation and carbon ions beams were systematically investigated in these heterostructures, namely damage on DNA by means vacuum ultraviolet (VUV), infrared (IR), X-Ray Photoelectron (XPS) and impedance spectroscopy. Experimental results revealed that UV affects furanose, PO_2^-, thymines, cytosines and adenines groups. The XPS spectrometry carried out on the samples allowed validate the VUV and IR results and to conclude that ionized phosphate groups, surrounded by the sodium counterions, congregate hydration water molecules which play a role of UV protection. The ac electrical conductivity measurements revealed that the DNA electrical conduction is arising from DNA chain electron hopping between base-pairs and phosphate groups, with the hopping distance equal to the distance between DNA base-pairs and is strongly dependent on UV radiation exposure, due loss of phosphate groups. Characterization of DNA samples exposed to a 4 keV C^{3+} ions beam revealed also carbon-oxygen bonds break, phosphate groups damage and formation of new species. Results from radiation induced damage carried out on biomimetic heterostructures having different compositions revealed that damage is dependent on sample composition, with respect to functional targeted groups and extent of damage. Conversely, LbL films of 1,2-dipalmitoyl-sn-Glycero-3-[Phospho-rac-(1-glycerol)] (Sodium Salt) (DPPG) liposomes, alternated with poly(allylamine hydrochloride) (PAH) revealed to be unaffected, even by prolonged UV irradiation exposure, in the absence of water molecules. However, DPPG molecules were damaged by the UV radiation in presence of water with cleavage of C-O, C=O and $–PO^{2-}$ bonds. Finally, the study of DNA interaction with the ionic lipids at liquid/air interfaces revealed that electrical charge of the lipid influences the interaction of phospholipid with DNA. In the presence of DNA in the subphase, the effects from UV irrladiation were seen to be smaller, which means that ionic products from biomolecules degradation stabilize the intact DPPG molecules. This mechanism may explain why UV irradiation does not cause immediate cell collapse, thus providing time for the cellular machinery to repair elements damaged by UV.

KEYWORDS: Biomimetic, Biomolecules, Impedance biosensor, Ion damage, Langmuir films, Liposome, UV Radiation damage, Thin films

RESUMO

O estudo do efeito da radiação em tecidos vivos constitui uma tarefa complexa uma vez que estes são constituídos por um conjunto de estruturas biológicas com interfaces e funções específicas e complexas. A complexidade aumenta quando se pretende estudar onde ocorre o dano numa primeira fase e os posteriores mecanismos de proliferação dos danos. Neste trabalho é utilizada uma nova abordagem para o estudo do efeito da radiação, recorrendo ao uso de heteroestruturas preparadas com moléculas bem identificadas que simulam o meio biológico. Neste trabalho foram desenvolvidas heteroestruturas em substrato sólido, compostas por diferentes combinações de ácido desoxirribonucleico (ADN), fosfolípidos e polieletrólitos que possibilitam a retenção das moléculas de água, e pela produção de camadas lipídicas na interface líquido/ar, com solução aquosa de ADN como subfase. Os danos por radiação ultravioleta (UV) e feixe de iões carbono (C^{3+}) foram caracterizados por espectroscopia de ultravioleta de vácuo (VUV), de infravermelho (IV), de fotoeletrões de raio-X (XPS) e de impedância. Os resultados revelaram que a radiação UV danifica as moléculas de furanose, timina, citosina, adenina e os grupos PO^{2-}. Os resultados de XPS obtidos permitiram não só validar os resultados já obtidos como também concluir que os grupos fosfato ionizados, rodeados por iões sódio, retêm água, protegendo-os da radiação UV. As medições de condutividade eléctrica do ADN revelaram que a condução processa-se por saltos de electrões entre os pares de base e os grupos de fosfato com a distância de salto igual à distância entre os pares de bases de ADN sendo, devido à perda de grupos fosfato, dependente da exposição à radiação UV. A caracterização de amostras de ADN exposta a um feixe de iões de C^{3+} revelou também a quebra de ligações carbono-oxigénio, danos nos grupos fosfato e formação de novas espécies. Dos resultados obtidos foi possível concluir que os danos induzidos pela radiação nas heteroestruturas biomiméticas, cuja composição varia entre estudos, dependem da composição da amostra, afetando diferentes grupos moleculares e em diferentes extensões. Por outro lado, filmes LbL de 1,2-dipalmitoil-sn-glicero-3-[fosfo-rac(1-glicerol)] (sal de sódio) (DPPG) lipossomas, alternado com poli (cloridrato de alilamina) (PAH) revelaram-se inalterados, mesmo em caso de exposição prolongada a radiação UV na ausência de moléculas de água. No entanto, as moléculas de DPPG foram danificadas por radiação UV na presença de água, com a quebra de ligações CO, C=O e -PO^{2-}. Finalmente, o estudo da interacção de ADN com lípidos iónicos nas interfaces líquido/ar revelou que a carga eléctrica do lípido influencia a sua interacção com o ADN. Na presença de ADN na subfase, os efeitos de radiação UV foram visivelmente menores, o que significa que os produtos iónicos de degradação das biomoléculas estabilizam as moléculas intactas de DPPG. Este mecanismo pode explicar por que a radiação UV não causa o colapso das células imediato, dando tempo para a célula ativar os mecanismos de reparação, corrigindo os danos causados pela radiação UV.

PALAVRAS-CHAVE: Biomimética, Biomoléculas, Biosensor de Impedância, Danos por iões, Danos por radiação UV, Langmuir filmes, Lipossomas, Filmes finos

CONTENTS

FIGURES

TABLES

ACRONYMS AND SYMBOLS

A	Absorbance
A	Adenine
A	Area
Abs	Absorbance
AC	Alternating Current
AFM	Atomic Force Microscopy
ASTRID	Aarhus Storage Ring in Denmark
a.u.	Arbitrary Units
B	Magnetic Field
BE	Binding Energy
BE	Bond Energy
B3LYP	Becke, Three-parameter, Lee-Yang-Parr
C	Cytosine
CAPES	Fundação Coordenação de Aperfeiçoamento de Pessoal de Nível Superior
CBH	Correlated Barrier Hopping
CD1	Setup to Circular Dichroism and Photoabsorption Spectroscopy Studies
CEMOS	Centre of Molecular and Optical Sciences
CNPq	Conselho Nacional de Desenvolvimento Científico e Tecnológico
COST	European Cooperation in Science and Technology
DF	Departamento de Física
DLS	Dynamic Light Scattering
DLTGS	Deuteriated L-Aniline Doped Triglycine Sulfate
DNA	Deoxyribonucleic Acid
DPPG	1,2-distearoyl-*sn*-glycero-3-phospho-(1'-*rac*-glycerol)
DSB	Double Strand Break
e	Electron Charge
E	Irradiance
EBIS	Electron Beam Ion Sources
EBIT	Electron Beam Ion Traps
ECCL	Electron Controlled Chemical Lithography
ECR	Electron Cyclotron Resonance
EDPPC	1,2-distearoyl-*sn*-glycero-3-ethylphosphocholine
EIPAM	Electron Induced Processing at the Molecular Level
EM	Electromagnetic
ESI	Electrospray Ion Sources
ESF	European Social Fund
EU	European Union
F	Force

f	Frequency
FAT	Fixed Analyser Transmission
FAPESP	Fundação de Amparo à Pesquisa do Estado de São Paulo
FCT	Faculdade de Ciências e Tecnologia
FCT	Fundação para a Ciência e Tecnologia
FTIR	Fourier Transform Infrared Spectroscopy
FWHM	Full Width at Half-maximum
G	Gaseous
G	Guanine
GRICES	Gabinete de Relações Internacionais da Ciência e do Ensino Superior
I	Radiation Detected
I	Current Intensity
ICA	Independent Component Analysis
I_0	Incident Radiation
Im	Imaginary Component
IR	Infrared
ISA	Institute for Storage Ring Facilities
J	Current Density
jX	Indutance
K	Kelvin
k	Boltzmann Constant
K_α	Transition Energy
K_S^{-1}	Compressional Modulus
KE	Kinetics Energy
ℓ	Length
LC	Liquid Condensed
LE	Liquid Expanded
LET	Linear Energy Transfer
LB	Langmuir-Blodgett
LbL	Layer-by-Layer
LINAC	Linear Particle Accelerator
LUV	Large Unilamelar Vesicles
m	Mass
MCI	Multiply Charged Ion
MEC	Ministério do Ensino e Ciência
MLV	Multilamelar Vesicles
M_w	Average Molecular Weight
N	Concentration of Pair Sites
PAH	Poly(allylamine hydrochloride
PAZO	Poly[1-[4-(3-carboxy-4-hydroxyphenylazo)benzene sulfonamide]-1,2-ethanediyl]

PEI	Polyethylenimine
pH	Hydrogen Potencial
PhD	Doctor of Philosophy
POMA	Poly(o-methoxyaniline)
PSS	Poly(styrene sulfonate)
PVS	Poly(vinylsulfonic acid Poly(o-methoxyaniline)sodium salt)
q	Electric Charge
QMT	Quantum Mechanical Tunnelling
QUB	Queen's University of Belfast
r	Radius
R	Correlation Coefficient
R_ω	Hopping Distance
R	Resistance
RADAM	Radiation Damage in Biomolecular Systems
RNA	Ribonucleic Acid
s	Thickness
S	Solid
SRS	Daresbury Synchrotron Radiation Source
SSB	Single Strand Break
STM	Scanning Tunneling Microscope
SUV	Small Unilamelar Visicules
T	Temperature
T	Thymine
UK	United Kingdom
UNL	Universidade Nova de Lisboa
USA	United States of America
UV	Ultraviolet
UV1	Experimental Setup to Photoabsorption Spectroscopy Studies
UVC	Ultraviolet C
v	Linear Velocity
V	Voltage
VUV	Vacuum Ultraviolet
WC	Watson-Crick
W_M	Energy Barrier
XPS	X-ray Photoelectron Spectroscopy
Z	Atomic Number
Z	Impedance
Z'	Real Component of Impedance
Z''	Imaginary Component of Impedance
2D	Two Dimensions

β	Exponential Coefficient
γ	Surface Tension
Γ	Adsorbed Amount per Layer per Unit Area
δ	Phase Angle
δ	Partial Derivative
Δt	Time Frame
ε	Absorbance Coefficient
ε	Dielectric Constant
ε_0	Permittivity of Free Space
π	Surface Pressure
π_c	Collapse Pressure
σ	Complex Conductivity
τ	Relaxation time
τ_0	Characteristic Relaxation Time
ω	Angular Frequency

1. INTRODUCTION

The mutagenic or lethal effects of ionising radiation at the cellular level can be traced to structural and chemical modification of the biomolecular environment and its constituents. As far as radiation is concerned, not only is deoxyribonucleic acid (DNA) found to be a sensitive biomolecule in living tissue, but also the effects on the cellular constituents, namely the cell membrane, are not to be discarded particularly when its role on the interface mechanisms within the cell are vital for the physiological balance survival. Although the radiation damage in biological tissues has been extensively investigated, the processes that occur at molecular level are not well understood [1]. In fact, it is known that when ionizing radiation attains the matter, it produces in very short periods of time large amount of ions, radicals, excited neutrals and ballistic secondary electrons with initial kinetic energies below 100 eV [2,3], which causes physical and chemical modifications in the medium. Moreover, it was shown that electrons with energies between 4 to 6 eV induce strand break formation in double-stranded supercoiled DNA [3,4]. Concerning the effect of low energies, in the ultraviolet range, several efforts have been developed in order to attain answers about interaction mechanisms leading to damage at the molecular level. Results of radiation damage carried out in DNA plasmid investigated using 7-150 eV synchrotron radiation [5], revealed DNA single-strand (SSB) and double-strand (DSB) breaks occurs in all energy range, for both dry and solution plasmid DNA. The presence of water molecules was seen to boost the radiation effect [6], due to $OH^{\bullet}$ radical and other reactive oxygen species, such as the superoxide radical and oxygen peroxide. It is now well established that low energy electrons (< 30 eV) on DNA/RNA and its constituents (the nucleotide bases, nucleosides and water) can increase the damage probability, at very specific incident energies or resonances [4,7]. Moreover, the effect of these low energy electrons through dissociative electron attachment processes have been found to be site and bond selective as a function of the energy [8].

Due to the complexity of biological tissues and to go further in the research of the radiation effects on biological molecules a new approach should be addressed in order to obtain well controlled biological samples in an environment close to the cell. This new approach involves the production of functional biomimetic heterostructures, namely, membranes and rudimentar cells at planar interfaces. In this context, will be necessary to keep the membrane in an as far as much natural aqueous environment, and for the sake of quantitative characterization, it is desirable to have it at a planar solid interface. A strategy to accomplish this is to assemble, at a liquid/solid interface, biological molecules as lipids, DNA, proteins and enzymes together with a soft cushion of adsorbed polyelectrolytes having high water content [9,10]. Another possibility is to produce lipid layers at a liquid/air interface and introducing cell constituents as DNA, through the liquid phase – Langmuir membranes [11]. These heterostructures can be exposed to radiation and the damage can be quantified in each constituent [12]. As DNA molecule is within the cell nucleus responsible for the transmission of the genetic information, stress should be made on of radiation damage to this molecule. The importance given by the scientific community to the study of DNA, the richness and diversity of the existing literature, motivated for the present doctoral project. Thus the effect of UV radiation and Carbon Ions beams onto DNA and phospholipids cast films and on biomolecular heterostructures has been addressed to

better understand radiation damage in these biological molecules under conditions close to the cell environment, where water molecules are known to play a relevant role. Due to past experimental results within this thematic, this work started with the characterization of the effect of UV radiation on DNA cast films by means of by vacuum ultraviolet spectroscopy (VUV), Fourier transform infrared spectroscopy (FTIR) and X-ray photoelectrons spectroscopy (XPS). The obtained results with the nitrogenous bases showed that the damage depends on the nature of the heterostructure in the study, thus it was considered more appropriate to the study of the DNA molecule instead of their various elementary units. The studies performed show that although these may be visible changes in the VUV spectrum of films of DNA, they are not sufficient to characterize the changes at the molecular level, unlike infrared spectroscopy that has shown that most characteristic bands of chemical bonds decreased in intensity, and generally the affected bonds are the C-O stretch of the furanose in backbone, in the PO_2^- groups, in the thymines, cytosines and adenines groups. UV radiation was shown to affect the thymines involved in reverse Hoogsteen third strand binding which is consistent with the observed decrease C2=O2 stretching of thymines involved in reverse Hoogsteen third strand binding, while the C2=O2 stretching vibration of thymine in single or double-stranded remain unchanged. The XPS spectroscopy allowed validate the VUV and IR results and conclude that ionized phosphate groups, surrounded by the sodium counterions, congregate hydration water molecules which play UV radiation protection a role. At a later stage of this work came the opportunity of also conducting studies on damage caused by ion beams, namely carbon ions. Since the exposure of carbon ions beam is being currently addressed for cancer therapy, measurements on their effect on DNA samples have also been included in this thesis.

In real biological systems the DNA molecule is within the nucleus, which consists of a phospholipid membrane, thus it was considered important, after the study of radiation damage in the DNA chain, understand if the phospholipid membrane comprises a barrier protective radiation or present other behaviour. It was considered important to carry out studies on the effect of UV radiation on phospholipids but, due to the short and limit period of time to access to the synchrotron facilities, just one phospholipid was selected, DPPG, because is an constituent of lung, that is one of most affected tissues in the case of carcinogenic pathology. DPPG solution and DPPG cast films were prepared and to facilitate the DPPG adsorption on the substrate and to preserve the water molecules in the sample, DPPG/PAH layer-by-layer films were prepared. The samples were irradiated and studied by UV spectroscopy and atomic force microscopy, allowing the UV spectrum characterization and concluding that the LbL films were not affected by prolonged UV irradiation in the absence of water molecules indicating that the VUV technique can be used for characterization of lipid heterostructures.

After isolated DPPG studies, to simulated the system nuclear biomembrane with DNA inside, phospholipid Langmuir monolayers were prepared with DNA in the subphase. The results allowed concluding that the presence of DNA in the subphase influences the stability of monolayers of DPPG due to the interaction of charges. To further understand the influence of ionic strength study were also conducted studies with EDPPC monolayers, that these results demonstrated the importance of the ionic nature of the monolayers, in this case, the monolayer stabilized by the presence of DNA. In the case of DPPG, given the importance of developing anti-cancer therapies for lung, the work progreed

with the study of the effect of radiation on DPPG monolayers, having concluded that at high surface pressures, corresponding to a real membrane, the DNA molecules decreased monolayer instability caused by irradiation.

Finally being the radiation necessary for the anticancer therapy emerged the idea to create a radiation biosensor that allows monitors the radiation exposure during the therapies. The electrical impedance sensors are the most adequate to this function, so DNA cast films electrical characterization was done by impedance spectroscopy. The obtained results reveals experimentally about the DNA electrical conduction mechanism was electron hopping between base-pairs and phosphate groups, where these work as electron acceptors. The hooping distance was calculated using the correlated barrier hopping (CBH) model and revealed to be equal to the distance between base pairs. The results obtained show that the electrical conductivity can be used to monitor DNA damage by UV radiation, condition important to the UV radiation biosensor. Moreover, it was found that the electrical conductivity is proportional to the number of phosphate groups in the DNA chain, and therefore, this conclusion allows explain the divergence found in the literature about its electrical properties where there is no agreement is DNA is conductor, semiconductor or insulator.

This thesis is organized into four more sections. Section two presents a literature review on fundamental concepts to focus the presents work, an explanation of biological environment and its main constituent, a description of the phenomena of radiation-matter interaction and finally the potential of mimicking the cellular medium and its application to the biosensors development. On section three the artificial membranes preparation techniques are addressed stressing materials and methods the details of particles sources used to irradiate the samples are presented and finally description of sample techniques characterization are summarized. In section four, the scientific papers which compile the experimental data obtained during the implementation of the PhD work are presented. Finally, the section five contain the principal conclusion obtained in this study, the future prospects and finally the publications and communications presents during the works period.

2. THE EFFECTS OF RADIATION ON BIOLOGICAL SYSTEMS

The study of physical and chemical damage occurring in models of the cellular environment, termed biomimetic systems, was the purpose of the work presented in this dissertation. This chapter examines the theoretical concepts necessary to understand the experimental results, in particular the cell model, the interaction between radiation and the cellular environment, processes for mimicking cell and the use of these models in the development of biosensors for radiation.

2.1. BIOLOGICAL ENVIRONMENT

2.1.1. THE CELL

The cell is the basic unit of life. It is the structural and functional unit of all living beings. The cells were first observed in 1665 by Robert Hooke [13] when examining cork slides under a crude microscope. A cell theory was only developed in 1847 by Theodor Schwann and Matthias Jakob Schleiden stating that all organisms are composed of one or more cells. All cells come from preexisting cells. Vital functions of an organism occur within cells [14], and all cells contain the hereditary information necessary for regulating cell functions and for transmitting information to the next generation of cells [15]. There are two main groups of cells, prokaryotic and eukaryotic cells.

(i) Prokaryotic: These cells are usually small, lack a nucleus and do not have any membrane-bound organelles (see figure 2.1.A). The genetic information of prokaryotes is typically in nucleoid of DNA strands arranged in a circular shape, but they may have additional DNA in a circular loop called a plasmid [16,17,18].

(ii) Eukaryotic: These cells are more complex than prokaryotic cells. Its volume is about 10 times higher than the prokaryotic cells and may reach volumes 1000 times larger. The main differences are the existence of many types of organelles and a nuclear membrane which stores the DNA that offers a spiral configuration associated with proteins (see figure 2.1.B). The complex of DNA and proteins is called chromatin. The membrane that surrounds this type of cell contains the same functions as a prokaryotic cell membrane, varying slightly in the configuration. Unlike in animals, plants present cell waals which prevent the cellular expansion after absorbing water [16,17,18].

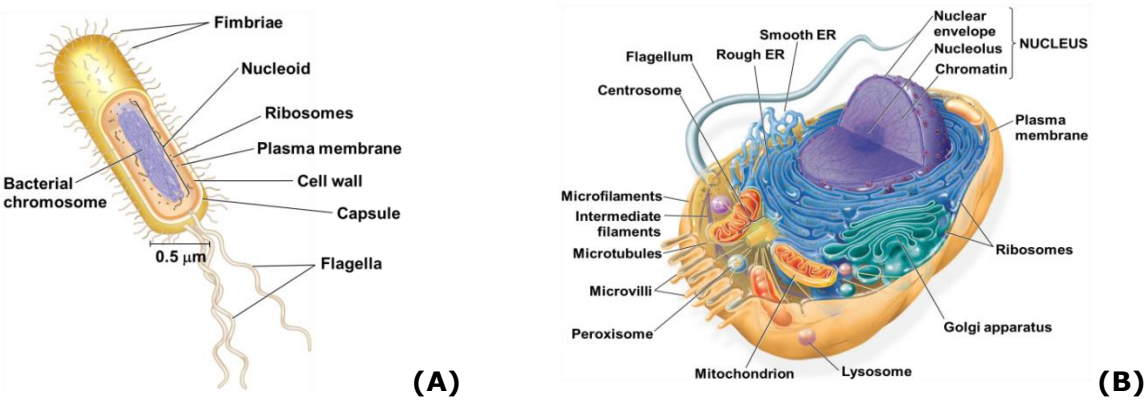

Figure 2.1. Cell structure: (A) Prokaryotic cell; (B) Eukaryotic cell [19].

2.1.2. CELL MEMBRANE

The cell membrane, also known as plasmatic or cytoplasmic, represents one of the main components of the cell, since it defines the bounds and adjusts the transport mechanisms across cell waals. The membrane structure obeys the Fluid-Mosaic model, suggested by Seymour Jonathan Singer and Garth L. Nicolson in 1972, which states that the membrane is considered a two-dimensional liquid where molecules diffuse freely [20]. Despite this model being the one accepted by the scientific community, research is still ongoing. It is, however, well known that the fluidity of the membrane depends on the type of connection that occurs between the phospholipids. Connections only occur between phospholipids and proteins, without any covalent bonds, resulting from hydrophobic forces and hydrogen bonds [16,17,18]. The cell membrane is essentially formed by a phospholipid bilayer with integral (intrinsic) and peripheral (extrinsic) proteins, as depicted in figure 2.2. The cell membrane displays characteristics such as high hygroscopicity, selective permeability, a porous surface, a system for active transport of ions and numerous enzymes across the membrane which help its molecular stabilization. In addition, eukaryotic membranes have significant amounts of cholesterol that decreases membrane fluidity due to the presence of its rigid planar ring structure [16,17,18].

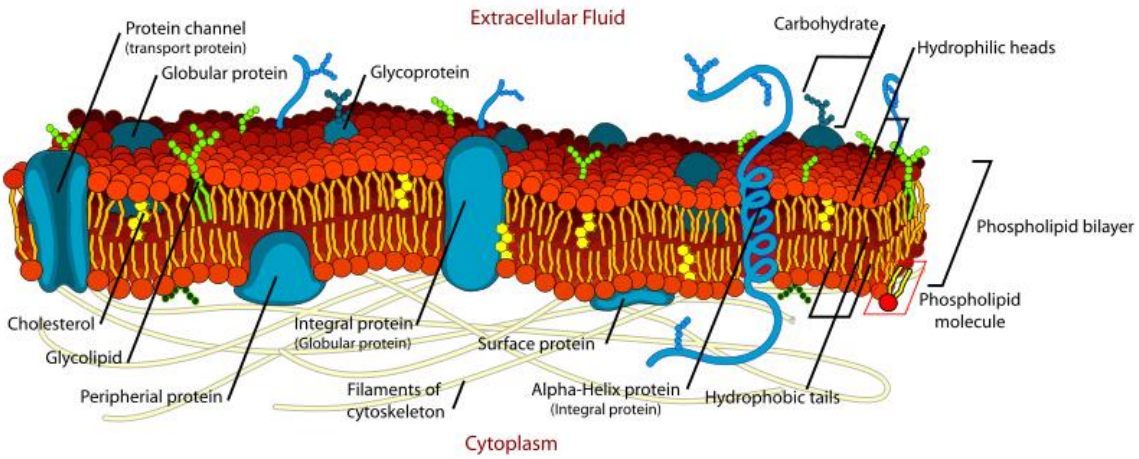

Figure 2.2. Eukaryotic cell membrane structure – Fluid-mosaic model [21].

2.1.3. PHOSPHOLIPIDS

As already mentioned, a phospholipid bilayer forms the body of the biological membranes. Although the lipid molecules belong to a quite heterogeneous family with diverse structures, they all exhibit water insolubility and solubility in organic solvents and are molecules formed by aliphatic chains that have –CH2– groups with at least eight carbons, where as there are rare exceptions having shorter chains. The lipids are classified according to the diagram displayed in figure 2.3 [16,17,18]:

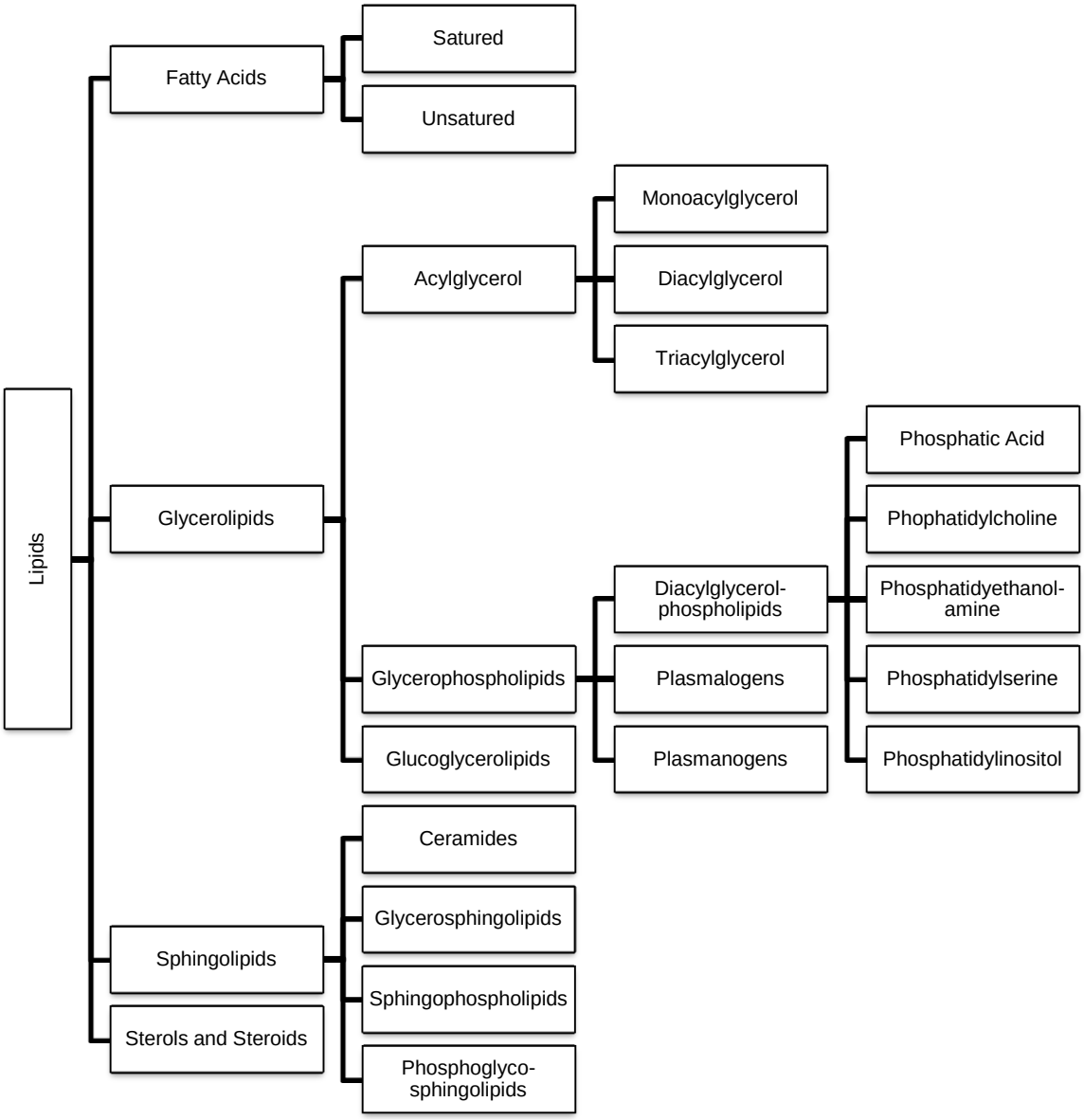

Figure 2.3. Shematic summary of lipids classification.

In the body these molecules are mediators of intra and intercellular signaling, they also constitute the main energy reserves (triacylglycerols) and lastly, they are the main structural elements of biological membranes. Although the relative amount of each type of lipid varies according to the organism the membranes hold [16,17,18]:

(i) Glycerophospholipids: They are the main constituents of biological membrane since they form the double lipid layer. They have a highly polar head group, integrated with a phosphate group, and a nonpolar aliphatic tail [16,17,18].

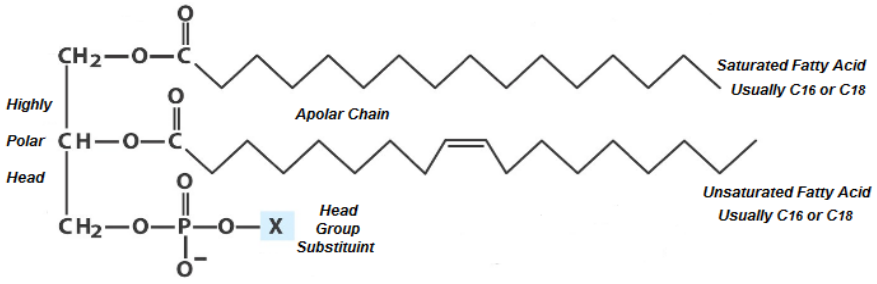

Figure 2.4. Glycerophospholipids structure [16,17,18].

Table 2.1. Example of glycerophospholipids composition [16,17,18].

Glycerophospholipid designation	Substituent Group designation	Substituent Group structure
Phosphatidic acid	Hydrogen	-H
Phosphatidylethanolamine	Ethanolamine	$-CH_2-CH_2-NH_3^+$
Phosphatidylcholine	Choline	$-CH_2-CH_2-N^+-(CH_3)_3$
Phosphatidylserine	Serine	$-CH_2-CH_2-N^+-(CH_3)_3$
Phosphatidylglycerol	Glycerol	$-CH_2-CHOH-CH_2OH$
Phosphatidylinositol	Inositol	$-CH(CHOH)_5$

(ii) Sphingolipids: Biological membrane's second class of lipids which mostly derives of sphingosine (C18) and has an amine chain link connecting the hydrophobic chain to the hydrophilic head [16,17,18].

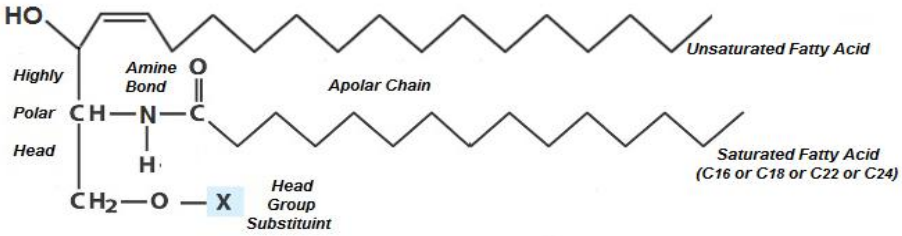

Figure 2.5. Sphingolip structure [16,17,18].

Table 2.2. Example sphingolip structure composition [16,17,18].

Sphingolipid designation	Substituent Group designation	Substituent Group structure
Ceramide	Hydrogen	-H
Sphingomyelin	Choline	$-CH_2-CH_2-N^+-(CH_3)_3$
Glycocerebroside	Glucose	$-CH-(CHOH)_4O$
Lactosylceramide	Lactose	$C_{12}H_{22}O_{11}$
Ganglioside	Complex Oligosaccharide and Sialic Acid	

(iii) Steroids: Structural lipids which provide rigidity to the membrane. Steroids are compounds possessing the skeleton of cyclopenta[*a*]phenanthrene or a skeleton derived therefrom by one or more bond scissions or ring expansions or contractions. Methyl groups are normally present at C-10 and C-13. An alkyl side chain may also be present at C-17. Sterols are steroids carrying a hydroxyl group at C-3 and most of the skeleton of cholestane. Additional carbon atoms may be present in the side chain [16,17,18].

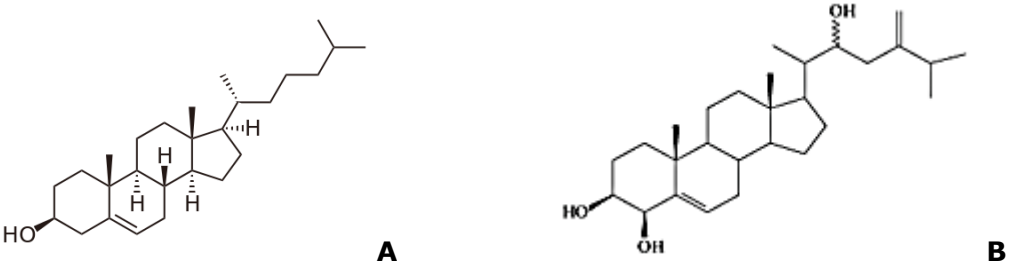

Figure 2.6. Examples of steroids: A) Cholesterol; B) 24-methylene-3β,4β,22-trihydroxycholesterol.

In the physiological environment phospholipid molecules aggregate in a crystalline state which allows an effective diffusion through biological membrane. The arrangement of hydrophilic heads and hydrophobic tails which allows selective diffusion is preventing the polar solute - amino acids, nucleic acids, proteins, ion – from crossing the membrane (its passage is made by a carrier protein) while the hydrophobic molecules pass through the membrane easily [16,17,18]. This is due to the special characteristics of phospholipids and the interactive forces between themselves - Colombian forces, hydrophobic and hydrogen bridges – making a cell capable to control its activity through exchanges between the intercellular medium and the extracellular medium. Inside the cell nucleus the same happens, such as it has a membrane formed by the same types of lipids that allow those types of exchanges.

2.1.4. CELL NUCLEUS

The nucleus is a membrane-enclosed organelle found in eukaryotic cells. It stores hereditary information as DNA and synthesizes RNA and ribosomes. The surface of the nucleus is bounded by two phospholipid bilayer membranes that form the nuclear envelope with a porous nature which confers permeability properties which allows efficiently exchanging substances with the cytoplasm [16,17,18].

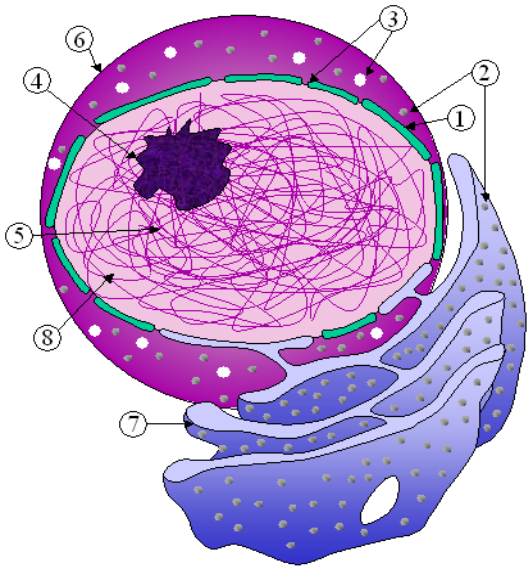

Figure 2.7. Cell nucleus structure: 1 – Nuclear envelope, 2 – Ribosomes, 3 – Nuclear pores, 4 – Nucleolus, 5 – Chromatin, 6 – Nucleus, 7 – Endoplasmic reticulum, 8 – Nucleoplasm [22].

When the cell is in a resting state there is chromatin in the nucleus. The chromatin clusters form the chromosomes that are thread-like structures located inside the nucleus of animal and plant cells. Each chromosome is made of protein and a single molecule of deoxyribonucleic acid. Passed from parents to offspring, DNA contains the specific instructions that make each type of living creature unique.

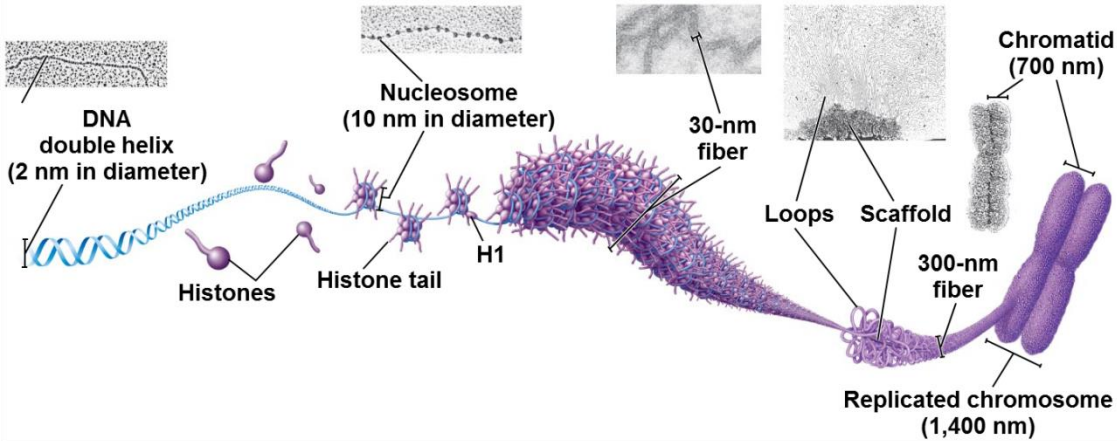

Figure 2.8. Cell nucleus: composition and structural units [14,15,16, 19].

2.1.5. DEOXYRIBONUCLEIC ACID

The most important molecule of life called deoxyribonucleic acid is found inside the nucleus. The presence of the DNA molecule in the cells was first detected in 1869 by the Swiss Friedrich Miescher [23] and its composition discovered by Russian Phoebus Aaron Levene in 1909 [24]. However, its structure was only published in 1953 by James Watson and Francis Crick [25]. Further in 1962, this discovery earned them a Nobel Prize of Medicine. The DNA is a long biopolymer whose monomers are nucleotides formed by a nitrogenous base (adenine, cytosine, guanine or thymine), a pentose and at least one phosphate group, and its sequence defines the genetic information that commands the development of any living being and its main vital functions. The DNA structure was also published in 1953 by Maurice Wilkins and Rosalind Franklin in two separate works featured in *Nature* magazine [26,27], where the DNA molecule patterns of x-ray diffraction exhibited a diagram in X-form. This method helped uncovering its structural properties, and revealed the presence of a helix, and even exterior arches which put in evidence the repetitive nature of the structural units.

These results were in agreement with the model proposed by Watson and Crick which argues that the DNA molecule (i) consists of two antiparallel helical polynucleotide chains coiled around the same axis to form a double helix (twisted in a right-handed fashion), (ii) provides the complementary base pairing which means the links between chains are made by pairs of specific molecules through hydrogen bonds, (iii) has the sugar and phosphate groups facing outwards in order to minimize the repulsive forces between the phosphate groups and nitrogen bases inside the helix (iv) obeys the rule of Chargaff, i.e. Adenine = Thymine and Guanine = Cytosine; (iv) is a very acidic species [16,17,18].

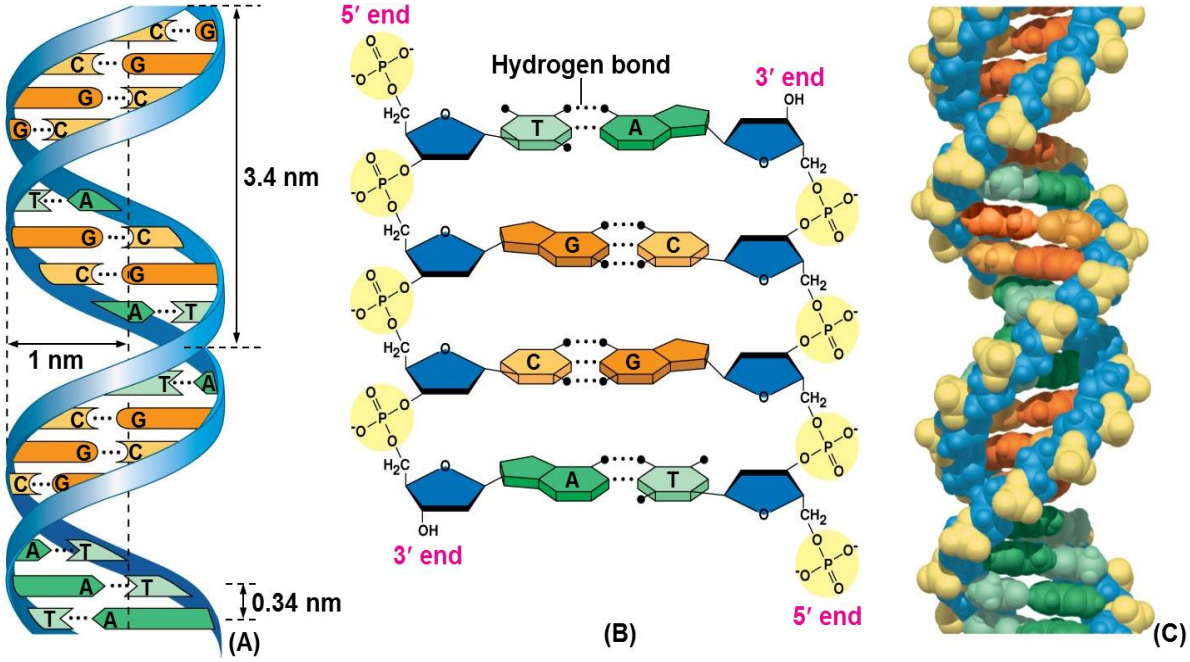

Figure 2.9. DNA double helix. (A and C) Helical structure. (B) Molecular composition and complementary base-pairing [19].

However, Watson-Crick Model does not mention this biopolymer's ability to acquire various structural conformations (figure 2.10); it solely postulates the principles of the DNA molecule structure.

In its most common form, B shape, the DNA molecule folds back upon itself in a complete loop every 10.5 base pair (bp) [28]; though this value may vary according to disturbances in the environment, such as A shape, conformation acquired when the molecule undergoes denaturation [29,30] or Z-form, called zig-zag, when the molecule undergoes chemical transformation, which is the least common structure [31]. The main features of the three structures that can be found in living organisms are presented in figure 2.10 – the most common B form, the rarer forms A and Z – note that other may be obtained by manipulation of the molecule.

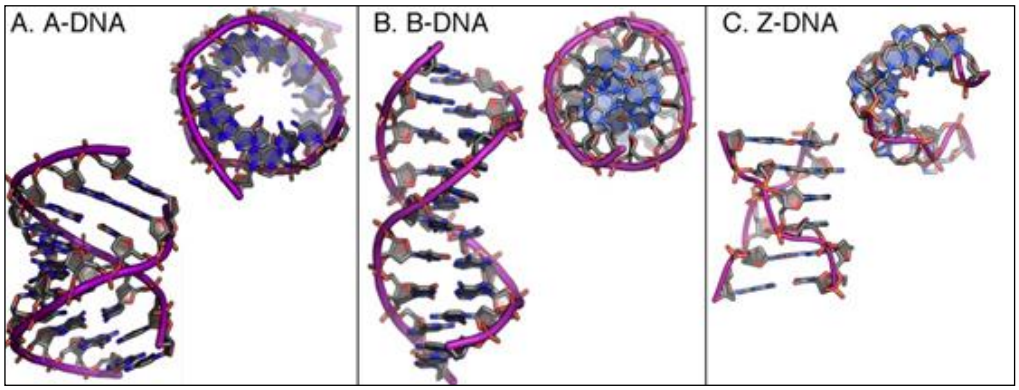

Figure 2.10. DNA double helix structure properties of A, B and Z forms [32].

Table 2.3. DNA double helix structure characteristics of A, B and Z forms [31].

	A form	**B form**	**Z form**
Helix Diameter	≈ 2.6 nm	≈ 2.4 nm	≈ 1.8 nm
Directional Torque	Right	Right	Left
Torque Angle	+32.7º	+34.6º	-30.0º
Helix Base Pairs per Turn	11.0	10.5	12.0
Major groove	2.8 nm	3.4 nm	4.5 nm
Minor groove	0.25 nm	0.33 nm	0.38 nm

The conformation acquired by the double helix is strongly influenced by the type of stabilization forces acting on the molecule. These forces are a consequence of the base-stacking between nitrogenous bases which varies accordingly with the type of base pairing, its repetition sequence, the hydrophobic interactions and the ionic interactions resulting of the negatively charged phosphate groups' protection by boding to divalent ions (repulsive forces). It is important to note that even though hydrogen bonds are extremely important in the double helix formation, these interactions do not have a role in stabilizing them [17].

2.2. RADIATION – MATTER INTERACTION

2.2.1. RADIATION

Radiation consists in energy emission and propagation through matter or space using perturbations with wave-particle duality properties. In order to simplify classifications of the type of radiation existing in nature, the scientific community divided radiation in two different types: (i) Corpuscular radiation, related to atomic and subatomic particles propagating at high speed; (ii) Electromagnetic radiation as a result of combining an electric field and a magnetic field which propagate simultaneously through space carrying energy. Electromagnetic radiation is classified according to its wavelength in the electromagnetic spectrum (See figure 2.11).

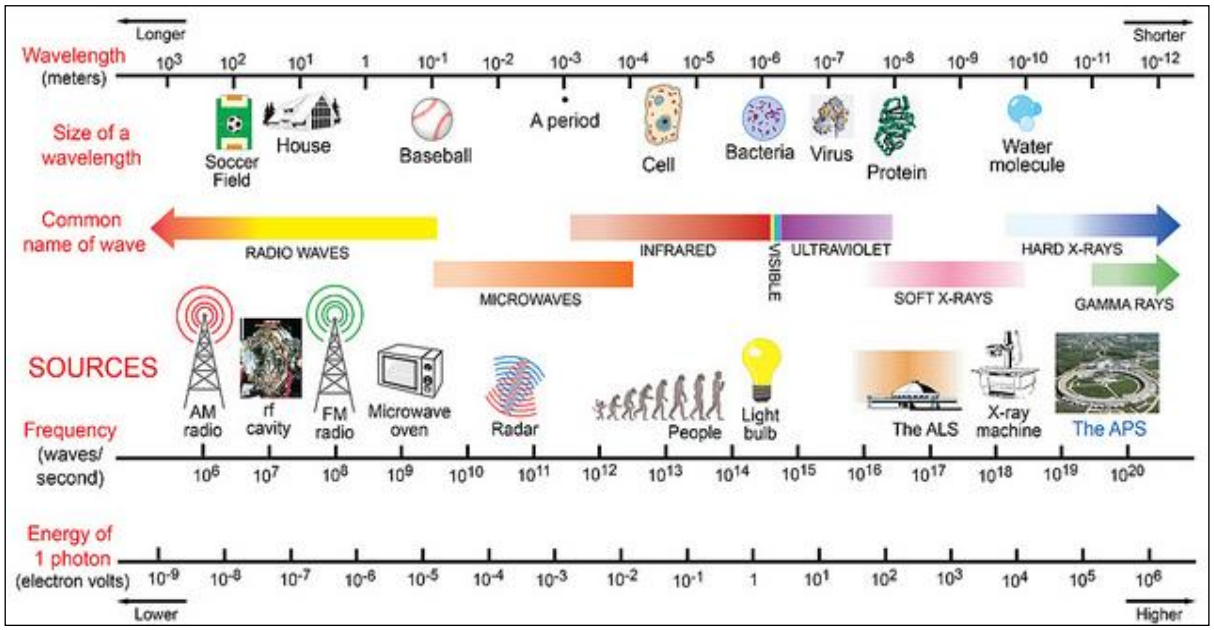

Figure 2.11. Regions of the electromagnetic spectrum and respective sources [33].

2.2.2. ELECTROMAGNETIC RADIATION AND BIOLOGICAL SYSTEMS

Electromagnetic radiation consistently produces effects on tissue or in any other kind of biological material in a situation in which there is energy transfer from radiation into the medium and the radiation is absorbed. Electromagnetic radiation is classified as non-ionizing and ionizing radiation depending on the produced effects. Non-ionizing radiation is all the absorbed radiation which leads to electronic excitation, i.e., an electron passage to a higher state of energy; it is an example ultraviolet radiation above 200 nm, visible radiation, infrared and microwave radiation. Ionizing radiation refers to the type of radiation which is absorbed and drives the liberation of one or more electrons of an atom or molecule; examples are Gama-rays, X-rays and UV rays under 200 nm [34].

2.2.2.1. Non-ionizing radiation

The main biological effects caused by non-ionizing radiation can be divided in two different types: thermal effects and non-thermal effects.

(i) Thermal effects: All the effects which produce an increase in the tissues temperature, which are a consequence of a direct heating of the biological tissue as a result of electromagnetic radiation absorption. Unlike non-ionizing radiation which has a higher wavelength, as in infrared radiation case, microwaves and radio-frequency radiation not only are absorbed by the skin but can also be absorbed by deeper layers of the tissues. Since temperature sensors can only be found in the skin, prejudicial effects can occur due to excessive heating in deeper regions which are not perceived by the living being [20,35].

(ii) Non-thermal effects: Electromagnetic energy non-thermal effects are the greatest concern basis because they involve the lowest energy fields. Unlike thermal effects which essentially depend on absorbed energy, non-thermal effects can significantly depend on the signal features, it being analogical or digital, and in addition, they can also depend on the type of modulation. Researchers defend that radio-frequency fields can influence cell membranes properties, including permeability, immune system response and also the activity of several enzymes. Nevertheless, studies have been inconclusive due to their inability to show cause-effect relations [36].

2.2.2.2. Ionizing radiation

Ionizing radiation can be classified in two different types according to its mode of interaction on matter: directly ionizing radiation and indirectly ionizing radiation.

(i) Directly ionizing radiation: Its energy is directly deposited through coulombian interactions on electrons contained in orbitals of atoms that constitute the medium. The main feature of this type of radiation is the fact that the ionizing particle is charged; examples include electrons, protons, alpha particles or heavy ions [34].

(ii) Indirectly ionizing radiation: The transfer process of radiation occurs in two stages:
(1) In the medium, release of a charged particle occurs which can be an electron released by a photon or a proton released by a neutron. (2) The released particles interact with other atoms or molecules of the tissue, in particular with water molecules, producing highly reactive free radicals which have the ability to diffuse and subsequently damage the molecules constituting the cellular tissue [34].

2.2.3. BIOLOGICAL EFFECT OF ELECTROMAGNETIC RADIATION

The effect of radiation on biological systems is characterized by progressive formation of events which differ according to a time scale leading ultimately to biological damage [20].

(i) Physical phenomena: They consist in interaction between charged particles and the atomic structures of tissues, which leads to ionization and ionic radicals formation in an extremely short time frame (around 10^{-18} s).

(ii) Chemical phenomena: Formation of ion pairs through an ionization process which leads to formation of free radicals and chemical bonds rupture (around 10^{-6} s).

(iii) Biological phenomena: The time that it takes to manifest biological damage after chemical bonds rupture is usually long, from a few hours to several days, weeks, months or even years. This type of damage is characterized by altering the proper functioning of cells or even cell death. Cellular activity is crucial for this kind of phenomena since cellular division requires DNA replication to be precisely performed; the higher the cellular activity is, the more vulnerable it becomes [37].
When a molecule is irradiated there are two types of changes which can occur. In high LET (Linear Energy Transfer) radiation, the direct action effects prevail which renders a molecule in stable yet damage state. Regarding ionizing radiation, damages caused by indirect action are more ordinary because the initial radiation does not directly affect the target molecule, it hits another molecule instead. In a situation where cells have a water content of approximately 70%, reactive centers produced intracellularly which interact with target molecules are essentially originated from changes in water molecules [34]. When radiation strikes a water molecule, formation of OH• and H• free radicals occurs which are characterized by a short half-life, high reactivity and by the presence of hydrated electrons [34]. The reactions occurring during water radiolysis will be promptly described:

Partial Reactions of Water:

$$H_2O \rightarrow H_2O^+ + e^-$$
$$e^- + H_2O \rightarrow H_2O^-$$
$$H_2O^+ + H_2O \rightarrow H^+ + H_2O + OH^\bullet$$
$$H_2O^- + H_2O \rightarrow OH^- + H_2O + H^\bullet$$
$$H^+ + OH^- \rightarrow H_2O$$

Global Reaction:

$$H_2O \rightarrow H^\bullet + OH^\bullet$$

OH• radicals produced will essentially react with nitrogenous bases, even though in the sugar molecule reduction of the hydrogen atom may occur. In pyrimidines' case (cytosine and thymine), OH• radicals are added to the double bond C(5)=C(6). Meanwhile, in pyridines' case (adenine and guanine), the radical is added to one of the molecule's double bonds, since any of them has reaction potential [38].

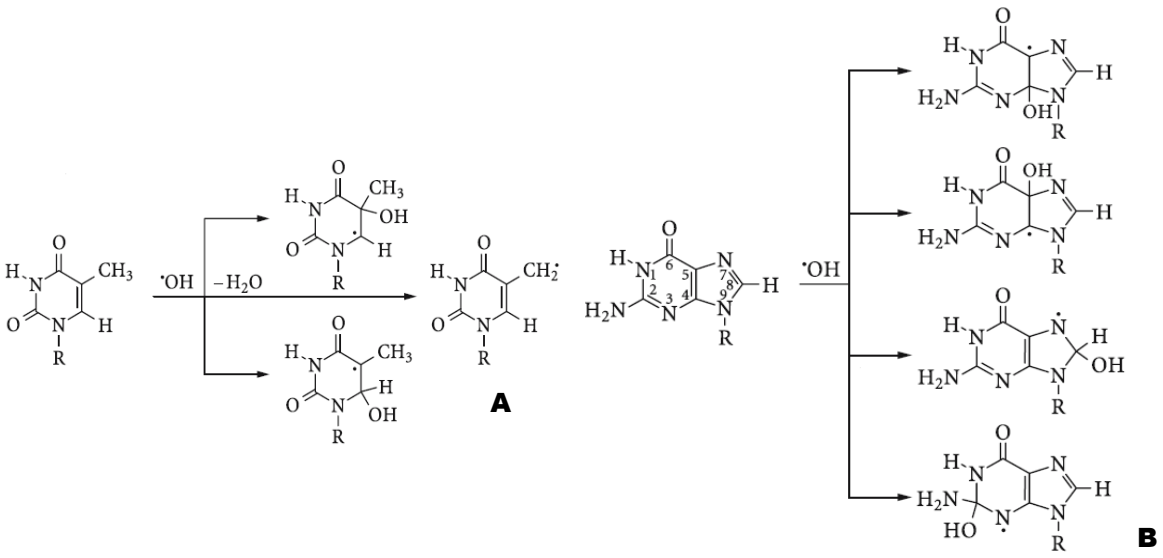

Figure 2.12. Example of the OH• radical representative reactions. (A) Pyrimidines; (B) Purines.

Analogous to OH• radical, H• radical is also an electrophile which confers a high affinity for electronegative centers, as in C=C double bonds case.

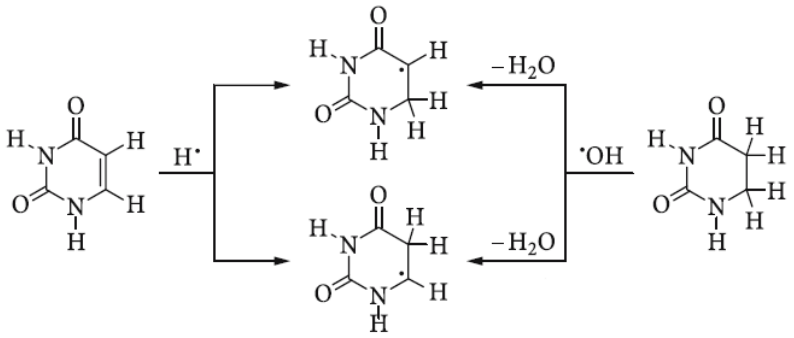

Figure 2.13. Example of the H• radical representative reactions in nitrogenous bases.

In the presence of oxygen, most radicals are converted to the corresponding peroxyl radicals, with the exception of radicals composed of central heteroatoms which do not react in substantial amounts with O_2 molecules [38].

Reactions Occurring in Aqueous Medium in the Presence of O_2

$$e^- + O_2 \rightarrow O_2^{-\bullet}$$
$$O_2^{-\bullet} + H_2O_2 \rightarrow OH^- + HO_2^\bullet$$
$$H^\bullet + O_2 \rightarrow HO_2^\bullet$$
$$HO_2^\bullet + H^\bullet \rightarrow H_2O_2$$
$$OH^\bullet + H_2O_2 \rightarrow H_2O^+ + HO_2^\bullet$$
$$R^\bullet + O_2 \rightarrow RO_2^\bullet$$

In basic or neutral medium, C(6)-peroxyl radicals show a sufficiently long half-life to experience a N(1) deprotonation followed by a $O_2^{\bullet-}$ radical elimination. In acid and basic medium where the radicals concentration is high, $O_2^{\bullet-}$ radical elimination is exceedingly slow and it becomes irrelevant when compared to the peroxyl radicals half-life [38].

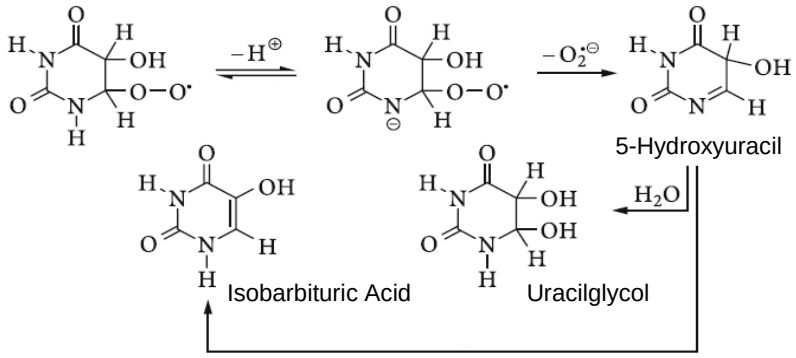

Figure 2.14. Example of reactions occurring in the presence of oxygen.

Ionizing radiation can also lead to structural changes in several macromolecules present in cells. In lipids case, radiation damage comprises the formation of unsaturated fatty acids peroxides which induce structural changes in the cell membrane, inactivation of membrane receptor molecules and permeability changes. Regarding nucleic acids, changes occurring are essentially loss or damage of bases, thymine dimers formation, single or double strand breaks and also DNA-protein dimmers formation (figure 2.15) [39,40], as well as liking chains and adducts [41].

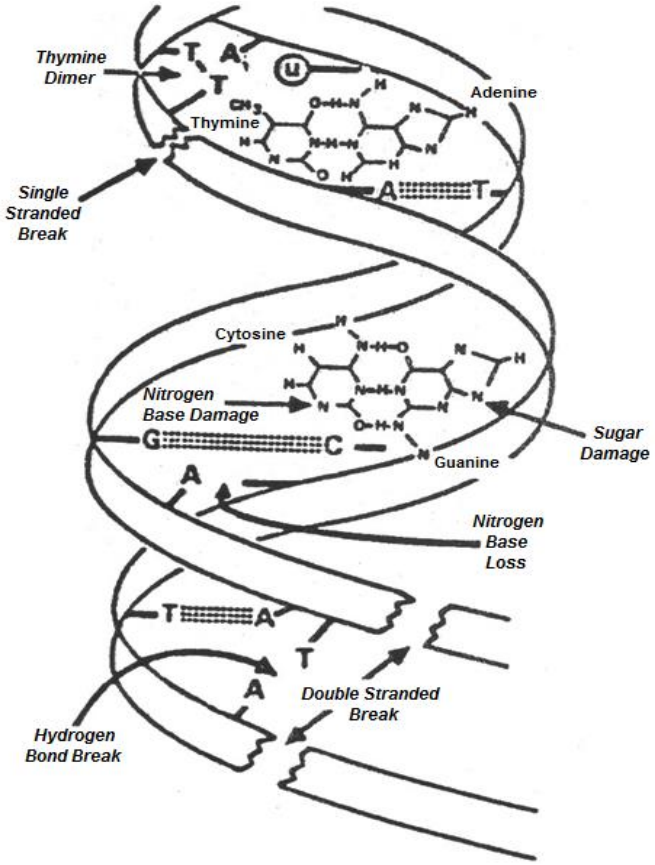

Figure 2.15. Types of damage produced by ionizing radiation in the DNA molecule.

2.3. CELL MEDIUM MIMETIZATION

2.3.1. BIONIC AND BIOMIMETICS

Biomimetics is a technologically-driven approach which employs fundamental principles of nature's design. According to Benyus [42] there are three factors that describe this new field of study.

(i) ***Nature as a model***: Study and mimicking of nature's models, using those as a source of inspiration for models and processes aiming to solve essential human problems.

(ii) ***Nature as a standard measure***: Use of ecological time scales to evaluate the relevance of human innovations. Nature, after four billion years of evolution, has optimized the things which work, last and are fit.

(iii) ***Nature as a mentor***: Observation and evaluation of nature from a different perspective aiming to the beginning of a new era based on what we can learn from Nature and not on what we can extract from it.

According to *Podborschi et al,* bionics or biomimetics is a science which studies the principles of nature followed by application of these principles [43]. Since biomimetics deals with application of biological system's principles, structures and processes, this field of study has become an interdisciplinary area which combines biology and engineering, architecture and mathematics [44,45].

Podborschi et al [43] classify bionics according to five primary categories:
(i) ***Total mimetics***: The product's material structure is indistinguishable from its natural model. Examples are the flying machine first attempts of construction.

(ii) ***Partial mimetics***: Modified version of the natural model, as an example is artificial wood.

(iii) ***Non-biological analogy***: Functional mimetics used, for example, in developing building support's surfaces and structures.

(iv) ***Abstraction***: Use of an isolated mechanism, an example is upgrading of fiber resistance of certain materials.

(v) ***Inspiration***: Driving creativity in developing architectonic materials and structures with similar engineering to plants, animals and insects.

Wahl suggests that bionics and biomimetics represent two distinct approaches to *design* and *nature* based in different conceptions of the relationship between nature and culture [46]. On one hand, bionics deals with predicting, manipulating and controlling nature; on the other hand, biomimetics aims

at having nature's participation, and as a consequence, holds a greater contribution to sustainability. According to this author, a switch to design-mediated sustainability requires a holistic and nature and culture supported approach inside a dynamic and interlinked system.

In literature a diverse array of definitions can be found, among them: Bionics is a science which studies the principles of nature and its application on searching for solutions against the problems humanity faces [43]. Additionally, biomimetics will continue to influence our lives because even though major progresses were accomplished, there is still a lot to know about nature.

2.3.2. Origin and Evolution of a New Science

In the history of mankind there are records of several designers using natural models as a source of inspiration for their works. According to Lodato [44], Leonardo Da Vinci could be considered the first Bionic researcher, since most of his creations were based on observations of nature.

The term Bionics appeared for the first time in 1968, introduced by Jack E. Steele, an engineer of the USA Air Force, while working in the Aeronautics Division. Steele defined bionics as "the analysis of the different ways living systems operate and the discovery of nature's artifices, representing them in hardware". Steele's Bionic concept was focused on mimicking biological forms and physiological structures of organisms, using induced biological characteristics as a starting point to technical development. The term Bionics, from the greek *element of life*, was officially used as a symposium title in September 1960 [47]. Only in 1997, scientist and writer Janine Banyus introduced the concept Biomimetics in her book *Biomimiry: Innovation Inspired by Nature*. This new concept was characterized by having wider significance domains then the bionics concepts until then known. Biomimetics not only considers the imitation of the biological form, but also includes the concept of replication of the living organisms' behaviour.

In the last years, engineers have shown an increase interest in capturing design concepts from nature, especially in the last decade [44]. This rise has been notorious since it became more frequent to find books, articles, conference sessions and university courses about Bionics and Biomimetics [48]. According to Dicksion, nowadays one of the reasons for the increase interest in Bionics is the production methods' high degree of sophistication. Only recently has Humankind came across with a group of sufficiently sophisticated tools able to mimic characteristics of biological structures which are very complex. Since there has been extensive innovation in the fields of Science of Materials, Electrotechnic Engineering, Chemistry and Molecular Genetics (among other science fields), it is possible to design and develop complex structures at a molecular level. Developing knowledge in plants and animals allows the biologist to identify specific relations between structure and function and, consequently, provides assistance to engineers when they come across with similar problems.

2.3.3. Biomimetics of Membranes

As noted previously, biological membranes are characterized by a single lipid bilayer whose function, among others, consists in the transport of molecules and ions. Molecules which take part in the lipid

bilayer do not form covalent bonds among themselves and consequently, are characterized by some degree of flexibility, ability of conformation switching and motility [49]. The most studied models among cell membrane biomimetic systems are: (i) Langmuir films composed of lipid molecules at the air/water interface [50]; (ii) Liposomes, phospholipids vesicles mimicking a sphere-shaped lipid bilayer [51]. Vesicles' method was developed in 1965 by Bangham and his collaborators when studying ion diffusion in the mimetic lipid membrane [52]. In the last years, study of liposomes has been focused in controlled incorporation and release of drugs – drug delivery – due to its protection ability, structural versatility, composition, fluidity and possible molecule incorporation independent of solubility and structure [53].

Liposomes are obtained by liposomal dispersion in aqueous medium, and they can exhibit different sizes and number of bilayers. Size, as well as number of bilayers intercalated with aqueous medium, can be manipulated with different preparation methods and lipids composition. The most common liposomes found in literature are multilamelar vesicles (MLVs), small unilamelar vesicles (SUVs), large unilamelar vesicles (LUVs) and multivesicular vesicles (MVVs).

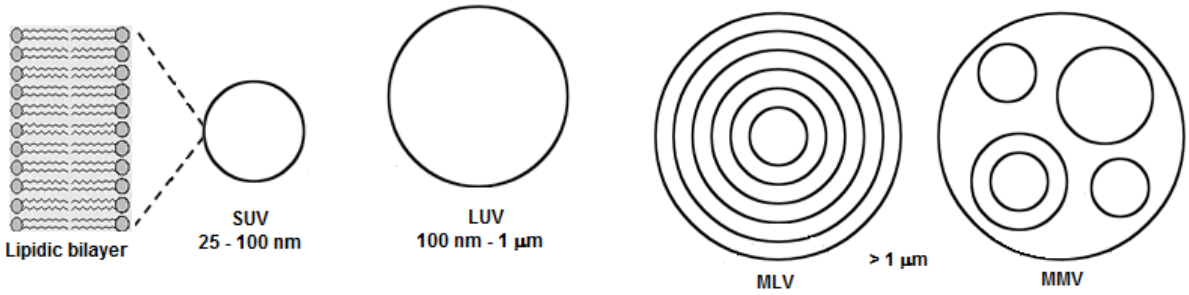

Fig. 2.16. Schematic representation of lipid bilayer and SUV, LUV, MLV and MMV.

Liposomes can be immobilized over a substrate in order to study interactions between membranes and molecules of biological interest, such as, proteins, peptides or drugs. Liposome immobilization and stabilization over solid surfaces play an important part in biosensors [54], whose development is based on interactions between immobilized lipids and specific proteins, and additionally, may require incorporation of drugs or proteins, as in the case of drug delivery.

In literature there is an array of different studies of the development of membranes in solid substrate model-systems, including Langmuir-Blodgett (LB) films and layer-by-layer (LBL) films. Since liposomes' interior and exterior layers are hydrophilic, surface interactions include electrostatic and hydration forces, besides van der Waals forces, and consequently, this technique will allow phospholipids to be assembled with multilayers of polyelectrolytes which constitute a suitable matrix to their immobilization. This technique also allows encapsulating biomolecules without altering the native aqueous environment by contact with polyelectrolytes [55].

2.4. BIOSENSORS

In literature, a Biosensor can be defined as an analytic device which contains a biological element capable of recognizing a certain substance connected or integrated in a transductor which converts a biological response in an electric or optical signal proportional to the detected compound concentration [56]. The typical components of a biosensor are: a) Bioreceptor, which interacts specifically with the analyte; b) Interface Architecture, where a specific biological molecule interacts with an analyte and originates a signal captured by the transductor; c) Transductor; whose signal is converted in an electrical signal and amplified by a circuit detector using an appropriate reference and sent to a processor; d) Software, it converts the effects in clean data; e) Display, presents data converted by software in order to facilitate a query. Biosensors can be used in different types of samples, such as animal fluids, food samples, cell cultures and environment samples.

2.4.1. BIOSENSORS DEVELOPMENT

Biosensors constitute a selective model due to the possibility of adjusting specific interactions to a certain biological compound through its fixation over an electrolyte surface. The most used molecules as biosensors are enzymes, nucleic acids, antibodies and antigens; enzymes are the most commonly found in literature [57,58,59]. A multiplicity of biosensors can be found in laboratory and some of them are fundamental tools for clinical diagnostic tests. Nevertheless, production of portable and cheap devices is limited to a well-known example, the glucose sensor [60]. In many cases, the major limitations of producing devices for diagnostic tests are the weak ability to improve the transduction principle and the production method low quality-cost ratio. As a consequence, clinical tests are limited to qualified users and to high cost equipments.

Biosensors can be classified according to the technique used to convert a biochemical process in an analogical signal, accordingly, the documented sensors include: a) Optical [61]; b) Piezoelectric [62]; c) Calorimetric [63]; d) Electrochemical [56]; e) Electrical [64]. They can also be classified according to the biomolecule which recognizes the target-analyte, as an example: i) Affinity sensors, when the bioreceptor uses only interactions between molecules, as in antigen-antibody's case [64]; ii) Enzymatic or catalytic sensors, when the analyte is the enzyme substrate which participates in a catalytic reaction; the latter is detected using the signal produced by the substrate or by the enzymatic reaction product [56]. Electrochemical techniques and electrical impedance allow measuring electrical properties in order to extract such informations from biological systems. Electrochemical biosensors are usually based on enzymatic catalysis of a reaction, which occurs in solution and produces and consumes electrons [56]. During this PhD work, the aim was to develop biosensors for application in solid/air interfaces and not in solid/solution interfaces. Therefore, instead of employing the electrochemical technique, the electrical impedance technique was used in the development of the radiation biosensors studied.

2.4.2. ELECTRICAL IMPEDANCE BIOSENSORS

Biosensors based on electrical impedance measurements can render different informations about the system, from film changes to medium changes. Such is owed to the ability of the impedance measurements with tension or alternating current (AC) of a material to combine both capacitive and resistive properties [65]. Frequency regions of AC tension can give us informations about the electrical properties of different events occurring in the analyzed system, as in biological reactions on electrode surfaces. The variety of biomolecules used as AC biosensors is extensive, just as the degrees of success obtained. Antibodies and recognition molecules have been immobilized over electrodes, and its detection is studied by changes in capacity and/or resistance when the antigen binds to the sensor [64]. Even though AC impedance measurements in the field of biological systems were not extensively explored, several works describe this detection model with sensors of polymeric films, such as the electronic tongue [66].

3. EXPERIMENTAL METHODS

Experimental studies using an array of different sample preparation methods, different radiation sources and some widespread physical chemistry characterization techniques of materials were developed to study particle damage in biomimetic membranes. In this chapter, the preparation of heterostructure techniques, the radiation sources and the characterization techniques used throughout this work will be thoroughly described.

3.1. THIN FILMS PREPARATION TECHNIQUES

In chapter two was reported the necessity to resort to a few simulated membranes techniques to study physical chemistry phenomena happening in the cellular membrane during the exposure to particle beams. To do so, cast, layer-by-layer and Langmuir techniques were adopted. In this section, the techniques mentioned will be described in detail.

3.1.1. CAST TECHNIQUE

Thin films production using the cast technique was applied in isolated material characterization. This technique consists in covering the substrate surface using a volume of an aqueous solution of the material studied. Using a rotator bomb, water evaporates by bombing, leaving the material in a condensed state deposited in the substrate surface. This technique allows the production of films composed of only one material having a micrometre thickness and the inexistence of high concentration of water molecules in the sample [66].

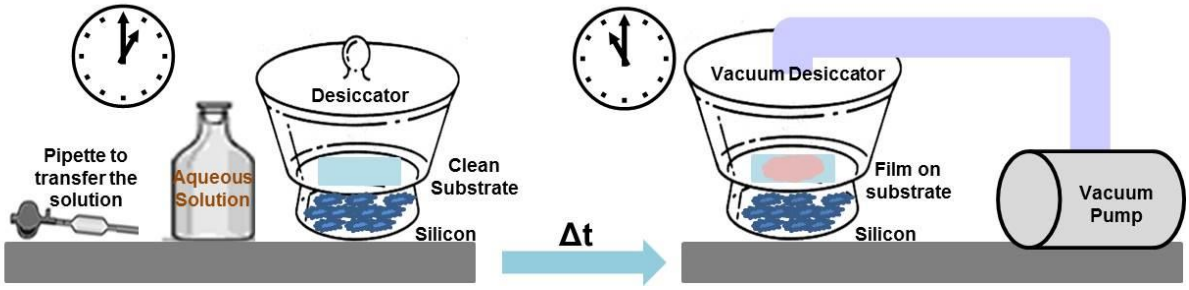

Figure 3.1. Scheme illustrating the film preparation using the spilling technique.

3.1.2. LAYER-BY-LAYER TECHNIQUE

Layer-by-layer technique is used to prepare self-assembled films of ionic molecules [67,68,69] since the film assembling process is based in electrostatic interactions. The substrate with its surface covered in OH^- ions, after a previous chemical treatment using piranha solution, is immersed in a

solution of cationic material during a time frame ∆t. Afterwards, the material is removed and washed in ultra-pure water and immersed in an solution of anionic material during a time frame ∆t´ (that can be the same as ∆t or not). After immersion, the substrate is removed and washed in ultra-pure water, and the process is repeated n times depending on the number of bilayers needed. In figure 3.2 the process of layer-by-layer film preparation is depicted.

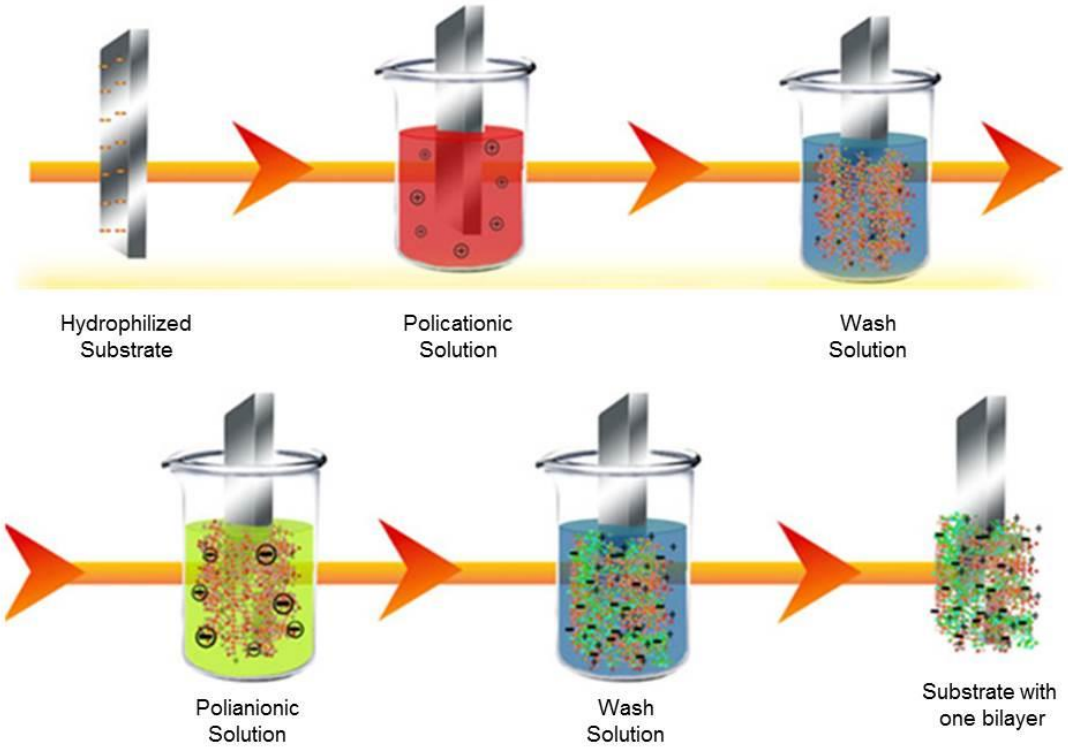

Figure 3.2. Scheme illustrating the layer-by-layer preparation method of a bilayer film.

In addition, the potential of this method is reinforced by the large variety of molecular systems that have been successfully used to assemble macromolecules such as polyelectrolytes, functional polymers, dendrimers, ceramic and biological molecules [70]. Particularly, with respect to biological molecules, proteins as cytochrome C, lysozyme, myoglobin, bacteriorhodopsin, glucose and/or diaphorase, enzymes, DNA and lipids have been successfully incorporated in a LbL structure [59]. Therefore, the LbL method has shown to be suitable for the creation of biomolecular heterostructures with different functionalities such as those in a living cell, or at least to mimic these biological structures. As the LbL technique requires adsorption at a solid/liquid interface, the kinetics of adsorption and layer proprieties greatly depends on adsorption parameters such as solution concentration, ionic strength, pH, temperature, molecular weight, molecule charge density and time of immersion.

3.1.3. LANGMUIR MONOLAYERS TECHNIQUE

Langmuir technique is used to prepare films composed of molecules with both hydrophilic and hydrophobic regions, which is the case of the phospholipids that were characterized in this work. This technique requires a specific device – a Langmuir probe – which consists in a plate coupled to a Langmuir trough working as in a surface tension sensor, and two movable barrier blocks that allow the probe surface area variation. This apparatus is described in detail in the section 3.3.5 On the other hand, Langmuir films or more accurately called Langmuir monolayers are prepared adding over the aqueous surface an amount of amphipathic molecules dissolved in a volatile and immiscible solvent, typically clorophorm, occupying the total surface area available. It is important to note that choosing between a pure solvent or a mixture of solvents is a decisive factor since it should favour the highest molecule dispersion possible over the aqueous phase surface [11]. When the solvent evaporates, the molecules will be disposed in an energetically favourable monolayer, having its polar groups immersed in the aqueous subphase and the hydrophilic tails directed in the opposite direction [71]. Afterwards, the monolayer is compressed leading to a decrease in the surface area available, which forces the molecules to gather, creating a compact monolayer. The monolayers obtained can be studied over the aqueous subphase or, alternatively, they can be deposited in a substrate, being the last ones called Langmuir-Blodgett films [72,73].

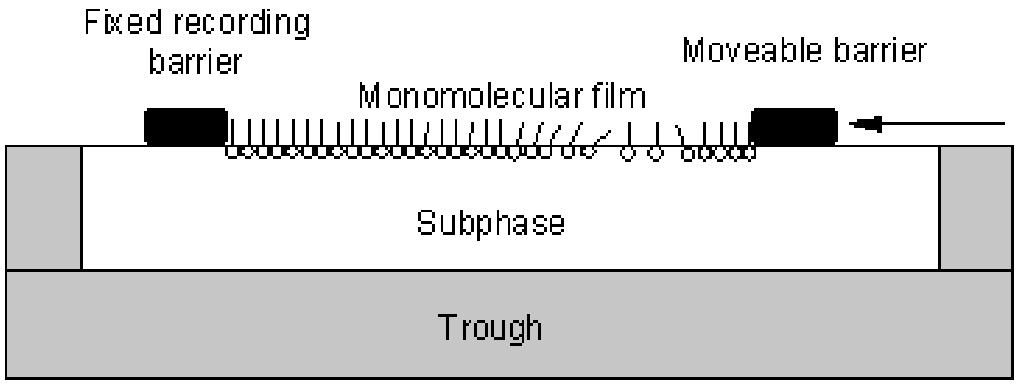

Figure 3.3. Scheme illustrating the preparation method of a Langmuir layer.

When preparing the Langmuir monolayers, after adding the solution to the surface water, the surface tension (γ) of the monolayer covered area will equal the surface tension of the clean water surface (γ_0) and consequently, the surface pressure measured (π) will be zero, since it is defined by $\pi = \gamma_0 - \gamma$.

3.1.4. SUBSTRATES

Throughout this work different substrates of different materials were selected depending on the characterization technique suitable to analyse each film obtained. Calcium fluoride (CaF_2) substrates and magnesium fluoride (MgF_2) substrates were analyzed in ultra-high vacuum ultraviolet spectroscopy and Fourier transform infrared spectroscopy. In impedance spectroscopy glass subtrates were used with interdigital gold electrodes. In X-ray photoelectron spectroscopy silicon and aluminium substrates were used. In studies of neutron reflectivity and atomic force microscopy, cubic crystalline structured silicon substrates were used. Substrate cleaning was performed as following: 1. Wash with water and a commercially available detergent; 2. Wash with an organic solvent (acetone and methanol); 3. *Piranha* solution immersion (H_2SO_4:H_2O_2/7:3) – *Attention: this solution is corrosive and obtained through an exothermal reaction;* 4. Wash with ultra-pure water to remove the waste left by the *piranha* solution bath; 5. Storage in ultra-pure water until use.

3.2. PARTICLES SOURCES

The study of the effect of particles sources in biomimetic membranes was done using photons and carbon ions. The photons used correspond to the ultraviolet region, namely between 140 and 340 nm (8,5 – 3,5 eV). The two photon sources and the ion sources used to study the effect of these particles in biological materials will be described below.

3.2.1. PHOTON SOURCES

3.2.1.1. Germicidal UVC lamps

A Germicidal UVC lamp (TUV PL-L 66W/4P HF 1CT) is a low pressure mercury lamp in which 35% of entry power is converted in UVC power. So, in the case of the lamp used (55 W) a UV power of approximately 19 W is obtained [74]. This lamp gives off UV radiation mostly around 254 nm (UVC), as depicted in figure 3.4, which shows the lamp spectral power emission distribution curve plotted against the wavelength.

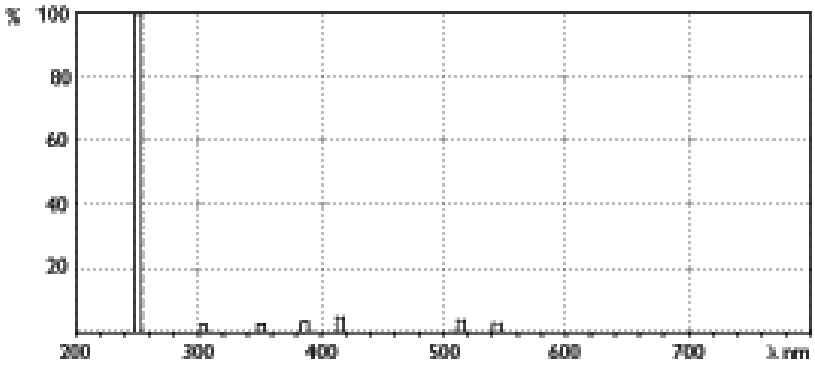

Figure 3.4. Spectral power emission relative distribution curve of UVC lamps. Adapted from [71].

Any low pressure lamp while working displays a relation between the lamp temperature and the output spectral intensity, in which the resonance line at 254 nm is the strongest for given mercury vapour pressure in the discharge tube. This pressure is determined by the operating temperature and it is optimized for a wall tube temperature of 40°C. Even though the lamp glass filters the mercury line at 185 nm, responsible for ozone formation when operating at an atmospheric pressure [75], emission at different wavelengths also leads to ozone formation. For that reason, an irradiation chamber was developed, as shown in figure 3.5 that allows the atmospheric ozone extraction and protects the operator from the UV radiation harmful effects.

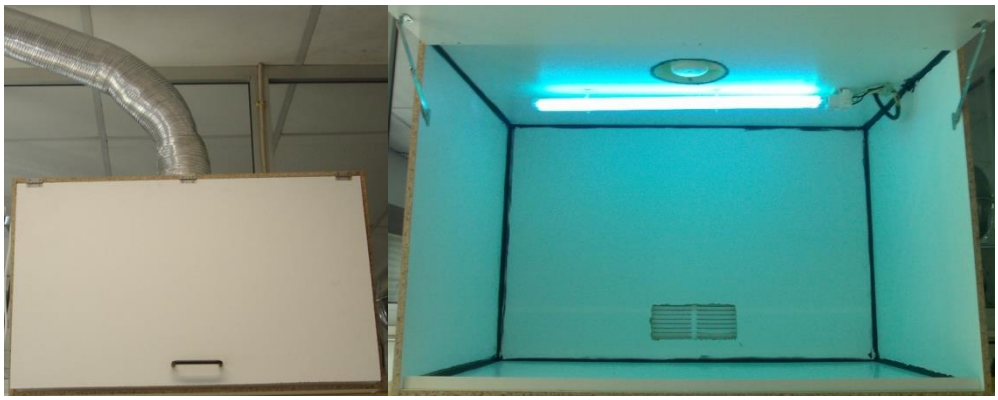

Figure 3.5. Extraction chamber developed to irradiate the samples with a 254 nm low pressure mercury lamp.

3.2.1.2. Synchrotron radiation

Synchrotron radiation is the radiation obtained through the deceleration of an electron beam when it is forced to travel in a curved path. This type of radiation main characteristics are: a) a high intensity (intense scintillation) surpassing other natural and artificial light sources [76]; b) being highly collimated; c) a high polarization; and d) allowing a high spectral resolution. Synchrotron radiation is emitted in a wide energy range, from near infrared to X-ray, emerging as a crucial energy source in the study of photophysics and photochemistry [77]. In addition, synchrotron radiation is highly polarized and has a short pulse emission nature allowing a continuous beam and the possibility to perform time dependent studies.

3.2.1.2.1. Synchrotron accelerator

Synchrotron radiation production process begins in the electron cannon, where a high voltage current passes through a cathode that emits electron pulses. The cathode is heated up until electron release occurs with enough energy to allow electron injection at the surface and acceleration towards the linear accelerator (LINAC). In the LINAC, 2 to 140 nanosecond electron pulses are produced which are then injected in the storage ring. Until a new storage ring refuelling occurs, the LINAC functioning is interrupted. This system operates in vacuum conditions to avoid the collision between accelerated electrons and residual gases molecules. When electrons reach energies around 2900 MeV, they are transferred through the injection system arriving inside the storage ring that is in a ultra-high vacuum state, where they move circularly during hours producing photons at each instant of beam deceleration by the trajectory curve. In the end of each round there is an aperture that allows light passage reaching the beamlines. Figure 3.6 depicts a schematic representation of a synchrotron accelerator. Collision of a few stored electrons with some residual gas particles produces a current decay, and as a consequence, it is necessary to perform a ring refuelling and an additional electron injection to maintain the needed current for the proper functioning of the system.

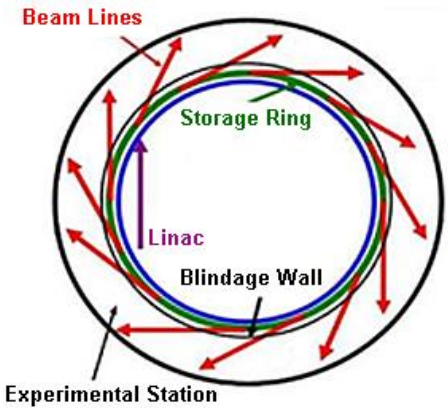

Figure 3.6. Simplified scheme of a synchrotron accelerator. Adapted from [82].

For the proper functioning of a synchrotron accelerator is essential to include some magnetic components responsible for acceleration and beam deflection inside the storage ring. These components are called dipole magnets, undulators and wigglers. Dipole magnets are used to alter electron direction occurring deflection at different degrees and consequently radiation is emitted. Undulators and wigglers (figure 3.7), composed of a series of periodic magnet, induce a come-and-go electron movement and consequently, create a collimated beam of higher intensity. Wigglers produce a wide X-ray range of high intensity, on the other hand, undulators produce for given energy range a higher X-ray intensity [78].

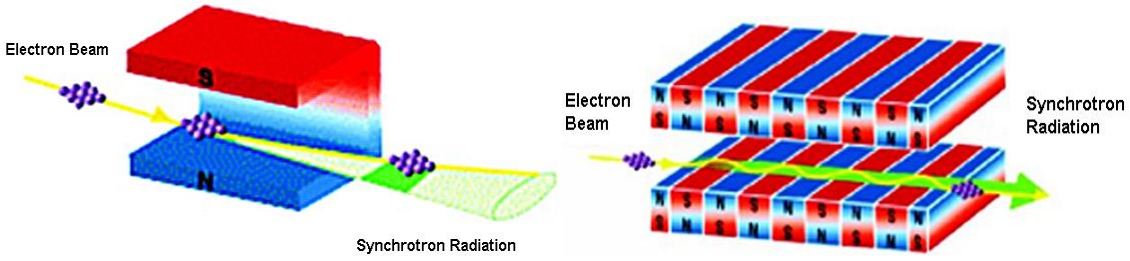

Figure 3.7. Schematic representation of the synchrotron accelerator magnetic components: A – dipole magnet; B – Wiggler. Adapted from [82].

Wavelength selection is performed using a monochromator followed by its focusing on the sample using a mirror system. In addition, each workstation is intended to distinct techniques. To study the radiation effect in membranes the two synchrotron accelerators described below were used.

3.2.1.2.2. Daresbury Synchrotron Radiation Source

In the early experiments performed in this study the synchrotron accelerator from Daresbury Science & Innovation Campus, United Kingdom, Daresbury Synchrotron Radiation Source (SRS) was used [79]. Figure 3.8 illustrates the array of components that make up the synchrotron accelerator and their respective workstations.

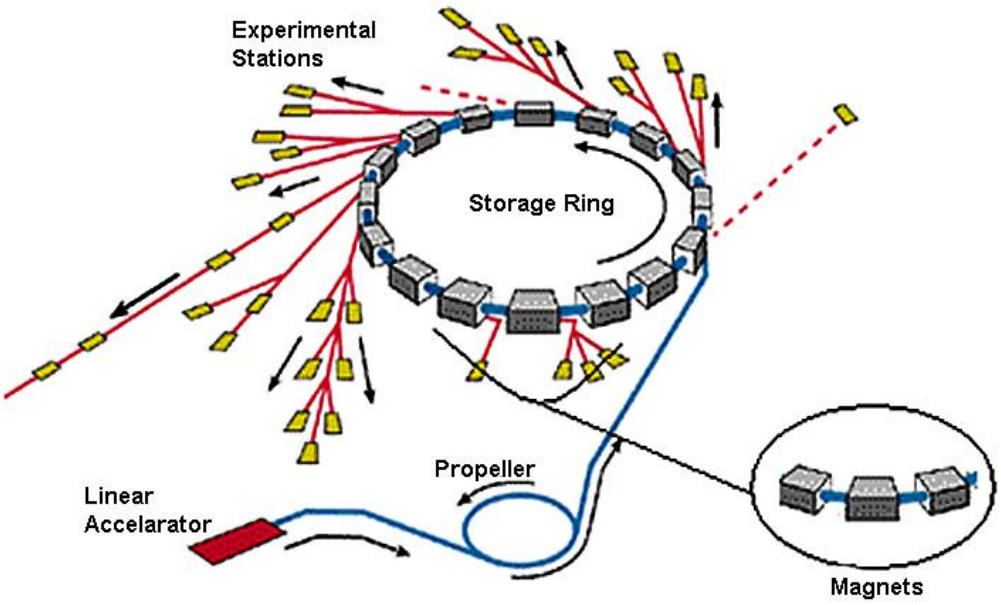

Figure 3.8. Schematic representation of the disposition of the various SRS components and their respective workstations. Adapted from [79].

SRS is an electron storage ring of 2 GeV which produces synchrotron radiation that will be used in different experimental techniques and, in addition, can function simultaneously using a diverse set of workstations. In the Figure 3.8 schematic representation, an illustration of the existing workstations in different ring points is depicted. Each workline is optimized for a given spectral zone of the energies obtained by the SRS. In this work, the experiments were performed in the 3.1 station, which is used for ultra-high vacuum ultraviolet, fluorescence and fragmentation processes spectroscopy studies. 3.1 station has a 1 m UV monochromator and functions between a 30 to 300 nm wavelength range with a resolution between 0,1 and 1 nm, and additionally, two diffraction nets are used in the swiping process [79]. The UV radiation beam used for the line proper functioning is provided by a focalizing mirrors system. Since this line can be used in different characterization techniques, SRS makes available for users only the radiation beam, and as a result, each user needs to assemble the remaining necessary components to accomplish the studies. Figure 3.9 depicts a schematic representation of the system which belongs to The Open University, United Kingdom, and whose main purpose is radiation and absorption spectroscopy studies, that will be presented in the next chapters. Vacuum symbology is in accordance with the DIN 28401 of Nov.76 norms. In the system, the zones referred as A and B are kept isolated using a metallic valve with a manual drawer (5). A Region possesses a four way clamp (2), a *piranni* type pressure sensor (3) and a flexible membrane (4). B region is composed of a six

valve clamp (6), a three way valve (7) and a *piranni* type pressure sensor (3). In the assembly inferior region, there is a pumping system which is composed of a turbomolecular pump (8), a rotary pump and a *piranni* type vacuometer (9) which connects the two pumps. In addition, the assembly also has a detection system that possesses a silicon junction photodiode p-n (11) developed by the International Radiation Detectors series AXUV, and also a measurement control unit with a digital indicator (12). To avoid sudden vacuum declines in the irradiation chamber there is an additional manual valve (13) which allows the air input control in the chamber [80].

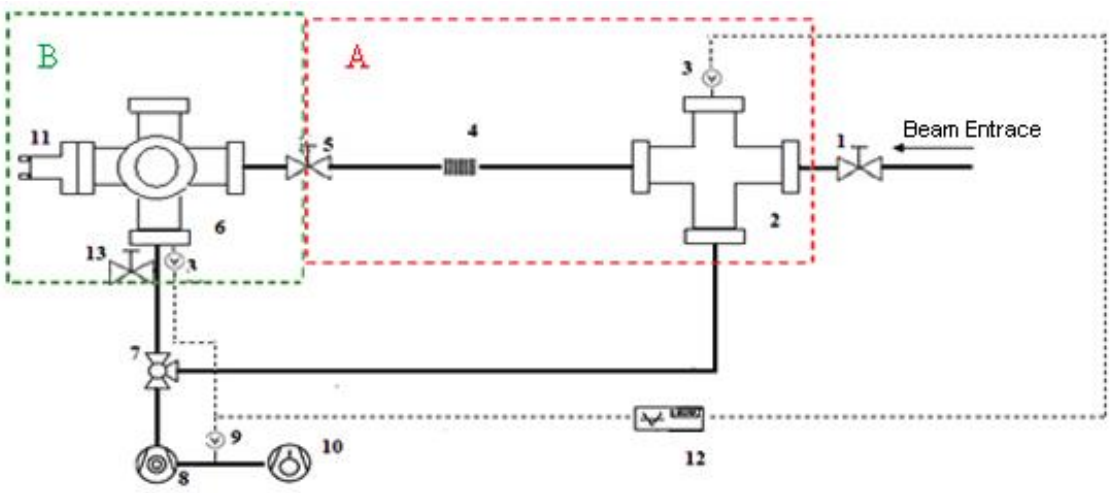

Figure 3.9. Schematic representation of the assembly used in obtaining an absorption spectra of vacuum UV synchrotron radiation: 1 – manual drawer valve with CaF2 window, 2 – four way crosshead, 3 – piranni type pressure sensor, 4 – flexible membrane, 5 – metallic valve with a manual drawer, 6 – six valve crosshead, 7 – three way valve, 8 – turbomolecular pump, 9 – piranni type pressure sensor, 10 – rotary pump, 11 – phalange with photodiode, 12 – measurement control unit with a digital indicator, 13 – manual escape valve. Adapted from [80].

This workstation beam has a maximum value of radiant power (Pmax) at 160 nm (7.4 eV) in the output line, and its value is $5x10^{-7}$ W. At this wavelength, the photon flux (Nf) is $4x10^{11}$ s^{-1} and the beam irradiance (E) value is $7x10^{-4}$ W/m^2. The beam total area is 734 mm^2. There is a beam decaying throughout time, so it is imperative to understand its behaviour in order to quantify the radiation dose that each sample is irradiated with. The beam decay curve is shown in figure 3.10, in which the beam relative intensity change during a 24 hour period after injection is represented [102].

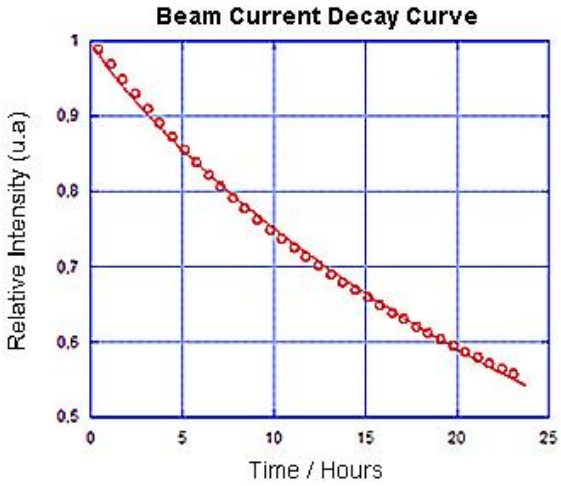

Figure 3.10. Normalized decay curve for the beam current during a 24 hour period after injection. Bold line corresponds to an extended exponential adjustment. Adapted from from de [80].

By analyzing figure 3.10. it is possible to verify that the beam decay follows a type $e^{-\left(\frac{t}{\tau}\right)^{\beta}}$ extended exponential. Adjusting the decay curve to an extended exponential using the least squares method the following values are obtained: relaxation time (τ) is 41.0 ± 0.1 hours, extended exponential coefficient (β) is 0.879 ± 0,002 with a correlation coefficient (R) of 0.999. In the sample position at 160 nm (7.4 eV), beam radiant power (P) is $2x10^{-7}$ W and irradiance (E) is $1x10^{-3}$ W/m^2. Beam area is 505.13 mm^2 with a irradiated sample area of 202.50 mm^2, which is approximately 40% of the total beam area in the sample.

3.2.1.2.3. Institute for Storage Ring Facilities

After SRS 3.1 line deactivation, experiments proceeded using UV1 and CD1 lines of the *Aarhus Storage Ring Denmark* accelerator (ASTRID) located in the Institute for Storage Ring Facilities, University of Aarhus, Denmark. ASTRID is a storage ring of electrons of smaller dimensions than the SRS, whose maximum energy is 580 MeV and characteristic decay time is around 60 hours [81]. Figure 3.12 depicts a simplified schematic representation of the ASTRID synchrotron accelerator.

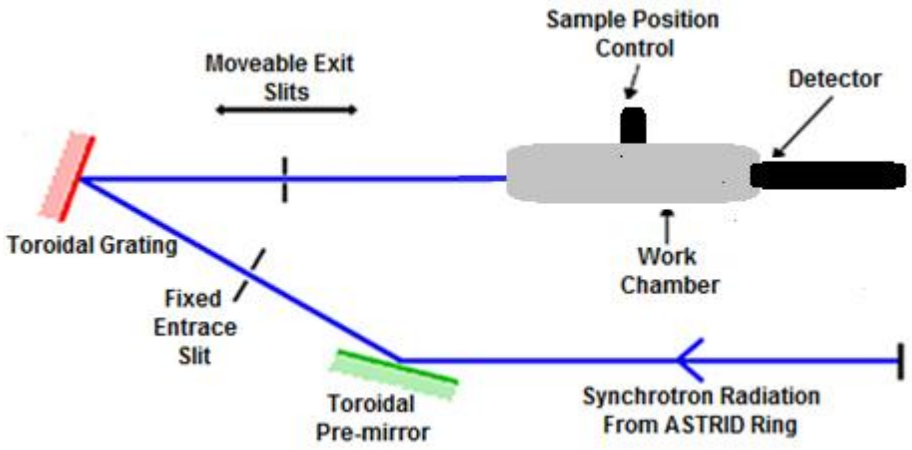

Figure 3.11. Schematic representation of the ASTRID synchrotron accelerator. Adapted from [82].

Samples irradiation was performed in the UV1 line essentially used for photoabsorption spectroscopy studies and in the CD1 line which is normally used for circular dichroism studies and also for absorption spectrophotometry studies. In the table below the main features of each line are indicated.

Table 3.1. Table depicting the main features of each workstation used in the sample irradiation protocol.

Workstation	UV1 line	CD1 line
Spectral range	100 – 350 nm (11.9 – 3.4 eV)	125 – 700 nm (9.5 – 1.7 eV)
Resolution	0.075 nm	1.0 nm
Photon flux	$2x10^{11}$ s^{-1}	$1x10^{12}$ s^{-1}
Area	40 x 40 mm	55 x 75 mm

Samples are placed inside the work chamber that is in primary vacuum state using a four cavity vertical positioner for 20 nm diameter circular substrates, with a position adjustment that enables the sample alignment with the radiation beam. The incident beam wavelength is selected by the control software and the irradiation time is selected by the security valve aperture time.

3.2.2. ION SOURCES

The ion radiation studies made use ion apparatus at Queen's University, Belfast (QUB) composed by two low energy ion accelerators, both equipped with electron cyclotron resonance (ECR) ion sources. One accelerator uses a conventional arrangement where the beam line is held at earth potential with the source at positive potential to achieve the desired ion energy. The second accelerator uses the same basic design but the beam analysis is carried out using a "floating" beamline arrangement where the beamline "floated" at -4 kV and the source again at positive potential to achieve the desired ion energy. The principal benefit of this design is that, in contrast to a conventional accelerator, analysis can be carried out a ion energies where the mass to charge resolution is good, even when the delivered ion energy is low. As a result, ions may be delivered from the system with lower energies than in conventional accelerator [83]**.**

3.2.2.1. Principles of ECR ion sources

Ion sources are used to produce intense beams of singly and multiply charged ions. Many different sources types are available ranging from those designed to make very highly charged atomic ions (electron beam ion sources/traps – EBIS/EBIT) through to those which can produce very large molecular ions (eletrospray ion sources – ESI). For the purpose of producing beams of small atomic ions, an ECR ion source is suitable and is capable of producing both singly and multiply charged ions. An ECR ion source extracts ions form a plasma [84] consisting of positive, negative and neutral species. In order to produce large number of positively charged ions, electrons within the plasma are accelerated using high frequency electromagnetic fields giving rise to electron impact ionization within the plasma. The production of a multiply charged ion (MCI) relies upon sequential electron impact ionization thus is linked to the time t it spends in the vicinity of the electron cloud, as well as to the electron velocity v and number density n. It follows that the desirable to increase t in order to increase the efficiency of MCI production. In the ECR ion source, this is achieved by confining the plasma within a magnetic structure [83].

Charged particles experience forces when they are within electric or magnetic fields. In a magnetic field, this force is perpendicular to the plane containing the particle velocity and the magnetic field and depends upon the particle velocity. The force *F* experienced by a singly charged particle moving at velocity *v* in a field *B* is given by:

$$F = e(v \times B) \tag{3.1}$$

The component of this in the direction of motion will be zero, hence a particle travelling parallel to the magnetic field lines will experience no force in this direction. The particle will however experience a force which is, at all times, perpendicular to its direction of motion and thus follow a helical orbit about the magnetic field lines. Using Newton's second law and equation 3.1:

$$F = \frac{mv^2}{r} = Bqv \tag{3.2}$$

Therefore:

$$r = \frac{mv}{qB} \tag{3.3}$$

This is known as the cyclotron, Larmor or the gyro-radius and the particles will travel in a helical orbit, about the magnetic field lines, with this radius. Since the radius depends on the charge q, electrons and ions will orbit the field lines in opposite directions: electrons rotate in the left-handed sense with respect to the magnetic field lines and ions in right-handed sense. The frequency of this will be given by the cyclotron frequency:

$$\omega_c = \frac{qB}{m} = 2\pi f_c \tag{3.4}$$

In ECR sources, the ions and the electrons are confined by a combination of two magnetic fields. Firstly a minimum B-field configuration – an axial field – is produced by solenoid coils or permanent magnets. Figure 3.12 shows a schematic diagram of such a magnetic field configuration.

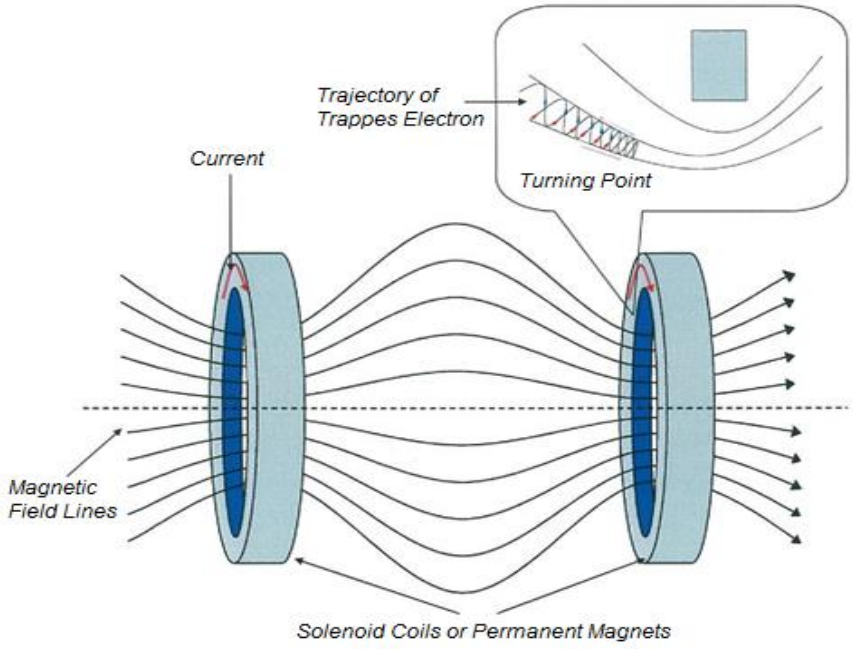

Figure 3.12. Minimum B-field configuration. Adapted from [83].

The second field is a radial field, produced by a hexapole magnet, superimposed on the axial field. The combination of the two fields produces a “magnetic well” with the minimum in the center and the magnetic field increasing in all directions, the field intensity in function of distance from the flange is displayed in figure 3.13.

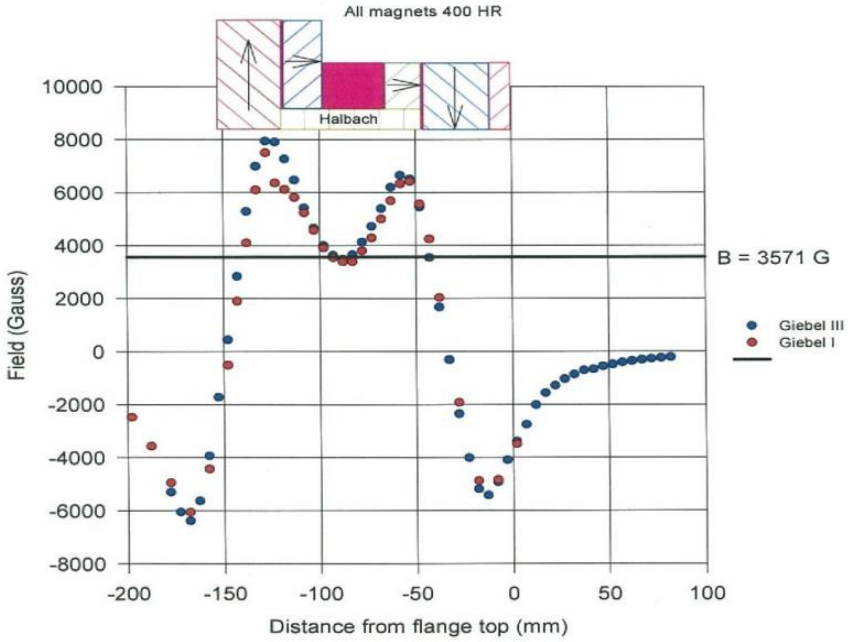

Figure 3.13. Combined axial and radial magnetic fields. Adapted from [83].

For an electron, the magnetic moment is given by:

$$\mu = A \times I \tag{3.5}$$

Where I is the current due to the rotating electrons (equal to ef_c) and A is the cross sectional area outlined by the electron motion (equal to πr^2).

$$\mu = \frac{\pi r^2}{\omega_c^2} \times \frac{e\omega_c}{2\pi} = \frac{1}{2} \times \frac{mv^2}{B} \tag{3.6}$$

Therefore, due to the conservation of magnetic moment, the transverse velocity of electrons increases with increasing magnetic field. However to conserve energy, the axial velocity must decrease. As result, electrons will eventually reverse their axial direction and travel back to the minimum B-field region, as shown in figure 3.12. The electrons have therefore been reflected i.e. a magnetic mirror has been created. In practice, the mirror is not perfect and has a net electron loss leading to a small net positive charge in the plasma known as the plasma potential.

In an ECR plasma, heating is achieved by the combined effects of an electromagnetic field and static B field. When the frequency of the EM field is equal to the cyclotron frequency of the electrons, energy is resonantly transferred to the electrons producing an efficient coupling of electromagnetic energy to the plasma.

3.2.2.2. Permanent Magnet ECR Ion Source and Ion Extraction System

The ECR ion sources use permanent magnets and 10 GHz microwave radiation for plasma heating. The sources were capable of producing beams of singly and multiply charged ions with low microamp currents with an energy resolution ~ 5q eV. In these sources, the radial field is provided by hexapole magnets made from NdFeB. This magnet was a 75 mm long "Halbach" magnetic structure [84] consisting of 24 trapezoidal segments whose axis magnetization varied by 45º from one segment to the next. This produced a magnetic field strength of 0.94 T at the plasma tube inner wall. Two outer NdFeB rings, magnetized radially with respect to the plasma chamber, and four smaller axially magnetized rings, positioned cover the hexapole magnet, produced the axial magnetic mirror field. Figure 3.14 shows the axial magnetic field along the mid-plane of the magnetic structure. This extraction electrode was located at the maximum of the magnetic field. Since the sources used permanent magnets, the plasma chamber was water-cooled and the magnets were also air cooled to prevent high temperatures and demagnetization (> 70ºC).

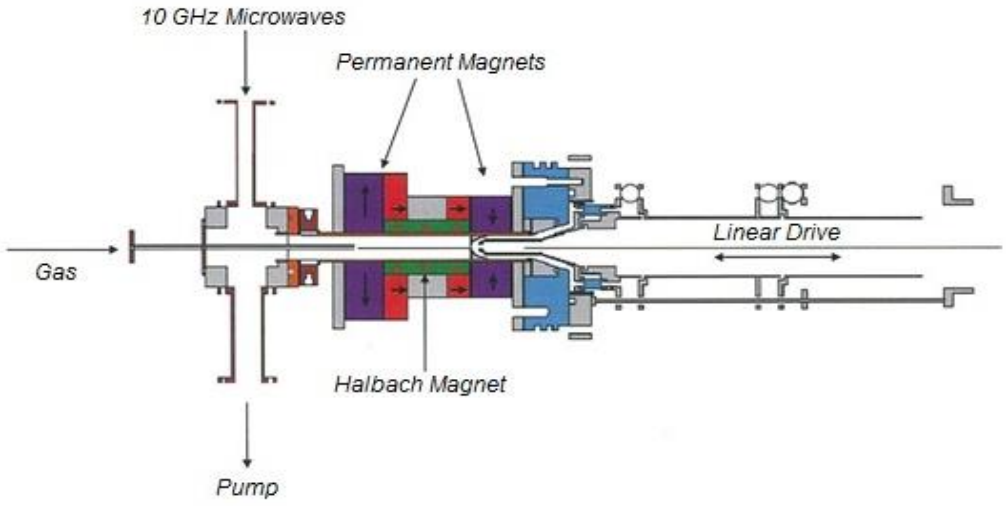

Figure 3.14. Schematic of the 10 GHz ECR ion source and extraction system. Adapted from [83].

The extraction and lens systems were situated in 150 mm bore, 6-way crosses, electrically isolated from the sources. On both systems, the extraction section was evacuated using a single 500 dm^3/s turbomolecular pump with a second, 200 dm^3/s, pump attached to the source (again electrically isolated). The base pressures in these sections were ~10^{-6} mbar, measured using penning/pirani vacuum gauges. The source and extraction sections were vacuum isolated from the rest of the system using ultra-high vacuum gate valves. In both systems, beam analysis was achieved using 90 degree bending magnets which selected ions based on the mass to charge ratio. For an ion of mass *m*, charge *q*, travelling at a velocity *v* in a magnetic field *B*, the force experienced is given by:

$$F = Bqv = \frac{mv^2}{R} \tag{3.7}$$

Where *R* is the bending radius. The kinetic energy of the ions is given by:

$$KE = \frac{1}{2}mv^2 = qV \tag{3.8}$$

Where *V* is the accelerating voltage.

$$B = \left(\alpha \frac{m}{q}\right)^{1/2} \tag{3.9}$$

Where $\alpha = \frac{2V}{R^2} = constant$. Thus, by choosing the correct magnetic field, ions of specific mass to charge ratio can be selected to travel along the bending radius and out through the exit aperture.

3.2.2.3. Conventional Accelerator

The conventional accelerator maintained the beamline and target at earth potential while the source was maintained at potential +Vs. In this design, the ion beam energy throughout was equal to qVs where q is the charge state of the ion species. The upper energy limit of this system was 6q keV (limited by power supply) while the lower limit is approximately 500 eV below which power supply stability, resolution of the magnet and ion beam blow up became problematic. A schematic of this accelerator is shown in [83].

3.2.2.4. "Floating Beam" Accelerator

In this arrangement the beamline and its elements were "floated" at -4 kV thus with a potential $+V_s$ applied to the source, extraction was at an energy of $(4+V_s)q$ keV. When ions exited the floating beamline section, they were referenced to earth (instead of -4 kV) and thus entered the experimental area with energy $V_s q$ KeV. Since transport and beam analysis were carried out at $(4+V_s)q$ keV, even as Vs tends towards zero, the beam energy was $>4q$ keV. Thus is possible to deliver beams with almost zero energy, at the accelerator exit. A schematic of this accelerator is shown in figure 3.17.

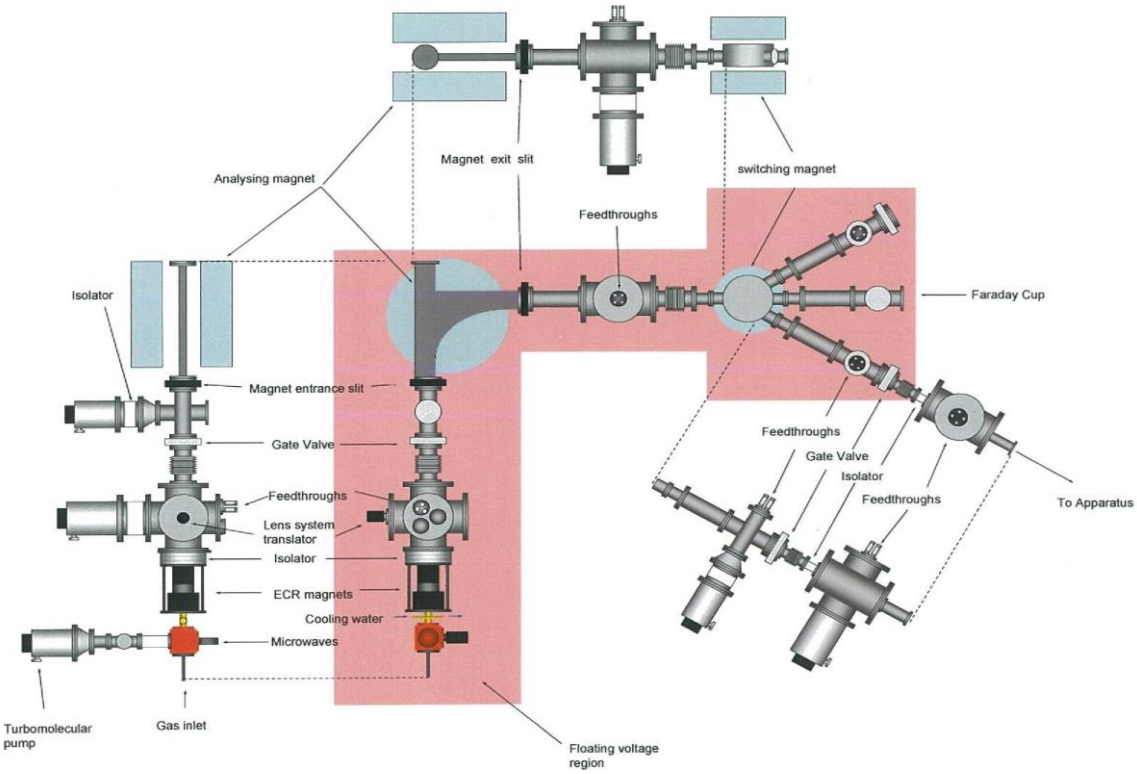

Figure 3.15. Schematic diagram of the “floating beamline” accelerator. Adapted from [83].

Since the beamline was held at high potential, it was shielded for safety reasons. In contrast, the conventional accelerator required only the source to be shielded in this way. Electrical isolation from the vacuum system was also required and was achieved by using ceramic breaks. Another consideration with this setup was the previously mentioned plasma potential. The value for this was ~+5 V, thus the source was biased negative by this amount in order that beam was produced near to 0 eV.

3.2.2.5. Measurements Chamber Design

The apparatus was based around an IR transmitting sample substrate which was mounted on a UHV chamber. The chamber was evacuated by two turbomolecular pumps which were connected, by flexible stainless steel pipes, to two of the remaining flanges on the 6-way cross. The pressure was measured by two gauges (one ionization and one penning/pirani) mounted in CF40 'T' pieces, between the 6-way cross and each of the pumps. During the experiments described, the base pressure for the system was measured by the ionization gauge to be a few 10^{-7} mbar.

To allow IR transmission spectroscopy, two differentially pumped, potassium bromide (KBr) windows were mounted on CF40 flanges on opposite sides of the cube. The sample mount was positioned at the center of the chamber, equidistant from the two windows. The entire copper mount was machined out of a single piece of OFHC (oxygen free, high conductivity) copper to avoid any additional

interfaces which may affect thermal conduction. The sample mount was attached to the base of the cryostat heat exchanger using four screws with a thin silver foil sandwiched between to improve thermal conduction. A zinc selenide window (giving high transmittance in the 0.6 - 20 micron range) was located in the copper mount and used as the substrate. This window sat in a groove in the copper mount and was secured by screws and oversized washers. When mounted, the substrate provided a circular sample area with diameter of 20 mm.

Between the main chamber and the floating beamline accelerator was a vacuum isolated section containing adjustable ion beam collimators (two sizes were used, 10 and 15 mm diameter) and an ion beam setup and monitoring assembly. The collimators were mounted either side of a 4-way CF40 cross. The beam measurement device was mounted on this cross and consists of an electrically isolated translator onto which was attached a faraday cup and a 90% transmission mesh. The faraday cup was translated into the beam path to allow measurement and optimization of the full beam. Once this was complete, and prior to irradiation of an ice, the ion mesh was moved into the beam path allowing 90% of the ions to be transmitted while the remaining 10% could be monitored. This allowed the ion beam to be monitored 'in situ' without the need to interrupt the irradiation. A schematic of this arrangement can be seen in figure 3.16.

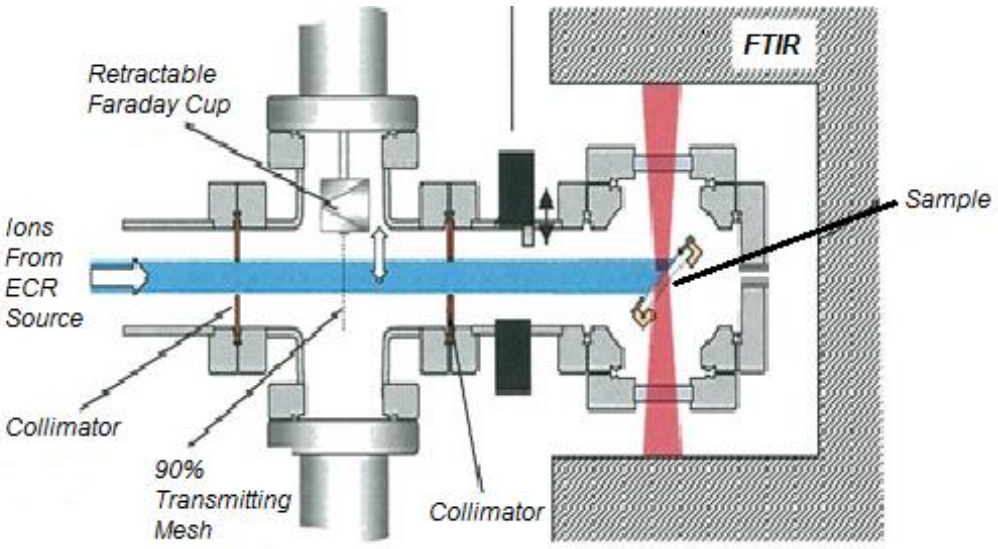

Figure 3.16. Schematic diagram irradiation and FTIR measurements setup. Adapted from [83].

3.3. CHARACTERIZATION TECHNIQUES

The radiation effect on biomimetic membranes study was performed using a few techniques that are recurrent in materials studies, allowing data crossover of obtained results and consequently validation of the conclusions obtained.

3.3.1. ULTRA-VACUUM ULTRAVIOLET ABSORPTION SPECTROSCOPY

Ultra-vacuum ultraviolet absorption spectroscopy is based on interactions between ultraviolet radiation and matter, allowing the characterization of materials based on electronic states of the molecules studied. Absorption spectra are obtained placing a sample between the radiation source and the detector, the sample absorbs radiation and consequently, its internal energy rises [85]. The internal energy rise value equals the absorbed photon energy and it is expressed using the Planck relation. The energy absorbed by the molecule will lead to electronic transitions that will allow a characteristic spectroscopic classification of each molecule depending on the energy values obtained. The electrons of molecules containing only single bonds are called σ electrons, on the other hand, the electrons that participate in double bonds are called π electrons. In systems composed of double bonds, π electrons prevail and consequently determine the valence electrons energy states, which are excited by visible or ultraviolet radiation absorption. Besides electrons that take part in covalent bonding, there are also unshared electrons that are called n electrons.

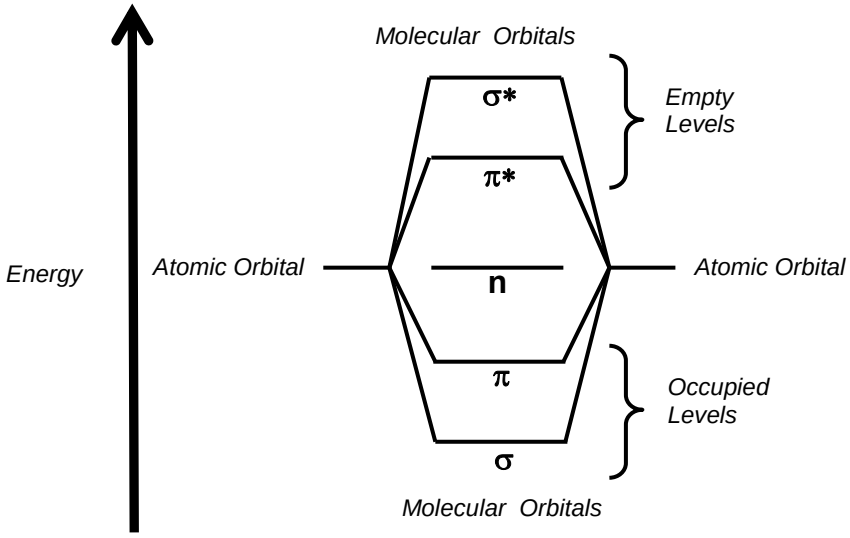

Figure 3.17. Schematic representation of the energy levels. Adapted from [85].

Electronic transitions can be grouped in three categories that are associated with energy absorption of given zones of the electromagnetic spectrum [85]:

I. Transitions from a stationary state orbital to a higher energy orbital, which means, π→π* transitions and σ→σ* transitions.

II. Transitions from an unshared atomic orbital to a higher energy molecular orbital, which means, n→π* transitions and n→σ* transitions.

III. Transitions from a stationary state orbital to higher energy orbitals, towards molecule ionization, that are designated Rydberg orbitals.

Table 3.2. Table showing the respective electronic transitions for each region of the electromagnetic spectrum. Adapted from [85].

Electronic Transitions	***Electromagnetic Spectrum Regions***
σ → σ*	Vacuum Ultraviolet
π → π*	Ultraviolet
n → π*	Near Ultraviolet
n → σ*	Far Ultraviolet or Near Ultraviolet (exceptionally)
Rydberg	Vacuum Ultraviolet

In the majority of organic molecules, absorption bands observed in the UV near zone and in the visible region spectra are owed to π → π* or n → π * transitions. The first ones are much more intense then the latter since, in this case, the unfavorable spatial orientation between n and π* orbitals gives place to low intensity transitions. On the other hand, bands observed in the vacuum ultraviolet region are owed to σ → σ* and n → σ* transitions [86].

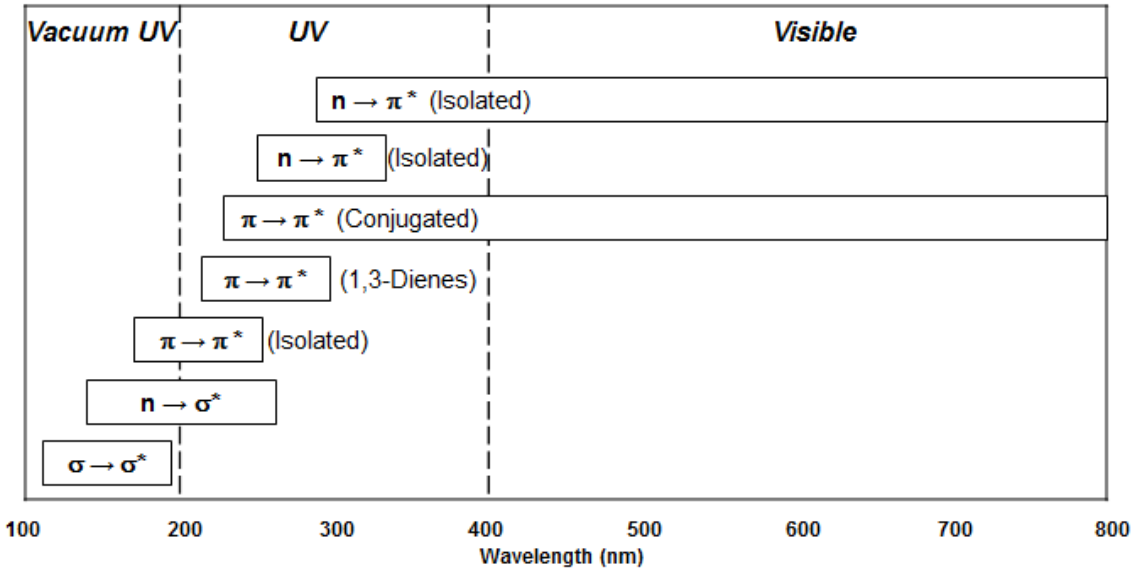

Figure 3.18. Schematic representation of the energy levels. Adapted from [86].

The transitions occurring when there are radiation and matter interactions are usually depicted using an absorbance spectrum in which absorbance is plotted against incident beam wavelength. This function is given by the Beer Law and it is defined as:

$$Absorbance = -\log\left(\frac{I}{I_0}\right) \tag{3.10}$$

In which I_0 is the incident radiation and I is the radiation reaching the detector after going through the sample. A maximum absorbance is reached at wavelengths where electronic transitions are observed, and these are called absorption bands. These are deconvoluted using specific software so that the several peaks composing the absorption band are obtained. Afterwards, the transitions associated with the obtained energy values are identified, allowing the characterization of the material studied. VUV (Vacuum Ultra-Violet) spectra were obtained using the Daresbury and Aarhus accelerators, described previously, and the following protocol: (i) radiation intensity transmitted by the substrate without absorbed material is measured (I_0); (ii) radiation intensity transmitted by substrate plus film absorbed at the surface is determined (I); (iii) a new measurement of the transmitted radiation intensity of the substrate without the film at the surface is made ($I`_0$). This last step is needed due to the beam intensity decay throughout time which consequently leads to a transmitted radiation intensity decrease caused, not by film absorption, but by the characteristic beam decay. In this case, Beer law must be adjusted and is defined the following way:

$$Absorbance = -\log\left(\frac{I}{(0.5I_0)+(0.5I_0')}\right) \tag{3.11}$$

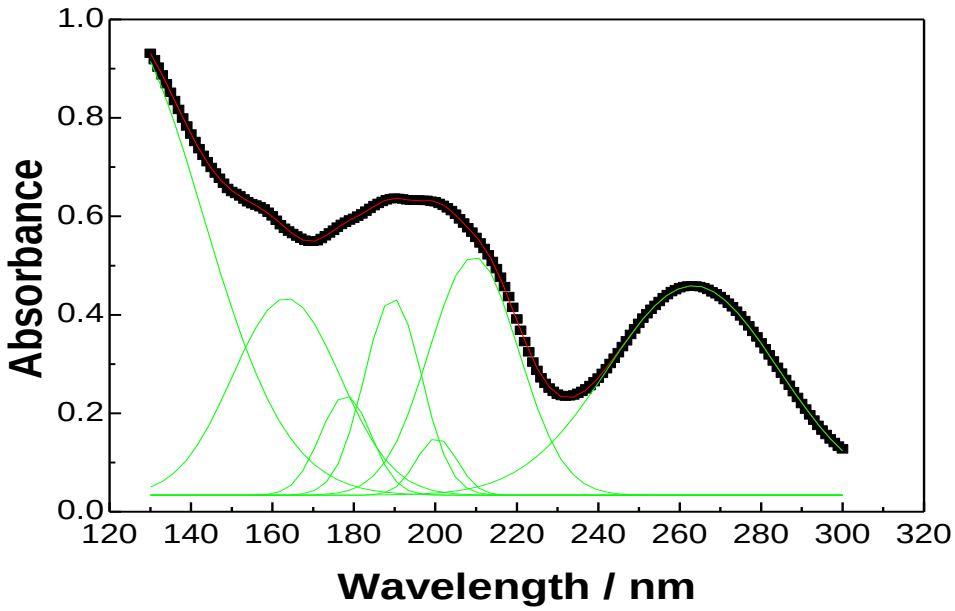

Figure 3.19. VUV absorbance spectrum of a DNA cast film, obtained in the region between 130 and 300 nm.

3.3.2. INFRARED FOURIER TRANSFORM SPECTROSCOPY

Molecular chemistry bonds possess specific vibration frequencies that are characteristic of each group of atoms and correspond to the vibrational levels of the molecules. For radiation absorption within infrared region wavelengths to occur, change of the molecule electric dipole moment must take place as a consequence of its vibrational movement. There are two types of molecular vibrations: stretching and deformation. Stretching vibrations consist in the rhythmic movement along the bond axis in a way that the interatomic distance increases or decreases. These vibrations are divided in two modes, symmetrical and asymmetrical stretching vibrations.

Figure 3.20. Stretching vibration modes: (A) asymmetrical and (B) symmetrical.

Deformation vibrations are defined as an angle change between bonds with a shared atom or as the movement of a group of atoms which move in relation to one part of the molecule, but not considering the remaining atoms of the other part of the molecule. For example, rotational vibrations, of balance and wagging, involve bond angle changes considering a set of arbitrary coordinates inside the molecule. Figure 3.21 depicts four modes of deformation vibrations, which are: scissoring, wagging, twisting and rocking.

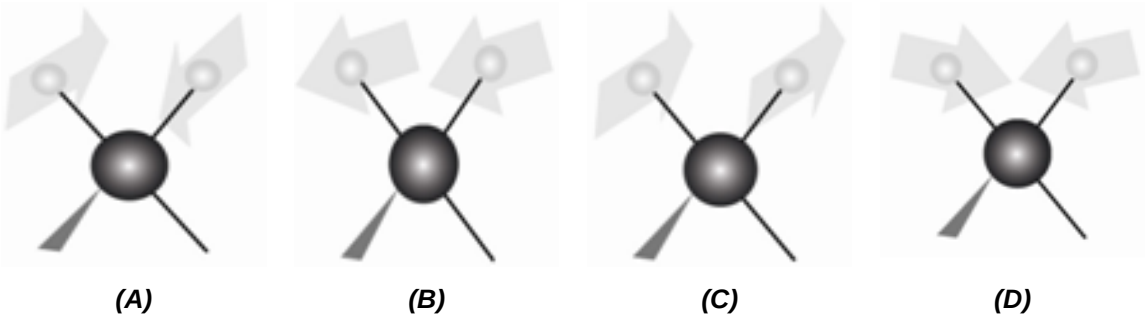

Figure 3.21. Schematic representation of the four modes of deformation vibrations.

Infrared spectroscopy is a simple instrumental technique of rapid acquisition which has the ability to detect several functional groups. Infrared radiation causes a rise in covalent bonds amplitude vibration between atoms and groups that compose the molecules studied, in agreement with the previously described modes. Currently, the technique in use is called FTIR (Fourier Transform Infrared), which allows obtaining a signal with less noise even when using samples with a low quantity of material.

Since functional groups of organic molecules include atomic bonding by specific arrays, a given organic molecule absorption of infrared energy depends on the types of bonds and atoms found in the specific functional groups of this molecule. Obtained vibrations are quantized and while they occur, compounds absorb IV energy in specific regions that are displayed in the shape of peaks in an absorbance spectrum plotted against wavelength [87].

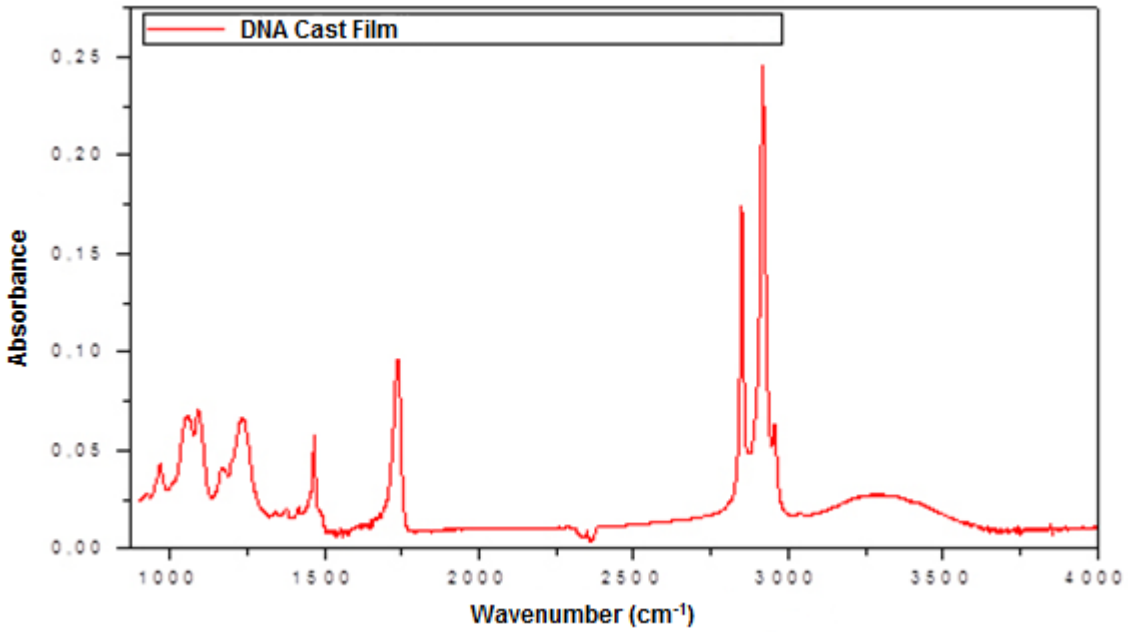

Figure 3.22. FTIR absorbance spectrum of a DNA cast film within 875 to 4000 cm^{-1} region.

FTIR technique constituted a vital tool in the progression of the studies performed that compose the body of this work. This technique has several limitations, including those regarding monoatomic molecules analysis, absence of asymmetry, and also, unsuitability for aqueous solution analysis. However, because there is low water quantity, this technique also possesses numerous advantages, examples include: operation cost is low, low material quantity is needed for adsorption at the substrate surface, working conditions are at atmospheric pressure, and in addition, absorption bands are distinct for similar molecules, allowing a precise distinction between the diverse functional groups.

3.3.3. X-RAY PHOTOELECTRON SPECTROSCOPY

XPS (X-ray Photoelectron Spectroscopy) allows the identification of all the periodic table elements with the exception of hydrogen and helium. When using this technique is also possible to determine the oxidation state of an element and the type of chemical specie to which is connected to. XPS is based on X-ray irradiation of the surface of interest followed by analysis of the surface emitted electrons kinetic energies until around a 10 nm thickness [88]. Figure 3.23 depicts a schematic representation of the typical XPS experimental arrangement.

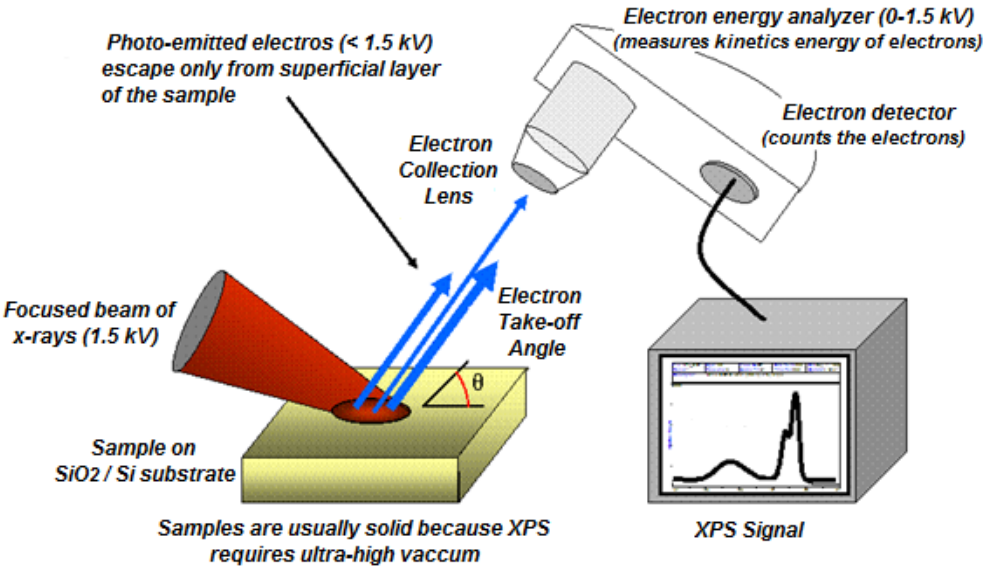

Figure 3.23. Schematic representation of the XPS apparatus. Adapted from [89].

To perform XPS analysis the Instituto Superior Técnico - Universidade Técnica de Lisboa equipment was used. The XPS apparatus consists in a XSAM800 (Kratos) operating in FAT (Fixed Analyzer Transmission) mode, where a double anode source was used, and where as an excitation source a Mg Kα photon beam can be used, with 1253.6 eV of energy, or alternatively, a Al Kα photon beam, with 1486,6 eV of energy can be used. Current and tension were around 10 mA and 13 kV, respectively. Samples were analyzed at room temperature and in ultra-high vacuum, at a pressure value around 10^{-7} Pa. All samples were analyzed in their central region, which is an area of 1x3 mm^2 and with an angle of 0° relative to the surface sample, using the high amplification mode. Spectra were acquired using a Sun SPARC Station 4 equipped with Vision software (Kratos) and a swiping step of 0.1 eV was used. X-ray sources satellites were subtracted. Experimental peaks fitting was performed with Voigt curves (Gaussian and Lorentzian) and using a nonlinear algorithm based in the least squares method. Subtracted base lines were Shirley or linear type. Charge compensation (flood gun) was not applied. Bond energies (BE) of the analyzed samples were corrected using as reference carbon C 1s bond energy (285 eV).

3.3.4. Atomic Force Microscopy

AFM (Atomic Force Microscopy) [90] is an essential technique in characterizing surfaces morphology, and its application is being extended to surface characterization of soft condensed matter studies. In the case of thin film studies, like for instance, self-assembled films, atomic force microscopy has shown to be an essential tool in quantitative and qualitative characterization of surfaces. As a result of surface studies using atomic force microscopy, a few examples stand out as being essential for the development of models which explain materials behaviour in films; those include: roughness statistical

parameters, topographic analysis and its interpretation using growth and fractality theoretical models applied to self-assembled films [91,92,93,94]. AFM technique emerged as a consequence of the Scanning Tunneling Microscope (STM) creation [95], and its mechanism is based on the tunnel effect observed between a sharp tip (probe) and the surface of interest when these are a few nanometers away from each other. The tip sweeps the sample surface (X and Y directions) at a controlled distance in Z direction. Movements in X,Y and Z directions are done using a stage with piezoelectric control known as a scanner or piezo [96]. Figure 3.25 depicts a schematic illustration of the atomic force microscope apparatus [97]. The tip is assembled under a flexible crossbeam responsible for performing movement in the horizontal plane (XY) over the sample surface. The light beam emitted by a laser reaches the crossbeam upper part and consequently, it is reflected by the crossbeam and detected in a four-quadrant photodetector. The position in which the reflected beam reaches the photodetector computes the position of the tip under the crossbeam whose change depends on the studied surface relief. The atomic force microscopy (AFM) measurements presents in this work was done in a Nanoscope III microscope (Digital Instruments) at Grupo de Polímeros Professor Bernhard Gröss, Brazil.

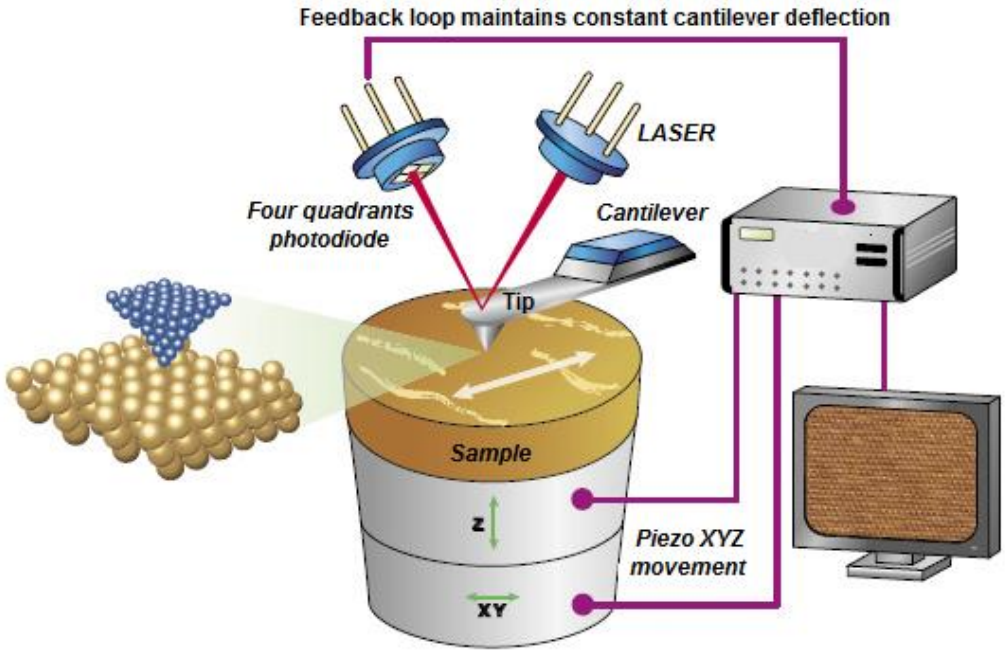

Figure 3.24. Schematic representation of the atomic force microscope (AFM) apparatus. The tip is fixed under a crossbeam where the light beam hits and consequently it is reflected, and whose purpose is detecting the crossbeam movement with a four-quadrant photodetector. Adapted from [97].

Several distinct forces are accountable for the interaction between tip and surface that include: Van der Waals forces, electrostatic forces or surface tension forces, being the first ones predominating. Figure 3.25 depicts a graph illustrating the existing forces between the tip and surface plotted against relative distance.

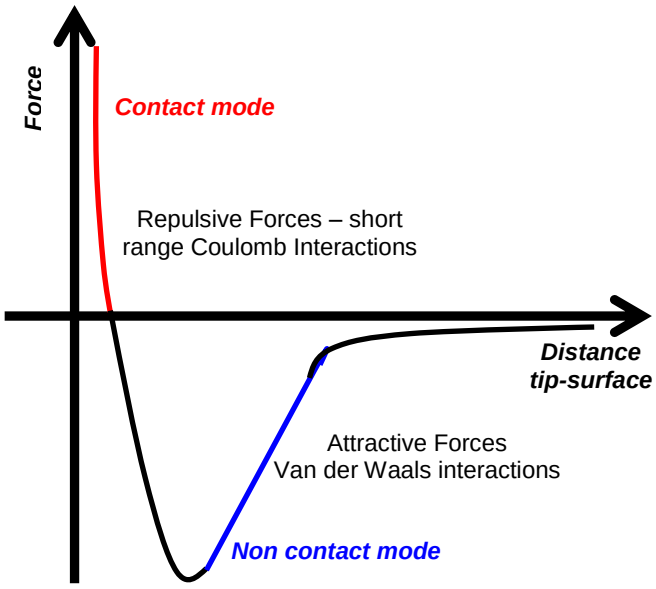

Figure 3.25. Schematic representation showing the existing forces between tip and surface plotted against relative distance.

Interaction force is almost null when there is a high distance value. However, as the tip progressively comes close to the sample, around distances that vary from 1 to 10 nm, the interaction force becomes attractive, and for distances beyond that range, the interaction force is repulsive, and of increasing intensity as it reaches a zero distance. The atomic forces microscope has the ability to work in these two regions. In the repulsive forces region, it works in a contact mode and on the other hand, in the attractive forces region, it works in a noncontact mode.

3.3.5. LANGMUIR BALANCE

Surface pressure isotherm data recording – area per molecule (π-A) and area per molecule – time stability curves (A-t) are crucial to characterize the monolayer formed in the air-water interface. To perform this kind of experiment a Langmuir trough is used. This equipment consists in a trough made up of hydrophobic material (Teflon) full with the aqueous subphase (ultra-pure water or a aqueous solution of a water soluble substance), two movable barriers which compress the monolayer while moving along the trough, and finally a surface pressure monitoring system. Compression velocity is possible to adjust using specific software and a thermostatic bath controls the temperature. Experiments were performed with two KSV Instruments Lda.® systems, models KSV 2000 and KSV 5000.

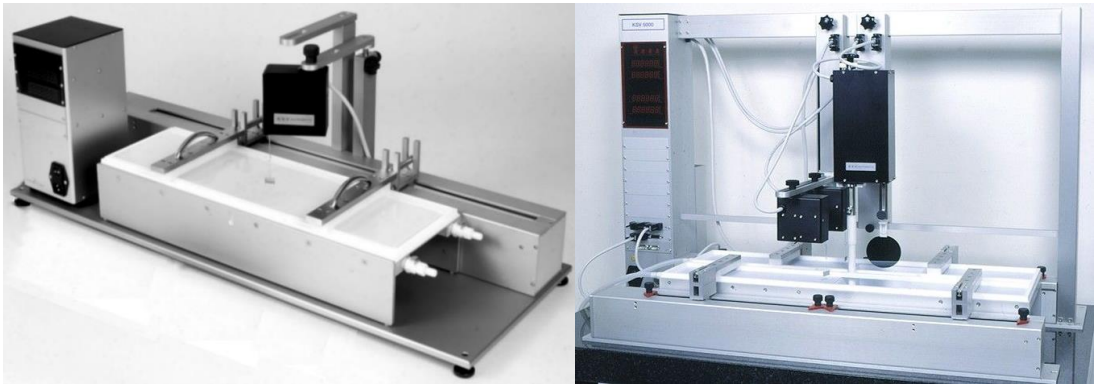

Figure 3.26. Langmuir trough used in Langmuir monolayer preparation: (a) KSV 2000; (b) KSV 5000.

Surface tension measurements were performed with a Wilhelmy system. Its experimental system is composed of a metallic blade partially immersed in the subphase and connected, through the opposite end, to high sensitivity electronic weighing scale. Among the forces acting on the blade, weight, impulse and surface tension, there is only surface tension change in the presence of the monolayer over the surface. For that reason, the difference in the measured force throughout the process is a consequence of the surface tension variation alone, and it is determined at each instant by the following mathematical expression (figure 3.27), which corresponds to the surface tension, as referred in 3.1.3.

$$\gamma = \frac{F}{l \times \cos\theta} \tag{3.12}$$

Where

$$l = 2d + 2w \tag{3.13}$$

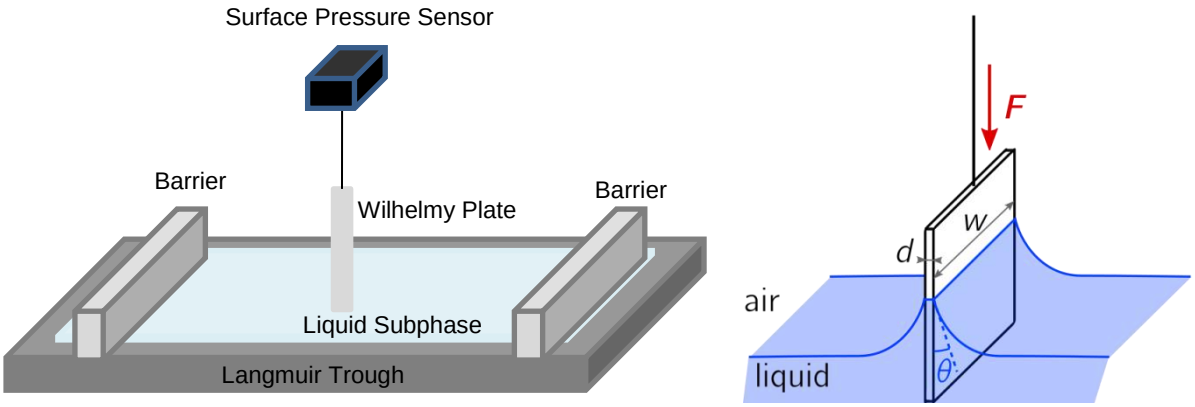

Figure 3.27. Scheme illustrating Wilhelmy method. (a) Experimental system; (b) Representation of the variables needed to determine the surface tension, γ [22].

Any surface tension determination method can be used to measure the surface pressure, namely the Willhemy method [98,99] or the Langmuir method [72]. After evaporation of the solvent, the monolayer is compressed by reducing the available surface area, thus increasing the density of molecules, decreasing γ and increasing π accordingly. Thus, the representation of a function π area per molecule (A) increases as the area decreases, making up the two-dimensional analogy isothermal pressure-volume (figure 3.28). After solvent evaporation, the monolayer is compressed reducing the available surface which allows a rise in the molecules density and consequently decreases γ (increasing π). Like this, π function plotted against the area per molecule (A) increases when the area decreases, creating a bidimensional analogy of a pressure-volume isothermal curve (figure 3.28). Using the π-A isothermal curve is possible to obtain parameters highly important in characterizing the Langmuir monolayers. The limit area value is possible to obtain extrapolating the final branch of the curve for a surface pressure equals to zero, which is analogue to the area per molecule in a maximum packing case. It is also possible to determine the maximum pressure value in which the monolayer loses its stability, called collapse pressure (π_c). The π-A isothermal curves display distinct regions which are related to the monolayers different organization states (or phases), and also to regions where different phases co-exist [73].

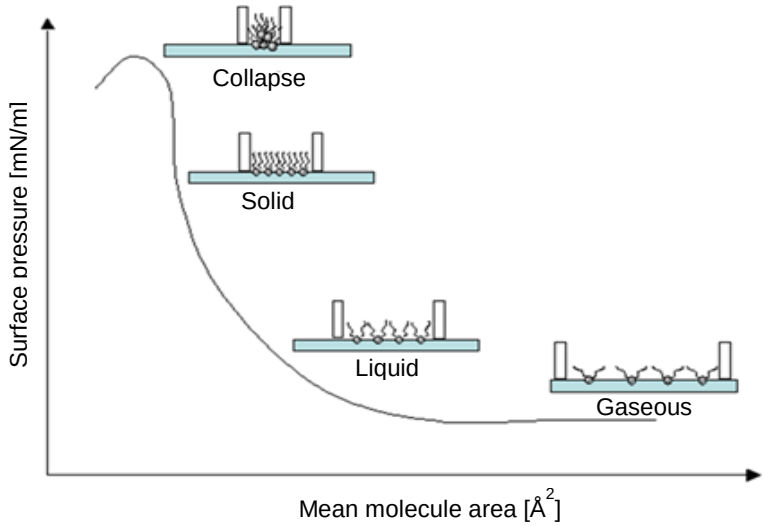

Figure 3.28. π-A isothermal curve displaying its distinct phases (variations may occur according to the system composition and the working temperature) and illustration of the molecules special disposition.

Figure 3.28 illustrates a isothermal curve where the theoretical different phases of a amphipathic substance are shown in accordance with the following description:

(i) ***Gaseous phase***: In the really low pressure zone the molecules are displayed in a highly spaced monolayer and consequently with a low interaction level. This phase is called bidimensional gaseous phase.

(ii) ***Liquid phase***: When the surface pressure rises, the compressed liquid phase is reached which is characterized by suitably intense attractive forces between the molecules. These interactions allow the formation of a compact structure, creating an liquid expanded (LE) phase. In between the gaseous phase and the expanded liquid phase, a condensation process occurs in which we have the coexistence of both states, G+LE (T1), characterized by a constant pressure, in accordance with a first order transition from state G to state LE [100,101].The pressure progressive rise originates a more condensed monolayer called liquid condensed (LC) phase. This compact monolayer displays a perpendicularly oriented hydrophobic region in relation to the monolayer-water interface. Between the expanded liquid phase and the condensed liquid phase, LE+LC (T2), a second transition is observed, which some authors argue as being a first order transition [102,103], while others postulate that is a transition of higher order [73,104].

(iii) ***Solid phase***: When increasing the monolayer compression before reaching a collapse situation, a solid state (S) is obtained, characterized by maximum packing of hydrophobic chains in an extremely rigid film structure.
It is important to note that the above description comprises a theoretical model, therefore, differences in the number and complexity of an isothermal curve phases are possible to occur depending on the studied system and the essays experimental conditions.

3.3.6. IMPEDANCE SPECTROSCOPY

Characterization of the electric properties of the samples studied was performed using impedance spectroscopy, also called dielectric spectroscopy or alternating-current (AC) electric conductivity, and is the measurements of the dielectric properties of a medium as a function of frequency, based on the interaction of an external field with the electric dipole moment of the sample. Therefore, it is possible to study processes like, charge transport, films conductivity or charge carriers diffusion coefficients [105]**,** among others, using impedance and phase angle measurements.
This technique requires applying a potential or a current disturbance in the sample of interest. System disturbance requires the application of a continuous potential followed by the additional overlapped application of a sinusoidal change of a small amplitude potential. This application potential method allows system disturbance using few milivolts which makes possible investigating electrical phenomena. It is also possible to disturb the system using different values of frequency since the applied potential is sinusoidal and it can be defined as:

$$V_s = V_0 \exp(j\omega t) \tag{3.14}$$

Since the system's disturbance is of low amplitude, this technique constitutes a nondestructive characterization method [106,107]. In impedance spectroscopy, as a result of applying a sinusoidal potential in the sample, a sinusoidal current emerges. The relation between the applied potential and

current is recorded and consequently complex impedance and current shift in relation to the applied potential are obtained, and it is called phase angle. Complex impedance is defined as:

$$Z^* = \frac{V}{I} = Z' + jZ'' \tag{3.15}$$

and it can be represented in the imaginary plane as depicted in figure 3.29.

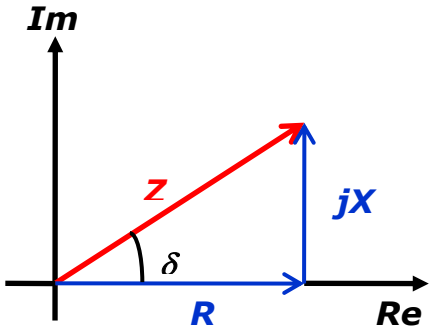

Figure 3.29. Graphical representation of complex impedance in the complex plane. Im – Imaginary component axis, Re – Real component axis, Z – Impedance, R – Resistance, jX – Inductance and δ – Phase angle.

The concept of impedance, originally introduced to describe the response of systems composed of capacitors, resistances and inductors, it was extended to biological and polymeric materials analysis, since countless processes can contribute to the link between the system's current and potential. The impedance is total resistive load of an AC circuit i.e., the sum of the resistance related to the energy loss in the form of heat (Joule effect) and the reactance, related to energy storage. The impedance indicates the total opposition that a circuit offers to the flow of an electric current varying in time.

For a thin film of thickness *s* in the area *A*, applied an electrical field, *E*, the current density, *J*, would be:

$$J = \frac{E\,s\left(Z' + jZ''\right)}{A\left(Z'^2 + Z''^2\right)} \tag{3.16}$$

For the complex permittivity, ε, has been:

$$\varepsilon = \varepsilon' + j\varepsilon'' \tag{3.17}$$

For the current density, *J*, has been:

$$J = j\varepsilon\varepsilon_0\omega E = \left(j\varepsilon' + \varepsilon''\right)\omega\varepsilon_0 E = \left(\omega_0\varepsilon_0\varepsilon'' + j\,\omega_0\varepsilon_0\varepsilon'\right) \tag{3.18}$$

where ω is angular frequency.

Comparing the expressions 3.16 and 3.18 we get the expressions of the real and the imaginary part of the relative permittivity:

$$\varepsilon' = -\frac{Z'' s}{A\omega\varepsilon_0\left(Z'^2 + Z''^2\right)} \tag{3.19}$$

$$\varepsilon'' = \frac{Z' s}{A\omega\varepsilon_0\left(Z'^2 + Z''^2\right)} \tag{3.20}$$

Where Z' and Z'' are the real and imaginary impedances. One can normalize ε' and ε on the dimensions of the sample, and write them in the form:

$$\varepsilon' \frac{A}{s} = -\frac{Z''}{\omega\varepsilon_0\left(Z'^2 + Z''^2\right)} \tag{3.21}$$

$$\varepsilon'' \frac{A}{s} = \frac{Z'}{\omega\varepsilon_0\left(Z'^2 + Z''^2\right)} \tag{3.23}$$

The tangent of loss angle, represented by δ, is given by:

$$tg\delta = \frac{\varepsilon''}{\varepsilon'} = \frac{Z'}{Z''} \tag{3.24}$$

The conductivity, σ, can also be given from the Ohm law by the relation:

$$J = \sigma E = \left(\sigma' + j\sigma''\right)E \tag{3.25}$$

Comparing the expressions 3.19 and 3.24 we get the relation between permittivity, ε, and conductivity, σ:

$$\left(\sigma' + j\sigma''\right)E = \left(\omega_0\varepsilon_0\varepsilon'' + j\omega_0\varepsilon_0\varepsilon'\right) \tag{3.26}$$

4. RESULTS

4.1. BIOMIMETIC HETEROSTRUCTURES FOR RADIATION DAMAGE STUDIES

Maria Raposo, Paulo J. Gomes, João M.C. Lourenço, Margarida Coelho,
Søren. V. Hoffmann, Ana M. Botelho do Rego, Robert W. McCullough, Nigel J. Mason,
Cláudia Lage, Paulo Limão-Vieira and Paulo A. Ribeiro

STATUS: Published in American Institut of Physics Conference Proceedings, 1080, 125-131, 2008

ABSTRACT

The present work describes a methodology that can be used for the creation of biomimetic membranes based in sequential assembling of biological molecules, to be used for radiation damage studies in an environment mimicking that of bio-systems. The major features of the method, the so called layer-by-layer technique, as well as the experimental parameters to take into account for heterostructures production are summarized here. Results for radiation damage in DNA containing biomimetic membranes prepared from different conditions methods revealed that the radiation induced damage is dependent on the heterostructure molecular composition, proving that the environment is of extreme importance for the extent of radiation induced damage in biological molecules.

INTRODUCTION

The mutagenic or lethal effects of ionizing radiation at the cellular level can be traced to structural and chemical modification of the biomolecular environment and its constituents. As far as radiation is concerned, not only is DNA found to be the most sensitive biomolecule in living tissue, but also the effects on the cellular constituents, namely the cell membrane, are not to be discarded particularly when its role on the interface mechanisms within the cell are vital for the physiological balance survival. The genotoxic effects of ionizing radiation as energetic photons, electrons, ions and neutrons in living cells are produced not only by the direct impact of the primary high energy projectiles but are also induced by secondary species generated by the primary ionizing radiation, such as electrons or even radical species from the physiological environment as is the case of $OH^{\bullet}$ from the water molecules and other reactive oxygen species, such as the peroxide radical. It is now well established that low energy electrons (< 30 eV) on DNA/RNA and its constituents (the nucleotide bases, nucleosides and water) can increase the probability that leads to damage for both single and double strand breaks, SSBs and DSBs, at very specific incident energies or resonances [4,7]. Moreover, the effect of these low energy electrons through dissociative electron attachment processes have been found to be site and bond selective as a function of the energy [8]. An approach to address radiation damage on a biosystem is to observe the radiation induced changes at chemical and physical levels on well controlled artificial biologic structures as biomimetic membranes obtained by assembling

layers of biological molecules in an environment containing water molecules. These membranes can be exposed to radiation doses and the damage can be quantified in each constituent. In this article, the preparation of biomimetic membranes by assembling biomolecules, can be attained via the layer-by-layer technique from the point of view of a set of well-studied molecules, e.g., polyelectrolytes, which can be easily extend to biological materials. Results on the radiation effects on different biomimetic membranes are also given, showing that the conditions of membrane preparation have clear influence in the extent of damage caused.

LAYER-BY-LAYER HETEROSTRUCTURES: BACKGROUND

The layer-by-layer (LbL) technique was developed by G. Decher and co-workers in 1992 and preliminary used for the buildup layered heterostructures of polyelectrolytes [67,108,109,110,111,112]. The production of LbL films consists on the alternated adsorption of polyelectrolytes of opposite electrical charges from aqueous solutions into solid surfaces, according to the following procedure: a solid substrate is immersed in a polycationic (or polyanionic) solution during a given period of time, after which the substrate with the adsorbed film is washed in pure water or in an aqueous solution with the same pH of the polyelectrolyte solution; the substrate is then immersed in the polyanionic (or polycationic) solution to complete a bilayer, substrate plus bilayer, being again washed to remove the weakly adsorbed molecules. Repetition of these steps may be performed to deposit the desired number of bilayers. Consequently, the typical buildup behaviour of the adsorbed amount per unit of area as a function of the number of bilayers is shown to be a straight line. The main features of LbL technique are: the production of ultra-thin molecular layers via a simple experimental procedure, attainment of well controlled film thickness, use of any size, shape and type of the adsorbing surface (e.g., quartz, hydrophilic and hydrophobic glass, silicon, mica, calcium fluoride, polymers or metals) and water soluble molecules. In addition, the potential of this method is reinforced by the large variety of molecular systems that have been successfully used to assemble macromolecules such as polyelectrolytes, functional polymers, dendrimers, ceramic and biological molecules [70]. Particularly, with respect to biological molecules, proteins as cytochrome C, lysozyme, myoglobin, bacteriorhodopsin, glucose and/or diaphorase, enzymes, DNA and lipids have been successfully incorporated in a LbL structure [59]. Therefore, the LbL method has shown to be suitable for the creation of biomolecular heterostructures with different functionalities such as those in a living cell, or at least to mimic these biological structures.

As the LbL technique requires adsorption at a solid/liquid interface, the kinetics of adsorption and layer proprieties greatly depends on adsorption parameters such as solution concentration, ionic strength, pH, temperature, molecular weight, molecule charge density and time of immersion. The contribution of these parameters for the adsorbed amount per layer and layer morphology are described below.

INFLUENCE OF TIME, CONCENTRATION AND IONIC STRENGTH

The adsorption time used in the preparation of the LbL films strongly influences the adsorbed amount as is shown in figure 4.4.1, where, as an example, adsorption kinetic curves of poly[1-[4-(3-carboxy-4-hydroxyphenylazo) benzene sulfonamido]-1,2-ethanediyl, sodium salt] (PAZO) adsorbed onto (poly(allylamine hydrochloride) (PAH)/PAZO)n/PAH LBL films are shown [113,114,115]. These curves represent the typical adsorption kinetics behaviour showing that the polyelectrolyte adsorption is ruled by two processes: an initial which has been associated with nucleation and another to diffusion [116]. As it can be seen from the two kinetics curves of figure 4.4.1, the initial adsorbed amount is dependent of the polyelectrolyte solution concentration. Results, not shown here, revealed a linear increase of the adsorbed amount for short adsorption periods with the polyelectrolyte solution concentration [113]. This behaviour has also been observed in adsorption curves of poly(o-methoxyaniline)(POMA) [117]. The initial linear adsorbed amount increase as a function of concentration can be attributed to the Columbic interactions between the polyelectrolyte molecules and the substrate as this is immersed in a solution. However, as the first molecules are adsorbed, they create a potential barrier that difficult that more polyelectrolyte molecules are adsorbed. This justifies the first observed plateau in the kinetics curves. Nevertheless, the presence of adsorbed charged molecules into the oppositely charged substrate allows that small ions, the polyelectrolyte counterions and/or solution ions when salt is added to solution, can be adsorbed into the substrate contributing for the potential barrier decrease, allowing that more molecules are adsorbed and also accounting for the second adsorption process. Moreover, the total adsorbed amount attained for longer adsorption times is concentration independent while the one associated only with the second process is concentration dependent as revealed by both adsorption kinetics characteristic times and adsorbed amounts. This model, for the creation of one layer, is corroborated by the observed increase to a maximum of surface roughness at short adsorption times, corresponding to the first adsorption plateau in the kinetics curve, and decreasing to a constant value which can be associated to adsorbed amount saturation. The kinetics curves behaviour is also strongly affected by the polyelectrolyte solution ionic strength. The increase of the salt amount in the polyelectrolyte solution leads to an increase of the total polyelectrolyte adsorbed to a maximum, followed by a decrease, behaviour which is accounted by the ions screening of both substrate charges and already adsorbed molecules.

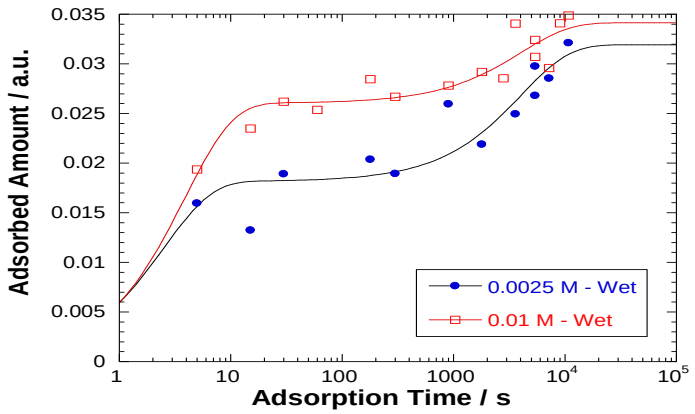

Figure 4.1.1. PAZO adsorption kinetics curves obtained from two different PAZO aqueous solutions concentrations. The layers were not dried during the film preparation (wet) [114].

INFLUENCE OF pH AND DEGREE OF IONIZATION

The ionic groups of the polyelectrolytes can behave as strong or weak acids or bases. When the acids or bases groups are strong, the degree of ionization is pH independent, while when they are weak the degree of ionization is pH dependent. Consequently, the adsorbed amount and morphology of an adsorbed layer is strongly dependent on the polyelectrolyte solution pH as this parameter controls the polyelectrolyte degree of ionization. Moreover, the stability of LbL films is: a) pH dependent, since the interactions leading to the formation of LbL films are essentially ionic in nature; b) dependent on the degree of ionization for the stability; c) dependent also on the adsorbed amount [118]. The washing solutions pH also contributes for the adsorbed amount and film stability. Surface morphology is also affected by the solution pH and ionization degree [119] by affecting strongly the conformation of weak polyelectrolytes in solution and the topography of surfaces having polyelectrolyte molecules adsorbed on it. In fact, for pH values where the ionisable groups are charged, the adsorbed amount is found to be small. According to theoretical models for polyelectrolyte adsorption, the adsorbed amount corresponds essentially to adsorbed polymer trains while the number of loops and tails is low. For pHs where the ionisable groups are uncharged and the adsorbed amount is higher. This situation corresponds to a larger number of loops, to some trains because the number of adsorbed trains decreases comparatively with the number for pH where the ionisable groups are charged, and to some tails. So, the pH effect on weak polyelectrolytes is to cause the chains to be more or less coiled, leading to more planar or rougher surfaces after adsorption.

WATER MOLECULES IN LAYER-BY-LAYER FILMS

The presence of water molecules inside the layers is of extreme importance for the production of heterostructures containing biological molecules, as the presence of entrained water allows the safeguarding of biomolecule environment and activity. Particularly, the presence of water near biological molecules plays an important role as far as radiation damage is concerned [6,120,121]. The presence of water molecules in LbL films has already been reported in the literature [117,119,122,123]. By studying the amount of counterions in poly(allylamine hydrochloride) (PAH) and poly(styrene sulfonate) (PSS) (PAH/PSS) LbL films, Lourenço *et al* [9,10 confirmed that the amount of counterions decreases by almost one order of magnitude if the film is dried under room conditions after adsorption of each layer. This was justified by water removal during the drying process, which allowed the formation of NaCl nanocrystals that subsequently dissolved into the solution during the adsorption of the next layer. For samples which were not dried during the preparation process, wet samples, the increase in salt concentration lead to a decrease in the number of NH_3^+ ionized groups, confirming a theoretical prediction made by Muthukumar [124], which accounts for the condensation of counterions on flexible polyelectrolytes. Therefore, the presence of bound water molecules in the films was seen to be conditioned by the fabrication process, in such a way that in wet samples, aggregates of water molecules are entrapped in the film. This conclusion resulted from the analysis of film composition via X-rays photoelectron spectroscopy (XPS) by analyzing the XPS spectra in the energy region were oxygen is expected. However, the number of water molecules in the PAH/PSS is

practically independent of salt concentration and revealed to be associated with the number of polyelectrolyte ionic groups. Taking into account these results, the composition of other polyelectrolyte LbL systems, mainly, poly(o-methoxyaniline)(POMA)/PSS was also determined using XPS as a function of film composition by changing the ionic strength of sodium chloride and potassium chloride of PSS aqueous solutions. Eight bilayers POMA/PSS LbL films were prepared from POMA solutions with a concentration of 0.6 g/L [116], while PSS solutions were prepared with a concentration of 10^{-2} M [9,10]. The adsorption period of time was 10 minutes for each layer and the samples have not been dried during the preparation. The XPS characterization procedure was similar to the one described elsewhere [9,10]. The polyelectrolyte POMA was chosen taking into account the obtained infrared results where hydrogen bonds associated to water were found [117,119]. In figure 4.1.2, the ratio between the percentage of oxygen atoms which are not related with the assembled polyelectrolytes and the percentage of ionic associated groups is plotted as a function of solution salt concentration. These results show that the number of adsorbed water molecules in the POMA/PSS decreases as the ionic strength increases, which can be related to the increase of number of counterions in the film. This result allows us to conclude that the type of salt ions possibly does not influence the amount of retained water molecules and the number of them in a biomimetic membrane obtained via the LbL technique can be controlled with precision.

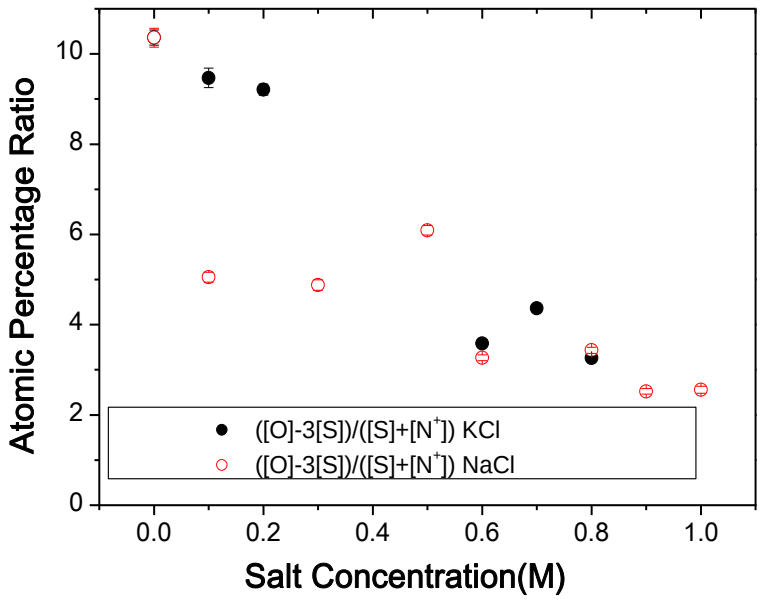

Figure 4.1.2. Plot of the ratio between the percentage of oxygen atoms which are not related with the assembled polyelectrolytes and the percentage of ionic groups associated to them. The POMA/PSS films were prepared from PSS aqueous solutions with the ionic strength of sodium chloride (NaCl) and potassium chloride (KCl).

BIOMIMETIC MEMBRANES FOR RADIATION DAMAGE STUDIES

As mentioned above, the LbL technique can be applied to the creation of molecular heterostructures composed by biomolecules such as proteins, enzymes, nucleic acids (DNA) and lipids, and used to investigate radiation damage in a membrane like structure. The LbL technique has been used to

prepare thin films of DNA bases [125], DNA and lipids. To compare the damage both in DNA containing LbL films and cast films, both type of samples were irradiated with vacuum ultraviolet synchrotron radiation (VUV) at 140 nm (8.85 eV) and a mean light intensity impinging the samples of the order of $9x10^{-4}$ W/m^2. The DNA LbL films were prepared alternating DNA layers with PAH. The DNA solutions were obtained dissolving deoxyribonucleic acid sodium salt from calf thymus (from Aldrich), in ultra-pure water to a concentration of 0.5 mg/mL. The PAH aqueous solutions were obtained with a concentration of 10^{-2} M. The adsorption period was 3 minutes in both polyelectrolytes and films have not been dried during its production. The film building up was monitored using VUV spectrophotometry by plotting the absorbance band intensity at 203 nm, the most intense band, as a function of the number of deposited bilayers. The expected linear growth behaviour with the number of DNA layers was observed, showing that the adsorbed amount of PAH and DNA are constant for each adsorbed layer. This proves the reliability of producing PAH/DNA films with accurate controlled thickness. Radiation damage was monitored with infrared spectrophotometry allowing the assignment of spectra peaks changes to characteristic DNA molecular vibrations. As in a previous work [12], it has been observed that the energy of 8.85 eV causes damage to DNA molecule as revealed by the decrease in the C-O stretch vibration of furanose in backbone, PO_2^- groups, thymines, cytosines and adenines groups. Moreover, the observed changes occur at different rates, indicating that several damage processes are taking place. To compare the DNA damage in both type of LbL and cast samples, the ratio between the area of the absorbance peak at 1090 cm^{-1} associated to the phosphate groups relatively to the area of the peak at 961 cm^{-1} which is associated with DNA skeletal bonds was plotted as a function of the irradiation time as shown in figure 4.1.3. The curves indicate that the damage in the phosphates groups is higher in DNA cast films than in LbL films, which can be accounted by the amount of water molecules in these samples to be quite different or due to the fact that PAH is acting as a DNA protective shield. In both cases further measurements have to be addressed to obtain precise information on the amount of water molecules and of radiation damage on PAH films.

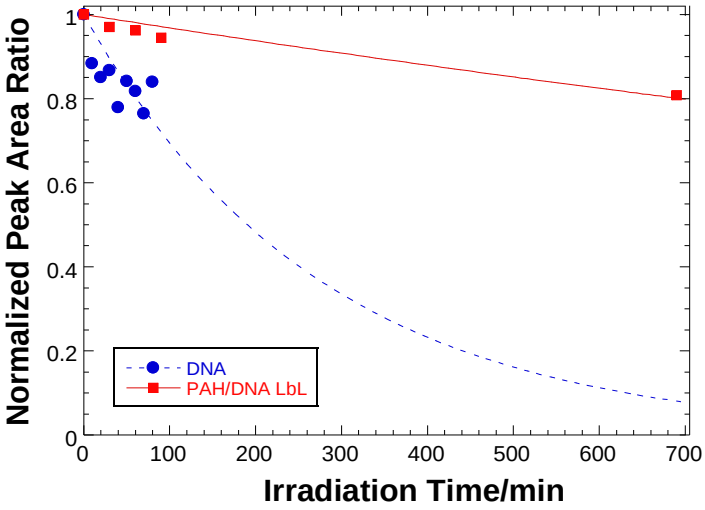

Figure 4.1.3. Normalized infrared peak area at 1090 cm^{-1} relative to peak area at 961 cm^{-1} of a DNA cast sample and PAH/DNA film irradiated for different periods of time with synchrotron radiation at 140 nm. The lines are imposed exponential decays.

Conclusions

Fabrication of biomimetic membranes was shown to be achieved via layer-by-layer (LbL) technique. The obtained layered heterostructures resulted from adsorption of alternated oppositely charged molecules from aqueous solutions into solid surfaces. The build-up and morphology of each layer depend on adsorption parameters such as solution concentration, molecular weight, temperature, time, pH, and ionic strength. These heterostructures contain bound water molecules near to the adsorbed macromolecules giving rise to the presence of water molecules in the final layered molecular structure, which is fundamental for keeping the biological molecules environment. In addition, the presence of water molecules in the heterostructures depend of the type of adsorbed species and the ionic strength of the solutions used to prepare the adsorbed layers. Results obtained in polyaniline LbL heterostructures showed that the increase of solution ionic strength leads to an increase of the number of counterions in the heterostructure and decrease in the number of water molecules per ionic group. However, this is not a general trend in such a way that in other polyelectrolytes the number of water molecules per ionic group was observed to be independent of salt concentration and number of counterions. As a consequence, it is fundamental to systematically analyses the processes that are leading to increase and control the number of water molecules within biomimetic membranar structures. This is particularly relevant in what concerns radiation damage studies of DNA containing biomimetic molecular heterostructures where different salt solution contents are leading to different damage levels. In this way, controlling water molecules within a biomimetic system is fundamental to understand the role of water in the radiation damage processes. Finally, the biomimetic membranes composed of biological molecules, promise to be a new approach to address the study of radiation damage on biological systems with the main objective to understand the physical processes that take place when radiation is impinging into the biological molecules within a supramolecular biological structure, which can then also have implications in radiation therapy, radiation sensors and radiation equivalent materials development.

ACKNOWLEDGMENTS

The authors acknowledge the support for the research by the EU Access to Research Infrastructure Action of the Improving Human Potential Programme, contract number RII3-CT-2004-506008 access to the ASTRID storage ring, Aarhus University, Denmark; to the Daresbury Laboratory Synchrotron (CCLRC) facility in the UK. This work forms part of the EU/ESF RADAM COST Action-P9, of the GRICES/CAPES 2007/2008 action (Procº.4.1.3/CAPES/CPLP) and also part of the ESF network programme EIPAM and ECCL COST Action CM0601.

4.2. PHOTOABSORPTION OF BIOMOLECULES AND RADIATION DAMAGE – STUDIES IN ADENINE FILMS

Paulo Limão-Vieira, Ana M. Costa, Susana Oliveira,
Paulo J. Gomes, Paulo A. Ribeiro and Maria Raposo

STATUS: Published in Journal of Physics: Conference Series, 88, 012004, 7 pages, 2007

ABSTRACT

The Layer-by-Layer (LbL) technique has recently been developed as a promising method for production of thin films functional molecular heterostructures since the interactions occurring are essentially ionic and hydrogen bonding patterns are found to be the identical to those observed in biological systems. Such films have been shown to be also potentially good mimics of biological membranes. Though, it is possible that a study of biological relevant molecules assembled in LbL films will provide a closer analogue to their role in cellular systems. Thin films of adenine (A) and the polyelectrolyte poly(vinylsulfonic acid sodium salt) (PVS), were prepared by cast and Layer-by-layer (LbL) techniques. In this article, the experimental results on the UV irradiation of adenine cast films are described and the effect of 140 nm irradiation, with an estimated dose of about 8.5×10^{-4} W/m^2, is evaluated at the molecular level.

INTRODUCTION

Synchrotron radiation (SR) has been used for studying photo-induced processes in research areas such as physics, chemistry, astronomy, biology and medicine, among many others. Due to its nature of high intensity, broad spectral range, high degree of polarization and collimation, makes SR a powerful tool for basic and applied research [126]. Since the UV1 beam line at the ASTRID synchrotron light source at the Institute for Storage Ring Facilities (ISA), University of Aarhus, Denmark became available at the end of 2001, we have been studying the spectroscopy of a wide variety of molecular targets, including aeronomic molecules contributing to global warming and ozone depletion [127]. Therefore, Vacuum Ultraviolet (VUV) photoabsorption investigations of several biomolecular targets in the gas phase have also been studied (see e.g. ref. [128,129]), providing results on the electronic state spectroscopy of these molecular systems. Although a few experiments have been carried out on the effects of radiation on key biological molecular targets, the knowledge of the photoabsorption processes are also extremely necessary to evaluate the role of these molecular systems in physiological environments. Nevertheless, and in order to assess the risks from radiation damage and modelling the effect of radiation on cellular material, a comprehensive understanding of the underlying interactions between the primary radiation (e.g. UV photons) and the biomolecules (e.g., DNA and its constituents) is required. This may, in turn, provide information about the molecular

pathways that lead from initial deposition of radiative energy to the formation of irreversible biomaterial damage.

Recently the effects of radiation on DNA and other biomaterials have been shown to be a consequence of local damage at the molecular level, which means, site specific reactions in the nucleotide's bases [130]. The early stages after irradiation (10^{-16} – 10^{-9} s) in the chronology of radiation damage have been well established to be physical and physical-chemistry in nature, which in turn means that the underlying mechanisms can be identified and described at the molecular level. Therefore, understanding mutagenesis as a consequence of radiation damage depends on the detailed knowledge of the spectroscopy and dissociation dynamics of key components in certain initiation reactions and/or of the biomolecular environment constituents [4].

Gas phase experiments often do not represent the medium in which photon interactions occur within the physiological environment. In order to gain some insight into how the spectroscopy and dissociation dynamics of certain molecules (e.g., water) is influenced by its environment, we have started a series of experimental measurements in both liquid and condensed phases [123]. The layer-by-layer (LbL) film technique has recently been developed as a promising method for production of functional molecular heterostructures [131,109] by alternated adsorption at solid/liquid interface of opposite charged polyelectrolytes, where the interactions occurring are essentially ionic and the hydrogen bonding patterns [116,119,131,132,] are found to be the same as those observed in biological systems. In addition such films are also potentially good mimics of biological membranes [108,133]. Therefore, it is possible that a study of the presence of biological relevant molecules assembled in LbL films will provide a closer analogue to their role in cellular systems [9,10]. Recent studies of the UV radiation effect on cast DNA, where films have been prepared by spreading the material solution into a solid substrate and allowing the solvent to evaporate, and LbL films, revealed an increase in the absorbance band intensity centered at 190–200 nm [12]. This band is associated with the electronic transitions of the nucleic bases. In order to infer on the transitions induced by UV radiation and the specific molecular site where damage is taking place, further parallel studies into solid films of nucleic bases were carried out. In this article, the experimental results on the UV irradiation of adenine cast films are described. Taking into account the recent experimental results, showing that the presence of water molecules are an important role in DNA damage, efforts have been done to obtain adenine layer-by-layer films in order to control the amount of water molecules present in these films. The conditions required to build adenine LbL molecular films are also addressed here.

EXPERIMENTAL SET-UP

CONDENSED PHASE MEASUREMENTS

The set-up used for film samples characterization in the VUV photoabsorption region consisted of a vacuum chamber containing a holder which supports up to three CaF_2 sample discs and one reference disk mounted on a MDC SBLM-266-4 push-pull linear motion. Synchrotron radiation passes through the sample and a photomultiplier was used to measure the transmitted light intensity. The

incident wavelength was selected using a toroidal dispersion grating with 2000 lines/mm providing a resolution of ~ 0.075 nm at FWHM. In both type of samples, the UV beam light passes through the samples and the transmitted intensity, I_t measured at 1.0 nm intervals. For wavelengths below 200 nm a flow of He gas is flushed through the small gap between the photomultiplier and the exit window of the gas cell to prevent any absorption by air contributing to the spectrum. The minimum and maximum wavelengths between which scans are performed, 115 – 320 nm (10.8 – 3.9 eV), are determined by the windows of the gas cell (LiF entrance and CaF_2 exit) and the grating, respectively. The synchrotron beam ring current is monitored throughout the collection of each spectrum in order that spectra can be corrected for any changes in incident photon flux during the period of spectral accumulation and each sample measurement was accompanied by a *background* scan recorded with the reference disk. The apparatus is calibrated using O_2 and SO_2. The Schuman-Rünge absorption band of O_2 (6.9 eV – 9.5 eV) [134] is used to calibrate the absolute cross section because its broad nature minimizes the effect of any changes in energy resolution. SO_2 is used to calibrate the energy scale as it has absorption bands with clearly defined sets of sharp absorption peaks in the ranges 3.8 eV to 5.1 eV [135] and 5.15 eV to 7.25 eV [136].

FILMS PREPARATION

Films were obtained from adenine (A) and the polyelectrolyte poly(vinylsulfonic acid sodium salt) (PVS), both from Sigma-Aldrich. Aqueous solutions were prepared dissolving these materials in ultra-pure water with 18.2 MΩ.cm resistivity supplied by a Millipore system (Milli-Q, Millipore GmbH). The polyelectrolyte monomer concentration was estimated to be 10^{-2} M and for adenine a concentration of 7×10^{-3} M.

Cast films were prepared by spreading the aqueous solutions of adenine into CaF_2 substrates. The films were led resting for a 24 hours period in order to allow water to evaporate. The substrates have been hydrophilized in a H_2SO_4/H_2O_2 (7:3) solution for 10 minutes previously to film deposition.

Layer-by-layer (LbL) films were also prepared from these materials and its production comprised the following steps: i) immersion of the substrate in a cationic solution (adenine) during 5 seconds; ii) substrate + cationic macromolecule layer washing in an aqueous solution with the same pH of the cationic solution; iii) immersion of the substrate + cationic macromolecule layer into the anionic solution (PVS) during 5 seconds; iv) substrate + cationic macromolecule/cationic macromolecule bilayer washing with an aqueous solution with the same pH of the anionic solution. By repeating steps i) to iv), a large number of bilayers can be deposited. In figure 4.2.1 the procedure sequence for production of layer-by-layer films is schematically shown.

Cast and LbL films were prepared and characterized with VUV synchrotron radiation. Cast films were irradiated with UV 140 nm wavelength with an estimated dose of about 8.5×10^{-4} W/m^2.

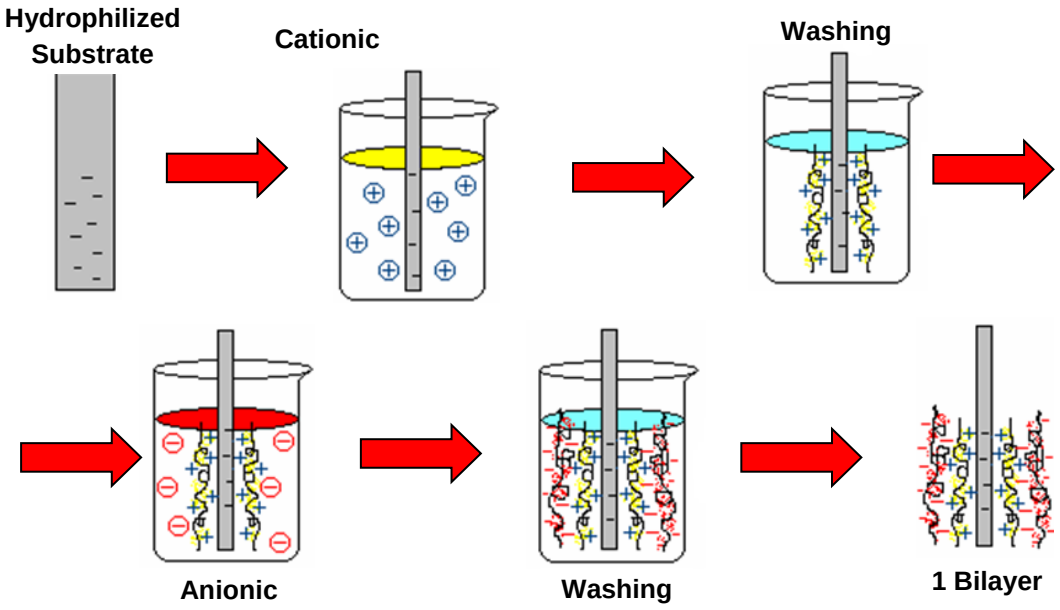

Figure 4.2.1. Schematic sequence of layer-by-layer (LBL) technique for membranes' production.

RESULTS

As it was already mentioned, recent studies of ultraviolet irradiation of DNA cast and LBL films showed an increase of the absorbance band centered at 190–200 nm [12]. This band has been associated with the adenine absorption peaks at 207 nm (5.90 eV) and at 179 nm (6.80 eV) and to the thymine absorption peaks at 208 nm (5.86 eV) and 173.5 nm (7.04 eV) [137], corresponding to ($\pi \rightarrow \pi^*$) transitions. In order to clarify the role of adenine as far as DNA damage is concerned, studies on the UV irradiation of adenine films were performed. Figure 4.2.2 shows the VUV absorption spectra of a cast adenine sample after and before irradiation at 140 nm with an estimated dose of about 8.5×10^{-4} W/m^2.

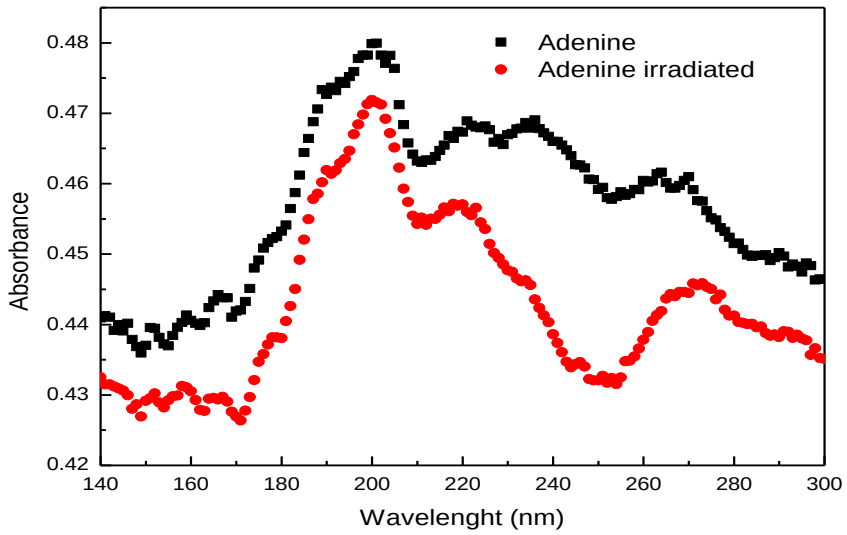

Figure 4.2.2. VUV absorbance spectra of a cast adenine film after and before irradiation at 140 nm with an estimated UV dose of about 8.5×10^{-4} W/m^2.

These spectra show that the irradiation has a strong influence in the molecule's electronic states since some of the intensity peaks are changed. In order to quantify the effects of radiation, spectral bands were fitted to Gaussian curves and the positions of the bands were compared with the literature available data [138,139,140,141]. Table 4.2.1 shows the calculated and relative peak areas before and after irradiation. The relative peak areas are obtained dividing the peak area by the total spectrum area without baseline. From table 4.2.1, it is noticeable the same proportion of decrease in the peak at 236 nm to the increase of the peak at 218 nm. This can be closely related to intramolecular rearrangement leading to change in the molecule's conformation, which can be attributed to the rupture of C_4=C_5 bond. We also noticed a significant decrease in the structure at around 236 nm but can only resume ourselves to some speculation on the change observed based on the previous assumptions. Therefore, our next investigations are to perform FTIR spectroscopy measurements in order to evaluate which sort of bond (and/or bonds) might be affected and which are probably being formed.

Table 4.2.1. Adenine absorption features, assignments, peak areas and relative peak areas after and before irradiation.

λ (nm)	ΔE (eV)	Assignment [138]	Assignment [141]	Peak Area		Area deviation	Relative Peak Area	
				Before irradiation	After irradiation		Before irradiation	After irradiation
266	4.66	$3\ ^1A'$	$S_1(n\rightarrow\pi^*)$	0.30±0.08	0.38±0.04	0.08±0.12	0.17	0.19
236	5.25	---	$S_2(\pi\rightarrow\pi^*)$ $S_3(\pi\rightarrow\pi^*)$	0.54±0.07	0.16±0.06	0.38±0.13	0.31	0.08
218	5.69	$4\ ^1A'$	$S_4(\pi\rightarrow Ryd)$ $S_5(n\rightarrow Ryd)$	0.23±0.08	0.57±0.08	0.34±0.16	0.13	0.29
202	6.17	$5\ ^1A'$	$S_7(n\rightarrow Ryd)$	0.38±0.05	0.52±0.06	0.14±0.11	0.21	0.26
190	6.53	$6\ ^1A'$	$S_8(n\rightarrow\pi^*)$	0.32±0.07	0.35±0.04	0±0.11	0.18	0.18

The preparation of LBL of nucleic bases films is not a straightforward procedure, mainly because they are small neutral molecules, much smaller and less charged than normally used polyelectrolytes, which makes adsorption from solution difficult [109]. Concerning the interactions accounting for molecules adsorption, ionic and secondary interactions such as hydrogen bonding and hydrophobic interactions have been reported [116,117,119,132] and a classification of the various types of LBL films in terms of mechanisms responsible for adsorption, has been proposed by Oliveira *et al* [139]. Marletta and co-workers [142] have shown that small molecules can be used in the production of LBL films. Changing the nucleic bases pH solution, molecules can acquire electrical charge allowing its adsorption at solid/liquid interface to take place. Layer-by-layer films of adenine alternated with PVS were successfully prepared from aqueous solutions at different pHs between 2 and 6. At pH = 3 adenine acquire positive electrical charge and LBL films can be obtained in agreement with the results of figure 4.2.3 where we show that absorbance at 257 nm versus the number of bilayers increases

linearly, therefore indicating that LBL films were successfully produced. At pH = 2, adenine continues electrically charged but its solubility in aqueous solutions is seen to increase which justifies that no LBL films can be produced.

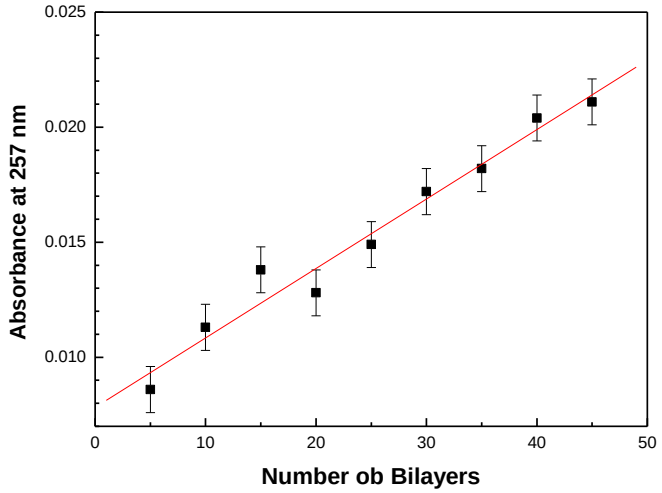

Figure 4.2.3. Absorbance at a fixed wavelength as a function of the number of bilayers for LbL films of adenine/PVS at pH=3.

CONCLUSIONS

Synchrotron radiation should be used as an important source for future investigations of biological relevant molecules. In this article it was shown that the UV radiation induces changes in the adenine molecule covalent bonds and that VUV spectrometry can be used to detect the induced changes and to some extent localize the damage. The VUV spectroscopy can also be used to monitor the adenine adsorbed amount during the formation of LbL films. In the present article, it was demonstrated for the first time the conditions that lead to the formation of adenine LbL films as a function of the pH solution.

FUTURE DIRECTIONS

The main goal at short/medium term is the understanding of the processes which occurs when well controlled membranes are exposed to radiation. For that, biological membranes and interfaces can be simulated by sequential layers obtained by the layer-by-layer technique using common polyelectrolytes, functional polymers and biological molecules as a result of alternated adsorption from aqueous solutions of molecular species having opposite electrical charges. In order to infer information about the membrane build up mechanism, it will be necessary to characterize the adsorption kinetics of the biological layers and the formation of self-organized sequential layers. Since the adsorption process comes from solution, and greatly dependent on solution parameters, adsorption kinetics should be fully characterized in terms of solution concentration, pH, ionic strength and temperature, which also influence the film final structure and characteristics. Adsorption models of macromolecules should also be addressed to interpret the experimental results. Optimized membranes can be used as a mimic to study the effect of radiation damage in soft condensed

biological materials when submitted to several radiation sources mainly X-rays, neutrons, electron beams, neutral particles beams and UV radiation both in a controlled environment and, to simulate the cell environment, in a solid/liquid interface. The description of radiation damage at the molecular level in these artificial (mimic) membranes can be performed by the traditional techniques of materials characterization, particularly adapted for in situ measurements. In addition, the LBL technique allows the incorporation of radiation sensitive polymer layers in the biomimetic membrane during its building-up process which in turn will allow to quantifying the radiation damage with the real radiation dose. Therefore, tissue equivalent materials can be built using the LbL technique. However, as far as we are aware, no studies concerning this approach have been done until now, which in turn means that several experimental and theoretical investigations are usefully needed.

ACKNOWLEDGMENTS

Support for the research undertaken by the authors is provided by the EU Access to Research Infrastructure Action of the Improving Human Potential Programme, contract number RII3-CT-2004-506008 access to the ASTRID storage ring, Aarhus University, in Denmark. We take this opportunity to thank Dr S V Hoffmann without whose expertise our synchrotron based research could not proceed, and also to Professor N J Mason for the helpful discussions over the years. MR, PAR, PJG and PLV acknowledge the visiting fellow position at CEMOS, the Open University, UK. MR acknowledges the Short Term Scientific Mission COST P9 –STSM 02196. AC, SO, PAR and PG are grateful to the CCLRC for access to the Daresbury facility in the UK.

4.3. UV DEGRADATION OF DEOXYRIBONUCLEIC ACID

Paulo J. Gomes, Paulo A. Ribeiro,
David Shaw, Nigel J. Mason and Maria Raposo

STATUS: Published in Polymer Degradation and Stability, 92, 2134-2141, 2009

ABSTRACT

The effects of UV synchrotron radiation on deoxyribonucleic acid (DNA) cast films have been systematically investigated by vacuum ultraviolet and infrared spectrophotometry as a function of irradiation time. Cast DNA films exposed at 140 nm (8.85 eV) for different irradiations times, revealed consistent changes in its VUV spectra which indicate a decrease of thymine groups and an increase of $\pi \rightarrow \pi^*$ transition spectral signature associated with the C=O group of the open sugar chain. This result was corroborated by a decrease in C-O stretching vibration at 1061 cm^{-1} observed in the infrared spectra. Both these results are consistent with the creation of single strand breaks in the deoxyribose component of DNA molecule and a decrease in the phosphate groups. It was also evidenced that UV radiation is effective in damaging the thymine groups involved in Hoogsteen base pairing with adenine. The analysis of the infrared data suggests that the usual spectroscopic fingerprints of DNA denaturation are not necessarily a reliable measure of DNA damage.

INTRODUCTION

Radiation induced damage in biomolecules is currently a hot topic in molecular physics since research has shown that irradiation with particle/photon energies below the ionizing potential can induce damage in deoxyribonucleic acid (DNA) [143]. However, how such radiation damage is induced at molecular level is still not well understood [1]. When ionizing radiation interacts with matter it produces, in very short time periods (femtoseconds), a large number of ions, radicals, excited neutrals and ballistic secondary electrons with initial kinetic energies below 100 eV [2,3], which can subsequently cause both physical and chemical modification in the biological media. Furthermore it has recently been shown that secondary electrons with energies between 4 to 6 eV can induce strand break formation in double-stranded supercoiled DNA [4]. Major experimental and theoretical studies have sought to determine the interaction mechanisms leading to such low energy and damage at the molecular level and dissociative electron attachment is now believed to be dominant mechanism. Complementary studies on the effect of radiation damage in DNA plasmid has been investigated using 7-150 eV synchrotron radiation [5] and results have revealed that DNA single-strand (SSB) and double-strand (DSB) breaks occur at all these measured energies, for both dry and solution plasmid DNA, with tissue damage being induced in the presence of water molecules which is more representative of the situation in real cells [6], as OH radicals are released to undertake chemical

rather than direct physical attack on the DNA. It should be remarked here that a large amount of studies about free radical chemistry of DNA have been performed [38,144 and references therein], and these studies are fundamental to understand the reaction processes which occur when the DNA molecule is irradiated in presence or not of water molecules.

A new approach is needed in which biological samples are studied within an environment that mimics the cell. This new approach involves the production of functional biomimetic membranes at planar interfaces. It is necessary to keep the membrane in, as far as possible, a natural aqueous environment and, for sake of quantitative characterization, it is desirable to have it at a planar solid interface. A methodology to accomplish this is to assemble, from a liquid/solid interface, biological molecules such as lipids, DNA, proteins and enzymes onto solid substrates covered with a soft cushion of adsorbed polyelectrolytes having a high water content [9,10]. A simple and versatile method for producing these architectures is the sequential buildup of layers of functional materials by the layer-by-layer (LBL) technique [109,131]. This technique, initially applied to the production of polyelectrolyte thin films, has also been found to be suitable for the production of functionalized biomolecular architectures [57,108,110,111,112] and is therefore a relevant methodology for producing biological mimics to address radiation damage studies. However, it is fundamental to characterize the radiation degradation of the biological macromolecules in vacuum. In this paper, the effect of UV radiation [140 nm] on condensed phase DNA cast films in vacuum is reported. Analysis by both UV and IR spectroscopies allows obtainins information about the effect of radiation damage on DNA's constituent molecules. The results obtained in the present work indicate that the main damage induced is the rupture of C-O-C deoxyribose bonds leading to the creation of C=O bonds and fragmentation of phosphate groups with damage to the thymine molecules which are involved in Hoogsteen base pairing.

It should be denoted that the conditions of DNA as a dry film are far away of the conditions of DNA in a living cell, being the radiation damage in vacuum conditions less effective than in wet real conditions where the presence of water molecules is significant and the interaction of water photolysis/radiolysis products with the DNA molecules takes place. However, the characterization of the UV radiation effect (140 nm) onto DNA molecules in vacuum as performed in this article is of extreme importance for comparison of the effect of UV radiation on DNA molecules surrounded by water molecules to infer its real contribution for the DNA damage. Actually, data not reported in this article, the amount of water molecules surrounding the DNA molecules is being controlled [145] taking into account the achievements of Lourenço *et al* [9,10] obtained with LbL films of common polyelectrolytes prepared from different salted aqueous solutions, and producing DNA LbL films.

MATERIALS AND METHODS

Cast films were prepared from deoxyribonucleic acid sodium salt from calf thymus (DNA), obtained from Aldrich. DNA was dissolved in ultra-pure water to a concentration of 0.5 mg/mL. The solution was deposited onto calcium fluoride (CaF_2) substrates and dried by 2 hours into vacuum desiccators. The cast DNA films were irradiated for different periods of time and characterized, after each exposure,

using synchrotron radiation at station 3.1 at the Daresbury Synchrotron Facility, UK. The mean light intensity impinging the sample at 140 nm was of the order of 8.5×10^{-4} W/m^2. Infrared spectra of the samples were measured using a Fourier transform infrared spectrophotometer Nicolet - model 530.

RESULTS AND DISCUSSION

1. EFFECT OF VUV RADIATION ON DNA ELECTRONIC TRANSITIONS

The absorbance spectrum of a DNA cast film prepared from aqueous solution deposited onto a CaF_2 substrate is shown in figure 4.3.1.

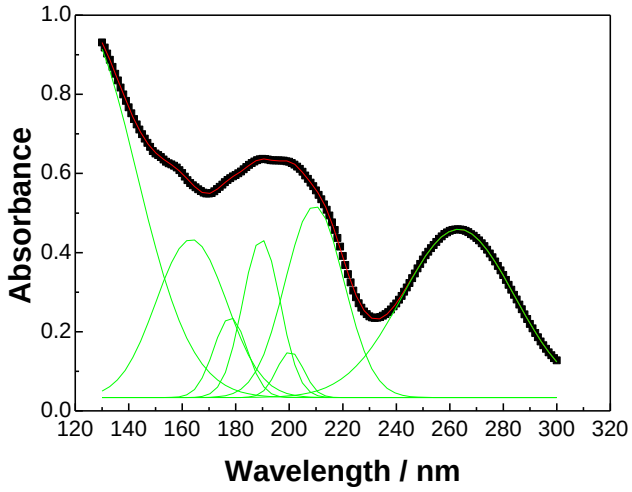

Figure 4.3.1. The vacuum ultraviolet absorbance spectrum of a DNA cast sample. The solid lines correspond to spectrum peak structure obtained by fitting of VUV spectrum with a set of Gaussians.

Although some evidence for fine structure could be seen in the spectrum, two main bands, one at about 260 nm and other at about 190-200 nm can be observed. The 260 nm band is the well-known DNA absorption band generally attributed to the DNA bases [146]. The band centered at about 190-200 nm may be attributed to the adenine peaks at 207 nm (5.90eV) and at 179 nm (6.80 eV) and to thymine base peaks at 208 nm (5.86 eV) and 173.5 nm (7.04 eV) [146]. In order to obtain more information about the peak structure, the spectrum was deconvoluted into a set of Gaussians with the features listed in Table 4.3.1. The values displayed in this table correspond to the average of peak positions and widths at half heights calculated using four different spectra.

Table 4.3.1. Characteristics of peaks observed in DNA cast films by VUV.

Peak Position (nm)	Peak Position (eV)	Peak Width (nm)	Assignment
119.8±1.1	10.4±0.1	42.5±1.4	Direct ionization of nucleobases
161.8±0.8	7.66±0.04	25.5±1.4	Thymine
177.4±0.5	6.99±0.02	12.2±1.0	Purine N(7)H and N(9)H
188.3±0.8	6.59±0.03	17.9±2.1	Purine N(7)H and N(9)H
201.5±1.6	6.15±0.05	11.5±1.6	Purine N(7)H and N(9)H
209.9±0.6	5.91±0.02	21.8±0.6	n→ π* guanine π→π* thymine
263.4±0.08	4.708±0.002	42.0±0.2	All bases

The peak centred at 119.8 nm (10.4 eV) is due to direct ionization of nucleobases [147]. The peak at 161.8 nm (7.66 eV) arises from strong thymine absorption as determined by Shlukla and Leszczynsky [148]. The peaks at 177.4 nm (6.99 eV), 188.3 nm (6.59 eV) and 201.5 nm (6.15 eV) are due to the strong transitions located at 6.28 (4^1 A'), 6.38 (6^1 A') and 6.81 (8^1 A') calculated by Borin *et al* [149] for purine N(7)H and N(9)H. The peak 209.9nm (5.91 eV) may be due to n → π* guanine transition and a π → π* transition in thymine [148] and the peak at 263.4 (4.708 eV) is generally assigned to all bases, see for example the recent work of So and Alavi [150], with assignments of vertical excitation energies displayed in [147]. In addition, the DNA molecule spectra should have contributions of deoxyribose and phosphate groups as will be discussed later.

The absorbance spectra obtained before and after different irradiation time periods of DNA cast films with synchrotron radiation are shown in figure 4.3.2. The films were irradiated at 140 nm which is close to the first ionization potential of several DNA constituents of about 9 eV [151].

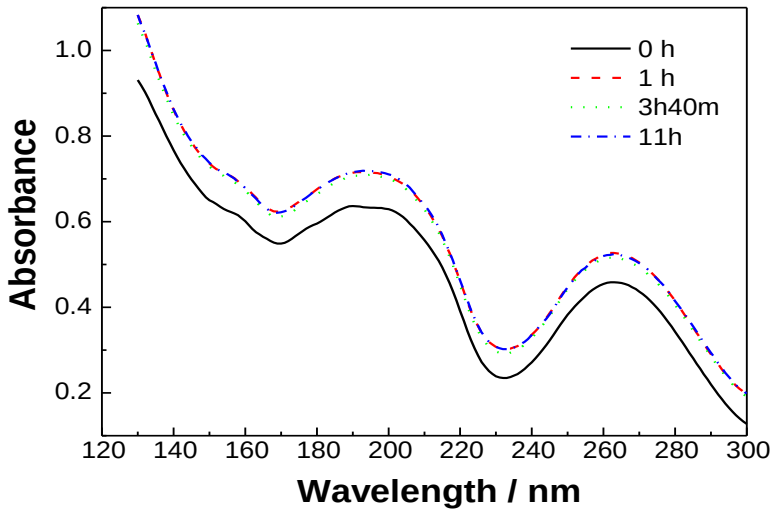

Figure 4.3.2. Absorbance spectra of a DNA cast sample for different irradiation time periods using 140 nm wavelength radiation.

It should be noted that the apparent increase of absorbance with irradiation time is due to an increase in the baseline absorption. Such changes in the baseline upon irradiation might be indicative of fragmentation. Baseline corrected DNA VUV spectra, in the 170 to 230 nm wavelength region, plotted for irradiation times are shown in figure 4.3.3. From these curves one can observe a slight increase in absorbance intensities and change in the behaviour of the absorbance curves after irradiation of the DNA samples which is indicating that some transitions are being promoted.

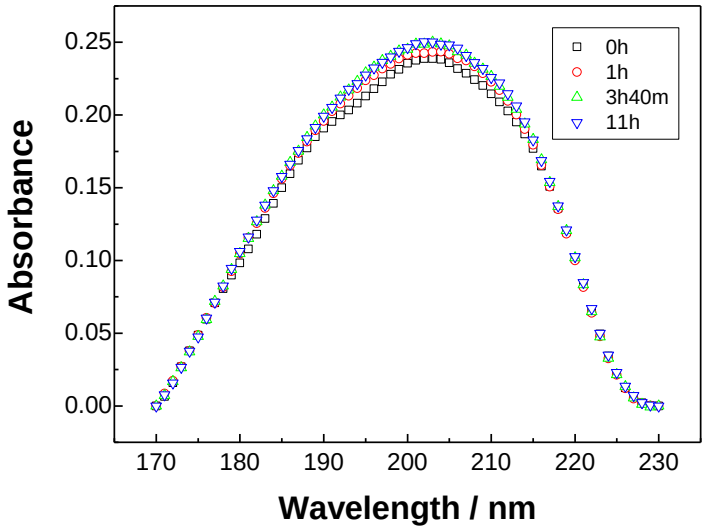

Figure 4.3.3. DNA VUV spectra, after correction for baselines, for different irradiation times in the 170 to 230 nm range.

The DNA spectra for different irradiation times were deconvoluted into Gaussians with the same characteristics as unirradiated samples (listed in table 4.3.1). The peak areas of each Gaussian were plotted versus the irradiation time as shown in figure 4.3.4 a), b) and c). These peak areas were found to decrease with irradiation time for the 162 nm and 263 nm peaks, indicating a decrease of thymine groups. However, one cannot discard that other DNA bases groups are not being affected. An increase of 188 nm and 202 nm peaks areas was also observed which indicates a modification in the DNA molecule. Recently, Nielsen *et al* [152] using VUV circular dichroism measurements on aqueous sugar solutions suggested the presence of a weak band at 188 nm associated with the $\pi \rightarrow \pi^*$ transition of the C=O chromophore in the sugar open-chain. Therefore the increase of absorbance observed at 188 nm can be ascribed to an increase in the C=O groups as a result of formation of sugar open-chains.

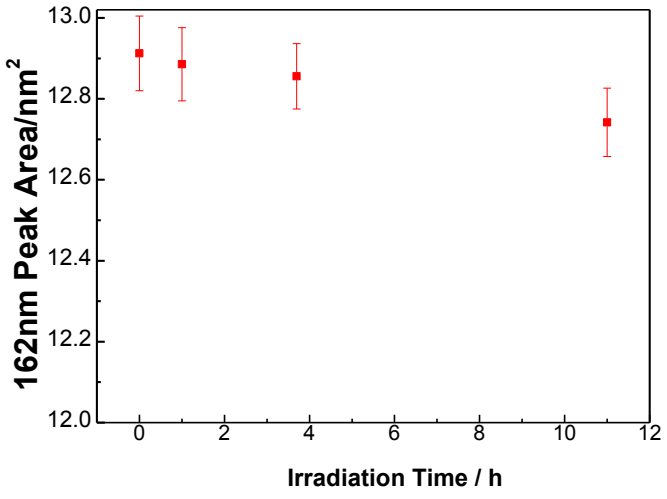

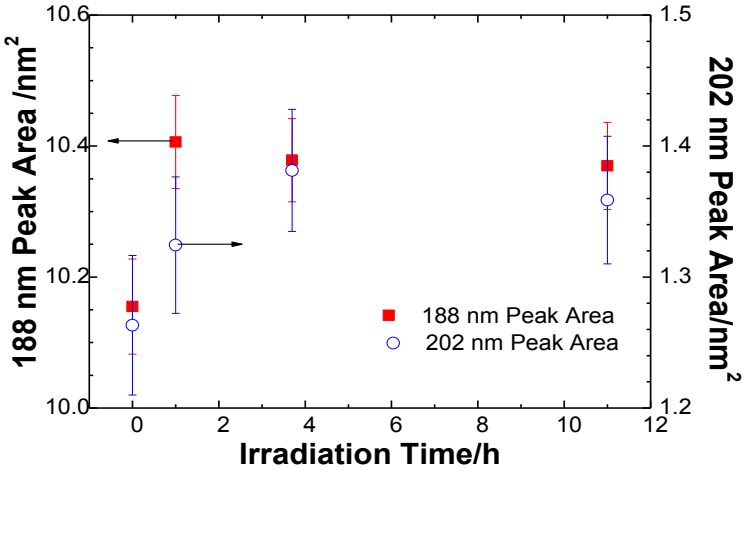

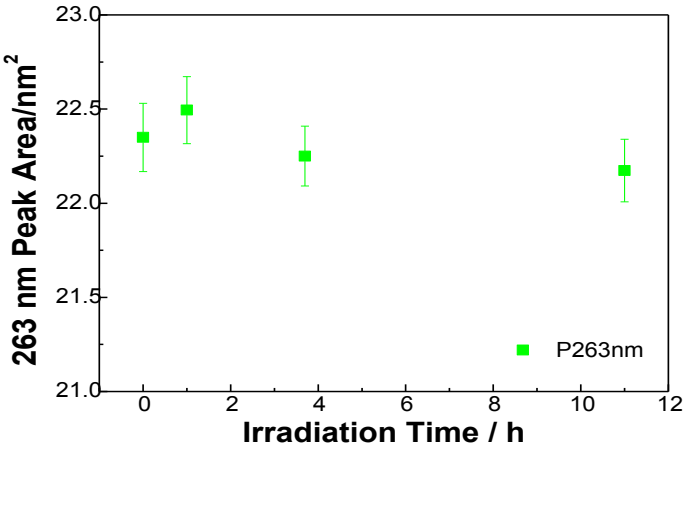

Figure 4.3.4. Peak area versus the irradiation time for a DNA cast film. Peak centered at: a) 162 nm; b) 188 nm and 202 nm and c) 263 nm.

Finally, it should be remarked here that after one hour of radiation exposure no further changes are observed in the spectra, which means that under the present experimental conditions irradiation of DNA films with 140 nm light of flux of 8.5×10^{-4} W/m^2 is sufficient to induce DNA damage in 10-15 minutes.

2. EFFECT OF VUV RADIATION ON THE VIBRATIONAL SPECTRA

2.1. DNA BANDS ASSIGNMENTS

As the duration of the scan of a VUV spectrum took about 15 to 20 minutes, the measurement of VUV spectra can clearly induce changes in the DNA. For this reason, the effect of the UV radiation on DNA films was further investigated by FTIR spectroscopy. The spectra in the 1800-900 cm^{-1} range of a DNA film before and after 80 minutes of irradiation at 140 nm are shown in figure 4.3.5. Three main regions can be observed in these spectra namely, at 1800-1500 cm^{-1}, 1500-1250 cm^{-1} and 1250-900 cm^{-1}. These regions are composed by a set of absorbance peaks components that can be associated with DNA molecular vibrations according the literature [153,154,155], as follows: *a) DNA bases (1800-1500 cm^{-1})* - This range is associated with the DNA bases and contains 6 peaks centered at 1711, 1693, 1651, 1605, 1581 and 1531 cm^{-1}; *b) Base-sugar (1500-1250 cm^{-1})* - This region corresponds to the IR absorption in the bases vibrations and base vibrations influenced by the sugar component. In this region, 8 peaks were found at 1485, 1446, 1414, 1390, 1366, 1297, 1280 and 1241 cm^{-1} ; and *c) Backbone (1250-900 cm^{-1})* - This region is associated with the phosphate backbone region and contains seven peaks centered at 1210, 1183, 1097, 1061, 1020, 961 and 927 cm^{-1}. The assignments of all these peaks are displayed in table 4.3.2.

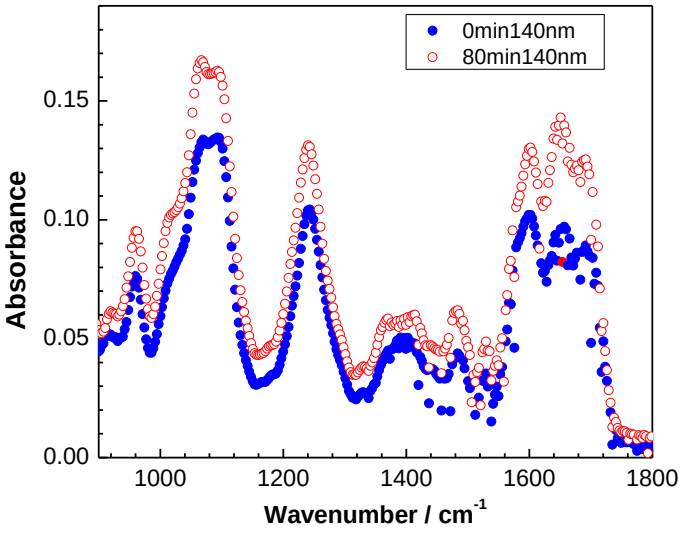

Figure 4.3.5. Infrared absorbance spectra of a DNA cast sample before and after irradiation with 140 nm UV light for 80 minutes.

Table 4.3.2. Characteristic infrared absorptions in DNA cast films. The Peak Area Ratio Tendency (PART) indicates the increase or decrease with irradiation time of each peak area relatively to the 961 cm^{-1} peak area. [153,154]

Wavenumber (cm^{-1})	**Peak Width (cm^{-1})**	**Literature Wavenumber (cm^{-1})**	**Assignment**	**PART**
Base frequency region				
1711 ± 1	23±1	1715 1712	C6=O6 stretching of guanines involved in Hoogsteen third strand binding and/or C2=O2 stretching of thymines involved in reverse Hoogsteen third strand binding	decrease
1693 ± 1	28±2	1698 - 1691	C2=O2 strength of thymine single stranded or double stranded	constant
1651 ± 1	50.8±0.2	1655 - 1657	C2=O2 strength of cytosine single stranded or double stranded	constant
1605± 1	22.0±0.2	1601	C=N ring vibration of guanine	decrease
1581± 1	33.2±0.5	1590 - 1575 1585	C=N ring vibration of Guanine single stranded or double stranded Ring vibration of guanine and adenine	decrease
1531± 1	19.0± 0.9	1527 - 1520 1530	In-plane vibration of cytosine single stranded or double stranded	constant
Base-sugar frequency region				
1485± 1	29.4± 0.5	1495 - 1476	Ring vibration of Adenine and Guanine N7C8H bend of Adenine/Guanine	constant
1446± 1	21.9± 0.5	1457 - 1453 1438 - 1434	Adenine A/B forms Adenine Z form	decrease
1414± 1	27± 2	1413 - 1408	C3'-endo deoxyribose in *A* form helices C3'-endo deoxyribose in *Z* form helices	decrease
1390± 1	23± 2	1389 - 1374	Calc: CH_3 Symmetric deformation of deoxyribose thymine	decrease
1366± 1	21.7± 0.7	1381 - 1369	Cytidine and guanosine in anticonformation	decrease
1297± 1	11.9± 0.1	1297 – 1285	C4-NH2 strength of cytosine [28], [29]	decrease
1280± 1	23.3± 0.6	1281 1275	C5=C6 vibration of cytidine CN3H bend of deoxyribose thymine	decrease
1241± 1	37.9± 0.3	1245 - 1235	Antisymmetric PO_2^- stretch in A-form	decrease
Backbone frequency region				
1210± 1	21.2± 0.1	1225 - 1220	Antisymmetric PO_2^- stretch in B-form	increase
1183± 1	20.9± 0.2		A form marker – Sugar phosphate backbone	decrease
1097± 1	36.7± 0.6	1090 - 1085	Symmetric PO_2^- stretching of Backbone	decrease
1061± 1	31.3± 0.7	1069 - 1044	CO stretch of the furanose in backbone	decrease
1020± 1	33.7± 0.4	1020 - 1010	Furanose vibrations	constant
961± 1	20.9± 0.2	970 - 950	CC stretch of the backbone	----
927± 1	25.6± 0.5	930 - 924	Z-form	constant

Several changes in the IR spectra have seen observed after irradiation. In order to better analyze the infrared spectra changes, spectra baselines were removed and the peaks which did not change as a result of exposure to UV radiation were identified. From this analysis, the peak area at 961 cm^{-1} wavenumber, which is associated with CC stretch of DNA backbone, was found not change under UV radiation and in such a way that this peak was used to normalize the obtained data, dividing the other peaks areas by the area of this peak, avoiding that the small changes due to the measurement of the infrared spectra in different regions of the sample are not affecting the observed peak areas decrease or increase.

In order to quantify the changes induced by UV radiation the spectra were fitted with Gaussian components after baseline removal. The peak characteristics namely, peak position and peak width, were calculated as free fitting parameters for each spectrum. Mean values for the peak positions and widths were then calculated from all fitted values and are displayed in table 4.3.2. These mean values were then used in new fittings and the peak areas were calculated. The calculated peak areas are essentially proportional to the number oscillators which lead a particular absorbance peak. These calculations allow to determinate peak area ratios relative to the 961 cm^{-1} peak area, which is associated with the backbone frequency region, as a function of irradiation time. In table 4.3.2 it is also displayed the general behaviour with the irradiation time, designed by increase, decrease or constant, of each peak area relative to that under the 961 cm^{-1} peak.

2.2. DAMAGE IN DNA SUGAR RELATED COMPONENTS

Since the VUV spectra results suggested that the UV radiation opens the deoxyribose ring, the related sugar components were investigated. In figure 4.3.6, the calculated area ratios of the furanose vibration (1020 cm^{-1}), of the C-O stretching vibration of nucleic acid sugar (1061 cm^{-1}) and of the PO_2^- stretching of backbone (1097 cm^{-1}) relative to bonds associated with the DNA backbone (961 cm^{-1}) are plotted as a function of irradiation time. This figure reveals that vibrations associated with the furanose are independent of the irradiation time, while those associated with C-O stretching of nucleic acid sugar (1061 cm^{-1}) and PO_2^- stretching vibrations are seen to decrease with the irradiation time. Such a decrease in the C-O bond stretching vibration of deoxyribose during irradiation has also been observed by Tang and Guo [156] in characterizing the effect of UVA and UVB irradiation on aqueous solutions of DNA calf thymus using Raman spectroscopy analysis. Therefore it can be concluded that 140 nm radiation is sufficient to open the sugar ring and to break the DNA phosphate groups. Although both C-O and PO_2^- stretching vibrations decrease with irradiation time the ratio between the peak areas of 1097 cm^{-1} and 1061 cm^{-1} peaks is also seen to decrease with the irradiation time which indicates that the effect of radiation is more dramatic in the PO_2^- groups.

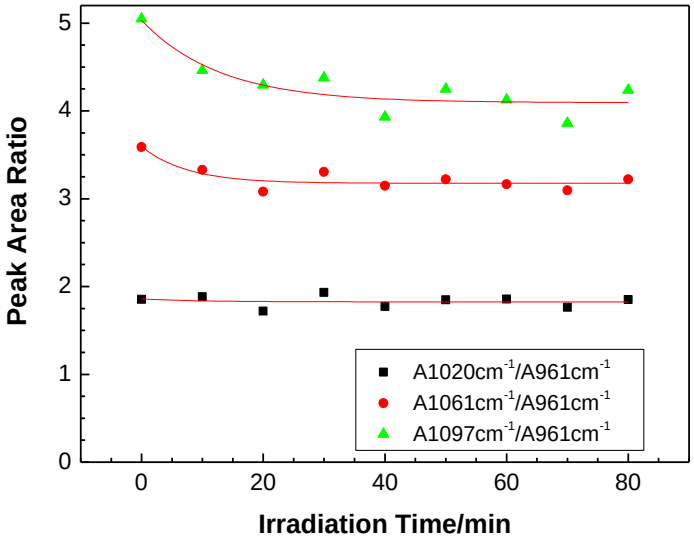

Figure 4.3.6. Ratios of the infrared peak areas at 1020 cm^{-1} (furanose vibrations), 1061 cm^{-1} (CO stretch of the furanose in backbone) and 1097 cm^{-1} (symmetric PO_2^- stretching of backbone) relative to the peak area of the 961 cm^{-1} feature. The peak area was calculated from infrared peaks obtained from spectra of DNA cast sample irradiated for different periods of time using 140 nm synchrotron radiation. The solid lines are guidelines.

Taking into account these results the ratios of the vibrations associated with the deoxyribose group were plotted as a function of irradiation time, figure 4.3.7. The graph shows the normalized peak area ratios for C-O stretching vibration of nucleic acid sugar (1061 cm^{-1}), PO_2^- stretching of backbone (1097 cm^{-1}), antisymmetric PO_2^- stretch in A DNA form (1241 cm^{-1}) and CN3H bend of deoxyribose thymine (1280 cm^{-1}) relative to the CC stretch in the DNA skeleton (961 cm^{-1}). All of these ratios decrease with irradiation time but the radiation effect on the sugar chain is weaker than CN3H bend of deoxyribose thymine (1280 cm^{-1}). The ratio for C-O stretching vibration of nucleic acid sugar (1061 cm^{-1}) decreases by 10%, while the intensity of the CN3H bending mode of deoxyribose thymine (1281 cm^{-1}) decreases by some 40%. This result shows that the effect of UV radiation is located essentially in the deoxyribose thymine groups. In addition, both PO_2^- stretching of backbone (1097 cm^{-1}) and antisymmetric PO_2^- stretch in A-form DNA (1241 cm^{-1}) decrease similarly, confirming the consistency of this method of analysis.

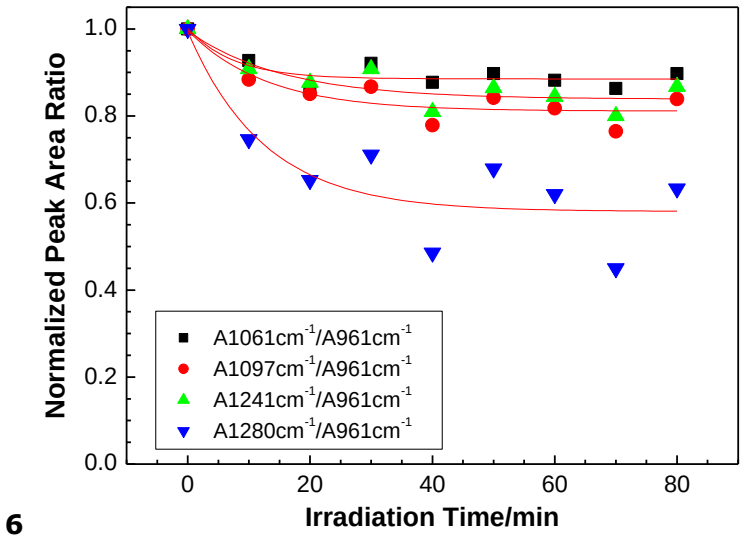

Figure 4.3.7. Normalized infrared peak area ratios at 1061 cm^{-1}(CO stretch of the furanose in backbone), 1097 cm^{-1} (symmetric PO_2^- stretching of Backbone), 1241 cm^{-1} (antisymmetric PO_2^- stretch in A-form) and 1280 cm^{-1} (C5=C6 vibration of cytidine and CN3H bend of deoxyribose thymine) relative to peak area at 961 cm^{-1} of a DNA cast sample irradiated for different periods of time with synchrotron radiation at 140 nm. The solid lines are guidelines.

The normalized peak area ratio between the CH_3 symmetric stretch with deformation of deoxyribose thymine (1390 cm^{-1}) relative to vibrations associated with DNA skeleton (961 cm^{-1}) also decreases with irradiation time, as is shown in figure 4.3.8, where this peak area ratio is plotted together with the normalized ratio between the CN3H bend of deoxyribose thymine (1280 cm^{-1}) peak area relatively to the peak area associated to DNA skeletal vibrations (961 cm^{-1}). Although, the ratio at 1390 cm^{-1} seems to decrease to smaller values, it can be observed that both ratios decrease in a similar way, within the error bars. As both these vibrations are related with deoxyribose thymine vibrations these similar decreases are consistent. For comparison with the effect of UV radiation in cytidines and guanosines, the normalized peak area ratio between the vibrations associated with cytidine and guanosine in anticonformation (1366 cm^{-1}) and the vibrations associated to DNA skeletal (961 cm^{-1}) is also observed to decrease with irradiation time, as is shown in figure 4.3.9, where this peak area ratio is plotted together with the normalized peak area ratio between the CH_3 symmetric deformation of deoxyribose thymine (1390 cm^{-1}), relative to the vibrations associated to DNA skeleton. From this plot one can conclude that the UV radiation effect is more severe in the deoxyribose thymines than in the cytidines and guanines.

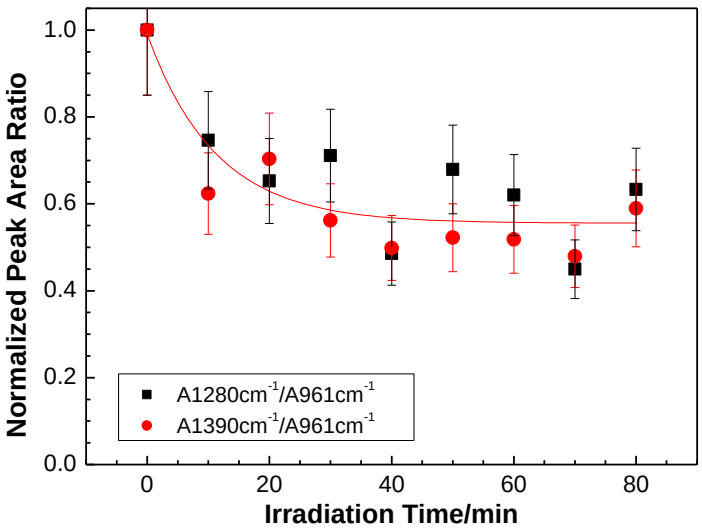

Figure 4.3.8. Normalized infrared peak area ratios at 1280 cm^{-1} (C5=C6 vibration of cytidine and CN3H bend of deoxyribose thymine), 1097 cm^{-1} (symmetric PO_2^- stretching of backbone) and 1241 cm^{-1} (antisymmetric PO_2^- stretch in A form) relative to peak area at 961 cm^{-1} of a DNA cast sample irradiated for different periods of time with synchrotron radiation at 140 nm. The solid lines are guidelines.

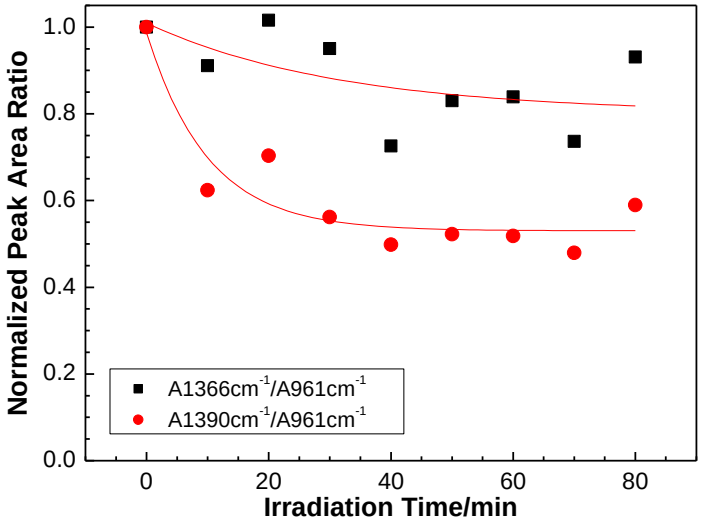

Figure 4.3.9. Normalized infrared peak area ratios at 1366 cm^{-1} (cytidine and guanosine in anticonformation) and 1390 cm^{-1} (CH3 Symmetric deformation of deoxyribose thymine) relative to peak area at 961 cm^{-1} of a DNA cast sample irradiated for different periods of time with synchrotron radiation at 140 nm. The solid lines are guidelines.

Related with the deoxyribose a similar decrease in the area ratios of 1414 cm^{-1} and 1446 cm^{-1} peaks, respectively, associated with C3'-endo deoxyribose in A and Z forms helices, and with adenine in A, B and Z forms, can be observed in figure 4.3.10. In this figure was also plotted the peak area ratio of the 1280 cm^{-1} which is associated C5=C6 vibration of cytidine and to CN3H bend of deoxyribose thymine for comparison. From this comparison, one can see that the decrease in the 1280 cm^{-1} feature is slightly more accentuated indicating that deoxyribose associated to thymines is more affected by the radiation. It should remarked here that DNA molecules are more easily attacked by ozone than RNA

molecules [157,158], suggesting that thymine groups are the DNA components more easily attain damage which corroborates these conclusions.

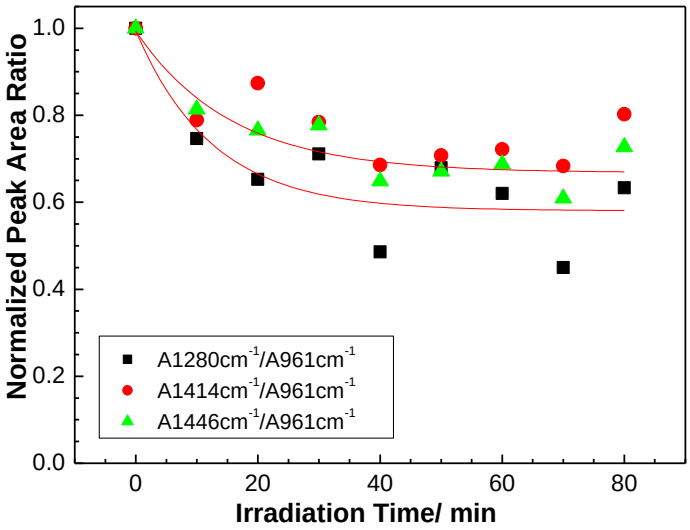

Figure 4.3.10. Normalized infrared peak area ratios at 1280 cm^{-1} (C5=C6 vibration of cytidine and CN3H bend of deoxyribose thymine), 1414 cm^{-1} (C3'-endo deoxyribose in A-form helices and C3'-endo deoxyribose in Z form helices) and 1446 cm^{-1} (adenine A, B and Z forms) relative to peak area at 961 cm^{-1} of a DNA cast sample irradiated for different periods of time with synchrotron radiation at 140 nm. The solid lines are guidelines.

2.3. DAMAGE IN THYMINE GROUPS

The above described results suggest that the infrared region associated with the thymine groups should be further explored. Moreover, it is known that two adjacent thymine groups when submitted to UV A and B radiation tend to dimerize. In fact, the cyclobutane pyrimidine dimer is the most abundant lesion caused by ultraviolet radiation and consists of a reaction of the carbon-carbon double bonds of two proximal pyrimidine bases to form a cyclobutane ring. This reaction has been recently investigated by femtosecond time–resolved infrared spectroscopy [159] and it was revealed that for DNA samples irradiated with 266 nm, the intensity of bands due to double-band stretch associated with the two carbonyl groups and the C5=C6, double bond (1632 and 1664 and 1693 cm^{-1}) decreases after several minutes of irradiation. On the other hand, the intensity of some peaks in the range of 1300 to 1500 cm^{-1} is seen to increase with the UV exposure. In the present work, related with the thymine there are three peaks respectively associated with CN3H bend of deoxyribose thymine (1280 cm^{-1}), CH_3 symmetric vibration of deoxyribose thymine (1390 cm^{-1}) and a peak at 1701 cm^{-1}, not listed in table 4.3.2, which is the sobreposition of two peaks, one associated with C2=O2 stretching of thymine in single or double-stranded (1693 cm^{-1}) and other associated to C2=O2 stretching of thymines involved in reverse Hoogsteen third strand binding and/or to C6=O6 stretching of guanines involved in Hoogsteen third strand binding (1711 cm^{-1}). The area of the 1701 cm^{-1} peak was calculated for comparison of the decay of the C2=O2 bond in all thymines. Figure 4.3.11 shows the plot of the normalized areas ratios of the peaks at 1280 cm^{-1}, 1390 cm^{-1} and 1711 cm^{-1} relative to the area of the 961 cm^{-1} peak. The peaks associated with both CN3H bend of deoxyribose thymine and CH3

symmetric deformation of deoxyribose thymine decrease by 40% and both showing a similar behaviour with irradiation time, whilst peaks due to C=O stretching of thymine decreases only by 10%.

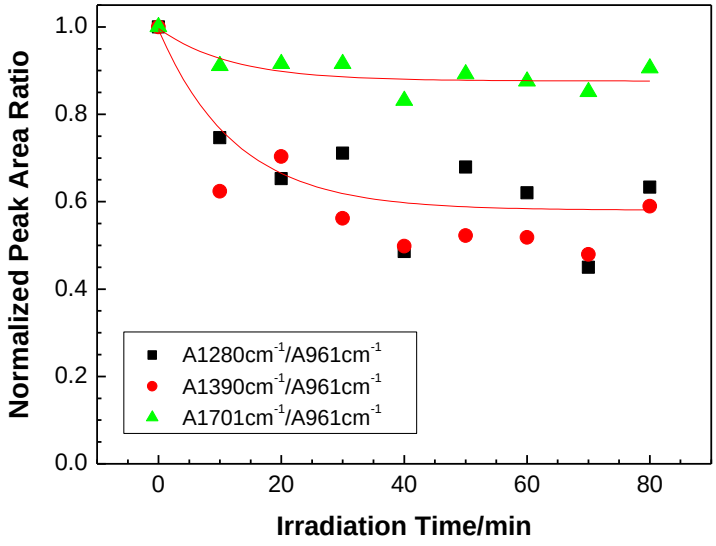

Figure 4.3.11. Normalized infrared peak area ratios at 1280 cm^{-1}(C5=C6 vibration of cytidine and CN3H bend of deoxyribose thymine), 1390 cm^{-1} (CH3 Symmetric deformation of deoxyribose thymine) and 1701 cm^{-1} (C2=O2 strength of thymine single stranded or double stranded and C6=O6 stretching of guanines involved in Hoogsteen third strand binding and/or C2=O2 stretching of thymines involved in reverse Hoogsteen third strand binding) relative to peak area at 961 cm^{-1} of a DNA cast sample irradiated for different periods of time with synchrotron radiation at 140 nm. The solid lines are guidelines.

Changes observed in the thymine group may be seen in the 1675 to 1750 cm^{-1} region, where two Gaussian components were found, taking into account that the C2=O2 strength of thymine single stranded or double stranded is associated to 1693 cm^{-1} vibrations and the C2=O2 stretching of thymines involved in reverse Hoogsteen third strand binding is present as a vibration peak at 1711 cm^{-1}. In figure 4.3.12, the normalized 1693 cm^{-1} and 1711 cm^{-1} peak ratios relative to 961 cm^{-1} are plotted. The area ratio considering only a peak at 1701cm^{-1} in this region was also plotted for comparison. From the plot, it can be seen that the UV radiation does not affect the peak at 1693 cm^{-1} associated with C2=O2 strength of thymine, while the C2=O2 stretching of thymines involved in reverse Hoogsteen third strand binding and/or to C6=O6 stretching of guanines involved in Hoogsteen third strand binding [1711 cm^{-1}] is affected. Moreover the decrease of the C=O peak is followed by an increase in the intensity of the 1210 cm^{-1} peak at the same rate of decrease in the 1711 cm^{-1} peak, which can be seen in figure 4.3.13.

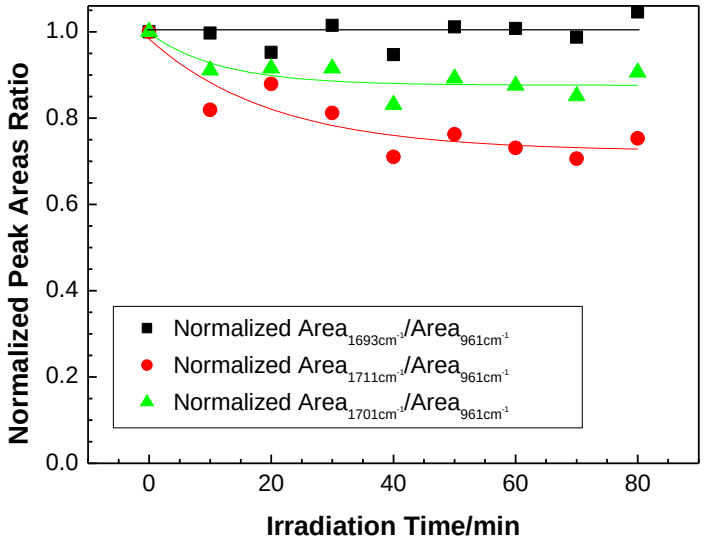

Figure 4.3.12. Normalized infrared peak area ratios at 1693 cm^{-1} (C2=O2 strength of thymine single stranded or double stranded), 1711 cm^{-1} (C6=O6 stretching of guanines involved in Hoogsteen third strand binding and/or C2=O2 stretching of thymines involved in reverse Hoogsteen third strand binding) and 1701 cm^{-1} (C2=O2 strength of thymine single stranded or double stranded and C6=O6 stretching of guanines involved in Hoogsteen third strand binding and/or C2=O2 stretching of thymines involved in reverse Hoogsteen third strand binding) relative to peak area at 961 cm^{-1} of a DNA cast sample irradiated for different periods of time with synchrotron radiation at 140 nm. The solid lines are guidelines.

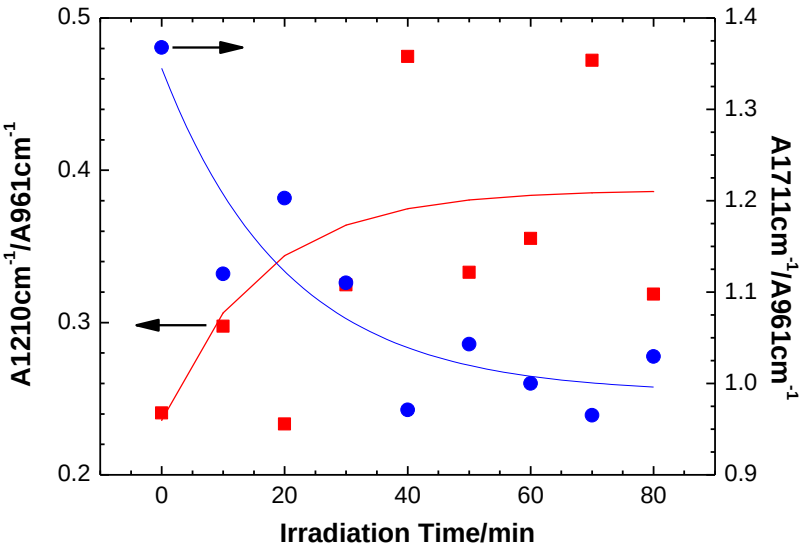

Figure 4.3.13. Normalized infrared peak area ratios at 1210 cm^{-1} (antisymmetric PO_2^- stretch in B form) and 1711 cm^{-1} (C6=O6 stretching of guanines involved in Hoogsteen third strand binding and/or C2=O2 stretching of thymines involved in reverse Hoogsteen third strand binding) relative to peak area at 961 cm^{-1}, of DNA cast sample irradiated for different periods of time with synchrotron radiation at 140 nm. The solid lines are guidelines.

However, here it should be remembered that the peak at 1210 cm^{-1} can be assigned to both antisymmetric PO_2^- stretch in B DNA form and to a normal C-O bond. Since an increase in the B-DNA form is not expected to occur, one can infer that the C=O bond of thymine is being replaced by C-O,

which can be accounted by the different spatial distribution of the adenine and thymine and the pairing between them. From the theoretical point of view Cubero *et al* [160] calculate average hydrogen-bond energies of -13.3 and -12.1 kcal/mol for Hoogsteen and Watson-Crick pairings, respectively, values which are in accordance with the ones calculated by Monajjemi and Chahkandi [161]. In addition, these authors also calculated the dipole moment for both Watson-Crick and Hoogsteen adenine thymine hydrogen bonds and achieved values of about 2 and 8 Debyes, respectively. Similar values for hydrogen bonds can be also found in [162]. Moreover, Kryachko and Sabin [163] investigated the variety of facets of the hydrogen-bond pattern of the Watson-Crick adenine-thymine (A-T) base pair of DNA obtaining the transition state of adenine-thymine which governs the conversion of the Watson-Crick pair of adenine-thymine into the Hoogsteen one and discussed the energetic and geometrical features of this conversion. In fact, these authors reported the transition state of adenine-thymine between the Watson-Crick and Hoogsteen base pairs of adenine-thymine, where the pairs are disposed nearly perpendicular to each other, being the barrier height, taken relatively to the WC pair comprise a value of 6.5 kcal/mol at the Hartree-Fock computacional level and 5.4 kcal/mol at the B3LYP method. Taking into account the described literature, our results show that the presence of Hoogsteen pairings, highly polarizabled, contributes for the degradation by UV and the Hoogsteen pairings are not being converted in Watson-Crick pairing as should be suggested by the theory.

2.4. DNA DENATURATION

Finally, in order to confirm that irradiation leads to DNA denaturation, the ratios between the intensities at 1690 cm^{-1} and 1652 cm^{-1} were evaluated. This ratio has been shown to be representative of denaturation (Miyamoto *et al* [164]). In fact, these authors in investigating the DNA hybridization and denaturation in aqueous solutions using infrared spectroscopy concluded that the ratio of absorbance of the C=O stretching peak at 1690 cm^{-1} to the absorbance peak at 1660 cm^{-1} provides a metric for DNA hybridization and denaturation. In DNA cast films the band at 1693 cm^{-1} can be assigned to the C6=O6 stretch of base paired guanines plus C2=O2 bond stretching vibration of thymines, while the 1651 cm^{-1} band is assigned to C2=O2 of cytosines plus C4=O4 stretching vibrations of thymines [165 and references therein]. However, when the intensity ratios at these wavenumbers are plotted as shown in figure 4.3.14, as a function of the irradiation time only a slight denaturation can be inferred, which is in contrast with the data discussed above. However, changes in DNA molecular conformation have been observed. It has been that vibrations associated with the antisymmetric PO_2^- stretch in A form decrease, while there is an increase in the antisymmetric PO_2^- stretch in B DNA form (1210 cm^{-1}). As discussed before this increase can be related to an increase in the C-O bond. These results allow concluding that the ratio proposed by Miyamoto *el al* is not necessarily a reliable indication of DNA damage or rather the method is only sensitive to one type of DNA damage. This conclusion is also corroborated by the work of Cataldo [157] which demonstrated that DNA is also remarkably damaged by ozone as revealed by the FTIR spectra of DNA samples submitted to ozone stream which change significantly in whole 700 to 1800 cm^{-1} wavenumber region in comparison with spectra of samples without ozone treatment.

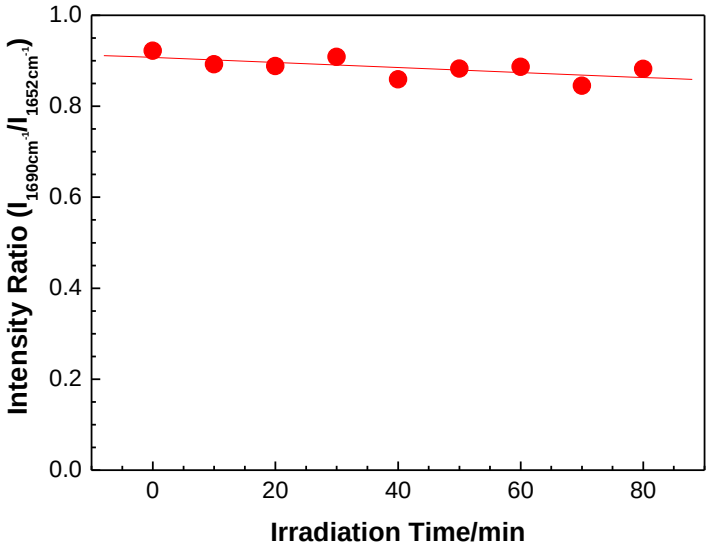

Figure 4.3.14. Infrared ratio of absorbance intensity at 1690 cm^{-1} relative to absorbance intensity at 1952 cm^{-1} for different periods of time with synchrotron radiation at 140 nm. The solid line corresponds to data fitting with a straight line.

CONCLUSIONS

Vacuum ultraviolet and infrared spectroscopies showed that vacuum synchrotron radiation at 140 nm (8.85 eV) induces damage in calf thymus DNA molecules. Although, only small changes in the VUV spectra were revealed during UV irradiation, spectra band deconvolution, allowed conclude that the contribution of transitions, associated to open sugar chain, tend to increase in magnitude during irradiation. At the same time, a decrease in the peaks associated with the DNA bases has been observed. Although such effects could be inferred from measured VUV spectra, this technique is not sensitive enough to characterize DNA damage at a molecular level. Infrared spectra of the samples allowed us to assign observed infrared absorbance peaks to particular DNA molecular vibrations. Analysis of changes in the infrared spectra after irradiation generally, revealed that UV radiation leads to a decrease in the magnitude of the absorbance peaks. A decrease is observed in the C-O stretch of the furanose in backbone, in the PO_2^- groups, in the thymines, cytosines and adenines groups. These changes occur at different rates indicating that several damage processes are involved. UV radiation was shown to affect the thymines involved in reverse Hoogsteen third strand binding which is consistent with the observed decrease C2=O2 stretching of thymines involved in reverse Hoogsteen third strand binding, while the C2=O2 stretching vibration of thymine in single or double-stranded remain unchanged. An increase in the anti-symmetric PO_2^- stretch in B form was also observed which has been related to an increase in the number of C-O bonds. It has been shown that the spectroscopic fingerprints suggested by Miyamoto *et al* [164] as characteristic of DNA denaturation are not necessarily a reliable measure of DNA damage and other spectroscopic signatures may be/should be used. Comparison of the obtained results with what is known about free-radical induced damage [109,131 and references therein] is being done. This study will be fundamental to understand the

reaction processes occurring when the DNA molecules are irradiated. To advance in this study it is fundamental control the amount of water molecules surrounding the DNA molecules which is being done using the LbL technique to produce water containing DNA films and characterize the effect of radiation on them.

ACKNOWLEDGEMENTS

The authors thank for the financial support to "Fundação para a Ciência e Tecnologia" (Portugal). MR, PAR and PJG acknowledge visiting fellowships within the Open University, UK. MR acknowledges the Short Term Scientific Mission COST P9–STSM 02196. PAR acknowledges the support received from the European Science Foundation (ESF) for the activity entitled 'Electron Induced Processing at the Molecular Level'. We are also grateful to the CCLRC for access to the Daresbury facility in the UK.

4.4. XPS ANALYSIS OF DAMAGE CAUSED BY UV RADIATION ON DNA: ENERGY THRESHOLDS FOR BREAKING DIFFERENT DNA GROUPS

Paulo J. Gomes, Ana M. Ferraria, Ana M. Botelho do Rego,
Søren. V. Hoffmann, Paulo A. Ribeiro and Maria Raposo

STATUS: To be submitted

ABSTRACT

This work stresses on the effects of damage caused by UV radiation, in the energy range of 3.5 to 8 eV, on deoxyribonucleic acid (DNA) cast films, observed by X-Ray Photoelectron Spectroscopy (XPS). The elements atomic percentages present on DNA samples irradiated at different energies were obtained from XPS spectra and the extent of damage, on bases, sugar and phosphate groups evaluated in terms of radiation energy. Nitrogen and carbon atomic percentages values point out to damage on pyrimidine groups as revealed by the decrease in both ratio between N-(C=O)-N and the total carbon and the ratio between the imine nitrogen and total nitrogen with the radiation energy increase. Analysis of the initial and final values of these ratios is indicating that thymine is the most damaged base, with hydrogen being removed from thymine and leading to the creation of thymine radical cations with resonance structures having lower ionization energies as predicted by theoretical results. Nevertheless, the energy value found to break thymine is about 5.7 eV, which is lower than the theoretical predicted values. Decrease in C-O groups was seen to take place at 6.8 eV, which is consistent with the opening of sugar rings. The phosphate groups are seen to be damaged at low energy values, <3.5 eV, which accounts for the observed distinct conductivities values of DNA samples reported in literature. Finally, analysis of sodium XPS data revealed that the degree of ionization of DNA increases with radiation energy this is explained by the presence of sodium atoms near phosphorous atoms congregate hydration water molecules which have an important role as UV radiation protection of phosphate groups.

INTRODUCTION

Radiotherapy is an effective technique for elimination of malignant cells due to its lethal action resulting from focused radiation. However, this treatment consists in the irradiation with high energy particles of a region with both diseased and healthy cells. The irradiation of healthy cells is a collateral effect with adverse outcomes which can be minimized if the nanoscale mechanisms of the direct effects of radiation in DNA are understood to make them more effective. As the high energy particles or radiation pass through the cell, they create a shower of excited and ionized molecules, electrons with lower energies which may also damage the DNA molecules and to make matters worse

irradiation with particle or photon beams, even at energies below the ionizing potential, is able to induce damage within deoxyribonucleic acid (DNA) molecules [3,4,5,6,12,143,170,172,173,174,175], namely by creating single and double strand breaks [167] and changing or removing parts [170]. For example, phosphate groups were seen to be removed from DNA cast films irradiated with visible 4.88 eV light, with consequent reduction of DNA chain conductivity, arising from electron hopping between base-pairs and phosphate groups [176]. Despite the different studies carried out making use of different approaches and techniques [177,178,179,180,181,182,183,184], the mechanisms taking place when DNA molecules are submitted to low energy radiation are not yet well understood, mainly due to the complexity of both the DNA molecule and the surrounding biological environment. For this reason, most of the data on the effect of radiation or particle beams has been obtained on DNA constituents, with only few works dedicated to this effect on DNA molecule and even less to DNA within a biological environment.

In this work, damage on DNA films caused by exposure to a vacuum UV radiation beam, in the range of 300 nm (3.5 eV) to 160 nm (8 eV), was studied using XPS. The same DNA here studied presents vacuum ultraviolet absorption spectrum which exhibits peaks assigned as follows [170]: the band at 263.4 nm (4.708 eV) was assigned to all the bases [147,150]; the peak at 209.9 nm (5.91 eV) was considered to be due to n → π^* guanine transition and a π → π^* transition in thymine [148]; the peaks at 177.4 nm (6.99 eV), 188.3 nm (6.59 eV) and 201.5 nm (6.15 eV) were referred to the strong transitions located at 6.28 eV (4^1 A'), 6.38 eV (6^1 A') and 6.81 eV (8^1 A') for purine N(7)H and N(9)H [149]; the peak at 188 nm was also associated with the π → $\pi*$ transition of the C=O chromophore in the sugar open-chain [152]; a peak at 161.8 nm (7.66 eV) was considered arising from strong thymine absorption as determined by Shlukla and Leszczynsky [148] and a peak centered at 119.8 nm (10.4 eV) was attributed to direct ionization of nucleobases [147]. From both qualitative (binding energies) and quantitative analysis (peak area combined with sensitive factors), as a function of the energy radiation, the damage thresholds will be estimated by XPS and correlated with the UV-Vis absorption spectrum.

EXPERIMENTAL DETAILS

Cast films were prepared using deoxyribonucleic acid sodium salt from calf thymus (DNA), obtained from Aldrich. DNA was dissolved in pure water, obtained from the Millipore Milli-Q system (resistivity ≥ 18.2 MΩ.cm), to a concentration of 0.5 mg/mL and cast onto silicon substrates which were previously hydrophilized in a *Piranha* solution – H_2SO_4/H_2O_2 (7:3) during 10 minutes. The films were dried for 2 hours in vacuum desiccators and exposed to a $1.14x10^{15}$ photons UV radiation beam in the range of 160 nm to 340 nm, from the Astrid Synchrotron radiation source (UV1) facility at Aarhus University, Denmark, was used [185,186]. The characterization of DNA samples was performed in an X-ray photoelectron spectrometer XSAM800 (KRATOS) operating in the fixed analyzer transmission (FAT) mode [187], with a pass energy of 10 eV, a power of 130 W and the non-monochromatised Mg Kα X-ray ($h\upsilon$=1253.7 eV) source. All the samples were analyzed on the central part of the sample, i.e. over

a 1×3 mm^2 spot area at an angle of 0º with respect to the sample surface normal using the high magnification mode. The measurement time was similar for all samples. The spectra were recorded with a Sun SPARC Station 4 with Vision software (Kratos) using a 0.1 eV step. The X-ray source satellites were subtracted, Shirley background and pseudo-Voigt profiles (Gaussian - Lorentzian products) were fitted to each region using a non-linear least-squares algorithm [188]. No charge compensation (flood-gun) was used. Binding energies (BE) were corrected by using aliphatic C 1s BE equal to 285.0 eV [189]. For quantification purposes, sensitivity factors were 0.66 for O 1s, 0.25 for C 1s, 0.42 for N 1s, 0.39 for P 2p and 2.3 for Na 1s. For the sake of damage referencing, the chemical structure of the DNA bases and a schematic DNA molecule fragment are displayed in figure 4.4.1.

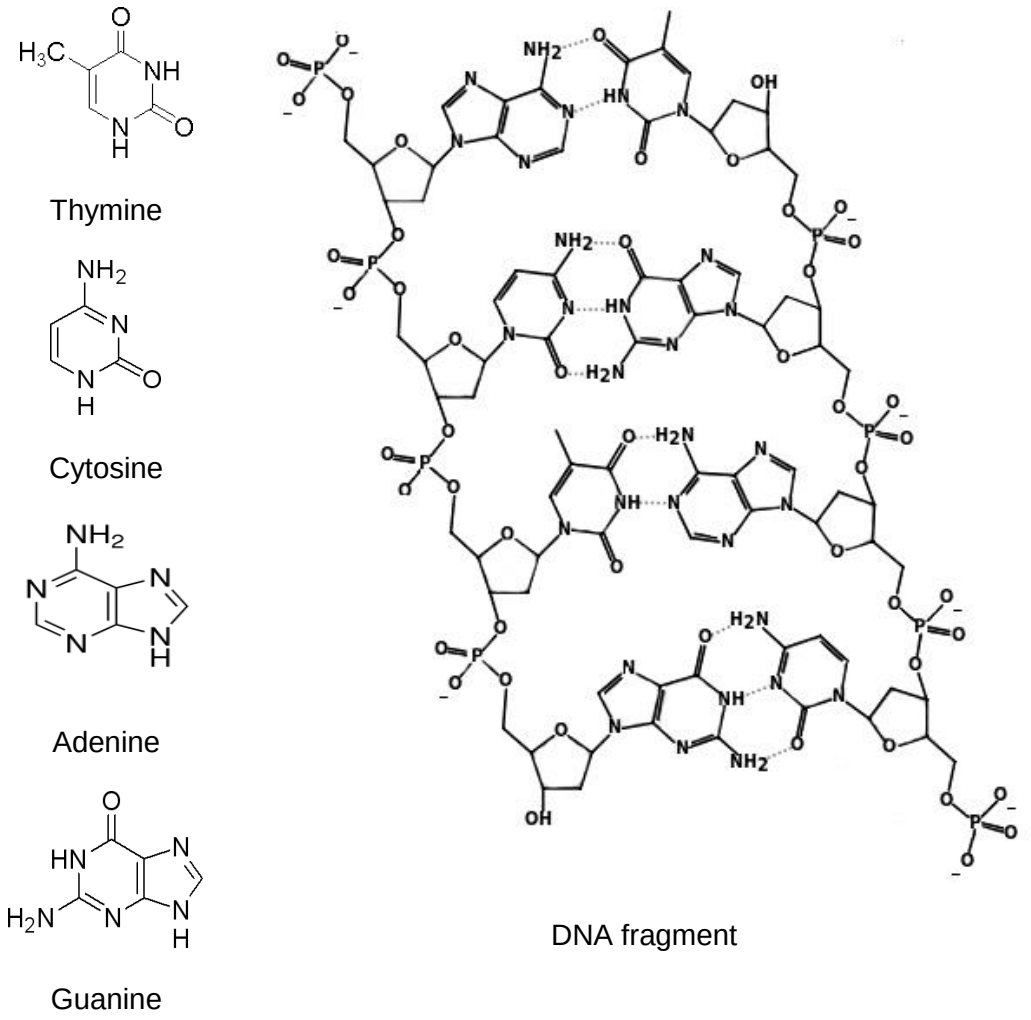

Figure 4.4.1. DNA bases chemical structures on the left and a schematic representation of a fragment of DNA molecule.

RESULTS AND DISCUSSION

XPS CHARACTERIZATION

A survey over XPS spectra of UV irradiated DNA films at different wavelengths revealed the presence of carbon, oxygen, nitrogen, phosphorus and sodium. The detailed spectra of carbon, oxygen and nitrogen presented several components, as shown in figures 4.4.2 a), b) and c), respectively, where the pseudo-Voigt profiles used to fit experimental peaks, for the sample irradiated with 160 nm wavelength UV radiation, have also been included.

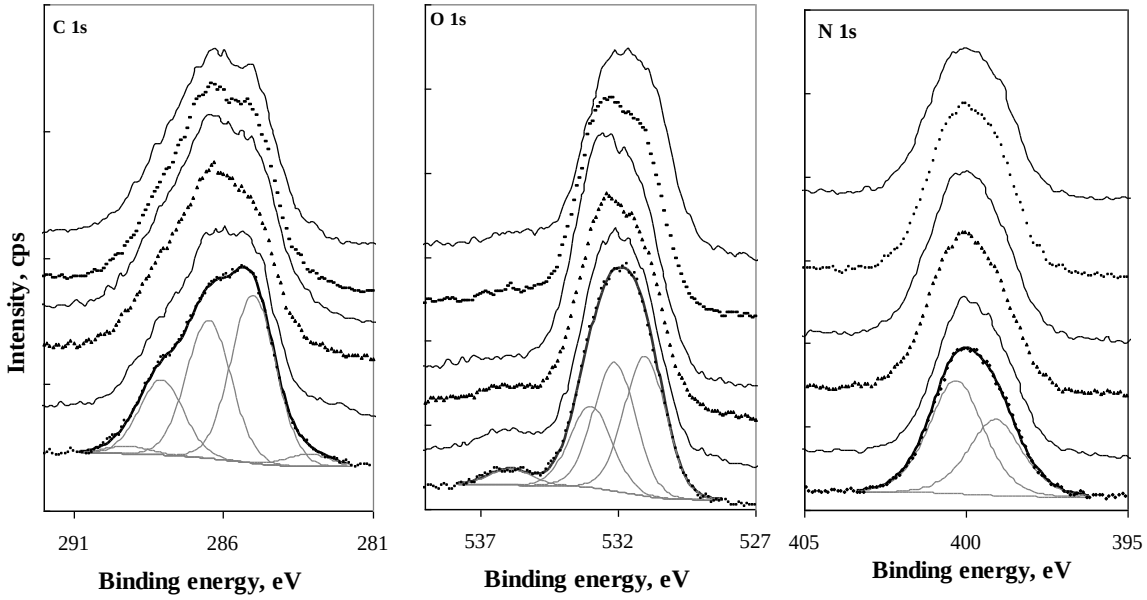

Figure 4.4.2. C 1s, O 1s and N 1s XPS spectra obtained at take-off angle of 0º with respect to the normal to the surface, for DNA samples h, from bottom to top, irradiated with 160 nm, 180 nm, 200 nm, 220 nm and 300 nm UV radiation. The top curves correspond to the non irradiated sample spectra. For the sake of simplicity, only the fittings with pseudo-Voigt profiles for the sample irradiated with 160 nm radiation are shown and curves were set off along the y axis.

The XPS C 1s region was fitted, for all the samples, with four components centered at 285.0 ± 0.1 (C1), 286.5± 0.1 (C2), 288.1 ± 0.1 (C3) and 289.3± 0.2 eV (C4). The first one is assignable to carbon in C-C or C-H and the last one to N-(C=O)-N groups. The two intermediary peaks correspond to a mixture of functions which should have binding energies between those two values. By increasing binding energy order, should correspond to the groups: C-N, C=N, C-O, N-C=N, N-C-O, N-C=O, $N=C(NH_x)_2$. These peaks are in accordance with literature [190,191,192,193]. The calculated atomic percentages for those components are displayed in table 4.4.1. At the low binding energies tail, a supplementary peak was required for a good fitting which is likely attributable to the sample holder carbonaceous contamination (not included in table 4.4.1).

The O 1s peak was fitted with four components: one centered at 531.0±0.1eV (O1) assigned to O=C bonds in an aromatic system; a second one centered at 532.1± 0.2 eV (O2), assigned to both O in phosphate group and carbonyl in an aliphatic chain; a third one centered at 532.9± 0.1 eV (O3), assigned to O in O–C bonds, and a fourth one centered at 536.1± 0.2 eV (O4) assignable to water entrapped in the film [194]. The N 1s spectrum was fitted, for all the samples, with two components, constrained to the same full width at half-maximum, FWHM = 2.0±0.1 eV and to the same Gaussian-

Lorentzian percentage, ranging from 46 to 57%, centered at 399.2 ± 0.2 and 400.4 ± 0.1 eV. These components are assignable, respectively, to sp^2 and sp^3 nitrogen atoms in accordance with XPS data of the DNA bases, in which N 1s spectra present two major peaks [195]. Usually, the peak at the lower binding energy (BE), around 398–399 eV, is attributed to imine nitrogen (–N=), while the peak at higher BE, around 400–401 eV, is attributed to the amine and/or amide nitrogen (–NH– or NH_2) [191-203]. Phosphorus P 2p region which, in all the samples, presented a single doublet with a spin orbit split of 0.9 eV and with the main component, P $2p_{3/2}$ centered at 133.4 ±0.1 eV, is assignable to phosphorus in phosphate group [185]. Finally, Na 1s was fitted with a single peak centered at 1071.3 ±0.3 eV. The FWHM was about 2.0 eV in all the samples, except for samples irradiated with 200 and 220 nm where it shifted to 2.2 and 2.7 eV, respectively. This observation suggests that part of the Na^+ ions, instead of being next to the DNA strand, are water solvated. This leads to the broadening of the Na 1s peak as a result of neighborhood diversity increase. Quantitative information may be also extracted from XPS data by taking into account the contribution to the total intensity of photoelectrons coming from different regions as demonstrated in ref. [204]. The obtained elemental composition values of DNA samples are listed in Table 4.4.1 together with the respective assignments.

Table 4.4.1. Element composition in percentage, obtained from XPS spectra taken at take-off angle of 0º relatively to normal surface of DNA cast films, irradiated with 1.14×10^{15} photons UV beam at different wavelengths. Relative errors are estimated to be less than ± 10% for components and less than ± 2% for the total. Sample not irradiated but submitted to ambient light conditions during handling was considered as irradiated at 340 nm.

Wavelength(nm)	**160**	**180**	**200**	**220**	**300**	**340**	**Assignment**
C1	22.0	20.5	17.9	18.7	19.7	19.8	C-C, C-H
C2	18.2	19.8	21.1	20.3	20.9	20.7	C-N, C=N, C-O
C3	10.2	9.8	10.2	9.5	9.4	9.8	N-C=O, N-C=N, $C(N)_3$ N-C-O
C4	1.5	1.5	1.8	1.9	1.8	2.2	N-(C=O)-N
Total C	51.8	51.7	50.9	50.5	51.9	52.4	----------
O1	10.7	9.8	9.5	9.8	9.9	10.5	Aromatic O=C
O2	10.4	9.8	8.4	7.7	6.6	7.5	PO_x + Aliph. O=C
O3	7.4	8.8	10.0	11.8	10.4	9.5	PO_x + O-C
O4	1.0	0.7	0.9	0.6	0.6	0.5	H_2O
Total O	29.4	29.1	28.8	29.9	27.5	28.0	----------
N1	5.2	5.3	6.5	5.9	7.0	6.8	N sp^2
N2	7.9	8.6	8.0	8.0	8.1	7.4	N sp^3
Total N	13.1	13.9	14.5	14.0	15.1	14.2	----------
P $2p_{3/2}$	1.5	1.7	2.0	1.9	2.2	2.1	Phosphate
P $2p_{1/2}$	0.9	0.9	1.0	1.0	1.1	1.1	
Total P	2.4	2.6	3.0	2.9	3.2	3.2	----------
Na 1s	3.2	2.8	2.8	2.8	2.3	2.3	Na^+

DAMAGE ANALYSIS

Since qualitative analysis of the elements shows that all the functional groups existing in the non-irradiated samples are kept in the irradiated ones, a quantitative analysis is required to follow the evolution of the relative amounts as a function of photon energy, using the values in table 4.4.1 It should be remarked that part of the degradation products may be in the gaseous state at room temperature escaping the sample once they are produced, which could be C, N, O and P based. Therefore, the only element which is not expectable to escape from the sample is sodium, which was then used as reference to evaluate the evolution of all the other elements with the UV energy increasing. All [X]/[Na] ratios are displayed in figure 4.4.3 as a function of the radiation energy, where X is total P, C, O, and N. The UV absorption spectrum was superposed to look for the causes for composition changes.

Since all samples have been submitted to ambient light conditions during handling, for the purpose of data consistency, non-irradiated samples will be considered as submitted to 340 nm wavelength radiation. Consequently, data relative to non-irradiated samples will be designated hereinafter as irradiated at 340 nm wavelength radiation.

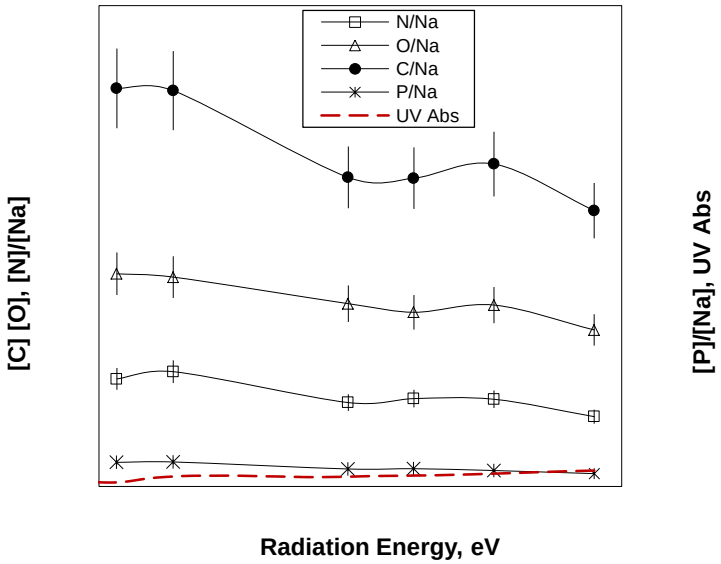

Figure 4.4.3. XPS atomic ratios between all the elements – carbon, oxygen, nitrogen and phosphorus – and sodium. The UV absorption spectrum is superposed.

From figure 4.4.3, two energy intervals may be identified where all the elements decrease their amounts with respect to sodium, strongly suggesting that dissociative degradation is taking place. Those intervals are ~4.2 eV to ~5.6 eV and ~7 eV to 7.8 eV. It should be noted that the first interval, a strong UV absorption band is centered. Other authors found thresholds for dissociative DNA degradation, leading to the production of oxygen and nitrogen based fragments, between 3.5 and 5 eV, when irradiated with electron beams [205]. Here, it is clearly above 4.2 eV. Present data shows also decrease in phosphate groups with UV irradiation.

The UV action may also promote chemical modifications without element releasing. Therefore, the analysis of the evolution of the fractions of each chemical group as a function of the irradiation energy may also be useful. These plots are shown in figure 4.4.4.

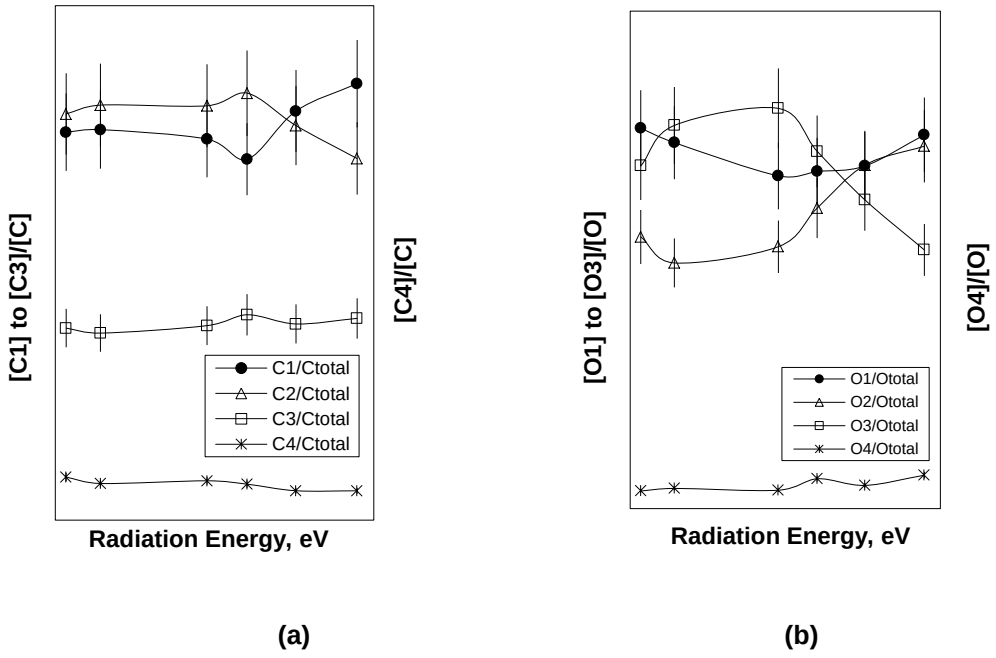

Figure 4.4.4. Fraction of element which is under the form of each fitted component: (a) carbon; (b) oxygen.

Plots of figure 4.4.4 a) reveal that the N-C=O, N-C=N and $C(N)_3$ N-C-O (C3) fractions are not being affected by radiation energy. All the other carbon group fractions are being affected: the C-C or C-H (C1) fraction increases while the C-N, C=N, C-O (C2) and N-(C=O)-N (C4) decrease, with increasing irradiation energy. The decrease of C2 fraction is, in principle, mainly related to the opening of sugar rings. The decrease of C4, since the group N-(C=O)-N exists only in thymine and cytosine, is related to the degradation of pyrimidines. The relative decrease of C2 occurs at the energy value of about 6.2 eV (200 nm), which falls within the vacuum ultraviolet (VUV) absorbance band in the spectrum, corroborating that the group which is being most affected by dissociation is the sugars C-O group [170]. Analysis of graphs of figure 4.4.4 b) reveal that increase in radiation energy keeps the aromatic O=C (O1) fraction almost unchanged, within the experimental error, trendily decreasing for low irradiating energies and slightly increasing for irradiating energies above 7 eV. O-C (O3) fraction keeps being rather constant till ~5.6 eV and clearly decreases for higher energies. This trend is indicating, once again, the rupture of sugar ring, which may transform the C-O bond into a C=O one, explaining the behaviour of the O1 fraction. Summarizing, quantitative analysis of XPS data related with carbon and oxygen elements indicates that radiation is affecting the DNA bases, mainly pyrimidines and sugar rings. However, since carbon and oxygen also exist in most common contaminants, oxygen is also bound to P and its binding energy may vary with the phosphate

degradation, the soundest elements to characterize samples degradation are nitrogen, phosphorus and sodium. Thus, the effect of UV radiation on these elements will be discussed below.

The effect of UV radiation on DNA bases can be better analyzed by plotting, the N sp^2 and N sp^3 atomic percentage ratios, calculated with respect to total nitrogen for the different DNA samples irradiated at different energies, as displayed in figure 4.4.5.

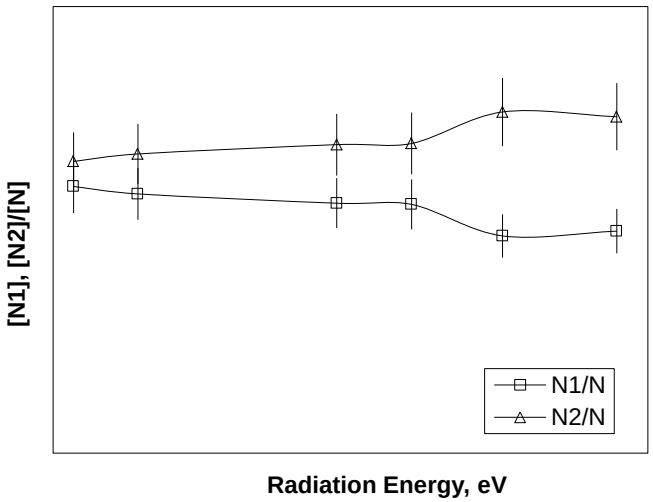

Figure 4.4.5. Fractions of N sp^2 (N1) and N sp^3 (N2) as a function of the UV irradiating energy.

Plots of figure 4.4.5 reveal that the fraction of the aromatic nitrogen decreases while the one for aliphatic nitrogen increases as the irradiation energy increases. In addition, the curves suggest that an inflexion is taking place round 6.0 eV. Comparing this value with the VUV absorbance spectrum, one can associate this inflexion to the threshold of the large absorption band associated with the excitation of π-π^* in purines (guanine, the main contributor of sp^2 nitrogen, and adenine). This means that the relaxation of this transition leads, at least partially, to the breaking of the π bonding and nitrogen changes from sp^2 to sp^3 bonding likely to a hydrogen atom. The initial and final values of N sp^2/N can give some idea about the amount of damaged bases. If all the bases are present in the same number in DNA samples, considering that all the DNA bases have a total number of imines and amines equal to 6 and 9, respectively, the ratio between the N sp^2 and total nitrogen atomic percentage should take the value of 0.4, which is below the experimental one of 0.48, measured for the non-irradiated samples. However, the XPS spectra of N 1s of thymines may be considered as composed by two peaks, one at a binding energy of 398.7 and another at 400.4 eV [193], thus the ratio N sp^2/N assumes the value of 0.47, corresponding to 7 N sp^2 per 15 total N (7/15), which is now much closer to the experimental value obtained for non-irradiated samples. On the other hand, the ratio C4/ Na decreases from 0.97 to 0.46 as the irradiation energy increases. This behaviour can be translated into a percentage value of 53% which can be obtained from (0.97-0.46)×100/0.97. Now, assuming that only thymines are being damaged by the UV radiation, i.e. the DNA samples are composed by 53% of thymines and 47% of cytosines, one can count [Nsp^2] = 0.53×4+0.47×3=3.53 and

Nsp^3=0.53×3+0.47×5=3.94. This means that under these conditions the ratio N sp^2/N assumes the value of 0.47, very close of the experimental one. Therefore, these results indicate that thymine is the most damaged base at these wavelengths. However, the damage could not be only associated to the N-(C = O)-N group since cytosine does not seem to be affected. Thence, the damage most likely should be due to the loss of imine group or to selective loss of H^- [178]. Results from atom molecule collisions studies are consistent with loss of hydrogen by electron harpooning mechanisms, which exclusively takes place from the N positions of methylated thymine [172,206] at about 7.6 eV. In turn, in dissociative electron attachment (DEA) studies, the minimum electron energy required to break thymine bonds as N1–H, N3–H, C6-H or CH2–H lies between 4 to 5 eV [207]. Thereby, the loss of hydrogen explain by itself why the N-(C=O)-N group is being destroyed as the UV energy increases since, from calculated geometries and ionization energies of DNA bases and their radical cations, Improta *et al* [208] found a match between the results of the kinetic characterization of thymine fragmentation and those of thymine electronic structure analysis, with the N1-C2 bond broken in a first step of the fragmentation reaction. In addition, Jochim *et al* [209] demonstrated that a loss of an H^- from the thymine group results in the creation of a thymine radical cation with m/z =126 and with an ionization energy of 8.82 eV, which can be decomposed into ions through Retro-Diels-Alder (RDA) reaction, by the rupture of N3-C4 and C2-N1 bonds. Consequently, it can be concluded that the effect of 5.7 eV radiation is the cleavage of hydrogen ions (H^-) from the thymine groups, followed by the creation of a lower ionization energy radical cation and by the fragmentation, leading to N-(C=O)-N group vanishing.

The effect of UV radiation is also critical on the phosphate groups; this can be clearly seen by establishing a relation between phosphorus and carbon percentage ratios since the stoichiometric ratios for these elements in DNA, neglecting end chain effects, should be C/P=20/2 for the A-T pair and 19/2 for the G-C pair. Therefore, the expected ratio C/P should be between 9.5 and 10, depending on DNA base composition. The ratios of total carbon atomic percentages relative to phosphorus percentages increase with the radiation energy as shown in plot of figure 4.4.6, indicating that phosphate groups are being removed by the UV radiation, at a rate larger than carbon [170]. To further analyze the behaviour of phosphate groups with the increase of irradiation energy, the phosphorus/nitrogen ratio will be also investigated. In intact DNA molecules, the phosphorus/nitrogen ratio is between 0.25 and 0.285 in such a way that each DNA stack has 2 phosphate groups per 7 nitrogen atoms in the adenine-thymine pair and per 8 nitrogen atoms in the guanine-cytosine pair. The atomic percentage ratio between phosphorus and nitrogen as a function of the UV irradiation energy, plotted in figure 4.4.6 b), is also seen to decrease with the increase of irradiating energy. In the irradiating energy range investigated, phosphorous decreases with respect to all the elements, suggesting that the threshold for damaging phosphate groups is lower than 3.5 eV. This energy value falls within the visible region and per se justifies the different conductivities values found in literature for DNA samples [210-221]. This conclusion is further corroborated by the fact that the DNA conductivity to be proportional to the loss of phosphates as demonstrated in ref. [222].

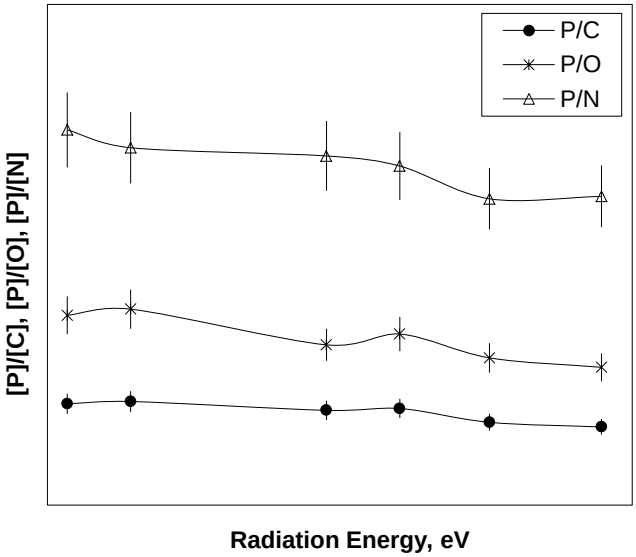

Figure 4.4.6. XPS atomic ratio between phosphorous and, from bottom to top, carbon, oxygen and nitrogen.

Also a quantitative analysis of the P/Na ratio (figure 4.4.3) is interesting to discuss: in non-irradiated samples, the atomic percentage of Na is, roughly, one half of the phosphorus atomic percentage, indicating that half of the phosphate groups are being neutralized by protons and, consequently, DNA is behaving as a polyelectrolyte with an ionization degree of 0.5. Since sodium atoms are not leaving from DNA and the ratio between sodium and phosphorus is tending to unity as the radiation energy increases, this means that protonated phosphate groups are leaving from DNA. This conclusion is further supported by the presence of sodium counterions which can also associated to DNA hydration [223], and is consistent with the observed presence of oxygen component associated to water (O4), and by the fact of water molecules starting to absorb UV radiation at energies above 6.5 eV [128]. Therefore, a small interaction of radiation with the phosphate groups that are surrounded by water molecules and counterions is expected. This can be outlined from the top plot of figure 4.4.6., where a stabilization of the [P]/[N] ratio as radiation energy increases is observed. This allows conclude that water molecules are playing a role of protecting the phosphate groups.

For summarizing, the values of energy required to damage different DNA components discussed are summarized in table 4.4.2. The agreement of values of energy when analysed the different elements for the same chemical group demonstrates the reliability of the obtained values.

Table 4.4.2. Summarization of the energy values of the different DNA groups damaged.

DNA Group Component	***Energy (eV)***	***XPS components***
Phosphate	< 3.5	(O2+O3) P
Purines	~ 6.1	Nsp2
Sugar Ring(deoxyribose)	6.8	C2 (C-O) O3 (O-C)

CONCLUSIONS

Synchrotron UV radiation in the energy range of 3.5 to 8 eV was shown to cause damage to several DNA components as revealed by XPS spectra analysis of DNA cast films. Analysis of XPS data show that all the elements decrease with respect to sodium, revealing that the absorption of UV leads to dissociative damage of DNA yielding gaseous products. Two main energy intervals were associated to that kind of damage. Besides, the analysis of each element fractions with radiation energy reveals some group transformations. Carbon fractions revealed that the set of N-C=O**,** N-C=N, $C(N)_3$ N-C-O (C3) groups is not affected by the radiation, while other carbon groups are affected: the C-C or C-H (C1) fraction increases and the C-N, C=N, C-O (C2) and N-(C=O)-N (C4) ratios decrease, when the samples are irradiated at higher energies. The decrease of C-O and N-(C=O)-N ratios indicate the opening of sugar rings and the breaking of pyrimidines, respectively. The rupture of sugar rings was confirmed by the O-C (O3) fraction decrease. This range of energies leads also to loss of DNA PO_4^- groups which pointed out by the decrease of all the ratios [P]/[X], X being any other element: Na, C, O and N.

Analysis of Nsp^2 and Nsp^3 atomic percentages allowed conclude that at 6.1 eV irradiating energy an important decrease (~17%) in the fraction of N sp^2 groups. This energy value is close of the VUV peak associated to π-π^* transitions of both guanine and adenine, suggesting that these bases can be affected. The decrease of N-(C=O)-N groups revealed also that the pyrimidines (thymines and/or cytosines) are being degradated.

Analysis of the XPS data, associated to phosphate groups, pointed out that an energy below 3.5 eV is sufficient to break DNA phosphates groups, fact which is useful to account the different conductivities values found in literature for DNA samples.

Finally, analysis of XPS [P]/[Na] ratio which changed from ~1.4 to ~0.8 as radiation energy increases, revealed mainly that the protonated phosphate groups are being removed and not the ionized ones. This allows to conclude that ionized phosphate groups, surrounded by the sodium counterions, congregate hydration water molecules which play UV radiation protection a role.

ACKNOWLEDGMENTS

The authors acknowledge the European Commission for access to the ASTRID facility at the University of Aarhus, Denmark and for their support through the *Access to Research Infrastructure* action of the *Improving Human Potential* programme. This work was supported also by the "Plurianual" financial contribution of "Fundação para a Ciência e Tecnologia" (Portugal) and by the Portuguese research Grants PEst-OE/FIS/UI0068/2011 and PEst-OE/CTM/LA0024/2013. PG acknowledges the fellowship SFRH/BD/35954/2007.

4.5. DNA DAMAGE INDUCED BY CARBONS (C^{3+}) BEAM ACCESSED BY INDEPENDENT COMPONENT ANALYSIS OF INFRARED SPECTRA

Maria Raposo, Margarida Coelho, Paulo J. Gomes, Pedro Vieira, Paulo A. Ribeiro, Nigel J. Mason, Christopher A. Hunniford and Robert W. Mc Cullough

STATUS: Published in International Journal of Radiation Biology, 90(5), 344-350, 2014

ABSTRACT

Damage caused to deoxyribonucleic acid (DNA) thin films as a result of exposure to 4 keV carbon ions beam was accessed by analyzing the infrared spectra, obtained *in situ* for different irradiation times, with both bidimensional correlation spectroscopy and independent component analysis. Results indicate that deoxyribose, phosphate and bases groups of the DNA molecule are being damaged and new reaction products as oxime and furfural groups are being formed. Damage on DNA bases is consistent with the formation of oxime products which react with DNA deoxyribose products forming furfural groups, confirming that DNA damage is caused by direct and indirect processes.

INTRODUCTION

Although ion-beams are being successfully used in cancer therapy, the underlying mechanisms that occur when an energetic ion interacts with biological tissue are not fully understood or quantitatively estimated at molecular level. This is primarily due to the fact that biologic tissues are complex multi-component materials which provide a challenge for traditional molecular and atomistic analytical techniques. Moreover, in radiotherapy, secondary species such as nuclear fragments, reactive radicals, electrons, low energy and excited neutral species are often produced [3,4,224,225,226] with energies that can range from a few hundred of electron volts up to ~1 keV and can present a variety of charge states [228]. These species are also known to cause damage within DNA. Damage induced by ions to DNA molecules is usually evaluated by the number of single and double strand breaks which lead to the production of short linear fragments arising from multiple double strand breaks [229]. Moreover, damage caused by low energy singly and doubly charged carbon ions to super coiled plasmid DNA was shown to follow an exponential dependence of strand breaks upon fluency, suggesting that the fragmentation dominates at high exposures [230]. To obtain further information about degradation processes and role of secondary species on DNA damaged fragments, the new reaction products should be also characterized.

In the present work, *in situ* infrared spectroscopy (FTIR) was used to monitor the damage on calf thymus DNA films exposed to 4keV C^{3+} ions beam in order to access where main changes are taking place within DNA molecules. From the small changes in FTIR spectra, the experimental data analysis was processed via bidimensional correlation spectroscopy and independent component analysis (ICA) methods.

EXPERIMENTAL DETAILS

Films of DNA calf thymus, obtained from Sigma Aldrich, were prepared by dissolving DNA in ultra-pure water to a concentration of 0.5 mg/mL. This solution was deposited onto calcium fluoride (CaF_2) substrates and dried for 2 hours in vacuum desiccators. The DNA films were introduced to a high vacuum chamber and exposed to triply charged carbon ($^{13}C^{3+}$) ions, derived from ^{13}CO gas, produced by a 10 GHz permanent magnet, compact Electron Cyclotron Resonance (ECR) ion source [231], coupled to a floating beamline accelerator [83,232]. The energy of C^{3+}, beam was set to 4 KeV and the ion fluxes were maintained at a low level with a value of ~ 2×10^{11} ions/second to ensure a linear damage response. Exposure was carried out over various time periods and characterized using a Fourier Transform Infrared (FTIR) spectrophotometer Nicolet-model 530, adapted for *in situ* measurements [154]. The spectrophotometer is provided with Deuteriated L-Alanine Doped Triglycine Sulfate (DLTGS) detector with a sensitivity of 1V/mW. The spectra were all collected with 64 scans and EZ-Scan software was used to instrument setting and data acquisition. The sample, with a diameter of 20 mm, was positioned at 45 degrees to the incident ion beam, which leads to an elliptical profile with a dimension of 14x10 mm^2 on it, and ensures that the entire FTIR probed area was subjected to ion exposure. Since DNA samples contain different DNA fragments composition, their IR spectra are slightly different, in such a way that the damage caused by the exposure to carbon beam was characterized as a function of irradiation time for each different sample. In addition, it should be referred that infrared difference spectroscopy [233] should be a straightforward technique to address the DNA damage, with the obtained data also treated by the advanced data analysis techniques as demonstrated by Mezzetti *et al* [234]. However, this technique was not used in this work because is not yet implemented in our laboratories.

RESULTS AND DISCUSSION

Figure 4.5.1 shows the infrared spectra in the 1800-900 cm^{-1} range, of a DNA film irradiated with carbon ions for several periods of times. No changes were observed after 15 minutes of C^{3+} beam exposure.

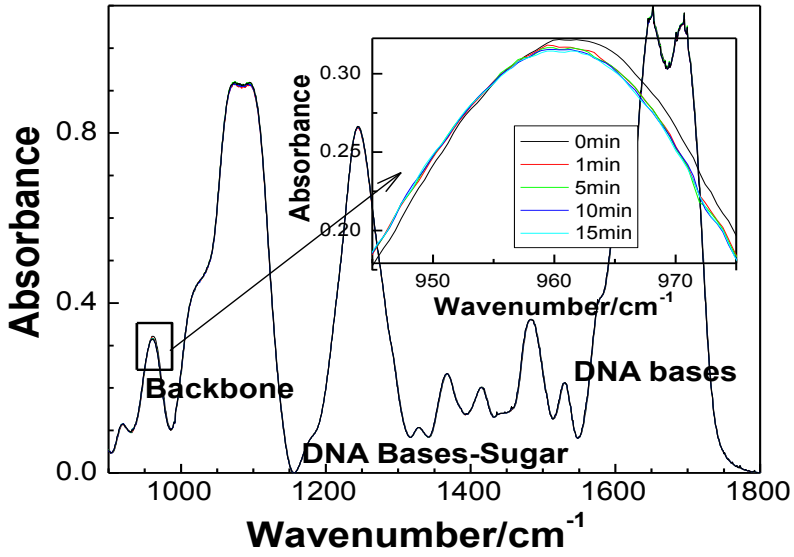

Figure 4.5.1. Infrared spectra of a DNA film exposed to 4 keV C^{3+} beam for different periods of time. Inset emphasizes the small changes observed.

Three main regions can be observed in these spectra, 1800-1500 cm^{-1}, 1500-1200 cm^{-1} and 1200-900 cm^{-1}. These regions contain a number of absorbance peaks that can be associated t DNA molecular vibrations [12,153,154,155] as follows:

I) DNA bases (1800-1500 cm^{-1}) - This range is associated with the DNA bases and is expected to contain contributions from six molecular vibrations: i) C6=O6 stretching of guanines involved in Hoogsteen third strand binding and C2=O2 bond of thymine involved in reverse Hoogsteen third strand binding (1711 cm^{-1}); ii) C2=O2 stretching of thymine in single or double-stranded (1693 cm^{-1}); iii) C2=O2 stretching vibrations of cytosine in single or double-stranded (1651 cm^{-1}); iv) C=N ring vibration of guanine (1605 cm^{-1}); v) C=N ring vibration of guanine in single stranded or double-stranded and ring vibration of guanine and adenine (1581 cm^{-1}); and vi) in-plane vibration of cytosine single stranded or double-stranded and in plane vibration of cytosine (1531 cm^{-1}).

II) Base-sugar (1500-1200 cm^{-1}) - This region corresponds to the IR absorption associated with the bases vibrations and the base vibrations influenced by the sugar groups. In this region, contributions from eight molecular vibrations are expected: i) ring vibration of adenine and guanine and N7C8H bend of adenine/guanine (1485 cm^{-1}); ii) adenine A, B and Z forms (1446 cm^{-1}); iii) C3'-endo deoxyribose in *A* form helices and C3'-endo deoxyribose in *Z* form helices

(1414 cm^{-1}); iv) CH_3 symmetric deformation of deoxyribose thymine (1390 cm^{-1}); v) cytidine and guanosine in anti-conformation (1366 cm^{-1}); vi) C4-NH_2 strength of cytosine and C5=C6 vibration of cytidine (1297 cm^{-1}); vii) CN3H bend of deoxyribose thymine (1280 cm^{-1}); and viii) antisymmetric PO_2^- stretch in A form (1241 cm^{-1}).

III) <u>Backbone (1250-1000 cm^{-1})</u> - This region is associated with the phosphate backbone region and contributions from seven molecular vibrations are expected: i) antisymmetric PO_2^- stretch in B form (1210 cm^{-1}); ii) A form marker, the sugar phosphate backbone (1183 cm^{-1}); iii) symmetric PO_2^- stretching of the backbone (1097 cm^{-1}); iv) CO stretching of the furanose in the backbone (1061 cm^{-1}); v) furanose vibrations (1020 cm^{-1}); vi) CC stretching in the backbone (961 cm^{-1}); and vii) z DNA form (927 cm^{-1}).

Changes caused by the carbon beam irradiation in the IR spectra are rather small, as emphasized in the inset of figure 4.5.1, where the 900-1000 cm^{-1} wavenumber region was plotted as an example. These small changes in the IR spectra are somehow expected since damage is essentially taking place at sample surface as carbon ions do not penetrate much further from the surface. It should also be denoted that after 15 minutes of irradiation no further changes are observed. As C^{3+} ions cause small changes in the IR spectra, computational methods as bi-dimensional correlation spectroscopy [235] and independent component analysis (ICA) [236] were addressed to infer about the DNA damage.

Bi-dimensional correlation spectroscopy allows analyse small intensity changes, band shifts and band shapes changes, arising from an external perturbation. The fluctuations of FTIR spectra obtained for different irradiation times, transformed into a 2D spectrum by using the correlation method, were obtained in the form of schematic contour maps of synchronous and asynchronous 2D correlation spectra. In figure 4.5.2, the synchronous contour map is displayed where diagonal peaks, or autopeaks, were marked. These diagonal peaks represent the overall susceptibility of the corresponding spectral region to change in intensity, as a result of the DNA sample exposure to the ions beam. In the synchronous contour map, it is also possible to define several correlation squares, discontinuous lines that form squares, which join the pair of cross peaks located at opposite sides of a diagonal line drawn through the corresponding autopeaks. These correlation squares prove the existence of coherent variation in the spectral intensity at these wavenumbers. In the present case, the observed changes in the wavenumber regions of each autopeak are correlated with the wavenumber region of the other autopeaks. This means that the changes in the 1750 to 1600 cm^{-1} region are synchronously correlated with those close at 1175 and 1000 cm^{-1}. In addition, some sequential or successive, but not coincidental, changes of spectral intensities can be inferred from the schematic asynchronous contour map, not shown here. However, the synchronous and asynchronous maps only indicate the wavenumber where absorbance intensity changes are taking place, not indicating whether there is an increase or a decrease in absorbance. Thus, to better discern about the extent of DNA damage, the IR spectra were analysed by Independent Component Analysis (ICA) method.

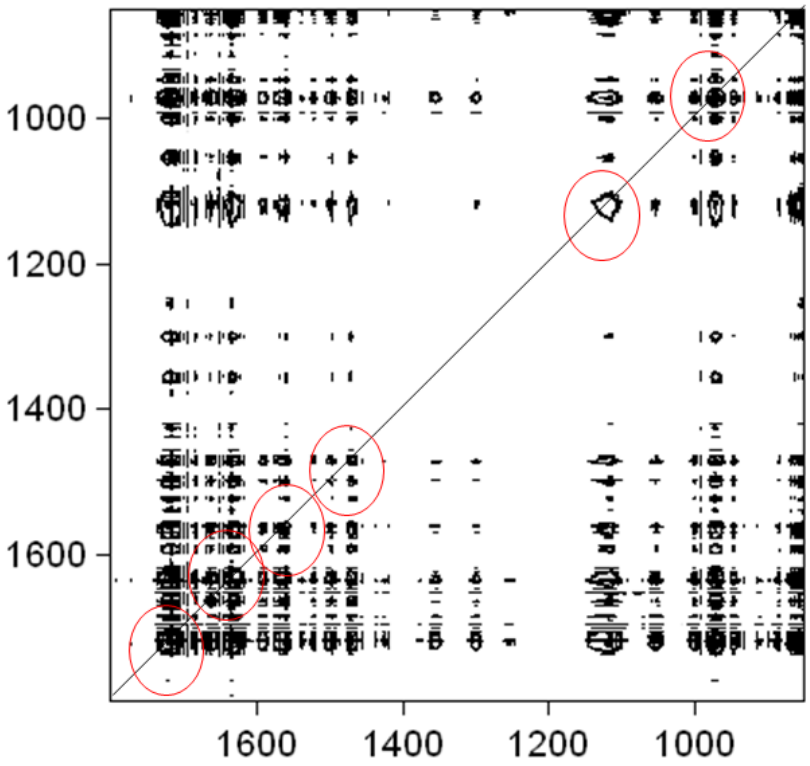

Figure 4.5.2. Contour map of the synchronous 2D correlation spectra of a DNA sample exposed to 4 keV C^{3+} beam for different periods of time. The scales in both maps correspond to wavenumber in cm^{-1}. The red circles represent diagonal peaks/autopeaks regions.

The ICA is a computational method for signal separation, often used in spectrum analysis of independent competitive processes [237]. The ICA algorithms, developed for blind source separation, are based on the principle that the multivariate signal being processed is the result of the addition of mutual statistical independent of the non-Gaussian source signals. In this study the standard Fast ICA implantation [238] was used and a dedicated MATLAB application was developed for automatic calculus. The full processing algorithm is as follows: a) Import data spectra corresponding to the different irradiation times in the region of interest [900-1800 cm^{-1}]; b) Apply the Fast ICA computational method was set for two signal decomposing components because in the present case it is expected to obtain as result only two independent spectra associated to non-degraded DNA and to DNA damage; c) As Fast ICA algorithms can produce output signals that are the inverse of the intended signal, the signal of both decomposition components was identified by addition of both decomposition components and comparing the result with the original DNA spectra; and d) Apply a low pass 5^{th} order Butterworld filter to smooth the signal in order to remove random higher frequency noise present in the signals.

The DNA IR spectra two independent components obtained from ICA method, namely, ICA component 1 associated with the infrared spectrum of non-irradiated DNA, and ICA component 2 associated with DNA damage are plotted in figure 4.5.3. However, the ICA component 1 can

only be associated with the non-irradiated DNA spectra if the normalized ICA signal 1 is considered to be the same as the normalized DNA infrared spectrum without ion exposure. These signals, the ICA component 1 and the FTIR of the non-irradiated DNA, both normalized to the 1241 cm^{-1} peak, after baseline removal, revealed to be coincident, in such a way that the ICA method is suitable for the analysis of DNA damage caused by carbon ions beam. Moreover, the ICA component 2 peaks are in accordance with the results obtained from the 2D correlation spectra contour maps, which guarantees the validity of the spectrum associated with the DNA damage.

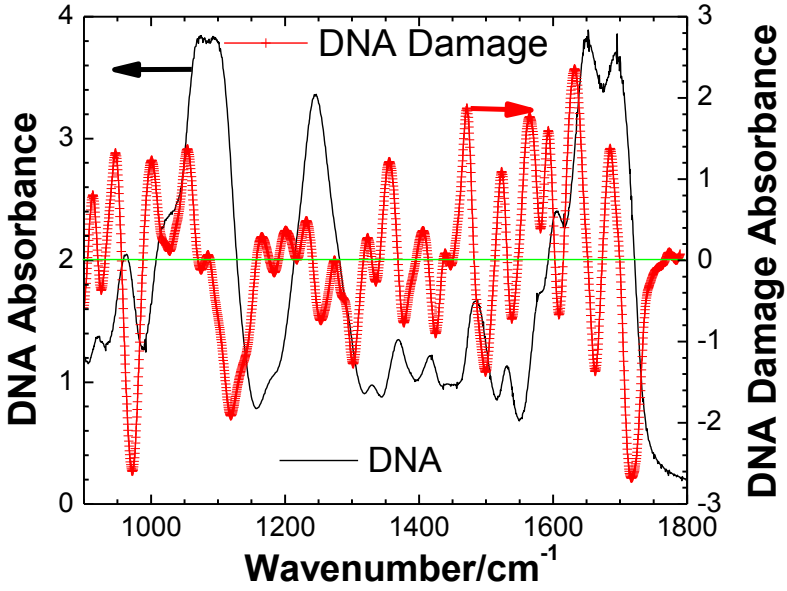

Figure 4.5.3. ICA signal components obtained from infrared spectra of a DNA film exposed to C^{3+}(4KeV) beam.

The ICA component 2 spectrum, associated with DNA damage when exposed to carbons beam, present positive peaks related to formation of new bonds and the negative peaks associated to decrease of the number of bonds associated to DNA molecules. The features of ICA component 2 spectrum, i.e., peak position, peak signal, corresponding literature peak position and respective assignments, are displayed in table 4.5.1. In the peak signal column, a signal "+" or "-" was attributed, respectively, if the absorbance peak of ICA component 2 spectrum is positive or negative. A positive peak is associated with a new bond formation and a negative peak represents a decrease of the chemical bonds number of a determined DNA group.

The reduction of the DNA number of bonds, leading to negative peak signals in table 4.5.1, are easily associated with damage caused by the carbon ion beam. The negative peak at 972 cm^{-1} indicates that carbon ions beam has a strong effect on the C-O-C deoxyribose bonds. This is confirmed with the creation of C=O bonds, increase of 1632 cm^{-1} peak. Similar behaviour has been observed during UV irradiation of DNA samples [12]. The negative peaks at 1301, 1253 and 1119 cm^{-1} are associated to PO_4^{2-} groups fragmentation. The damage on thymine, cytosine, adenine and guanine groups is indicated by the negative peaks at 1717, 1663, 1539 and 1499

cm^{-1}. However, it should be referred that carbons ions are effective in all DNA bases damage by opposition to UV radiation [12] or ozone [158,157], for which thymine is the most affected DNA base.

The ICA component 2 spectrum positive peaks require a more detailed discussion as they result from several reactions that lead to the formation of new bonds and, consequently, new products. The obtained positive peaks will be individually discussed as follows:

i) The 1685 cm^{-1} peak is associated with the C=N bond within the oxime group (C=NOH) [239]. The presence of this group is also revealed by an increase of absorbance at 947 cm^{-1} which is related to N-O stretching vibration of oxime group. Oxime groups are also evidenced by reactions between the native a basic sites, a product of oxidation of 2-deoxyribose in DNA with methoxyamine [240] which can be formed by the carbon ion beam action. The presence of these oxime groups in DNA indicate that reactions can occur in the DNA bases, similar to those occurring with various (heterocyclo) carbonyl mono-oxime esters of anthraquinone who exhibited ability for DNA cleavage upon UV irradiation [241].

ii) The absorbance increase of the 1632 cm^{-1} peak is associated to C=O stretching of guanine in Z form which is consistent with DNA conformation changes [242].

iii) The 1593 cm^{-1} peak is associated to C=N stretch in guanine [243] being the absorption coefficient dependent of DNA conformation. A study about the B-Z conformational transition of DNA oligonucleotides showed that a peak at 1683 cm^{-1} moves to 1664 cm^{-1}, the experimental band at 1579 cm^{-1} increases in intensity and a shoulder at 1562 cm^{-1} evolves into a peak [242]. From these, one can imply the absorbance increase result from a DNA conformation conversion to Z form.

iv) The presence of peak at 1565 cm^{-1} is associated with the stretching of nitroso compounds, the peak at 1523 cm^{-1} can be associated to asymmetric stretching of aromatic nitro compounds NO_2 and the peak at 1355 cm^{-1} is associated to symmetric stretching of aromatic nitro compounds, NO_2 [239, 244].

v) The peak at 1471 cm^{-1} is related to C=C in phase stretching in a specific position, namely, if the double bond is conjugated to a carbonyl group [245], meaning the presence of this group is related with furfural. The presence of this product is in accordance with literature since it is related with degradation products of nucleoside-5´-aldehyde which in turn is a product of oxidation of 2-deoxyribose in DNA [246].

vi) The absorbance increase of the peak at 1055 cm^{-1} can be also be associated with loss of water molecules due to DNA sample to be submitted to vacuum during irradiation. This loss of

water is known to improve the delocalization of sugar-phosphate modes [242] and also leading to DNA conformation changes.

vii) The peak at 1001 cm^{-1} is associated with phosphate groups directly bonded to a metal ion [247], suggesting that the interaction of PO_3^{2-} groups with sodium ions is increasing meaning that water molecules are being removed by vacuum.

viii) The increase of 913 cm^{-1} peak is associated to change of DNA conformation to Z form.

Table 4.5.1 Features of ICA Component 2 spectrum associated with DNA damage.

Peak Position (cm^{-1})	***Peak signal***	***Literature Peak Position (cm^{-1})***	***Peak Assignment***
1717	-	1715; 1712; 1711 [243, 12]	C6=O6 stretching of guanines involved in Hoogsteen third strand binding and/or C2=O2 stretching of thymines involved in reverse Hoogsteen third strand binding
1685	+	1665 ± 15 [239]	C=N stretching of C=NOH (oxime)
1663	-	1655 -1657 [12,242,243]	C2=O2 stretching of cytosine single stranded or double stranded
1632	+	1634 [242]	C=O Stretching of guanine in Z form
1609	-	1605 [12]	C=N ring vibration of guanine
1593	+	1590 [243]	C=N stretch in guanine
1565	+	1550 ± 50 [239, 244]	N=O stretching of nitroso compounds
1539	-	1531 [12] 1538 [243]	In-plane vibration of cytosine single stranded or double stranded Vibrations of the bonds within sugar rings
1523	+	1530 ± 20 [243]	N=O Assymetric stretching
1499	-	1495-1476; 1485 [243]	Ring vibration of adenine and guanine
1471	+	[245]	Furfural
1424	-	1414 [12]	C3'-endo deoxyribose in *A* form helices
1378	-	1389-1374; 1390 [12]	CH3 Symetric deformation of deoxyribose thymine; Cytidine and guanosine in anticonformation
1355	+	1350 ± 30 [239]	Stretching vibration of N=O
1301	-	1297 [12]	C4-NH2 strength of cytosine
1253	-	1245-1235	Antisymmetric PO_2^- stretch in A-form
1119	-	1097 [12]	Symmetric PO_2^- stretching of Backbone
1055	+	1061 [12]	CO stretch of the furanose in backbone Loss of water molecules which improves the delocalization of sugar-phosphate modes
1001	+	1001-1014 [247]	Phosphate groups directly bonded to a metal ion
972	-	972 [243]	Sugar Ring vibrations
947	+	945±15 [239]	N-O stretching of C=NOH (oxime)
913	+	927 [12]	DNA Z-form

CONCLUSIONS

In summary, the damage of DNA films as a result of irradiation with C^{3+} ions reveals the rupture of C-O-C deoxyribose bonds and consequent creation of C=O bonds, fragmentation of PO_4^{2-} groups and the decrease in the number of thymine, cytosine, adenine and guanine groups. Damage on DNA bases leads to the formation of oxime products, which in turn react with DNA deoxyribose products forming furfural groups. Loss of structural water and DNA conformational changes were also observed. As a final remark, this work shows that the use of infrared spectroscopy together with bidimensional correlation spectroscopy and ICA methods is a suitable method for the characterization of molecular damage to DNA or other biological molecules caused by charged particles or radiation.

ACKNOWLEDGEMENTS

The work described in this paper was carried out at the distributed LEIF-Infrastructure at QU-LEIF, Queen's University Belfast, supported by Transnational Access programme. The authors thank for the financial support to "Fundação para a Ciência e Tecnologia" (Portugal). MR, PAR and PJG acknowledge visiting fellowships within the Open University, UK. MR acknowledges the Short Term Scientific Mission COST P9 –STSM 02196. PAR acknowledges the support received from the European Science Foundation (ESF) for the activity entitled 'Electron Induced Processing at the Molecular Level'. PG acknowledges the fellowship SFRH/BD/35954/2007.

4.6. CHARACTERIZATION OF PAH/DPPG LAYER-BY-LAYER FILMS BY VUV SPECTROSCOPY

Andreia A. Duarte, Paulo J. Gomes, Jorge H.F. Ribeiro, Paulo A. Ribeiro,
Søren V. Hoffmann, Nigel J. Mason, Osvaldo N. Oliveira Jr., Maria Raposo

STATUS: Published in The European Physical Journal E – Soft Matter, 36(9), 9912-9919, 2013

ABSTRACT

The spectroscopic characterization of layer-by-layer (LbL) films containing liposomes is essential not only for determining the precise film architecture but also to guide the design of drug delivery systems. In this study we provide the first report of vacuum ultraviolet spectroscopy (VUV) characterization of LbL films made with liposomes from 1.2-dipalmitoyl-sn-Glycero-3-[Phospho-rac-(1-glycerol)] (Sodium Salt) (DPPG) alternated with poly(allylamine hydrochloride) (PAH). Measurements in the 6.0–9.5 eV range allowed us to identify the electronic transitions responsible for the spectra, which were assigned to carboxyl, hydroxyl and phosphate groups in DPPG while the PAH spectra were governed by electronic transitions in the amino groups. The surface mass density of the LbL films could be determined, from which the formation of a DPPG bilayer was inferred. This rupture of the liposomes into bilayers was confirmed with atomic force microscopy measurements. In subsidiary experiments we ensured that the UV irradiation in vacuum had negligible damage in the DPPG liposomes during the course of the VUV measurements. In addition to demonstrating the usefulness of VUV spectroscopy, the results presented here may be exploited in biological applications of liposome-containing films.

INTRODUCTION

The formation of layer-by-layer (LbL) films [67] from phospholipid liposomes may find several applications, including the modelling of cell membranes and the incorporation of pharmaceutical drugs or biomolecules for drug delivery [248,249]. Liposomes formed from self-assembly of lipids are important cell membrane models since lipids are basic building blocks of cells, representing approximately 50% of their membrane mass. Their immobilization in LbL films is suitable to exploit important characteristics of these films for biological materials, especially the ability to preserve the bioactivity and serve as template for surface functionalization, e.g. in tissue engineering. In fact, the effectiveness of LbL assemblies has been proven for many other biological materials such as proteins, enzymes, DNA and viruses [59]. Polyelectrolyte-supported lipid liposomes in LbL films offer key advantages over the direct use of liposomes [250]. For

example, melanin encapsulated in LbL films made with liposomes retained its fluorescence properties, but this did not occur for melanin films without protection in liposomes [251]. Therefore, the combination of liposomes and LbL films is useful for encapsulating biological molecules with activity preserved. Tanaka and Sackmann [252] used the LbL method to investigate the properties of membranes and membrane-associated proteins, while Yamuchi *et al* [253] prepared lipid/DNA LbL films for stent-assisted gene transfer.

During adsorption liposomes may remain intact in the LbL films [248,254,255] or suffer rupture to form bilayers [256,257,258]. Recently, it is shown that the surface roughness influences the adsorption of DPPG liposomes onto surfaces covered by an electrically charged PAH polyelectrolyte layer giving rise to its rupture or maintenance of its integrity [259]. Low roughness was shown to induce liposome rupture while high roughness induces adsorption of whole liposomes. Determining the true conformation of the liposomes may be crucial for interpreting data on the films or for specific applications. LbL films may be characterized by a variety of experimental methods (for a review see ref. [109]), some of which allow one to determine the structure of the materials adsorbed. Delejon *et al* [260] employed neutron reflectivity to study charge effects on the adsorption processes of LbL films. In this paper we used vacuum ultraviolet (VUV) spectroscopy measurements to determine the adsorbed amount of 1.2-dipalmitoyl-sn-Glycero-3-[Phospho-rac-(1-glycerol)] (Sodium Salt) (DPPG) layers in the LbL films with poly(allylamine hydrochloride) (PAH), which confirmed the rupture of DPPG liposomes during adsorption. To our knowledge this is the first report of VUV for DPPG, which also served to verify possible damage of prolonged UV irradiation on DPPG-containing LbL films, with the implications for biological systems. The characterization of LbL films was complemented with atomic force microscopy (AFM).

MATERIALS AND METHODS

MATERIALS

Highly pure (>99%) synthetic 1.2-dipalmitoyl-sn-Glycero-3-[Phospho-rac-(1-glycerol)] (Sodium Salt) (DPPG), with molecular weight of 744.96 $g.mol^{-1}$ and structure shown in figure 4.6.1 a), was purchased from Avanti Polar Lipids. Small unilamellar vesicles (SUV) were obtained by dissolving 5 mM DPPG in methanol:chloroform (2:8). After solvent evaporation using a gentle stream of nitrogen, the lipid film was hydrated overnight in pure water supplied by a Milli-Q purification system (resistivity 18.2 MΩ.cm and pH~5.7). The dispersion was vortexed intermittently leading to multilamellar vesicles (MLVs). The SUV or liposomes were then obtained by extruding this dispersion in a mini-extruder from Avanti Polar Lipids in a polycarbonate membrane with 0.1 μm pores. A mean hydrodynamic diameter of 162 nm was found for DPPG liposomes in a dispersion prepared in similar conditions. The hydrodynamic diameter value was determined by dynamic light scattering (DLS) using a Zetasizer Nano-ZS Series ZEN3600 DLS device from Malvern Instruments, which makes use of a 4 mW He-Ne Laser (633 nm) light source, passing through a 1x1 cm^2 section polystyrene latex cuvette. The

DPPG aqueous solutions have pH~7 and the formed liposomes have negative electrical charge, which allows for the fabrication of LbL films. This is one of the reasons why DPPG was chosen here, in addition to its being one of the most studied lipids in model membranes. In the preparation of LbL films, polycationic aqueous solutions of poly(allylamine hydrochloride) (PAH) (average Mw = 50.000–65.000 g/mol) with a monomeric concentration of 10 mM and pH~4 were used. Under these conditions, PAH is positively charged [261]. PAH was obtained from Sigma–Aldrich and has the molecular structure of Figure 4.6.1 b).

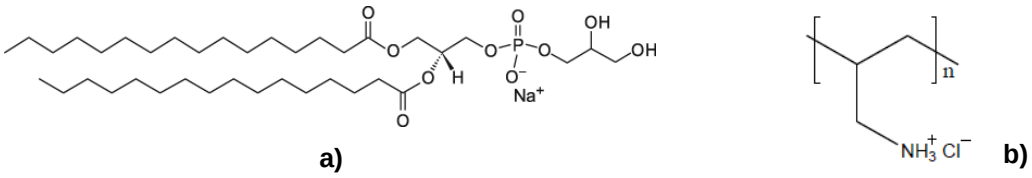

Figure 4.6.1. Chemical structure of 1.2-dipalmitoyl-sn-Glycero-3-[Phospho-rac-(1-glycerol)] (Sodium Salt) (DPPG) (a) and poly(allylamine hydrochloride) (PAH) (b).

THIN FILMS

The films were deposited on calcium fluoride, quartz and silicon substrates for spectroscopy studies. The substrates were cleaned with a “piranha” solution containing hydrogen peroxide and a sulfuric acid (7:3) bath for 1 h and then rinsed exhaustively with pure water. The layer-by-layer (LbL) films were obtained by immersing the substrate in the PAH solution during 3 min, rinsing with water, then immersing the substrate in the DPPG dispersion for 30 min., followed by another rinsing with water. The periods of time for adsorption were chosen based on adsorption kinetics studies [254,262]. After deposition of each bilayer the samples were dried with a gentle nitrogen flow. This adsorption procedure was repeated to obtain the number of bilayers desired. Bilayer in this context means a layer of PAH adjacent to a DPPG layer. The DPPG layer itself can consist of one or more lipid bilayers or entire liposomes adsorbed or a mixture of lipid bilayers and entire liposomes. Film growth was monitored with vacuum ultraviolet spectroscopy (VUV) spectroscopy measurements. Cast films of DPPG and PAH were obtained by casting DPPG dispersion and PAH solution onto calcium fluoride and quartz substrates, respectively. The water solvent was removed by submitting the samples to primary vacuum during 12 h. The films were prepared at room temperature as well as all the characterizations.

VACUUM ULTRAVIOLET (VUV) SPECTROSCOPY

The high resolution VUV photo-absorption spectra of the LbL films were recorded at the ultraviolet beam line (UV1) [185] in the Synchrotron Radiation facility ASTRID at Aarhus University, Denmark. The setup consists of a sample vacuum chamber containing up to three CaF_2 sample disks and one reference disk mounted on a MDC SBLM-266-4 push-pull linear motion. The VUV beam light passed through the disks and the transmitted intensity was measured at 1.0 nm intervals using a photomultiplier detector (Electron Tubes Ltd., UK). The

transmitted light intensity and the synchrotron beam ring current were measured at each wavelength, with a typical resolution better than 0.08 nm. The sample chamber has a LiF entrance window and a MgF_2 exit window in front of the photomultiplier. The minimum wavelength is determined by the CaF_2 substrates so that the lowest wavelength at which reliable data could be collected was ~125 nm. In order to avoid absorption from molecular oxygen in air for wavelengths below 190 nm, the small gap between the sample chamber exit window and the photo multiplier detector was flushed with helium gas. To calculate the absorbance, the light intensity spectra of the CaF_2 disc/or quartz cuvette were measured before and after measuring the spectrum of the disc covered with the LbL film or DPPG dispersion or PAH solution. The average of those two spectra and the spectrum of the coated solid support (with film, dispersion or solution) are used to calculate the absorbance using the Beer-Lambert equation.

ATOMIC FORCE MICROSCOPY

The surface morphology of a PAH/DPPG LBL film deposited onto silicon substrate, was characterized by atomic force microscopy (AFM) in a Nanoscope III microscope (Digital Instruments). Commercial Si cantilevers with a spring constant between 20 and 100 N/m and free oscillation interval between 250 and 300 Hz were used. The topographies were obtained using tapping mode.

RESULTS AND DISCUSSION

VUV CHARACTERIZATION OF DPPG AND PAH MOLECULES

To our knowledge, there are no VUV studies for DPPG or any other phospholipid in condensed or gas phases. For the sake of comparison, we first obtained the VUV absorption spectra of DPPG and PAH cast films which were fitted with Gaussian curves as indicated by the solid green curves in the figures. Gaussian curves were chosen because they provide the best fits to the experimental data. The inset in figure 4.6.2 a) shows an absorbance spectrum for a DPPG cast film. The spectra of DPPG and PAH cast films are shown in figure 4.6.2 b), to be used in comparison with the spectra of LbL films containing the two components. Since the PAH film was cast onto a quartz substrate, the spectrum was measured only down to 160 nm. The peak positions and Full Width at Half Maximum (FWHM) obtained in the fitting are listed in table 4.6.1. The error bars are obtained from the fitting.

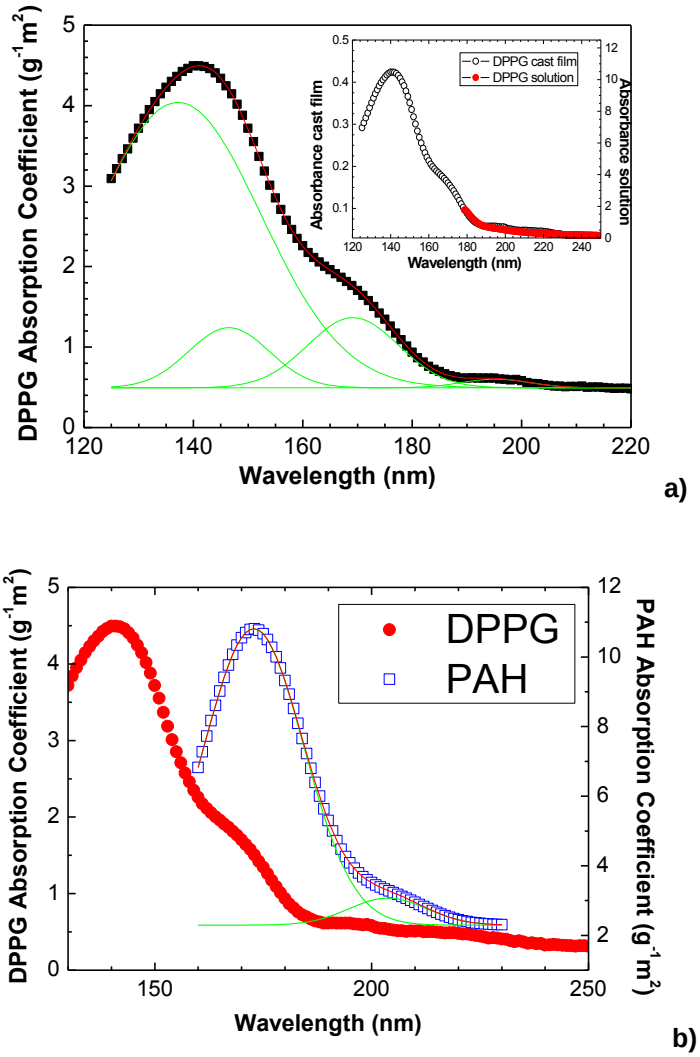

Figure 4.6.2. a) Absorption coefficient spectrum obtained from VUV absorption measurements for a DPPG cast film. Green curves depict the fitting of the absorption spectrum with Gaussian curves with bands at 138.2±0.4 nm, 145.8±0.4 nm, 169.8±0.3 nm and 192±2 nm. In the inset are shown the VUV spectra of DPPG cast film and of a DPPG dispersion. b) Absorption coefficient spectrum obtained from VUV absorption measurements for DPPG and PAH cast films. The green lines correspond to the fitting of PAH spectrum with Gaussian functions with bands at 172.9±0.1 nm and 203.8±0.8 nm.

The smallest peak for the DPPG cast film at 194.4±0.7 nm (6.38±0.04 eV) is assigned either to the $n_O \rightarrow \pi^*_{CO}$ transition from the lone-pair on the carbonyl oxygen to the antibonding π_{CO}-valence orbital [263,264] and to the valence shell electronic excitations of hydroxyl groups [265,266,267,268,269]. For the peak at 168±3 nm (7.38±0.09 eV) several assignments are possible:

i) $n'_O \rightarrow \pi^*$ transitions, where n'_O is the second lone pair orbital on the carbonyl group oxygen [263];

ii) $n_O \rightarrow \sigma*$ transition in the carboxyl group, from the atomic orbital n (ground state) to the antibonding σ -valence orbital [263,264];

iii) $n_O \rightarrow \sigma^*$ transition due to the promotion of an electron from the highest filled molecular orbital to an antibonding orbital (σ^*_{O-H}), which normally appears from 165 to 200 nm (6.2-7.5 eV) [265];

iv) water dissociation [128].

The peak at 147.2±0.2 nm (8.424±0.009 eV) is assigned to the phosphate group [264,270,271]. The strongest peak at 138.2±0.8 nm (8.97±0.03 eV) is ascribed to $\pi_{C=O} \rightarrow \pi^*_{CO}$, where a valence transition from the bonding π orbital to the antibonding π-valence orbital occurs [263, 264]. The amount of DPPG in the film can be estimated from the VUV spectrum, but this requires a precise measurement of film thickness, which is hampered by the non-uniformity of the cast film. Therefore, in a control experiment we obtained the VUV spectrum of a 5 mM aqueous solution of DPPG. The measurement was performed only up to 170 nm owing to the use of aqueous solutions [272]. The absorption coefficients were estimated by assuming that DPPG molecules absorb similarly in the liquid and in cast films, which is justified by the similarity in the spectra for the film and solution, as shown in the inset of figure 4.6.2 a). Using the Beer-Lambert law, the DPPG absorption coefficient at 180 nm was calculated from DPPG solution spectra. This absorption coefficient calculated from the DPPG solutions spectra was then used for the DPPG cast films, from which the absorption coefficients could be calculated for small wavelengths, as displayed in figure 4.6.2 a). The DPPG absorption coefficient curve was fitted with four Gaussians which allows one to calculate the partial absorption coefficients, ε_p, at peak position by considering the maximum absorbance of the peak. These values are displayed in table 4.6.1. As the PAH spectrum was not measured for small wavelengths, the partial absorption coefficient (ε_{p138nm}) of 3.7±0.4 g^{-1} m^2 calculated for the maximum absorption peak at 138 nm for DPPG allows us to determine the adsorbed amount of DPPG in LbL films. The absorption coefficient, ε, at peak position are also listed in table 4.6.1.

Using the VUV spectra of PAH aqueous solutions and the Beer-Lambert law, the PAH absorption coefficient spectrum was calculated and shown in figure 4.6.2 b). Absorption from the nitrogen group was expected according to the literature, as excitation energies below 8 eV have been found for ammonia [273,274,275,276] and amine molecules [278]. The spectrum for the PAH cast film could be fitted with two Gaussian curves, as shown in figure 4.6.2 b), whose parameters are given in table 4.6.1. The more intense peak at 172.9±0.1 nm (7.172±0.004 eV) is assigned to electronic $n_N \rightarrow 3pa$ transitions from the lone-pair electrons on nitrogen to nitrogen atomic-like orbitals [274,278]. This peak is superimposed onto another at 203.8±0.8 nm (6.08 eV) in figure 4.6.2 b) which can be assigned to the $n_N \rightarrow 3sa$ transitions [274,278,279]. The partial absorption coefficients for the peaks at 173 nm and 204 nm were estimated as 8.51±0.02 and 0.77±0.01 $g^{-1}.m^2$, respectively, while the absorption coefficients attain 10.81±0.02 and 3.33±0.02 g^{-1} m^2 values, respectively.

Table 4.6.1. Peak position and FWHM parameters for the peaks obtained from fitting the VUV spectra and corresponding assignments of DPPG and PAH cast films and PAH/DPPG LbL films. The absorption coefficients (ε) and partial absorption coefficients (ε_p) were calculated for each peak position. [a]Reference [264]. [b]Reference [263]. [c]Reference [270]. [d]Reference [128]. [e]Reference[265]. [f]Reference [266]. [g]Reference [277]. [h]Reference [273]. [i]Reference [278]. [j]Reference[274]. [k]Reference [275]. [l]Reference[279].

Peak parameters for VUV data of DPPG cast film				***Literature***	***Assignment***	
Peak position (nm/ev)	*FWHM (nm)*	ε_p ($g^{-1}.m^2$)	ε ($g^{-1}.m^2$)	*Peak position (eV)*	*Electronic transition*	*Functional group*
138.2 ± 0.4 8.97 ± 0.03	31.8 ± 0.3	3.7 ± 0.4	4.42 ± 0.02	8.4[a] , 8.5[a,b]	$\pi_{C=O} \rightarrow \pi^*_{CO}$	Carboxyl
145.8 ± 0.4 8.50 ± 0.02	13.0 ± 1.0	0.50 ± 0.05	4.24 ± 0.02	8.5[c]	----	Phosphate
169.8 ± .3 7.30 ± 0.01	14.5 ± 0.6	0.66 ± 0.07	1.70 ± 0.02	7.7[a] , 7.1[a,b] 7.4[d] 6.2-7.5[e] , 7.8[a,b]	$n'_O \rightarrow \pi^*$ ---- $n_O \rightarrow \sigma^*$	Carboxyl Hydroxyl
192.0 ± 2.0 6.46 ± 0.07	34.0 ± 5.0	0.17 ± 0.02	0.61 ± 0.02	5.8[a,b] 6.2-7.5[e] , 6.4[f]	$n_O \rightarrow \pi^*$ $n_O \rightarrow \sigma^*$	Carboxyl Hydroxyl

Peak parameters for VUV data of PAH cast film				***Literature***	***Assignment***	
Peak position (nm/ev)	*FWHM (nm)*	ε_p ($g^{-1}.m^2$)	ε ($g^{-1}.m^2$)	*Peak position (eV)*	*Electronic transition*	*Functional group*
172.9 ± 0.1 7.172 ± 0.004	22.9 ± 0.2	8.51 ± 0.02	10.81 ± 0.02	8.19[g,h] 7.14[g] 7.01[g], 7.1[i, j], 7.0[i, j], 7.927[k]	n_N **– 3p**	Amine
203.8 ± 0.8 6.08 ± 0.05	18.0 ± 2.0	0.77 ± 0.01	3.33 ± 0.02	6.4[g] 6.51[h] 5,77[g] 5.83[g], 5.7[i] 5.8[i], 6.0[j], 6.392[k] , 6.56[l]	n_N **– 3s**	Amine

Peak parameters for VUV data of DPPG/PAH cast film				***Literature***	***Assignment***	
Peak position (nm/ev)	*FWHM (nm)*	ε_p ($g^{-1}.m^2$)	ε ($g^{-1}.m^2$)	*Peak position (eV)*	*Electronic transition*	*Functional group*
136.0 ± 2.0 9.12 ± 0.07	28.0 ± 3.0	3.7 ± 0.4	---	8.4[a], 8.5[a, b]	$\pi_{C=O} \rightarrow \pi^*_{CO}$	DPPG
147.2 ± 0.2 8.424 ± 0.009	13.0 ± 2.0	0.50 ± 0.05	---	8.5[c]	----	DPPG
168.0 ± 3.0 7.38±0.09	18.0 ± 3.0	---	---	7.7[a], 7.1[a, b] 7.4[d] 6.2-7.5[e], 7.8[a, b] 8.19[g,h],7.14[g], 7.01[g],7.1[i, j], 7.0[i,j], 7.927[k]	$n'_O \rightarrow \pi^*$ $n_O \rightarrow \sigma^*$ n_N **– 3p**	DPPG PAH
194.4 ± 0.7 6.38 ± 0.04	15.0 ± 2.0	---	---	5.8[a, b], 6.2-7.5[e] 6.4[f], 6.4[g], 6.51[h], 5.77[g], 5.83[g], 5.7[i], 5.8[i] 6.0[j], 6.392[k], 6.56[l]	$n_O \rightarrow \pi^*_{CO}$ $n_O \rightarrow \sigma^*$ n_N **– 3s**	DPPG PAH

PAH/DPPG LbL Films

The VUV spectra for PAH/DPPG LbL films are shown in figure 4.6.3 a), which were fitted with four Gaussian curves, as indicated in the inset. Since DPPG has four and PAH has two components, this fitting points to overlapping of PAH and DPPG peaks. Taking into account the assignments above for DPPG and PAH molecules, one can assign the peaks for PAH/DPPG LbL films as follows: those at 194.4±0.7 nm and 168±3 nm are due to both types of molecules while the other peaks are only due to DPPG. With peaks associated with only one type of molecule (DPPG in this case), it is possible to use the VUV data for the films to estimate the adsorbed amount of DPPG, and then ascribe the remainder to PAH. Table 4.6.1 gives the parameters from these fittings and the assignment to electronic transitions in each bilayer and type of molecule.

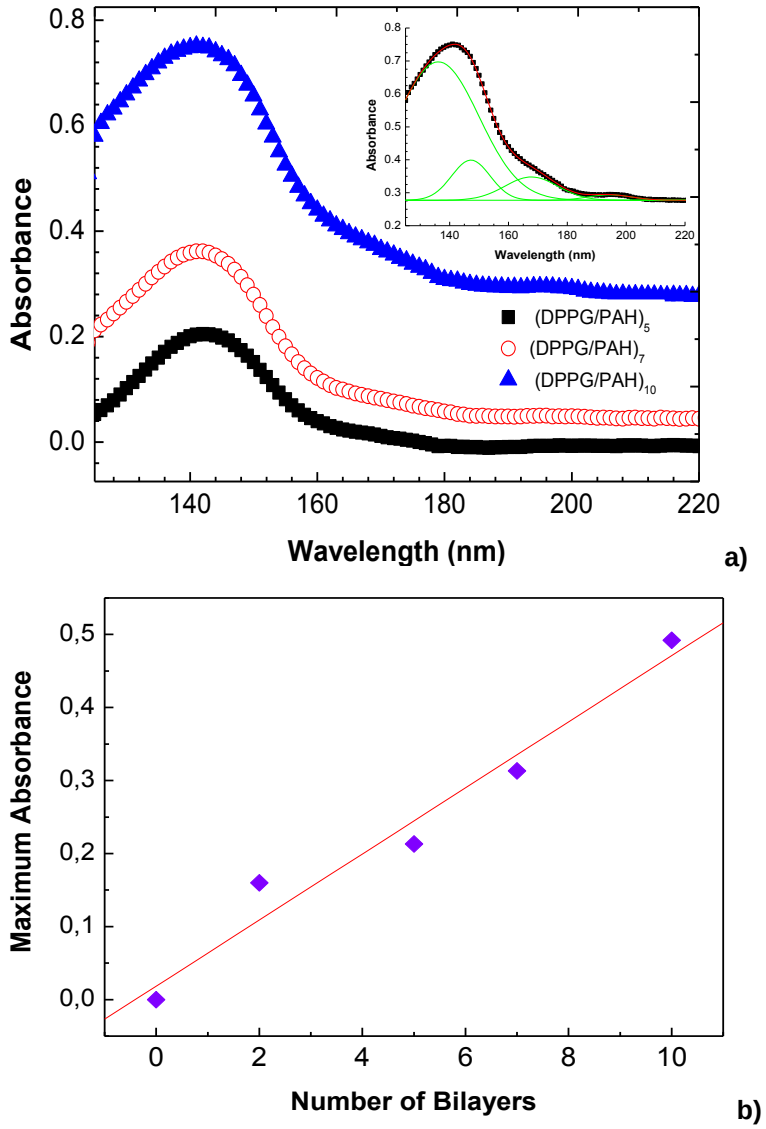

Figure 4.6.3. a) VUV Absorption spectra for LbL PAH/DPPG films with distinct numbers of bilayers. In the inset is shown the VUV spectrum of the $(PAH/DPPG)_{10}$ film. The green lines in the inset indicate the fitting with Gaussian functions, with bands at 136±2 nm, 147.2±0.2 nm, 168±3 nm and 194.4±0.7 nm. b) Maximum absorbance (142 nm) with baseline correction versus the number of bilayers in the PAH/DPPG LbL film.

The adsorbed amount per bilayer can be estimated because the PAH/DPPG LbL films grow linearly with the number of bilayers, as indicated in figure 4.6.3 b) for the maximum absorbance with baseline correction. This is in accordance with results by Constantino *et al* [280,281] who measured the conventional UV-vis. absorption spectra of DPPG/PAH LbL films, and found that the absorbance at 200 nm increased linearly with the number of bilayers. This linear growth is due to adsorption processes governed by electrostatic interactions between NH_3^+ groups from PAH and PO_4^- groups from DPPG without significant increase of roughness. These interactions are sufficiently strong to break the liposomes adsorbed on each layer, as we shall see from the adsorbed amounts calculated below from the VUV spectra data. The amount of DPPG adsorbed per bilayer was calculated by taking the intensity of the 136±4 nm peak in the VUV spectra for PAH/DPPG LbL films, since it is due only to adsorption of DPPG molecules (Table 4.6.1). From the absorbance intensity using the Beer-Lambert law, one obtains the adsorbed amount per layer per unit area (Γ_{DPPG}) using the partial absorption coefficient at 138 nm calculated from aqueous solutions and cast films in figure 4.6.2 a):

$$\Gamma_{DPPG} = \frac{Abs_{p138\,nm}}{2\varepsilon_{p_{138\,nm}}} \tag{4.6.1}$$

The factor 2 in the denominator appears because the PAH/DPPG film was deposited on both sides of the substrate. The mass of a DPPG adsorbed layer per unit area was calculated 6±1 mg/m^2 per layer, as shown in table 4.6.2, corresponding to 3.8×10^{18} (=$2\times1.9\times10^{18}$) molecules/m^2. This is a reasonable value if one considers that the surface density of DPPG molecules in a Langmuir monolayer is 2.1×10^{18} molecules/m^2 [280,281,282,283,284]. The latter density was obtained for a condensed monolayer with surface pressure of 30 mN/m and mean molecular area of 45 Å^2. The good agreement indicates that the vesicles collapsed into a lipid bilayer in the LbL film, which would lead to a mass of 5.5 mg/m^2 to be compared with the measured value of 6±1 mg/m^2. Moreover, this value is totally in accordance with the DPPG amount per unit of area adsorbed onto a PAH layer of 4.93±0.09 mg/m^2 measured by crystal quartz balance [259]. The amount of PAH adsorbed can be calculated from the absorbance at 168 nm peak, for which both DPPG and PAH molecules contribute, since the adsorbed amount of DPPG was already calculated, by using a simple absorbance values relation:

$$\Gamma_{PAH} = \frac{\frac{Abs_{168\,nm}}{2} - \Gamma_{DPPG} \times \varepsilon_{DPPG168nm}}{\varepsilon_{PAH168nm}} \tag{4.6.2}$$

Where Γ_{PAH} is the adsorbed amount per layer per unit area, Abs_{168nm} is the absorbance at 168 nm per bilayer and the $\varepsilon_{PAH168nm}$ and $\varepsilon_{DPPG168nm}$ where the absorption coefficients at 168 nm of PAH and DPPG, respectively. Using the absorption coefficients at 168 nm presented in figure 4.6.2 a), Γ_{PAH} was estimated as ~ 0.9 mg/m^2, consistent with 0.4 mg/m^2 obtained by Baba *et al* [262] for a dried PAH layer measured with a quartz crystal microbalance.

Table 4.6.2. Properties of PAH/DPPG LbL films, where Γ is the adsorbed amount per layer. i) Measured by atomic force microscopy.

Layer	***Γ (mg/m²)***	***Γ from literature (mg/m²)***	***Molecules (or monomers) per Area (m⁻²)***	***Roughness (nm)***
DPPG	6.0 ± 1.0	5.5 (lipid bilayer)	$3.8\times10^{18} = 2\times1.9\times10^{18}$ (Literature Langmuir layer = 2.1×10^{18})[278-282]	0.3 i)
PAH	~0.9	0.4 [109]	9×10^{15} - 12×10^{15}	---

Because the LbL films were dried in between the adsorption process for each bilayer and submitted to vacuum, changes may have occurred in the adsorbed amounts and in the surface roughness [91]. In order to better analyse the DPPG layer, its surface morphology after drying was characterized by atomic force microscopy.

SURFACE CHARACTERIZATION OF A DPPG LAYER

The surface of one bilayer PAH/DPPG film adsorbed onto silicon substrate was characterized by AFM. A topographic image in figure 4.6.4 a) points to a quasi-flat surface with a roughness (Rms) of only 0.3 nm. The values of 3.24 and 20.9 for Skewness and Kurtosis functions, respectively, obtained from a statistical and frequency analysis of the topographic data, indicate that the surface has more peaks than valleys. The valleys can be explained by adsorption of liposomes on the PAH surface which were then ruptured and formed a lipid bilayer. In these regions the roughness was lower than the average for the whole sampled area. The valleys are surrounded by regions (peaks) that are two-bilayer thick, then leading to one-bilayer thick peaks in the AFM image of figure 4.6.5 b). The unfolding of liposomes to form lipid bilayers was proposed by Reimhult *et al* [285]. The sites where liposomes were adsorbed could be determined from the distance between peaks varying from 80 to 150 nm and from 200 to 300 nm in figure 4.6.4 b). The largest diameters correspond to twice the original diameter of the liposomes, suggesting that the entire liposome spreads on the substrate. It should be referred that AFM topographies of DPPG cast films revealed intact liposomes. The small valleys with the dimensions of twice liposome diameter, see figure 4.6.4 b), are surrounded by several peaks caused by an increased roughness when liposomes at the edges do not have space to spread completely into a bilayer or even to surface irregularities due to PAH adsorption. This explanation is consistent with models [285,286,287] for the formation of supported lipid bilayers onto solid substrates. An important requirement for the rupture of DPPG liposomes is a high adhesion strength between PAH and DPPG regions, which is expected as the PAH molecules were almost fully ionized for the film fabrication at pH 4 [261].

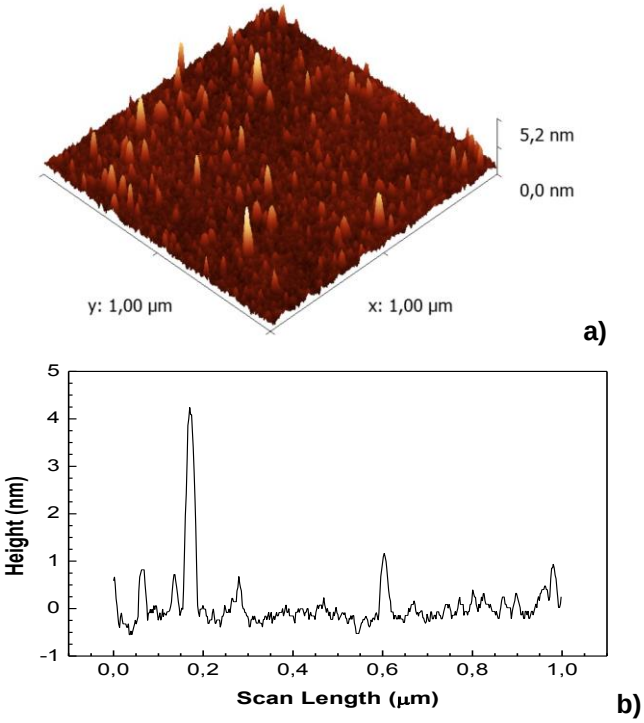

Figure 4.6.4. a) AFM topographic image; b) Topographic profile of a 1-bilayer PAH/DPPG LbL film.

EFFECTS FROM ULTRAVIOLET (UV) IRRADIATION ON A PAH/DPPG FILM

Since UV irradiation is known to affect biological systems, with effects being noted at the molecular level for cell membrane models, we verified whether damages on the PAH/DPPG LbL films could bring artefacts to the VUV data. No significant changes were noted in the spectra upon irradiating the films with UV at a fixed wavelength (140 nm) during one hour, as shown in figure 4.6.5. This result allows us to conclude that the VUV technique can be used for characterization of this type of heterostructures since the measurements were performed with the samples in vacuum and no noticeable damage caused by radiation occurs for the duration (ca. 20 min.) of the experiment.

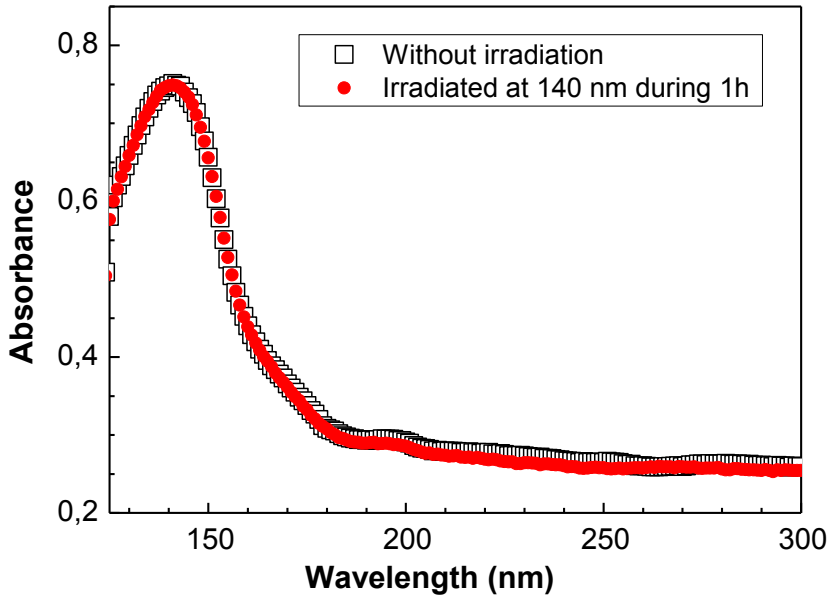

Figure 4.6.5. VUV spectra of a $(PAH/DPPG)_{10}$ biomimetic membrane before and after being irradiated at 140 nm during 1 h in vacuum.

CONCLUSIONS

We reported VUV measurements of DPPG in aqueous solutions, and in cast and LbL films. From the spectra we could assign the electronic transitions responsible for the light absorption and determine the amount of DPPG adsorbed on LbL films with PAH. Significantly, the adsorbed amounts pointed to adsorption as a lipidic bilayer, which means that the DPPG liposomes were ruptured during the adsorption process. The final structure of the LbL films was reflected on the film topography investigated with AFM, for the images showed terraces with thicknesses again corresponding to lipid bilayers. The LbL films were not affected by prolonged UV irradiation in the absence of water molecules indicating that the VUV technique can be used for characterization of lipid heterostructures. We therefore propose VUV spectroscopy as a new powerful tool for LbL film characterization which we hope will be useful in, among others, cell membrane modelling and drug delivery studies based on phospholipids.

ACKNOWLEDGMENTS

The authors acknowledge the European Commission for access to the ASTRID facility at the University of Aarhus, Denmark and for their support through the Access to Research Infrastructure action of the Improving Human Potential programme. This work was supported also by the "Plurianual" financial contribution of "Fundação para a Ciência e Tecnologia" (Portugal) and by FAPESP and CNPq (Brazil). It resulted from taking part in the COST Action CM0601, Electron Controlled Chemical Lithography (ECCL) and in bilateral collaboration projects under the programs CAPES-Brazil/Grices-Portugal. A. A. Duarte and P. J. Gomes acknowledge the fellowships SFRH/BD/62229/2009 and SFRH/BD/35954/2007, respectively.

4.7. INTERACTION OF DNA WITH LANGMUIR MONOLAYERS OF OPPOSITE CHARGED PHOSPHOLIPIDS

Paulo J. Gomes, Amélia M.P.S. Gonçalves da Silva,
Paulo A. Ribeiro, Osvaldo N. Oliveira Jr. and Maria Raposo

STATUS: To be submitted

ABSTRACT

The study of DNA interactions with lipids is of particular importance for the development of biosensors, nanodevices, drug delivery systems and radiation studies on biological molecules. This work addresses the interaction studies of two phospholipids, the anionic 1,2-distearoyl-*sn*-glycero-3-phospho-(1'-*rac*-glycerol) (DPPG) and the cationic 1,2-distearoyl-*sn*-glycero-3-ethylphosphocholine (EDPPC), with deoxyribonucleic acid (DNA). The surface pressure – area (π–*A*) isotherm of DPPG progressively deviates to larger areas at low surface pressures with the DNA concentration in the subphase, becoming nearly invariant at high surface pressures up to the collapse of the monolayer. This means that DNA penetrates in the expanded regime of DPPG monolayer, being excluded from the condensed regime due to repulsive electrostatic interactions. Differently, the π–*A* isotherm of EDPPC is not significantly affected in the expanded regime, while becomes steeper in the condensed regime and the collapse surface pressure increases with the DNA content in the subphase. DNA in the water subphase clearly stabilizes the cationic EDPPC monolayer.

INTRODUCTION

Langmuir monolayers at air-liquid interface are commonly used to characterize the interactions between phospholipids and biological molecules such as proteins but are also valuable tools for studying interaction between lipids and deoxyribonucleic acid (DNA). Indeed these studies are essential for developing DNA-based pharmaceuticals for gene therapy, biosensors and nanodevices [288] and determining effects from irradiation of biological molecules [289]. However, only a few studies of interaction of lipids with deoxyribonucleic acid (DNA) at air-water interface are available in the literature. In fact, Cardenas *et al* [290] studied the behaviour of monolayers of dioctadecyldimethylammonium bromide (DODAB) and of DODAB/disteroylphosphatidylcholine (DSPC) deposited onto a DNA aqueous solution subphase and demonstrated that in presence of DNA, the surface pressure versus area isotherms of the cationic lipid shift to larger mean molecular areas due to the electrostatic interaction with DNA while the typical liquid expanded-liquid condensed phase transition for DOBAB monolayers disappear and the monolayer remains to be in the liquid expanded phase.

The interaction of calf thymus DNA with 1,2-dimyristoyl-phosphatidylethanolamine (DMPE) monolayers in presence of Ca^{2+} or Mg^{2+} ions was studied and it was observed that DNA adsorption only in presence of the divalent ions and at low lateral pressure DNA partially penetrates into the lipid monolayer but is squeezed out at high pressure [291]. Interactions of native DNA with octadecylamine (ODA) and hexadecyl dimethylammonium bromide (HTAB) monolayers at the air/water interface were also studied and it had been shown that the microscopic structure of ODA-DNA complexes is definitely consistent with a single-stranded form for DNA while with HTAB, DNA complexes in its native form. This crucial difference in the behaviour of these two fairly similar lipids was interpreted as due to the presence of the amine group in ODA [292]. Antipina *et al* [293] characterized the DNA interaction with the cationic lipids 2-tetradecylhexadecanoic acid-{2-[(2-aminoethyl)amino]ethyl}amide (CI) and 2-tetradecylhexadecanoic acid-2-[bis(2-aminoethyl)amino]ethylamide (CII) and demonstrated the ability of these cationic lipids to couple with DNA at low as well as at high pH value. Those authors also found that the observed DNA structuring does not seem to depend on subphase pH conditions.

In this work, we analyse the interaction between 1,2-distearoyl-*sn*-glycero-3-phospho-(1'-*rac*-glycerol) (DPPG) and 1,2-distearoyl-*sn*-glycero-3-ethylphosphocholine (EDPPC) monolayers with DNA molecules at air/liquid interface and the effect of UV radiation on the DPPG and DNA system. The choice of these lipids was based on both to be amphiphilic molecules, composed of two saturated chains and a hydrophobic tail and to present opposite charges, DPPG is negatively charged while EDPPC is positive. Nonetheless, Langmuir monolayers of DPPG are well-documented in the literature [294,295] while Langmuir monolayers of EDPPC are understudied although ethylphosphocholine lipids as EDPPC are highly biocompatible cationic amphiphiles that can be used for the formulation of liposomal DNA vectors, with negligible toxic effects on cells and organisms [296].

EXPERIMENTAL DETAILS

MATERIALS

The anionic 1,2-distearoyl-*sn*-glycero-3-phospho-(1'-*rac*-glycerol) (DPPG) and the cationic 1,2-distearoyl-*sn*-glycero-3-ethylphosphocholine (EDPPC) lipids both with purity higher than 99% were obtained from Avanti Polar Lipids®. The chemical structures of these lipids are shown in figure 4.7.1. Highly pure ($A_{260/280nm} \approx 1.6$) lyophilized deoxyribonucleic acid sodium salt from calf thymus (DNA) was obtained from Aldrich®. The solvents chloroform and ethanol were spectroscopic grade from Merck®. The ultrapure water was distilled twice and purified with the Millipore Milli-Q system (resistivity ≥ 18.2 MΩ.cm).

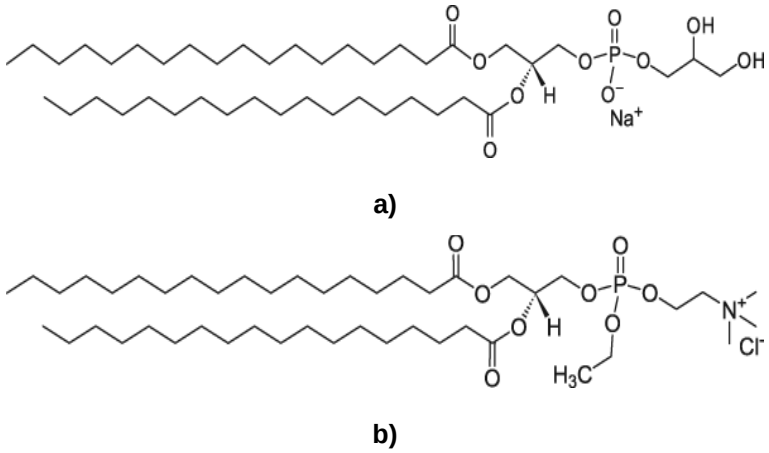

Figure 4.7.1. Chemical structures of the lipids: a) 1,2-distearoyl-*sn*-glycero-3-phospho-(1'-*rac*-glycerol) (DPPG) and b)1,2-distearoyl-*sn*-glycero-3-ethylphosphocholine (EDPPC).

METHODS

Phospholipid solutions prepared in chloroform and ethanol (4:1) at 1 mM were spread on the aqueous subphase to yield an initial mean area per molecule of 1.6 nm^2. The solvent was allowed to evaporate for 10 min before compression started. The subphase was either ultrapure water or DNA solutions at three concentrations, prepared with ultrapure water. Measurements were carried out at room temperature on a computer controlled KSV 5000 Langmuir-Blodgett system (KSV Instruments, Helsinki), according to procedures described elsewhere [297]. For the π-A isotherms (either in single compressions or in compression-expansion cycles), a asymmetric compression (or expansion), with a constant barrier speed of 5 $mm.min^{-1}$, was used. Several isotherms were performed for each system, with the same or different solutions.

For investigating monolayer stability, the same procedure to obtain a π-*A* isotherm was adopted, except that the compression was stopped at a target surface pressure, π_0, which is kept constant by the continuous adjustment of the barriers position while the area A was recorded as a function of time (*A*-*t*). For the π-*t* measurements, the surface pressure π was recorded as a function of time at constant area A_0 (stopped barriers).

RESULTS AND DISCUSSION

Effects induced by incorporation of DNA solutions into the subphase for EDPPC and DPPG monolayers are shown in figure 4.7.2 a) and b), respectively. The surface pressure (π-*A*) isotherm for a neat monolayer of the cationic EDPPC displays a liquid-expanded (LE) phase below 25 $mN.m^{-1}$, with a phase transition to the liquid condensed state (LC) up to $\pi \approx 35$ $mN.m^{-1}$, and LC continues until collapse at 45 $mN.m^{-1}$. A comparison of figures 4.7.2 a) and b) points to the bulky hydrophilic group of EDPPC occupying a larger area per molecule (90 $Å^2$) than the DPPG hydrophilic group (50 $Å^2$), as the monolayer of the anionic DPPG is condensed, consistent with the literature [298]. The EDPPC monolayer is not significantly

affected by DNA in the expanded, low pressure regime, but the isotherms become steeper in the condensed phase. More importantly, the collapse pressure increases with the DNA content in the subphase, which reveals that the anionic biopolymer DNA stabilizes the EDPPC monolayer. In contrast, as shown in figure 4.7.2 b) DNA causes the DPPG monolayers to be more expanded at low pressures, and seems to be excluded from the condensed phase, since the isotherms practically coincide with that of neat DPPG. The expulsion at high surface pressures may be ascribed to repulsive, anionic-anionic electrostatic interactions.

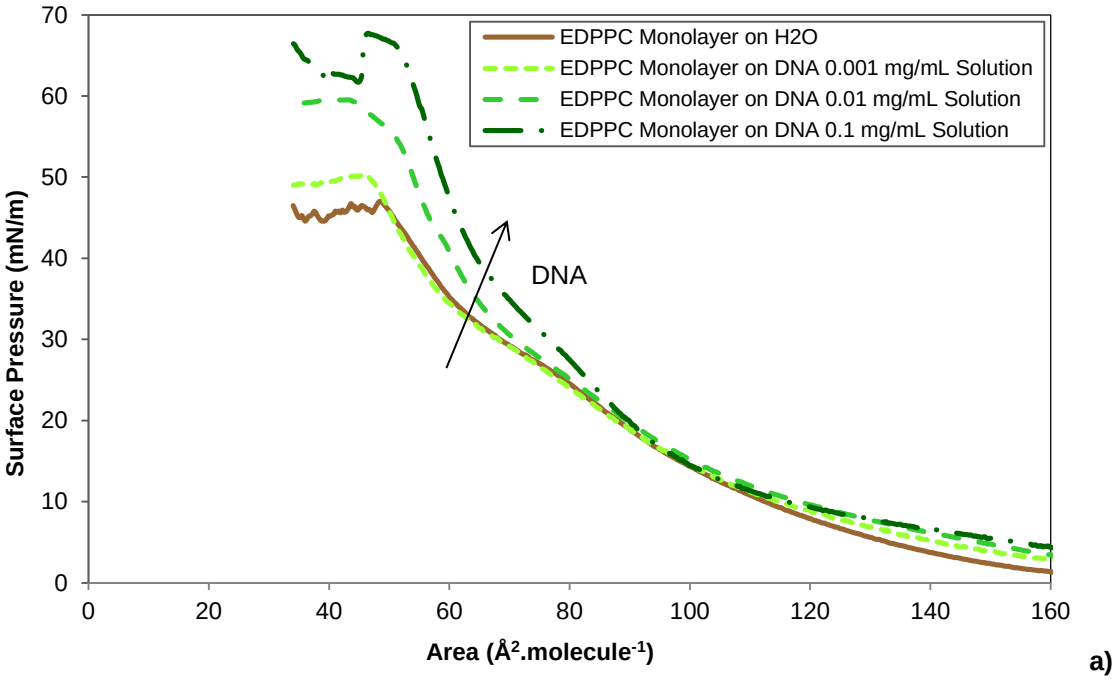

a)

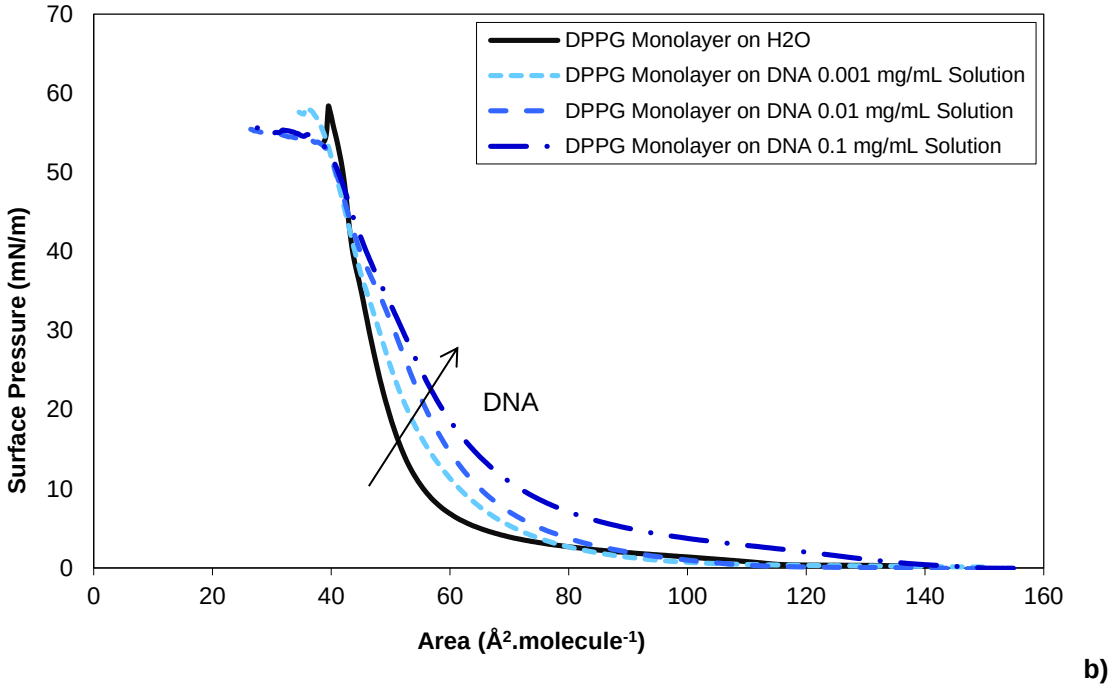

b)

Figure 4.7.2. Surface Pressure for a) EDPPC and b) DPPG and monolayers at water interface.

Marked differences in the effects from DNA on EDPPC and DPPG monolayers are clearly seen in the compressional modulus calculated from the surface pressure isotherms of figure 4.7.2, defined as:

$$k_s^{-1} = -A\left(\frac{\partial \pi}{\partial A}\right)_T \qquad 4.7.1.$$

Figure 4.7.3 shows that the modulus increases with the DNA concentration for EPPPC whereas, generally, it decreases for DPPG. The only exception to this behaviour is the lowest DNA concentration for the EDPPC monolayer, as commented upon later on. Overall, DNA causes the EDPPC monolayer to become more rigid, and in contrast it induces higher fluidity in DPPG monolayers.

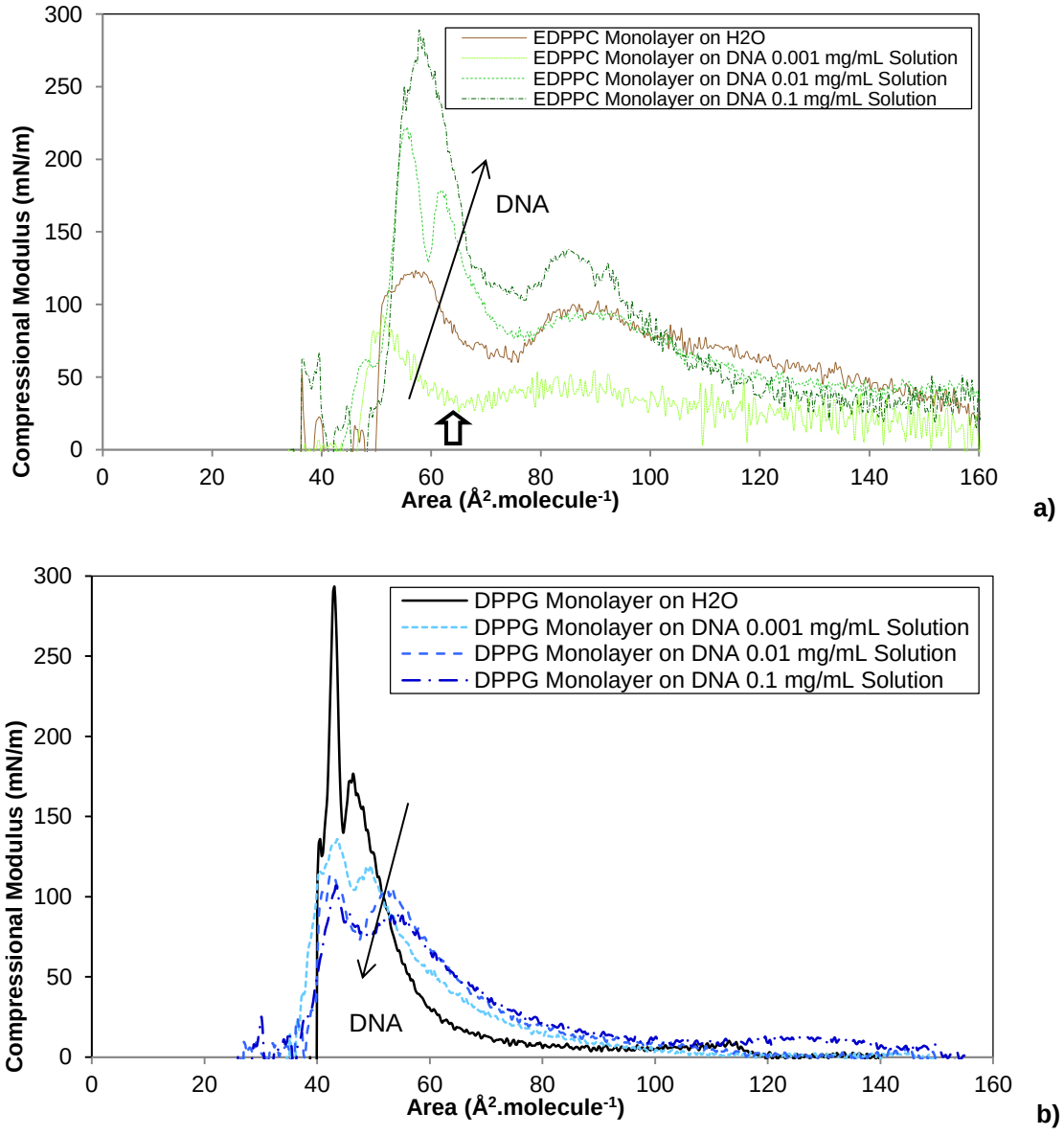

Figure 4.7.3. a) Compressional modulus values vs area per molecule plots for a) EDPPC and b) DPPG and monolayers at the air/water interface.

The stabilizing effect from DNA on EDPPC monolayers is readily apparent in relaxation kinetic studies, which are suitable to investigate processes involving material loss from the interface [299,300]. Here, the EDPPC and DPPG monolayers on DNA subphases were compressed at a constant speed of 5 mm.min^{-1} up to a target surface pressure π_0 = 30 mN.m^{-1}, corresponding to the pressure of a real cell membrane [301,302,303,304]. Then, the area per molecule *A* was monitored as a function of time *t*. Figure 4.7.4 a) and b) show the normalized (normalized A/A$_0$) *A-t* decay curves for EDPPC and DPPG, respectively. For EDPPC, the decay rate decreased with the DNA content except for the lowest DNA concentration. Therefore, DNA helped stabilize the EDPPC monolayer, in agreement with the results from the surface pressure isotherms. We have not investigated further the distinct behaviour for the lowest DNA concentration, but it may probably be associated with the insufficient amount of DNA to neutralize the head group charges. In contrast, adding DNA causes the DPPG monolayers to become less stable, as indicated by the increased decay rates.

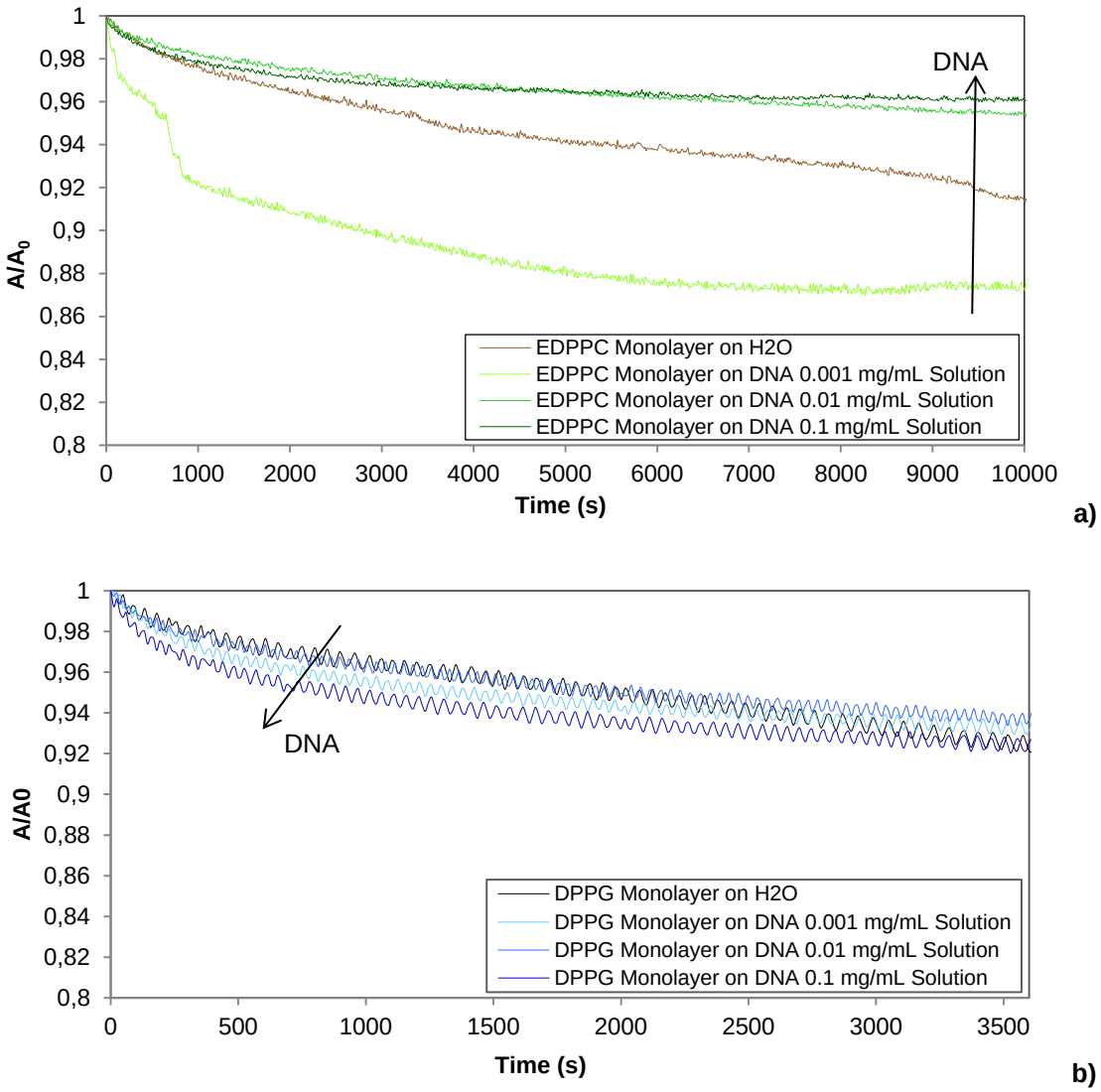

Figure 4.7.4. Relaxation kinetics with A-t decay curves, normalized A/A0, at constant surface pressure, π0 = 30 mN.m^{-1}, for a) EDPPC and b) DPPG monolayers on pure water and DNA-containing subphases.

Surface pressure isotherms obtained after the relaxation study (1 h) confirmed the increased stability of EDPPC and decreased stability for DPPG. These curves are shown in figure 4.7.5 a) and b), respectively, where for a DNA-containing EDPPC monolayer the isotherms taken before and after the relaxation study almost coincide. This is consistent with the stabilizing effect promoted by DNA; significantly, for EDPPC figure 4.7.5 a) shows strong deviation for the isotherm on pure water due to monolayer instability. On the contrary, for DPPG the DNA-containing monolayer displays an isotherm after relaxation that further deviates from the initial one.

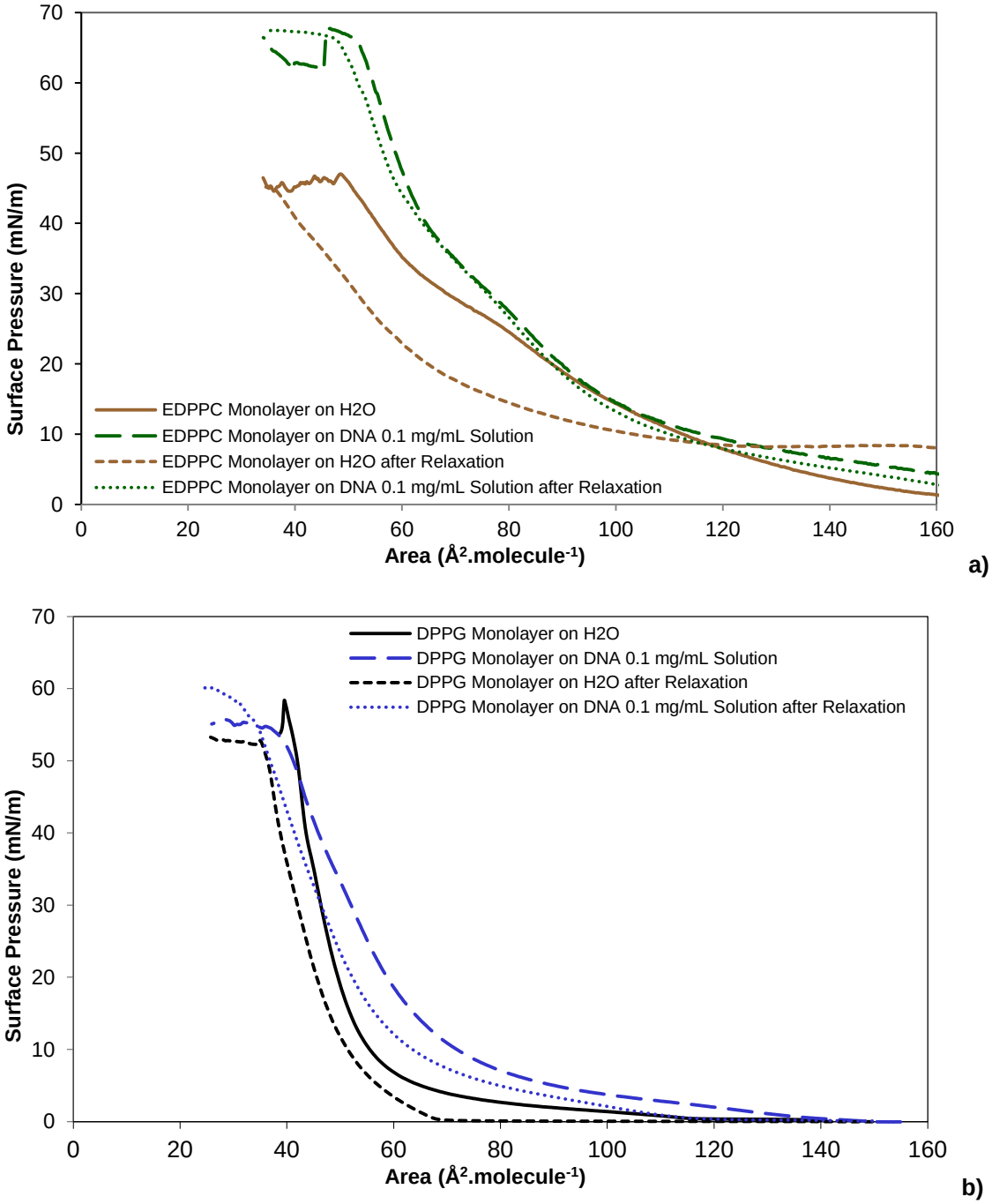

Figure 4.7.5. Surface pressure-area (π-A) compression curves for a) EDPPC and b) DPPG monolayers on pure water and DNA different concentrations subphases.

CONCLUSIONS

This study allowed us to conclude that at low pressure regime, the presence of DNA in the subphase does not affect the cationic EDPPC monolayer. Nevertheless, in the condensed phase the DNA presence increases collapse pressure indicating that EDPPC monolayer is stabilized by DNA. For DPPG monolayer, the presence of DNA leads to expansion of the monolayer at low pressures indicating that DNA penetrates in the expanded regime of DPPG monolayer, being excluded from the condensed regime probably due to repulsive electrostatic interactions.

ACKNOWLEDGMENTS

This work was supported also by the "Plurianual" financial contribution of "Fundação para a Ciência e Tecnologia" (Portugal) and by the Portuguese research Grant No. PEst-OE/FIS/UI0068/2011 through FCT-MEC(Portugal), by FAPESP and CNPq (Brazil). PG acknowledges the fellowship SFRH/BD/35954/2007.

4.8. RADIATION DAMAGE ON LANGMUIR MONOLAYERS OF THE ANIONIC 1,2-DISTEAROYL-SN-GLYCERO-3-PHOSPHO-(1'-RAC-GLYCEROL) (DPPG) PHOSPHOLIPID AT THE AIR-DNA SOLUTION INTERFACE

Paulo J. Gomes, Amélia M.P. S. Gonçalves da Silva,
Paulo A. Ribeiro, Osvaldo N. Oliveira Jr. and Maria Raposo

STATUS: To be submitted

ABSTRACT

The resilience of cells to ultraviolet (UV) irradiation is probably associated with the effects induced in biological molecules such as DNA and in the cell membrane. In this study, we investigated UV damage on the anionic 1,2-distearoyl-*sn*-glycero-3-phospho-(1'-*rac*-glycerol) (DPPG) phospholipid, which is an important component of cell membranes. In films cast from DPPG emulsions, UV irradiation induced cleavage of C-O, C=O and $–PO_2^-$ bonds, while in Langmuir monolayers at the air/water interface representing the cell membrane this irradiation caused the monolayer stability to decrease. When DNA was present in the subphase, however, the effects from UV irradiation were smaller, since the ionic products from degradation of either DPPG or DNA stabilize the intact DPPG molecules. This mechanism may explain why UV irradiation does not cause immediate collapse of cells, thus providing time for the cellular machinery to repair elements damaged by UV.

INTRODUCTION

Deoxyribonucleic acid (DNA) molecules are degraded with scission of single and double strands when irradiated with low energy electrons or photons [2,3,4,5,6]. Ultraviolet (UV) irradiation with synchrotron radiation, for instance, affected thymine, CO and phosphate groups of DNA cast films, according to vacuum ultraviolet and infrared spectra [12]. The electrical conductivity of DNA films was also found to decrease upon UV irradiation, since the loss of phosphate groups compromised electron hopping from base-pairs along the DNA chain [176]. Stronger effects from UV radiation occur in the presence of water [305], as DNA is altered directly by radiation and indirectly by secondary reaction products. Similar processes are expected to occur in the cell when DNA is irradiated, which should also affect the lipids comprising the cell membrane framework.

Because studying these molecular mechanisms in real cell membranes is not possible with present technologies, one may resort to model membranes such as Langmuir monolayers. Interaction between DNA and lipids at the air-water interface has been studied in a few systems.

DNA in the subphase caused monolayers of dioctadecyldimethylammonium bromide (DODAB) and DODAB/ disteroylphosphatidylcholine (DSPC) mixtures to expand, in spite of an expected attractive electrostatic interaction with the lipids [290]. The latter authors assumed that DNA macromolecules did not penetrate into the hydrophobic region of the lipid monolayer, since the headgroup area of the lipids increased only slightly in the presence of DNA. This small increase in area was ascribed to increased disorder of the cationic lipid monolayer. With cationic monolayers, DNA is denatured adopting a single-stranded form in octadecylamine (ODA), but complexes in its native form with hexadecyl dimethylammonium bromide (HTAB) [292]. This crucial difference for two fairly similar lipids was interpreted as being due to the amine group in ODA, which could change DNA conformation. In zwitterionic monolayers of 1,2-dimyristoyl-phosphatidylethanolamine (DMPE), calf thymus DNA only adsorbed at low surface pressures and in the presence of divalent (Ca^{2+} or Mg^{2+}) ions, being squeezed out at high pressures [291]. To our knowledge, studies about interaction between DNA and negatively charged lipids have not been published.

As for studies involving UV irradiation of Langmuir monolayers, various effects have been reported, from lipid degradation to rearrangement of polymer molecules. UV-irradiation induced oxidation in Langmuir monolayers of 1,2-dilinoleoyl-sn-glycero-3-phosphocholine (DLPC) [306] and 1,2-dilinoleoyl-sn-glycero-3-phosphocholine (DLoPC) [307]. Reaction between photosensitizers and 1,2-di-O-linoleoyl-3-sn-phosphatidylcholine (1,2-DLPC) in Langmuir monolayers were induced by prolonged UV-irradiation [308], while chiral structures could be induced by irradiating monolayers of achiral biopolymers [309].

In this work, we analyze the interaction between 1,2-distearoyl-*sn*-glycero-3-phospho-(1'-*rac*-glycerol) (DPPG) monolayers with DNA molecules at the air/liquid interface, including effects from UV irradiation. DPPG was chosen because its Langmuir monolayers have been well documented in the literature [294,295], in addition to being one major component of lung surfactant [310,311].

EXPERIMENTAL DETAILS

MATERIALS

The phospholipid 1,2-distearoyl-*sn*-glycero-3-phospho-(1'-*rac*-glycerol) (DPPG) shown in figure 4.8.1 was purchased from Avanti Polar lipids® and had purity higher than 99%. Highly pure ($A_{260/280nm} \approx 1.6$) lyophilized deoxyribonucleic acid sodium salt from calf thymus (DNA) was obtained from Aldrich®. The solvents chloroform and ethanol were spectroscopic grade from Merck®. The ultrapure water was distilled twice and purified with the Millipore Milli-Q system (resistivity ≥ 18.2 MΩ.cm).

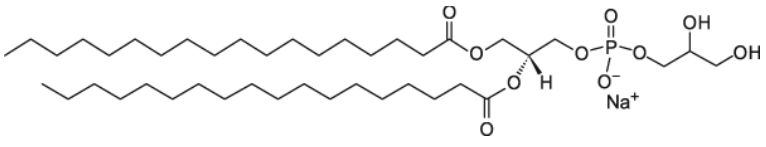

Figure 4.8.1. Chemical structure of 1,2-distearoyl-*sn*-glycero-3-phospho-(1'-*rac*-glycerol) (DPPG).

METHODS

Phospholipid solutions prepared in chloroform and ethanol (4:1) at 1 mM were spread on the aqueous subphase to yield an initial mean area per molecule of 1.6 nm^2. The solvent was allowed to evaporate for 10 min before compression started. The subphase was either ultrapure water or DNA solutions at three concentrations, prepared with ultrapure water. Measurements were carried out at room temperature on a computer controlled KSV 5000 Langmuir-Blodgett system (KSV Instruments, Helsinki), following procedures described elsewhere [297]. For the π-A isotherms (either in single compressions or in compression-expansion cycles), asymmetric compression (or expansion) was used with a constant barrier speed of 5 mm/min. Several isotherms were performed for each system, with the same or different solutions, in order to warrant reproducibility.

For investigating monolayer stability, the same procedure to obtain a π-*A* isotherm was adopted, except that compression was stopped at a target surface pressure, π_0, while the area A was recorded as a function of time (*A*-*t*). For the π-*t* measurements, the surface pressure π was recorded at constant area A_0 (stopped barriers). These π-*t* measurements were also performed upon irradiating the DPPG monolayer with a 254 nm UVC germicide lamp, model TUV PL-L 55W/4P HF 1 CT from Philips®, whose UV radiance was 1.9 W/m^2. FTIR measurements in cast films of DPPG on calcium fluoride were obtained with a spectrophotometer Thermo Scientific Nicolet-model 530 (Waltham, MA, USA).

RESULTS AND DISCUSSION

The effects induced by incorporation of DNA on DPPG monolayers are shown in figure 4.8.2. The surface pressure (π-*A*) isotherm for a neat monolayer of the cationic DPPG displays a liquid-expanded (LE) phase below 15 $mN.m^{-1}$, with a phase transition to the liquid condensed state (LC) up to $\pi \approx 30$ $mN.m^{-1}$, and the LC continuing until collapse at 55 $mN.m^{-1}$. The extrapolated area to zero pressure is approximately 50 $Å^2$, consistent with the literature [298]. DNA causes the DPPG monolayers to be more expanded at low pressures, and seems to be excluded from the condensed phase, since the isotherms practically coincide with the one for neat DPPG at $\pi > 40$ $mN.m^{-1}$. The preferential interaction of DNA with the polar region of the DPPG monolayer may explain the squeezing out of the DNA from the condensed monolayer into the subphase forming an adsorbed layer at the interface.

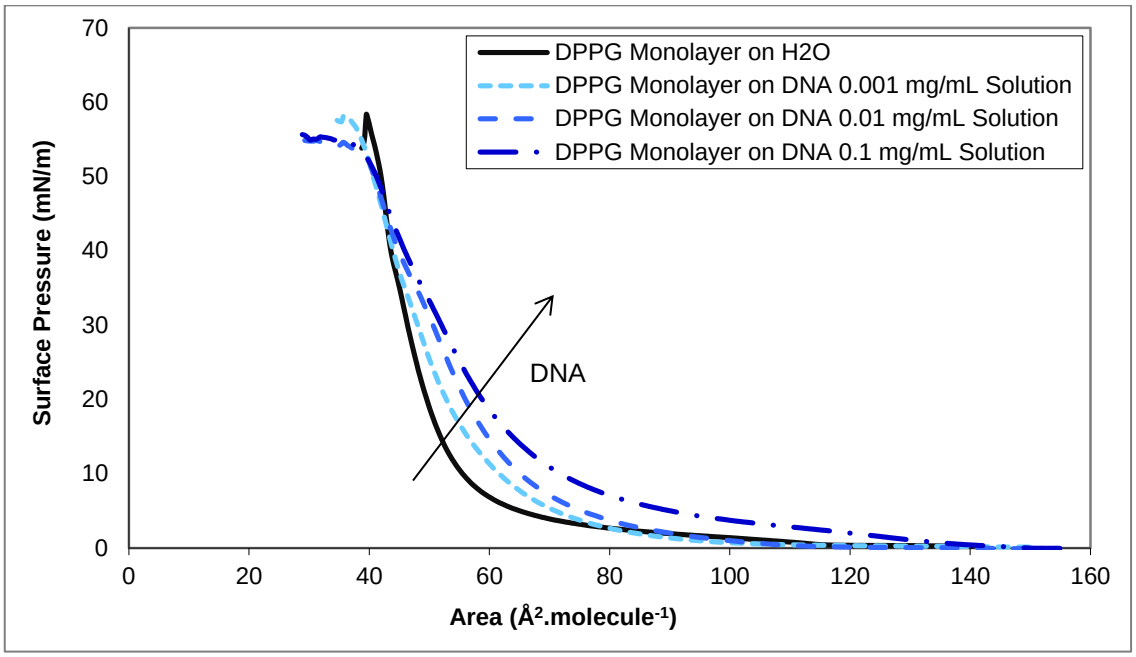

Figure 4.8.2. Surface Pressure for DPPG monolayers on ultrapure water and on subphases containing DNA.

The DPPG monolayers on DNA subphases were compressed at a constant speed of 5 mm.min^{-1} up to a target surface pressure π_0 = 30 mN.m^{-1}, corresponding to the value prevailing in a real cell membrane [302,304]. The decrease in the normalized area (A/A_0) with time in figure 4.8.3 shows that adding DNA causes the DPPG monolayers to become more expanded and less stable. The decreased stability for DPPG with the DNA-containing monolayer was confirmed by surface pressure isotherms obtained after the relaxation study (1 hour), which further deviated from the initial isotherm to lower molecular areas.

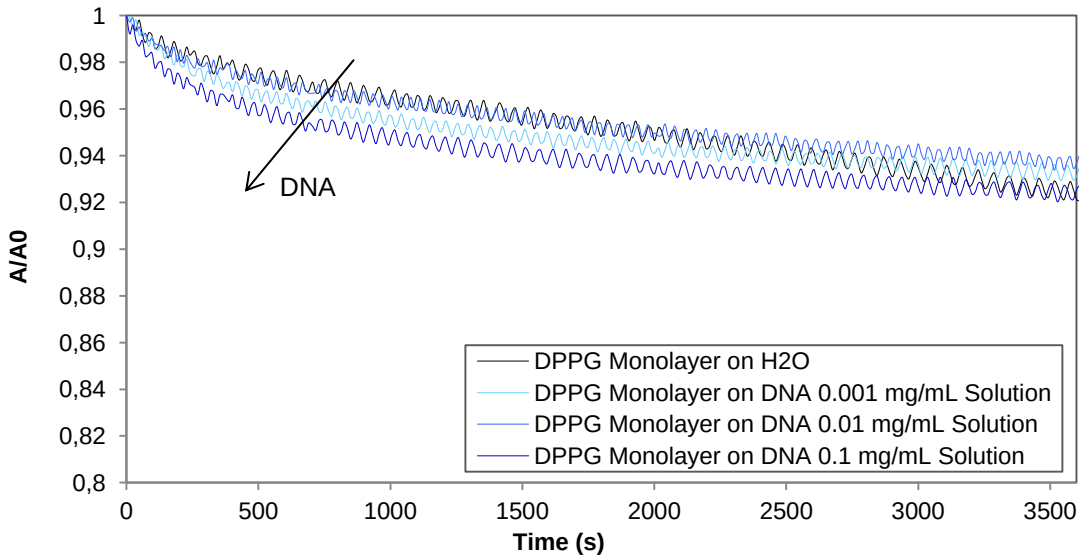

Figure 4.8.3. Relaxation kinetics with A-t decay curves, for normalized A/A0, at constant surface pressure, π0 = 30 mN.m^{-1}, for DPPG monolayers on pure water and DNA-containing subphases.

To analyze the UV radiation effect on DPPG monolayer on water and on DNA subphase area kinetics experiments (A-t) were performed. After compressing the monolayer at constant speed up a surface pressure of 30mN/m, the area as a function of time at constant pressure was recorded. The constant pressure was maintained constant by moving the barriers. During several intervals of time the monolayer was irradiated with UV light. Figure 4.8.4 shows these obtained curves.

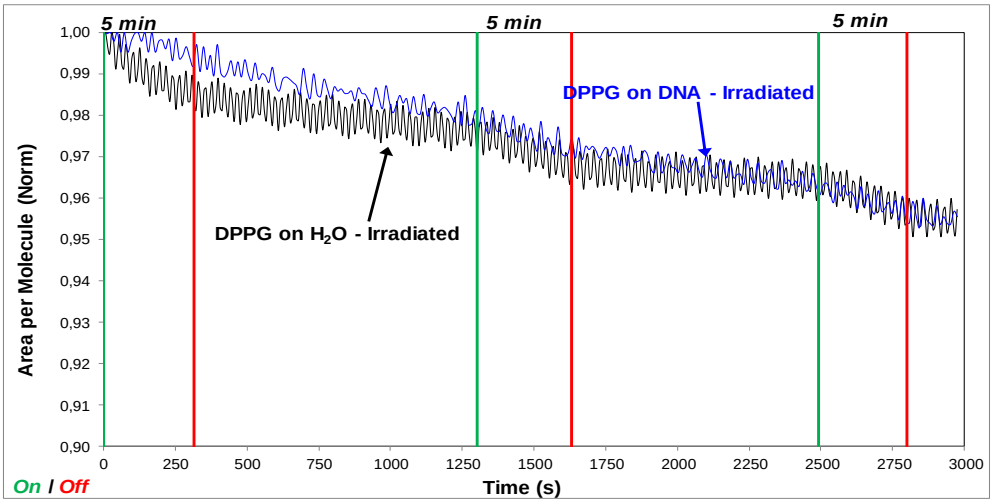

Figure 4.8.4. Relaxation in molecular area, *A-t* decay curves, normalized A/A_0, at constant surface pressure, π_0 = 30 $mN.m^{-1}$, of DPPG monolayers on pure water and DNA with 0.1mg/mL concentration subphases. The monolayers were irradiated during several periods of time of 5. The periods during which exposure to UV irradiation took place are marked with vertical lines.

To compare the effect of radiation on the relaxation kinetics curves of DPPG on water and on DNA aqueous solution subphases, the relaxation curves without and with first irradiation were plotted in figure 4.8.5 a) and b), respectively for pure water and for DNA with 0.1 mg/mL concentration subphases. The relaxation kinetics in figure 4.8.5 a) shows that UV irradiation decreases the monolayer stability. In order to quantify the effects, we fitted the A-t decay curves with an exponential function:

$$\left(y = y_0 \exp\left(-\frac{t}{\tau} \right) \right) \qquad (4.8.1)$$

and obtained the characteristic time constants, τ. For neat DPPG, the time constant decreased from 14±2 h to 6.2±0.8 h upon irradiating the monolayer, thus confirming the UV-induced instability. The opposite effect was observed when DNA was in the subphase, as shown in figure 4.8.5 b), whose curves were fitted with exponentials with time constants of 7.5±0.6 h and 19±3 h, without and upon UV irradiation, respectively.

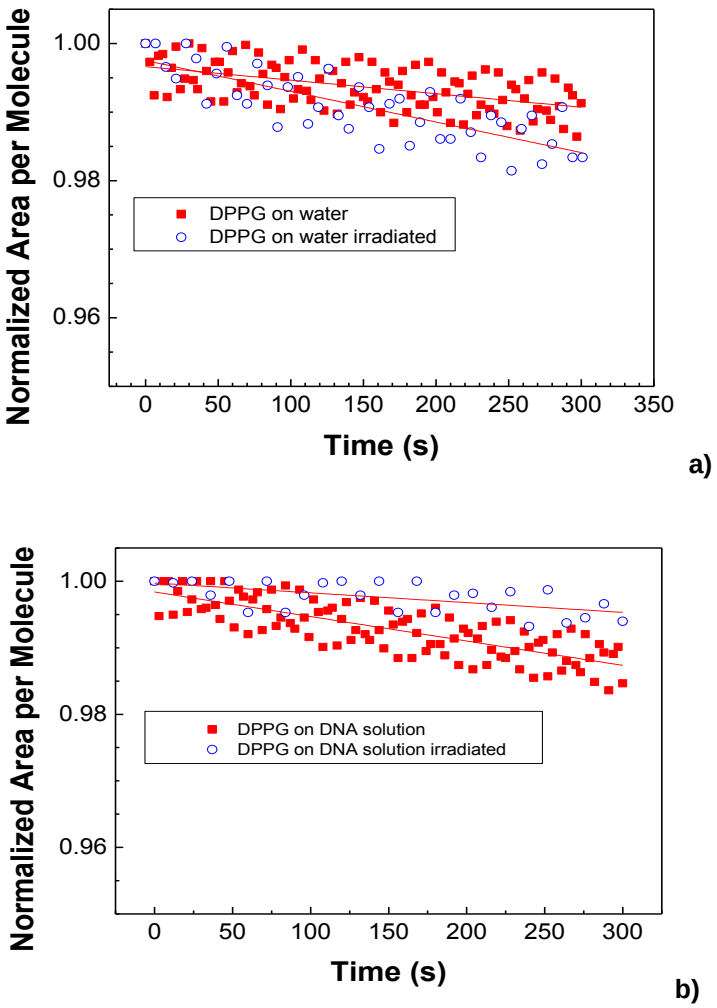

Figure 4.8.5. Relaxation in molecular area, *A-t* decay curves, normalized A/A_0, at constant surface pressure, π_0 = 30 mN.m^{-1}, of DPPG monolayers without and upon exposure to UV irradiation on: a) pure water and b) DNA with 0.1mg/mL concentration subphases.

The damages from UV radiation on DNA molecules are well documented [12], but it has been reported that UV does not damage DPPG molecules in vacuum [314]. Since no reports appear to have been made on UV effects on lipids in water emulsions, we performed UV irradiation experiments on DPPG molecules in cast films from emulsions and in monolayers. The infrared spectra in figure 4.8.6, whose assignment is given in table 4.8.1, indicate that UV radiation does damage DPPG molecules in cast films, essentially by cleaving C-O, PO_4^- and C=0 groups. This is inferred from the decreased intensity caused by irradiation in several bands, as indicated by the difference in the two spectra, before and after irradiation, in figure 4.8.6. The bands affected range from 1044 to 1102 cm^{-1}, 1150 to 1240 cm^{-1} and 1578 to 1697 cm^{-1}, assigned to CO-P, C-O-C, CO-O-C, PO_4^- and embedded hydrogen bonds C=0 groups, respectively.

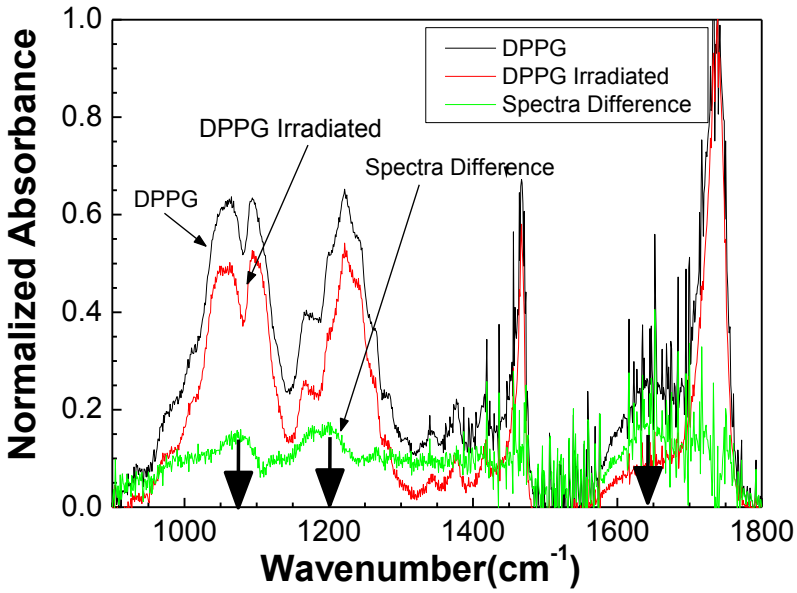

Figure 4.8.6. Infrared spectra of DPPG cast films prepared from DPPG aqueous solutions without and with UV irradiation. To visualize the damage induced in DPPG by exposure to radiation, the difference between the spectra was also added. The vertical arrows indicate the wavenumber of bands that disappear upon irradiation.

Table 4.8.1. Characteristic infrared absorptions in DPPG cast films.

Wavenumber (cm^{-1})	***Assignment***	***References***
1738	Stretching of carbonyl group (C=O)	[315,316,317]
1638	Vibrations of C=O groups embedded in hydrogen bonds; DPPG unfolded structure; DPPG unordered conformations	[318,319] [320] [321,322]
1467	CH_2 scissoring	[306,307,308,309]
1414	In-plane bending of C–O–H group.	--------
1241	Antisymmetric stretching of hydrated PO_4^- group	[323]
1222	P=O antisymmetric stretching of PO_4^- group	[306,307,308,309]
1169	Asymmetric stretching of CO–O–C groups	[158]
1070	Symmetric stretching of CO–O–C groups	
1096	Symmetric stretching of CO–O–C groups	[300,306, 307, 308,309]
1057	Symmetric stretching of C–O–C groups	
1047	Symmetric stretching of C–O–P groups	

The reason why DNA increases stability of DPPG monolayer under UV irradiation is as follows. The damage to DNA molecules from UV induces formation of ionic products that stabilize both the intact DPPG molecules and the DPPG byproducts resulting from UV irradiation. The effects from DNA practically disappear for prolonged irradiation times (ca. 2500 s), as shown in figure 4.8.4, probably because the reaction products from damaged DNA diffuse to the subphase and are no longer able to stabilize the DPPG monolayer.

CONCLUSIONS

UV irradiation of DPPG molecules in cast films obtained from emulsions induced cleavage of C-O, C=O and $–PO_2^-$ bonds, in contrast to the lack of effects for DPPG under vacuum reported in the literature. Hence, the presence of water seems crucial for degradation, and this was confirmed in DPPG monolayers at the air/water interface, whose stability decreased when irradiated with UV. Significantly, the effects from UV irradiation were mitigated if DNA molecules were incorporated into the subphase. DNA caused the DPPG monolayer to expand at low pressures, with molecules penetrating into the monolayer. In condensed monolayers, however, the DNA molecules were excluded probably due to repulsive electrostatic interactions. Nevertheless, even at high surface pressures corresponding to a real membrane, the underneath adsorbed layer of DNA decreased monolayer instability caused by irradiation. This was attributed to the formation of ionic products from degradation of either DPPG or DNA, which would stabilize both the intact DPPG molecules and the DPPG products resulting from UV irradiation. Such mechanism could explain why cells do not collapse immediately after irradiation. Cell stability is maintained until the elements damaged by UV can be repaired by the cellular machinery.

ACKNOWLEDGMENTS

This work was supported also by the "Plurianual" financial contribution of "Fundação para a Ciência e Tecnologia" (Portugal) and by the Portuguese research Grant No. PEst-OE/FIS/UI0068/2011 through FCT-MEC(Portugal), by FAPESP and CNPq (Brazil). PG acknowledges the fellowship SFRH/BD/35954/2007.

4.9. PROBING RADIATION DAMAGE BY AC CONDUCTIVITY AS A METHOD TO CHARACTERIZE ELECTRON HOPPING IN DNA MOLECULES

Paulo J. Gomes, Margarida Coelho, Madalena Dionísio,
Paulo A. Ribeiro and Maria Raposo

STATUS: Published in Applied Physics Letters, 101, 123702, 4 pages, 2012

ABSTRACT

Analysis of AC electrical conductivity of deoxyribonucleic acid (DNA) thin films, irradiated with ultraviolet (UV) light, revealed that electrical conduction is arising from DNA chain electron hopping between base-pairs and phosphate groups, with the hopping distance equal to the distance between DNA base-pairs, as calculated from correlated barrier hopping model. Loss of conductivity with irradiation time was shown to be associated with the decrease of phosphates groups. In the high frequency regime, at a given frequency, real part of conductivity strongly depends on irradiation time particularly for low dose, levels suggesting the use of DNA films for UV radiation sensors.

INTRODUCTION

In the last decade many efforts have been made to understand the effects of non-ionizing radiation on biological molecules as deoxyribonucleic acid (DNA). This interest has been boosted from early studies on the effect of 7-150 eV synchrotron radiation in DNA plasmid, showing that DNA single-strand (SSB) and double-strand (DSB) breaks can occur at all of these energies, for both dry and solution plasmid DNA [5]. Also irradiation with particles or photons at energies below the ionizing potential revealed to be capable of inducing DNA damage, [12, 143,157,158,174 and references therein]. As DNA is a macromolecule consisting of a long chain of monomers, its electrical properties are also expected to change as a result of chain breaks, feature that might be used to probe the DNA damage induced by radiation. Experimental outcomes of DNA electrical conductivity proved to be amazingly diverse with respect to conductivity regimes observed [210,211,212,213,214,215,216,217,218,219,220, 221], making difficult to clarify the conduction processes which are taking place within DNA molecules. Nevertheless, it was demonstrated that double stranded DNA is one-dimensional semiconductor and AC impedance spectroscopy can be an effective method to measure the

electrical conduction on DNA samples [217]. In order to establish if radiation damage can be inferred from electrical properties, in this work, the electrical conductivity of DNA thin films was characterized through impedance spectroscopy, in the 0.01 Hz to 10 MHz range, in terms of exposure to 254 nm ultraviolet radiation (UV).

EXPERIMENTAL DETAILS

Cast films were prepared from 0.5 mg/mL solutions of calf thymus lyophilized DNA sodium salt obtained from Aldrich®. Solutions were prepared by dissolving the DNA in deionized water with a resistivity of 18.2 MΩ.cm (Milli-Q, Millipore GmbH). The DNA solutions were spilled onto glass substrates having deposited interdigitated gold electrodes for electrical conductivity measurements and onto calcium fluoride substrates for spectroscopic measurements. All substrates were previously cleaned with ultra-pure water and dried under nitrogen flux. Cast DNA films were obtained after drying the deposited solution for 2 hours in vacuum desiccators. The samples were irradiated for different periods of time by means of a 254 nm UVC germicide lamp, model TUV PL-L 55W/4P HF 1CT from Philips®, in a ventilated chamber at room conditions. The UV irradiance was 1.9 W/m^2. Complex impedance spectra of the samples were measured before and after each period of irradiation using an Alpha-N analyzer from Novocontrol GmbH, covering a frequency range from 10^{-1} Hz to 10 MHz, being the AC potential applied to the two gold interdigitated electrodes. The electrical measurements were performed at 25±0.5 ºC controlled temperature and under a nitrogen atmosphere. Infrared spectra of the DNA thin film samples, prepared on calcium fluoride solid supports, were measured using a Fourier transform infrared spectrophotometer Nicolet-model 530.

RESULTS AND DISCUSSION

The electrical conductivity curves of DNA films obtained for different UV radiation exposures, are shown in figures 4.9.1 a) and 4.9.1 b) where, respectively, the real part of conductivity and the loss tangent curves are displayed as a function of frequency for different irradiation times. From figure 4.9.1 a) it can be seen that the real component of the conductivity is practically linear with frequency with the slope decreasing as the irradiation time increases. These curves when plotted in log scales, as shown in figure 4.9.1 a) inset, suggests that the conductivity follows a frequency power law. Since the slope of the inset curves is practically irradiation time independent, one expects that the conduction processes which are occurring are similar for all irradiation exposures. For the case of loss tangent curves, figure 4.9.1 b), a shoulder can be seen in the 1 kHz to 500 kHz range, which does not change monotonically in frequency position with irradiation time. This shoulder is likely due to polarization processes occurring in DNA molecules and hardly can be associated to only one type of DNA damage caused by irradiation. In addition, both real and imaginary permittivity components follow the behaviour observed by

Laudát and Laudát [324] for the frequency dependence of the complex permittivity of dry solid sodium DNA.

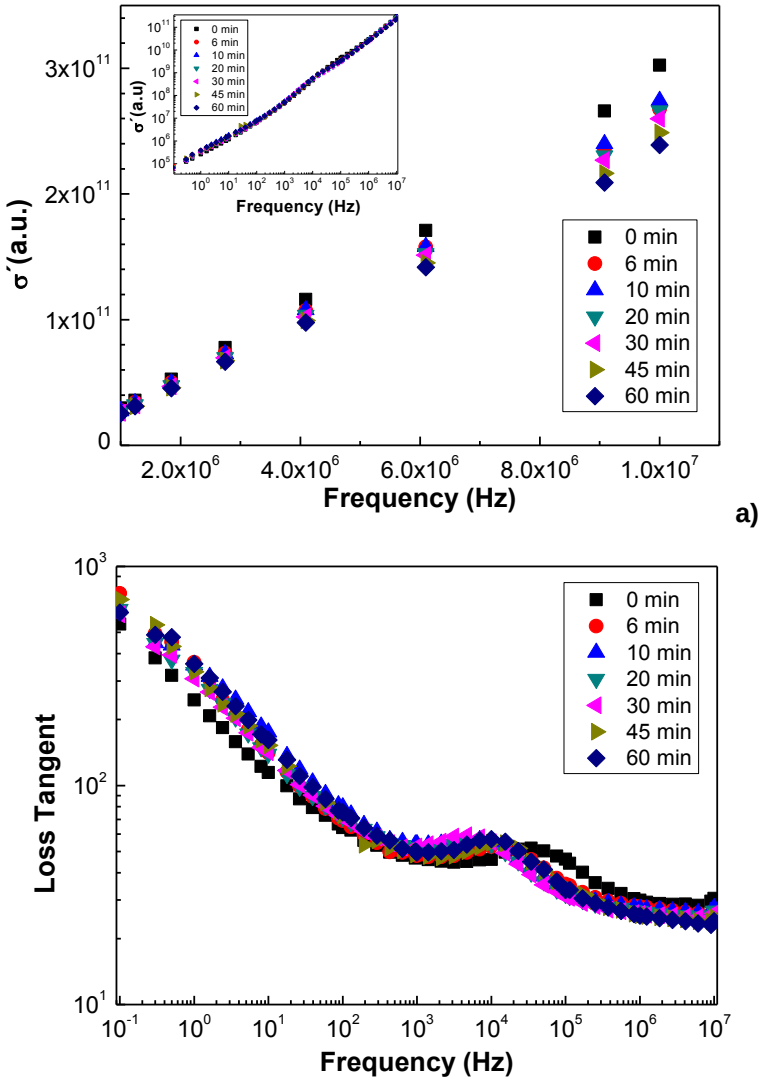

Figure 4.9.1. a) Real component of complex conductivity spectra, in the inset the same curves are displayed in log-log plots, and b) loss tangent spectra of a DNA cast film irradiated for different periods of UV irradiation time.

For frequencies above 1 MHz, each tangent loss curve obtained tends to a constant value, which decreases as the irradiation time increases. If one plots these values as a function of irradiation time at fixed frequency, for example 1 MHz, they are found to follow the real component conductivity behaviour as shown in figure 4.9.2. The exponential behaviour for the real conductivity with irradiation time suggests that this variable can be used to probe the effect of radiation on DNA molecules, since for short irradiation times; say first 20 minutes, the conductivity at fixed frequency presents a quasi linear response.

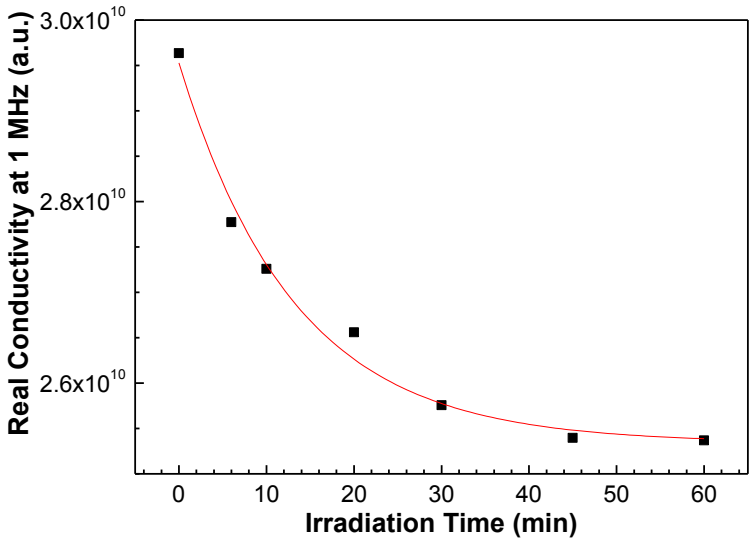

Figure 4.9.2. Real component of conductivity at 1 MHz, plotted as a function of irradiation time. The solid line is the fit of experimental data to a decay exponential curve.

Concerning conduction processes within DNA molecules, several theoretical models such as band transport [325,326,327], polaronic transport [328,329], fluctuation facilitated charge migration [330,331] and multistep hopping [332,333,334] have been addressed to account for DNA conductivity behaviour. By analyzing the real part of conductivity curve of figure 4.9.1 a), a power law, as observed in [324], dependence can be found as follows:

$$\sigma(\omega) \propto \omega^{s} \qquad 4.9.1$$

where ω is the frequency and s is a constant.

As a remark, equation 4.9.1 is usually used to describe conductivity driven by electron hopping and tunneling phenomena [335]. Predictions for these models were systematized in terms of $\sigma(\omega)$ dependence and calculated *s* values [336]. In the case of the quantum mechanical tunneling (QMT) through a barrier model [337], s is predicted to be temperature independent but frequency dependent, decreasing in value with the increase of frequency. In the QMT model and when the carriers become nonoverlapping small polarons, s becomes temperature dependent and increases as temperature increases. For large polaron tunneling [338], the polaron distortion cloud overlaps appreciably and s is both temperature and frequency dependent. For the correlated barrier hopping (CBH) of electrons, s is both temperature and frequency dependent. However, if the ratio W_M/kT assumes large values, being W_M the value of site separation energy, s is close to unity and effectively independent of frequency.

This systematization allows infer about the adequate model to explain the current experimental results. Fitting data of figure 4.9.1 a), at high frequencies, to equation 4.9.1, a mean value of 0.97±0.01 was obtained for s. Thus, s values are close to unity and, excluding the frequency range centered at 100 kHz associated to polarization phenomena, s is essentially frequency independent. Moreover, although the present data was obtained at room temperature, recent ac

measurements at 200 K and 300 K gave similar conductivity values [339], indicating that s should be considered frequency independent in the frequency range considered. Additionally, with respect to conductivity trend, proportionality with frequency is observed. These results are pointing out to correlated barrier hopping (CBH) of electron model proposed by Pike [335], where the electron is transferred by thermal activation over the barrier between two adjacent sites. Under this model, the AC conductivity was calculated in the narrow band limit, to be [340]:

$$\sigma(\omega) = \left(\frac{\pi^3}{24}\right) N^2 \varepsilon\varepsilon_0 \omega R_\omega^6 \qquad 4.9.2$$

where ε is the dielectric constant, ε_0 is the permittivity of free space, N is the concentration of pair sites and R_ω is the hopping distance, given by the expression:

$$R_\omega = \frac{e^2}{\pi\varepsilon\varepsilon_0\left[W_M - kT\ln\left(1/\omega\tau_0\right)\right]} \qquad 4.9.3$$

where W_M is the energy barrier and τ_0 is a characteristic relaxation time. The frequency exponent s can then be expressed as:

$$s = 1 - \frac{6kT}{W_M - kT\ln\left(1/\omega\tau_0\right)} \qquad 4.9.4$$

Both, hopping distance and pair sites concentration can be now calculated as a function of irradiation time. For these calculations, the frequency was fixed at 1 MHz, the considered relative permittivity of dry DNA value was of 5 in accordance with [324] and the value of 3.75 eV, given from spectrophotometric data [210], was used for the energy barrier. This energy barrier value is in accordance with Iguchi calculations [341] which showed that the nucleotides present semiconducting character with a gap energy of several eV. However, it should be remarked that calculations on the electronic structure of guanine and cytosine based DNA gave rise to values of gap energies The calculated values of N when plotted as a function of irradiation time revealed to follow the conductivity behaviour, decreasing exponentially with irradiation time. These achievements suggest that conductivity is in fact governed by hopping between DNA bases pairs and phosphates and/or sugar-phosphate groups, known to be strongly affected by UV radiation [5,12,210,211,213]. This explanation is also supported by the Iguchi calculations which demonstrated the nucleotides groups behave as donors while the sugar-phosphates behave as acceptors [343]. To prove that conductivity is really due to hopping between base pairs and the sugar-phosphate groups, DNA cast films prepared onto calcium fluoride were irradiated on different periods of time and the damage was analyzed by infrared spectroscopy in the range of 900 to 1300 cm^{-1}, where DNA presents backbone, sugar and phosphate groups vibrations [158]. The IR spectra for DNA cast films obtained for different

irradiation times are plotted in figure 4.9.3, showing the peaks associated to CC stretch of the backbone (966 cm^{-1}), furanose vibrations (1018 cm^{-1}), CO stretch of the furanose in backbone (1053 cm^{-1}), symmetric PO_2^- stretching of backbone (1088 cm^{-1}), A-former marker-sugar phosphate backbone (1183 cm^{-1}), anti-symmetric PO_2^- stretch in B-form (1210 cm^{-1}), anti-symmetric PO_2^- stretch in A-form (1241 cm^{-1}), C5=C6 vibration of cytidine and CN3H bend of deoxyribose thymine (1281 cm^{-1}) and C4-NH2 strength of cytosine (1296 cm^{-1}), all in accordance with ref. [158]. of 12 and 17 eV [342], which when applied to CBH of electron model leads smaller mean hoping distances. Recently, Yamada and Iguchi [343] also assumed energy differences between HOMO and LUMO of about 2 eV to 3 eV to apply the effective tight-binding models for electrons in DNA conduction and found if the π stacking of the base is perfect, there are two channels for π-electron hopping: one is the channel through the base stacking and the other is the one through the backbone chain of the sugar-phosphate groups. Taking into account the discrepancy of theoretical energy values, the energy barrier given by spectrophotometric results has been considered. The values of R_ω were then determined for all irradiation times resulting in an average value of 3.3899 ± 0,0002 Å which is remarkably close to 3.4 Å [210], the distance between base-pairs in the DNA molecule. Note that the small uncertain is given by the closeness of R_ω values individually calculated from different conductivity data.

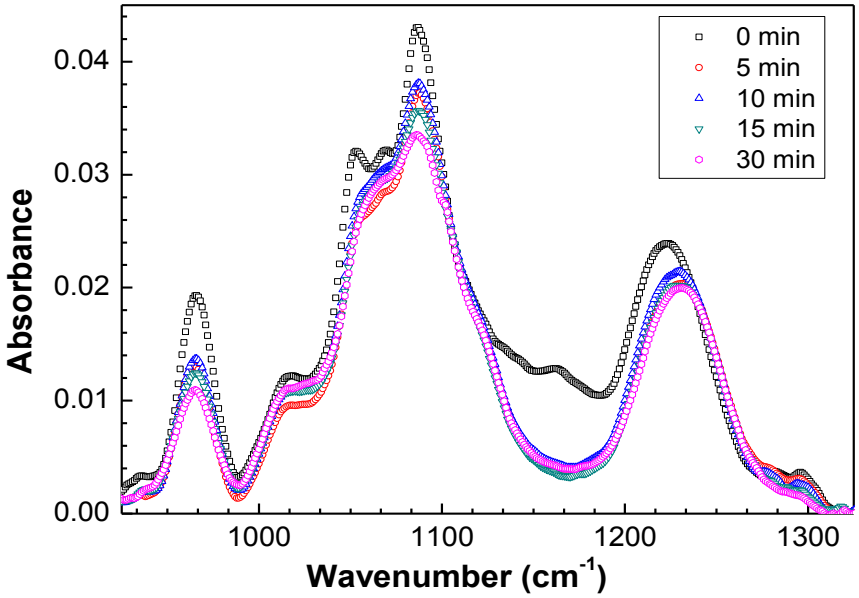

Figure 4.9.3. Infrared absorbance spectra of a DNA cast sample irradiated with 254 nm UV light for different periods of time.

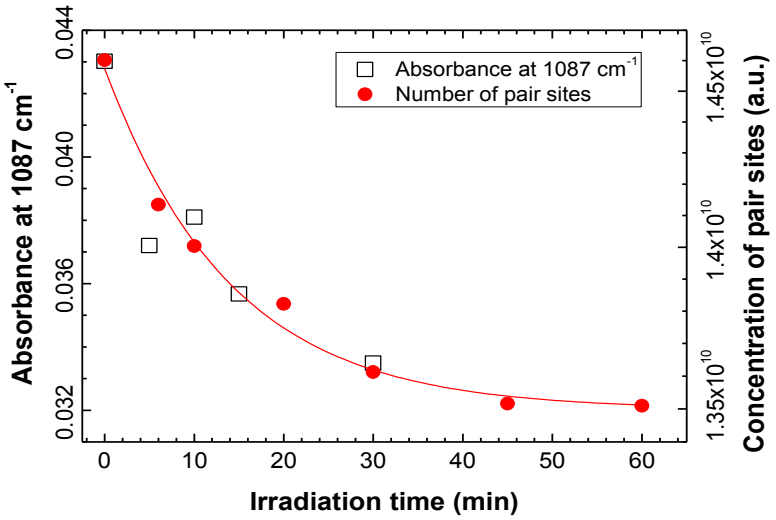

Figure 4.9.4. Absorbance at 1088 cm^{-1} associated with symmetric PO^{2-} stretching of backbone vibrations and concentration of pair sites calculated by equation 4.9.2 as a function of irradiation time.

By analyzing the behaviour of the infrared peaks, a decrease in magnitude with irradiation time can be observed at different rates for each peak, indicating that the damage kinetics is dependent of each DNA group. With respect to symmetric PO_2^- stretching of backbone (1087 cm^{-1}) vibrations, the number of vibrations is seen to decrease similarly to the decrease of conduction pair sites concentration as calculated from CBH model, equation 4.9.2. This behaviour can be seen in graph of figure 4.9.4 where both, absorbance at 1088 cm^{-1} associated with symmetric PO_2^- stretching of backbone vibrations and pair sites concentration calculated from equation 4.9.2 where plotted as a function of irradiation time. This allows conclude that at high frequencies the conductivity behaviour follows the DNA damage with respect to phosphate groups.

CONCLUSION

In summary, DNA conductivity depreciation due to UV radiation exposure is associated with the decrease of the number of phosphate groups, which work as electron acceptors in the DNA conduction process, caused by electron hopping between base-pairs and phosphate groups. This conclusion was supported by the calculated hooping distance using the CBH model and by the similar decrease of both phosphate groups and CBH model hooping pair sites number with the irradiation time. Results obtained here also show that the electrical conductivity can be used to monitor DNA damage.

ACKNOWLEDGEMENTS

This work was supported by the "Plurianual" financial contribution of "Fundação para a Ciência e Tecnologia" (Portugal). PG acknowledges the fellowship SFRH/BD/35954/2007.

5. FINAL REMARKS

5.1. CONCLUSIONS

This work contributes for the knowledge about radiation damage on relevant biomolecules such as DNA and phospholipids when placed in an environment closer to that of a cell, through the development of biomimetic heterostructures that can be changed in composition into some extent. The conclusions of scientific work carried out can be summarized as follows:

- Biomimetic heterostructures can be achieved via cast, layer-by-layer (LbL) and Langmuir techniques. These heterostructures can contain bound water molecules near to the adsorbed macromolecules giving rise to the presence of water molecules in the final layered molecular structure, which is fundamental for keeping the biological molecules environment. In addition, the presence of water molecules in the heterostructures depends of the type of adsorbed species and the ionic strength of the solutions used to prepare the adsorbed layers. This is particularly relevant in what concerns radiation damage studies on DNA containing biomimetic molecular heterostructures where different salt solution contents are leading to different damage levels.

- Synchrotron radiation is an important resource for research of the damage on biological relevant molecules. Obtained data proves that the UV radiation induces changes on covalent bonds of DNA and DPPG molecules and that VUV spectroscopy can be used to detect the induced changes and therefore some extent localize the damage. The VUV spectroscopy can also be used to monitor adsorption amount during the formation of LbL films.

- Radiation at 140 nm (8.85 eV) was shown to induce damage in calf thymus DNA molecules. Band deconvolution in the VUV spectra allowed concluding that the contribution of transitions, associated to open sugar chain, tend to increase in magnitude during irradiation. At the same time, a decrease in the peaks magnitudes associated with the DNA bases has been observed. Although such effects could be inferred from measured VUV spectra, this technique is not sensitive enough to characterize DNA damage at a molecular level. Infrared spectra of the samples allowed us to assign observed infrared absorbance peaks to particular DNA molecular vibrations. Analysis of changes in the infrared spectra after irradiation generally, revealed a decrease in the C-O stretch of the furanose in backbone, in the PO_2^- groups, in the thymines, cytosines and adenines groups. These changes occur at different rates indicating that several damage processes are taking place. A decrease in C2=O2 stretching of thymines involved in reverse Hoogsteen third strand binding has also been observed, while the C2=O2 stretching vibration of thymine in single or double-stranded remain unchanged. An increase in the anti-symmetric PO_2^- stretch in B form was also observed which has been related to an increase in the number of C-O bonds.

- UV radiation in the energy range of 3.5 to 8 eV was shown to cause damage to several DNA components as revealed by XPS spectra analysis of DNA cast films. Results revealed that all the elements decreased relatively to sodium which indicates dissociative damage of DNA yielding gaseous products. Two main energy intervals were associated to this kind of damage.

In addition analysis of each element fractions with irradiation energy also indicated functional group transformations. Carbon fractions revealed that the N-C=O, N-C=N, $C(N)_3$ N-C-O (C3) groups were not affected by the radiation, while: the C-C or C-H (C1) fraction increased and the C-N, C=N, C-O (C2) and N-(C=O)-N (C4) ratios decreased, when the samples have been irradiated at higher energies. The decrease of C-O and N-(C=O)-N ratios indicate the opening of sugar rings and the breaking of pyrimidines, respectively. The rupture of sugar rings was confirmed by the O-C (O3) fraction decrease. This range of energies was also lead to loss of DNA, PO_4^- groups which as pointed by the decrease of all the ratios [P]/[X], X being any other element: Na, C, O and N. The analysis of N sp^2 and N sp^3 atomic percentages allowed to conclude that at 6.1 eV irradiating energy, a decrease (~17%) in the fraction of N sp^2 groups. This energy value is close of the VUV peak associated to π-π* transitions of guanine and adenine, suggesting that these bases can be affected of the decrease of N-(C=O)-N groups shows that also the pyrimidines (thymines and/or cytosines) degradation occurs. Analysis of the XPS data, associated to phosphate groups, points out that energies below 3.5 eV are sufficient to break DNA phosphate groups this result is consistent with three different conductivities values found in literature for DNA films. Finally, the [P]/[Na] ratio changed from ~1.4 to ~0.8 when radiation energy increases, reveals that the radiation energy mainly removes the protonated phosphate groups and not the ionized ones. This allows to conclude that ionized phosphate groups, surrounded by the sodium counterions, congregate hydration water molecules which play an important role as UV radiation protection of them.

- The damage of DNA films as a result of irradiation with C^{3+} ions reveals the rupture of C-O-C deoxyribose bonds and consequent creation of C=O bonds, fragmentation of PO_4^{2-} groups and the decrease in the number of thymine, cytosine, adenine and guanine groups. Damage on DNA bases leads to the formation of oxime products, which in turn react with DNA deoxyribose products forming furfural groups. Loss of structural water and DNA conformational changes were also observed.

- From the VUV spectra of DPPG in aqueous solutions, and in cast and LbL films, we could assign the electronic transitions responsible for the light absorption and determine the amount of DPPG adsorbed on LbL films with PAH. Significantly, the adsorbed amounts pointed to adsorption as a lipidic bilayer, which means that the DPPG liposomes were ruptured during the adsorption process. The final structure of the LbL films was reflected on the film topography investigated with AFM, for the images showed terraces with thicknesses again corresponding to lipid bilayers. The LbL films were not affected by prolonged UV irradiation in the absence of water molecules indicating that the VUV technique can be used for characterization of lipid heterostructures. We therefore propose VUV spectroscopy as a new powerful tool for LbL film characterization which we hope will be useful in, among others, cell membrane modelling and drug delivery studies based on phospholipids.

- In concern of Langmuir films studies, the presence of DNA in the subphase does not affect the cationic EDPPC monolayer at low surface pressures. Nevertheless, at condensed phase the DNA presence increases the value of the pressure collapse indicating that the EDPPC

monolayer is stabilized by DNA. In the case of DPPG monolayer, the presence of DNA leads to expansion of the monolayer at low pressures indicating that DNA penetrates in the expanded regime of DPPG monolayer, being excluded from the condensed regime probably due to repulsive electrostatic interactions. UV irradiation of DPPG molecules in cast films obtained from emulsions induced cleavage of C-O, C=O and $–PO^{2-}$ bonds, in contrast to the lack of effects for DPPG under vacuum. Hence, the presence of water seems crucial for degradation, and this was confirmed in DPPG monolayers at the air/water interface, whose stability decreased when irradiated with UV. Significantly, the effects from UV irradiation were mitigated if DNA molecules were incorporated into the subphase. DNA caused the DPPG monolayer to expand at low pressures, with molecules penetrating into the monolayer. In condensed monolayers, however, the DNA molecules were excluded probably due to repulsive electrostatic interactions. Nevertheless, even at high surface pressures corresponding to a real membrane, the DNA molecules decreased monolayer instability caused by irradiation. This was attributed to the formation of ionic products from degradation of either DPPG or DNA, which would stabilize both the intact DPPG molecules and the DPPG products resulting from UV irradiation. Such mechanism could explain why cells not collapse immediately after irradiation. The stability of the cell is maintained during a determined time period until the damaged elements by UV to be repaired.

- Finally, DNA conductivity depreciation due to UV radiation exposure is associated with the decrease of the number of phosphate groups, which work as electron acceptors in the DNA conduction process, caused by electron hopping between base-pairs and phosphate groups. This conclusion was supported by the calculated hooping distance using the CBH model and by the similar decrease of both phosphate groups and concentration of pair sites with the irradiation time. These results also allow conclude that the electrical conductivity can be used to monitor DNA damage.

5.2. FUTURE WORK

The results and conclusions coming out from this work, allowed a significant advance in understanding the damage in biological materials caused either by photons or ions. The application of a diverse set of techniques, namely the LBL technique, addressed for the preparation of biomimetic heterogenic samples, together with the use of well known characterization techniques, succeed in obtaining information on damage caused by radiation in these biomimetic structures. Given the wide variety of existing materials in biological systems, and the features of the LBL technique, more realistic models are worth to be attempted. The buildup of more complex molecular structures designs require study of adsorption kinetics of the molecules to be include in the molecular structure. In addition, the conditions controlling the amount of water in the final structure is also a relevant issue to be addressed. The use of models with different combinations of biomolecules may allow understanding the molecular damage mechanisms causing some genetic lesions. This knowledge will allow a development in other areas, particularly in anti-cancer therapy and in its prevention. Taking into account the probes that nowadays are being attempted towards a more efficient radiotherapy techniques and procedures other radiations sources, namely electrons, positrons, protons and ions will be worth to use with these biomimetic structures. For this purpose it is also relevant to evaluate the doses necessary to damage a given biomolecule within a structure.

Finally, attentive to the fact that most of the constituent materials of biological medium are composed of long chains where the electron transfer play an important role in electrical conductivity, the mechanisms driving the electrical current in thin films are worth to be further investigated toward the development of radiation biosensors.

5.3. PUBLICATIONS AND COMMUNICATIONS RELATED TO PHD WORKS

5.3.1. PAPERS IN INTERNATIONAL JOURNALS

1. "Radiation damage on Langmuir monolayers of the anionic 1,2-distearoyl-sn-glycero-3-phospho-(1'-rac-glycerol) (DPPG) phospholipid at the air-DNA solution interface", P.J. Gomes, A.M.P. S. Gonçalves da Silva, P.A. Ribeiro, O. N. Oliveira Jr., M. Raposo, *To be submitted.*

2. "Interaction of DNA with Langmuir monolayers of opposite charged phospholipids", P.J. Gomes, A.M.P. S. Gonçalves da Silva, P.A. Ribeiro, O. N. Oliveira Jr., M. Raposo, *To be submitted.*

3. "XPS Analysis of damage caused by UV radiation on DNA: energy thresholds for breaking different DNA groups", P.J. Gomes, A.M. Ferraria, A.M. Botelho do Rego, S.V. Hoffmann, P. A. Ribeiro, M. Raposo, *To be submitted.*

4. "DNA damage induced by carbons (C^{3+}) beam accessed by independent component analysis of infrared spectra", M. Raposo, M. Coelho, P.J. Gomes, P. Vieira, P. A. Ribeiro, N. J. Mason, C.A. Hunniford, R. W. Mc Cullough***,*** International Journal of Radiation Biology, 90(5), 344-350, 2014

5. "Characterization of PAH/DPPG Layer-by-layer films by VUV spectroscopy", A.A. Duarte, P.J. Gomes, J.H.F. Ribeiro, P.A. Ribeiro, S.V. Hoffmann, N. J. Mason, O. N. Oliveira Jr., M. Raposo, The European Physical Journal E – Soft Matter, 36(9), 1-8, 2013

6. "Probing radiation damage by alternated current conductivity as a method to characterize electron hopping conduction in DNA molecules", P.J. Gomes, M. Coelho, M. Dionisio, P.A. Ribeiro e M. Raposo, Applied Physics Letters, 101(12), 123702, 2012

7. "Polymeric scaffolds for enhanced stability of melanin incorporated in liposomes", M.L. Moraes, P.J. Gomes, P.A. Ribeiro, P. Vieira, A.A. Freitas, R. Koehler, O.N. Oliveira Jr. and M. Raposo, Journal of Colloid And Interface Science, 350, 268-274, 2010

8. "UV degradation of deoxyribonucleic acid", P.J. Gomes, P.A. Ribeiro, D. Shaw, N.J. Mason and M. Raposo, Polymer Degradation and Stability, 94, 2134-2141, 2009

9. "Photoabsorption of biomolecules and radiation damage –studies in adenine films", P. Limão-Vieira, A.M. Costa, S. Oliveira, P.J. Gomes, P.A. Ribeiro, M. Raposo; J. Phys. Conf. Series, 88(012004), 1-7, 2007

5.3.2. PROCEEDINGS IN INTERNATIONAL CONFERENCES

1. "Biomimetic Heterostructures for Radiation Damage Studies", M. Raposo, P.J. Gomes, J.M.C. Lourenço, M.Coelho, S.V. Hoffmann, A.M. Botelho do Rego, R. W. McCullough, N. J. Mason, C. Lage, P. Limão-Vieira and P. A. Ribeiro, Proceedings of the Radiation Damage in Biomolecular Systems - RADAM´08, Debrecen, Hungry, 13th – 15th June 2008

2. "Biomolecular chemistry with synchrotron radiation", P.J. Gomes, Q. Ferreira, J.M.C. Lourenço, P.A. Ribeiro, M. Raposo and P. Limão-Vieira, 5th Iberian Vacuum Meeting, Guimarães, Portugal, 18th – 21th September, 2005

5.3.3. INVITED ORAL COMMUNICATIONS

1. "Impedance Spectroscopy - A Tool for DNA Irradiation Studies", Electron Controlled Chemical Lithography - 2nd Meeting of COST Action CM0601, Istanbul, Turkey, 7th June 2009

2. "Efeito da Radiação UV em Membranas Biomiméticas", Departamento de Física, Universidade Nova de Lisboa, Caparica, Portugal, 26th May 2008

3. "Efeito da Radiação em Membranas Biomiméticas", Instituto de Física de São Carlos, Universidade de São Paulo, São Carlos, Brasil, 28th August 2007

4. "Biomimética de Membranas", Universidade Federal do Rio de Janeiro, Rio de Janeiro, Brasil, 9th August 2007

5.3.4. ORAL COMMUNICATIONS

1. "VUV Radiation Effect on DNA", P.J. Gomes and M. Raposo, XX International Summer School on Physics and Chemistry of Condensed Matter, 4th – 11th July 2009, Bialowieza, Poland

2. "Biomimetic of membranes – a new approach to address radiation damage", P.J. Gomes, M. Coelho, C. Lage, S.V. Hoffman, P.A. Ribeiro and M. Raposo, Advanced Nano Materials (ANM), 22nd – 25th June 2008, Aveiro, Portugal

3. "Study of the effect of Ultra-violet radiation on DNA layer-by-layer films", P.J. Gomes, P.A. Ribeiro, P. Limão-Vieira, N.J. Mason, M. Raposo, 12th International Conference on Organized Molecular Films (LB-12), 1st – 5th July 2007, Kraków, Poland

5.3.5. POSTER COMMUNICATIONS

1. "Ionic Phospholipids in Langmuir Monolayers to DNA irradiation studies", P.J. Gomes, A.M.P.S. Gonçalves da Silva, R.S. Romão and M. Raposo, Electron Controlled Chemical Lithography - 2nd Meeting of COST Action CM0601, Istanbul, Turkey, 4th - 7th June 2009

2. "Characterization of DNA Intercalation with 2,2'-Bipyridyl on Solid Surfaces", M. Coelho, L. Martins, P.J. Gomes, P.A. Ribeiro, P. Tavares and M. Raposo, Electron Controlled Chemical Lithography - 2nd Meeting of COST Action CM0601, Istanbul, Turkey, 4th - 7th June 2009

3. "Interactions of DNA with Ionic Phospholipids in Langmuir Monolayers at the Air Water Interface", P.J. Gomes, A.M.P.S. Gonçalves da Silva, R.S. Romão and M. Raposo, XX International Summer School on Physics and Chemistry of Condensed Matter, Bialowieza, Poland 4th – 11th July, 2009

4. "Electrical Characterization of UV damage on Deoxyribonucleic Acid Cast Films", P.J. Gomes, M. Dionísio, P.A. Ribeiro and M. Raposo, International conference on Science and Technology of Synthetic Metal, (ICSM 2008), 6th – 11th July 2008, Porto Galinhas – Pernambuco, Brazil

5. "Polymeric Scaffolds for Enhanced Stability of Melanin Incorporated into Lipossomes", M.L. Moraes, P.J. Gomes, P.A. Ribeiro, A.L. Maçanita, D. Gonçalves, R. Köhler, O.N. Oliveira Jr. and M. Raposo, International conference on Science and Technology of Synthetic Metal, (ICSM 2008), 6th – 11th July 2008, Porto Galinhas – Pernambuco, Brazil

6. "Electrical Properties of Poly(o-methoxyaniline) layer-by-layer films – influence of counterions", M.Raposo, J.M.C. Lourenço, P.J. Gomes, A.M. Botelho do Rego, M. Dionísio, P.A. Ribeiro, International conference on Science and Technology of Synthetic Metal, (ICSM 2008), 6th – 11th July 2008, Porto Galinhas – Pernambuco, Brazil

7. "Biosensor array for detecting Agriculture Contaminants", P.J. Gomes, R. Ramos, C. Ribeiro, D. Gonçalves, A. Marletta, P.A. Ribeiro and M. Raposo, Advanced Nano Materials (ANM), 22nd – 25th June 2008, Aveiro, Portugal

8. "Chemical Changes on DNA films induced by UV Radiation", P.J. Gomes, P.A.Ribeiro, N.J.Mason and M. Raposo, Radiation Damage in Biomolecular Systems - RADAM´08, 13th – 15th June 2008, Debrecen, Hungry

9. "Carbon Ions Interaction with PAH and DNA Cast Films", P.J. Gomes, B.W. McCullough, P.A.Ribeiro, N.J.Mason and M. Raposo, Electron Controlled Chemical Lithography (ECCL), 13th – 15th March 2008, Lisbon, Portugal

10. "Study of Radiation Effect on DNA LBL Films", P.J. Gomes, S.V. Hoffmann, P.A. Ribeiro and M. Raposo, Electron Controlled Chemical Lithography (ECCL) , 13th – 15th March 2008, Lisbon, Portugal

11. "X-rays Effect on Biomimetic Membranes Studied by Neutron Reflectivity", P.J. Gomes, M.L. Moraes, R. Köhler, P.A. Ribeiro and M. Raposo, Electron Controlled Chemical Lithography (ECCL), 13th – 15th March 2008, Lisbon, Portugal

12. "Effect of UV Radiation on Langmuir Films", P.J. Gomes, F. Pavinatto, P.A. Ribeiro, O.N. Oliveira Jr. and M. Raposo, Electron Controlled Chemical Lithography (ECCL), 13th – 15th March 2008, Lisbon, Portugal

13. "XPS Study on the Influence of Ultra-Violet Radiation Energy on DNA Cast Films", P.J. Gomes, A.M.B. Rego, S.V. Hoffmann, P.A. Ribeiro and M. Raposo, Electron Controlled Chemical Lithography (ECCL) , 13th – 15th March 2008, Lisbon, Portugal

14. "Irradiation of Lipids Solutions with VUV Radiation", M. Raposo, N. C. Jones, P.A. Ribeiro and P.J. Gomes, Electron Controlled Chemical Lithography (ECCL) , 13th – 15th March 2008, Lisbon, Portugal

15. "The Role of Water on UV Radiation Damage in Biomimetic Membranes", P.A. Ribeiro, P.J. Gomes, N.J. Mason and M. Raposo, Electron Controlled Chemical Lithography (ECCL) , 13th – 15th March 2008, Lisbon, Portugal

16. "Radiation Effect at Solid-Liquid Interface", N. C Jones, P.J. Gomes, J.P. Afonso, P.A. Ribeiro and M. Raposo, Electron Controlled Chemical Lithography (ECCL) , 13th – 15th March 2008, Lisbon, Portugal

17. "Development of Biomimetic Membranes to study the effect of DNA targets to create intelligent lesions during cancer therapies", M. Coelho, P.J. Gomes, C. Lage, P.A. Ribeiro P. Limão-Vieira and M. Raposo, Electron Controlled Chemical Lithography (ECCL) , 13th – 15th March 2008, Lisbon, Portugal

18. "Influence of counterions in presence water molecules in layer-by-layer films", J.M.C. Lourenço, P.J. Gomes, Q.Ferreira, A. M. Botelho do Rego, P.A. Ribeiro and M. Raposo, Electron Controlled Chemical Lithography (ECCL) , 13th – 15th March 2008, Lisbon, Portugal

19. "Effect of Ultra-violet Radiation onto Lipid Membranes", P.J. Gomes, P.A. Ribeiro, T.P. Nixon, N. St.J Braithwaite, N.J .Mason and M. Raposo, 8º Encontro Nacional de Química Física, 21st – 22nd June 2007, Luso, Portugal

20. "Effect of Electron Beam Irradiation in Thin Films of DNA and DNA Nucleic Bases", P.J. Gomes, A.Stypczynska, P.A. Ribeiro, T.P. Nixon, N. St.J. Braithwaite, N.J. Mason, M. Raposo, Radiation Damage in Biomolecular Systems - RADAM´07, 19th - 22nd June 2007, Dublin, Ireland

21. "Effect of Ultra-violet radiation in lipid layer-by-layer films", P.J. Gomes, P. A. Ribeiro, N.J. Mason, M. Raposo, Radiation Damage in Biomolecular Systems - RADAM´07, 19th - 22nd June 2007, Dublin, Ireland

22. "VUV irradiation of DNA films", P.A. Ribeiro, P.J. Gomes, P. Limao-Vieira, N.J. Mason, M. Raposo, Radiation Damage in Biomolecular Systems - RADAM´07, 19th - 22nd June 2007, Dublin, Ireland

23. "Biomimetic of Membranes", M. Raposo, P.J. Gomes, Q. Ferreira, J.M.C. Lourenço, P.A. Ribeiro, Radiation Damage in Biomolecular Systems - RADAM´07, 19th - 22nd June 2007, Dublin, Ireland

24. "Ultra-Violet irradiation of DNA containing LBL films", P.A. Ribeiro, P.J. Gomes, Ana M. Costa, Susana M. Oliveira, P. Limao-Vieira, M. Raposo, N.J. Mason, Symposium on Radiation Effects of Biomedical Interest, 22nd – 25th February 2007, Madrid, Spain

25. "Lipid bio-mimetic membranes for radiation studies", M. Raposo, P.J. Gomes, M.Y. Teruya, M.L. Moraes, P.A. Ribeiro, N.J. Mason, Symposium on Radiation Effects of Biomedical Interest, 22nd – 25th February 2007, Madrid, Spain

26. "Biomolecular Membrane Mimicking VUV Spectroscopy by High Resolution Synchrotron Radiation", P.J. Gomes, P.A. Ribeiro, M. Raposo, N.J. Mason, S.V. Hoffmann, P. Limão-Vieira, Biology and Medicine with Low Energy Synchrotron Radiation/ISA Users meeting 2006, Aarhus (Denmark), November 1-3, 2006

27. "Biomolecular Chemistry with Synchrotron Radiation", P.J.Gomes, Q. Ferreira, J.M.C. Lourenço, P.A.Ribeiro, M.Raposo e P.Limão-Vieira, RIVA 5 - 5th Iberian Vacuum Meeting , Guimarães (Portugal), September 18-21, 2005

6. BIBLIOGRAPHY

(1) M. Benderitter, L.Vincent-Genod, J.P. Pouget, P. Voisin, *Radiation Research*, 159, 471, (2003).

(2) V. Cobut, Y. Frongillo, J.P. Patau, T. Goulet, M.J. Fraser, J.P. Jay-Gerin, *Radiation Physics and Chemistry*, 51, 229 (1998).

(3) M.A. Huels, B. Boudaiffa, P. Cloutier, D. Hunting, L. Sanche, *Journal of the American Chemical Society*, 125, 4467-4477 (2003).

(4) B. Boudaiffa, P. Cloutier, D. Hunting, M.A. Huels, L. Sanche, *Science*, 287, 1658 (2000).

(5) M. Folkard, K.M. Prise, B. Brocklehurst, B.D. Michael, *Journal of Physics B: Atomic, Molecular and Optical Physics*, 32, 2753 (1999).

(6) M. Folkard, K.M. Prise, *Acta Physica Polonica A*, 109(3), 265 (2006).

(7) M. A. Huels, B. Boudaiffa, P. Cloutier, D. Hunting and L. Sanche, *Journal of the American Chemical Society*, 125, 4467 (2003).

(8) S. Ptasinska, S. Denifl, P. Scheier, E. Illenberger, T. D. Märk, *Angewandte Chemie International Edition* , 42, 6941 (2005); S. Ptasinska, S. Denifl, V. Grill, T. D. Märk, E. Illenberger, P. Scheier, *Physical Review Letters*, 95, 093201 (2005) and references therein.

(9) J.M.C. Lourenço, P. A. Ribeiro, A. M. Botelho do Rego, F. M. Braz Fernandes, A.M.C. Moutinho, M. Raposo, *Langmuir*, 20, 8103-8109 (2004).

(10) J.M.C. Lourenço, P. A. Ribeiro, A. M. Botelho do Rego and M. Raposo, *Journal of Colloid and Interface Science*, 313, 26-33 (2007).

(11) T. Ishii, *Thin Solid Films*, 47, 178 (1989).

(12) P.J. Gomes, P.A. Ribeiro, D. Shaw, N.J. Mason, M. Raposo, *Polymer Degradation and Stability*, 94, 2134-2141 (2009).

(13) R. Hook, “Micrography”, Royal Society, London, 1665 – Online on: http://www.roberthooke.org.uk/micro1.htm

(14) T. Schwann, M.J. Schleyden “Microscopical researches into the accordance in the structure and growth of animals and plants”, Sydenham Society, London, 1847 – Online on: http://vlp.mpiwg-berlin.mpg.de/library/data/lit28715/index_html?pn=1&ws=1.5

(15) A.M. Hopkins, J. Johnson, S. LaHart, D.Q. Warner, M. Wright, D. Jill, *Cells Building Blocks of Life*, New Jersey: Prentice Hall (1997).

(16) D. Voet, J.G. Voet, C.W. Pratt, *Fundamental of Biochemistry*, John Wiley & Sons, New York (1999)

(17) D.L. Nelson, M.M. Cox, *Lehninger Principles of Biochemistry – 4th Edition*, W.H. Freeman and Company, New York (2005)

(18) J.H. Weil, *Bioquímica Geral – 2ª Edição*, Fundação Calouste Gulbenkian, Lisboa (2000)

(19) http://www.pearsoned.com/

(20) S.J. Singer, G.L. Nicolson, *Science*, 175, 720 (1972).

(21) http://www.homodiscens.com/home/ways/models/index.htm

(22) http://www.wikipedia.org/

(23) P.A. Levene, *Journal of Biological Chemistry*, 40, 415 (1919).

(24) J.R. Dahm, *Developmental Biology*, 278, 274 (2005).

(25) J.D. Watson,F.H.C. Crick, *Nature*, 171, 737 (1953).

(26) M.H.F. Wilkins, A.R. Stokes, H.R. Wilson, *Nature*, 171, 738 (1953).

(27) R.E. Franklin, R.G. Gosling, *Nature*, 172, 156 (1953).

(28) G. Hayashi, M. Hagihara, K. Nakatani, *Nucleic Acids Symposium Series,* 49, 261 (2005).

(29) M. Wahl, M. Sundaralingam, *Biopolymers*, 44, 45 (1997).

(30) X.J. Lu, Z. Shakked, W.K. Olson, *Journal of Molecular Biology*, 30, 819 (2000).

(31) S. Rothenburg, F. Koch-Nolte, F. Haag, *Immunological Reviews*, 184, 286-298 (2001).

(32) *DNA Replication-Current Advances*, edited by Herve Seligmann, InTech (2011).

(33) https://c1.staticflickr.com/7/6142/5940581568_1db150f055_z.jpg

(34) E.D. Podgorsak, *Radiation Physics for Medical Physicist*, Springer, Heidelberg (2006).

(35) J.H. Bernhardt, *Physics on Medicine and Biology*, 37, 807 (1992).

(36) J.D. Bronzino, *The biomedical engineering handbook*, CRC Press & IEEE Press (1995).

(37) J.E. Moulder, Power Lines, Cancer FAQ's, in *Electromagnetic Fields and Human Health*, Medical College of Wisconsin (2005).

(38) C. von Sonntag, *Free-Radical-Induced DNA Damage and Its Repair - A Chemical Perspective*, Springer, Heidelberg (2006).

(39) C. Kielbassa, I. Roza, B. Epe, *Carcinogenesis*, 18, 811 (1997).

(40) J.L. Ravanat, T. Douki, J. Cadet, *Journal of Photochemical and Photobiology B: Biology*, 63, 88 (2001).

(41) D.K. La, J.A. Swenberg, *Mutation Research/Reviews in Genetic Toxicology*, 365(1-3), 129-146 (1996).

(42) *Biomimicry: Innovation Inspired by Nature*, edited by Janine M. Benyus, William Morrow & Co. (1997).

(43) V. Podborschi, M. Vaculenco, V. Ajder, Technical University of Moldova, *Chişinău, Seminarul National de Organe de Maşini*, Braşov, (2005)

(44) F. Lodato, *Design Management Review,* 16, 56-61 (2005).

(45) P. Reed, *The Technology Teacher*, 23-27 (2004).

(46) *Bionics vs. biomimicry: from control of nature to sustainable participation in nature. in: Brebbia C.A., Design and Nature III: Comparing Design in Nature with Science and Engineering*, Edited by Whal, D., Wessex Institute of Technology, UK, p.289-298 (2006).

(47) Hsiao, Chou, *Using biomimetic design in a product design course*, World Transactions on Engineering and Technology Education, vol.6(1) (2007).

(48) M. Dickinson, *Bionics: Biological insight into mechanical design*, Department of Organismal Biology, University of California; Berkeley, 96(25), 14208-14209 (1999).

(49) A.J. Hulbert, P.L. Else, *J. Theor. Biol.*, 199, 257-274 (1999).

(50) G. Brezesinski, H. Möhwald, *Surfaces Advanced Colloid Interface Science*, 100-102, 563-584 (2003).

(51) Y.H. Chan, S.G. Boxer, *Current Opinion in Chemical Biology*, 11(6), 581-587 (2007).

(52) A.D. Bangham, M.M. Standish, J.C. Watkins, *Journal Molecular Biology*, 13(1), 238-52 (1965).

(53) P. Vladimir, *Nature Reviews Drug Discovery*, 4, 145-160 (2005).

(54) M.I Fisher, T. Tjärnhage, *Biosensensors and Bioelectronic*, 15, 463-471 (2000).

(55) L. Wang, M. Schönhoff, H. Möhwald, *Journal of Physical Chemistry B*, 106(35), 9135-9142 (2002).

(56) D. Grieshaber, R. Mackenzie, J. Vörös, E. Reimhult, *Sensors*, 8, 1400-1458 (2008).

(57) K. Ariaga, T. Nakanishi, T. Michinobu, Journal of Nanoscience and Nanotechnology, 6(8), 2278-301 (2006).

(58) J.F. Rusling, E.G. Hvastkovs, D.O Hull, J.B. Schenkman, *Chemical Communications*, 14(2), 141-54 (2008).

(59) Z. Tang, Y. Wang, P. Podsiadlo, N.A. Kotov, *Advanced Materials*, 18(24), 3203–3224 (2006).

(60) J. Wang, *Electroanalysis*, 13(12), 983–988 (2001).

(61) X. Fan, I.M. White, S.I. Shopova, H. Zhu, J.D. Suter, Y. Sun, *Analytica Chimica Acta*, 620(1-2), 8-26 (2008).

(62) S. Tombelli, M. Minunni, M. Mascini*, Methods*, 37(1), 48-56 (2005).

(63) A.A. Karyakin, E.E. Karyakina, L. Gorton, *Talanta*, 43, 1597–1606 (1996).

(64) V. Zucolotto, K.R. Daghastanli, C.O. Hayasaka, A. Riul Jr., P. Ciancaglini, O.N. Oliveira Jr., Analytical Chemistry, 79(5), 2163-2167 (2007).

(65) D.M. Taylor, A.G. Macdonald, *Journal of Physics D: Applied Physics*, 20,1277-1283 (1987).

(66) A. Riul Jr., L.H.C. Mattoso, F.J. Fonseca, D.M. Taylor, S.V. Mello, E.C. Venancio, *"Sensor à base de plásticos condutores e lipídios para avaliação de paladar de bebidas (Língua Eletrônica)"*. BR n. PI 0103502-9 (2001).

(67) G. Decher, J.D. Hong, J. Schmitt, *Thin Solid Films*, 210/211, 831 (1992).

(68) Y. Lvov, H. Haas, G. Decher, H. Möhwald, *Journal Physical Chemistry*, 97, 12835 (1993).

(69) Y. Lvov, H. Haas, G. Decher, H. Möhwald, *Langmuir*, 9, 481 (1993).

(70) M. Raposo, O. N. Oliveira Jr., *Brazilian Journal of Physics*, 28(4), 2 (1998).

(71) G.L.J. Gaines, *Insoluble Monolayers at Liquid-Gas Interfaces*, Wiley-Interscience: New York (1996).

(72) I. Langmuir, *Journal of the American Chemical Society*, 39, 1848 (1917).

(73) K. Blodgett, *Physical Reviews*, 51, 964 (1937).

(74) http://www.lighting.philips.com/gl_en/index.php?main=global&parent=global&id

(75) http://prolight.info/pdf_specs/Philips_UV_tech_brochure.pdf

(76) Inc., Canadian Light Source. Synchrotron Facts. Canadian Light Source. (Online) Canadian Light Source Inc. (Cited: May 01, 2007.) http://www.cls.usask.ca/education/whatis.php

(77) M. Schwell, H.-W. Jochims, H. Baumgärtel, F. Dulieu, S. Leach, *Planetary and Space Science*, 54(11), 1073-1085 (2006).

(78) M. Altarelli, A. Salam, *Europhysics News*, 35 (2004).

(79) Lab., SRS Daresbury. World-class Synchrotron Radiation Science and Discovery. SRS Daresbury Laboratory. (Online) SRS Daresbury Laboratory. http://www.srs.ac.uk/srs/.

(80) A.M.F. Costa, Master Thesis, New University of Lisbon, Portugal (2007).

(81) http://www.isa.au.dk/facilities/astrid/astrid-technical.html

(82) J.M.C. Lourenço, PhD Thesis, New University of Lisbon, Portugal (2009).

(81) C.A. Hunniford, PhD Thesis, Queen's University of Belfast, United Kingdom (2006).

(84) R. Geller, Electron Cyclotron Resonance Ion Sources and ECR Plasmas, IOP publishing (1996).

(85) W. Butter, *Ultra-Violet and Visible Spectroscopy*, Butterworth & Co, p.1-20 (1975).

(86) Michael K. Denk, CHEM 2070. CHEM 2070. (Online) UV-Vis & PES, 2005. (Cited: May 16, 2007.) http://131.104.156.23/Lectures/CHEM_207/uv-vis.htm.

(87) G. Solomons, C. Fryhle, *Organic Chemistry*, John Wiley & Sons, p.64-66 (2004).

(88) D.A. Skoog, F.J. Holler, T.A. Nieman, *Principles of Instrumental Analysis*, 5th Edition, Thomson Learning, London (1998).

(89) http://en.wikipedia.org/wiki/X-ray_photoelectron_spectroscopy

(90) G. Binning, C. Quate, C.H. Gerber, E. Weibel*, Physical Review Letters*, 56, 930 (1986).

(91) N.C. de Souza, J.R. Silva, M.A.P. da Silva, M. Raposo, R.M. Faria, J.A. Giacometti, O.N. Oliveira Jr., *Journal of Nanoscience and nanotechnology*, 4(5), 548 – 552 (2004).

(92) M.A.P. da Silva, D.T. Balogh, C. Eiras,; M.U. Kleinke, R.M. Faria, *Molecular Crystals and Liquid Crystals Science* , 374, 191 - 200 (2002).

(93) M. Palumbo, C. Pearson, M.C. Petty, *Thin Solid Films*, 483, 114-121 (2005).

(94) M. Raposo, P.A. Ribeiro, M.A. Pereira-da-Silva, M.Raposo, O.N.Oliveira Jr., *Current Issues on Multidiscipplinary Microsocpy Research and Education*, Edited by A. Méndez-Vilas, L.Labajos-Broncano, Formatex Microsocpy Book Séries, vol.2, p.224 (2004).

(95) G. Binning, H. Rohrer, C.H. Gerber, E. Weibel, *Physical Review Letters*, 49, 57 (1982).

(96) G. Binning, D.P.E. Smith, *Review of Scientific Instruments*, 57(8), 1688 (1986).

(97) http://blog.brukerafmprobes.com/guide-to-spm-and-afm-modes/contact-mode-afm/

(98) L. Wilhelmy, Annals of Physics, 119, 177 (1863).

(99) M.W. Kim, D.S. Cannell, Physical Review A, 13, 411 (1987).

(100) N.R. Pallas, B.A. Pethica, *Journal of the Chemical Society, Faraday Transactions I*, 83, 585 (1987).

(101) H. Kuhn, D. Möbius, H. Bücher, *Physical Methods of Chemistry*, John Wiley & Son: New York (1972).

(102) D.A. Cadenhead, F. Müller-Landau, B.M. Kellner, *Ordering in two dimensions*, Elsevier North Holland Publication (1980).

(103) N.R. Pallas, B.A. Pethica, *Langmuir*, 1, 509 (1985).

(104) O. Albrecht, H. Grulerand, E. Sackmann, *Journal of Colloid Interface Science*, 79, 2 (1981).

(105) J. Jiang, A. Kucernak, *Journal Electroanalytical Chemistry*, 64, 520 (2002).

(106) M. Sluyters-Rehbech, *Pure Applied Chemistry*, 1994, 66 (1931).

(107) A.J. Bard, L.R. Faulkner, *Electrochemical Methods: Fundamentals and Applications*, Wiley: New York (1980).

(108) I. Ichinose, K. Kuroiwa, Y. Lvov, T. Kunitake, *Multilayer Thin Films*, Edited by G. Decher, J.B. Schlenoff, J.-M. Lehn, Wiley-VCH Verlag, Weinheim (2003).

(109) O.N. Oliveira Jr., M. Raposo, A. Dhanabalan, *Handbook of Surfaces and Interfaces of Materials*, edited by H. S. Nalwa, Ed. Academic Press, New York, p.1-63 (2001)

(110) N. Jessel, *Advanced Materials*, 15, 692-95 (2003).

(111) N .Benkirane-Jessel, *Advanced Functional Materials*, 14, 174-182 (2004).

(112) J.D. Mendelsohn, S.Y. Yang, J.A. Hiller, A.I. Hochbaum, M.F. Rubner, *Biomacromolecules*, 4, 96-106 (2003).

(113) Q. Ferreira, PhD Thesis, New University of Lisbon, Portugal (2007).

(114) Q. Ferreira, P.J. Gomes, Y. Nunes, M.J.P. Maneira, P.A. Ribeiro, M. Raposo, *Microelectronic Engineering Journal*, 84(3), 506-511 (2007).

(115) Q. Ferreira, P.J. Gomes, M.J.P. Maneira, P.A. Ribeiro, M. Raposo, *Sensors and Actuators B: Chemical*, 126, 311-317 (2007).

(116) M. Raposo, R. S. Pontes, L.H.C. Mattoso, O.N. Oliveira Jr., *Macromolecules*, 30, 6095-6101 (1997).

(117) M. Raposo, O.N.Oliveira Jr., *Langmuir*, 16(6), 2839-2844 (2000).

(118) J.Choi, M.F.Rubner, *Macromolecules*, 38, 116-124 (2005).

(119) M. Raposo, O.N. Oliveira Jr., *Langmuir*, 18, 6866-6874, (2002).

(120) E. Scifoni, E. Surdutovich, A. Solov'yov, I. Pshenichnov, I.Mishustin, W. Greiner, *AIP Conference Proceedings*, 1080, 104-110 (2008)

(121) A.V. Solov'yov, E. Surdutovich, E. Scifoni, I. Mishustin, W. Greiner, *AIP Conference Proceedings*, 1080, 40-50 (2008)

(122) R.Steitz, V.Leiner, R. Siebrecht, R. von Klitzing, *Colloids Surface A*, 163, 63-70 (2000).

(123) R. Mota, R. Parafita, M. J. P. Maneira, N. J. Mason, G. Garcia, P. A. Ribeiro, M. Raposo, P. Limão-Vieira, *Radiation Protection Dosimetry*, 122 (1-4), 66-71 (2006).

(124) M. Muthukumar, *Journal of Chemical Physics,* 120, 9343-9350 (2004).

(125) P. Limão-Vieira, A.M. Costa, S. Oliveira, P.J. Gomes, P.A. Ribeiro, M. Raposo, *Journal of Physics: Conference Series,* 88, 012004 (2007).

(126) R.D. Hudson, *Reviews of Geophysics: Space Physics*, 9, 305 (1971).

(127) N.J. Mason, A. Dawes, R. Mukerji, E.A. Drage, E. Vasekova, S.M. Webb and P. Limão-Vieira, *Journal of Physics B*, 38, S893 (2005) and references therein.

(128) R. Mota, R. Parafita, A. Giuliani, M-J. Hubin-Franskin, J.M.C Lourenço, G. Garcia, S.V. Hoffmann, N.J. Mason, P.A. Ribeiro, M. Raposo, P. Limão-Vieira, *Chemical Physics Letters*, 416, 152 (2005).

(129) P. Limão-Vieira, A. Giuliani, M-J. Hubin-Franskin, J. Delwiche, R. Parafita, R. Mota, D. Duflot, J-P. Flament, E. Drage, P. Cahillane, N.J. Mason, S.V. Hoffmann, *Chemical Physics*, 324, 339 (2006).

(130) L. Sanche, *European Physics Journal D*, 35, 367 (2005) and references therein.

(131) G. Decher, *Science*, 277, 1232 (1997).

(132) R.S. Pontes, M. Raposo, C.S. Camilo, A. Dhanabalan, O.N. Oliveira Jr., *Physica Status Solidi A*, 173, 41 (1999).

(133) Y. Lvov, H. Möhwald, *Protein arquitecture: Interfacing molecular assemblies and immobilization biotechnology*, Marcel Dekker Ed., New York (2000).

(134) K. Watanabe, *Advanced Geophysics*, 5, 153 (1958).

(135) A.C. Vandaele, P.C. Simon, J.M. Guilmot, M. Carleer, R. Colin, Journal of Geophysical Research, 99 25599 (1994).

(136) D.E. Freeman, K. Yoshino, J.R. Esmond and W.H. Parkinson, Planetary and Space Science, 32 1125 (1984).

(137) M. Isaacson, *Journal of Chemical Physics*, 56, 1803 (1972).

(138) M.P. Fülsher, L. Serrano-Andrés and B.O. Roos, *Journal of the American Chemical Society*, 119, 6168 (1997).

(139) O.N. Oliveira Jr., J-A. He, V. Zucolotto, S. Balasubramanian, L. Li, H.S. Nalwa, J. Kumar, S.K. Tripathy, *Handbook of Polyelectrolytes and Their Applications*, S.K. Tripathy, J. Kumar, H.S. Nalwa, Ed: American Scientific Publishers, 1, 1 (2002).

(140) R. Panajotovic, M. Michaud and L. Sanche, *Physical Chemistry and Chemical Physics*, 9, 138 (2007).

(141) T. Fleig, S. Knecht and C. Hättig, *Physical Chemistry and Chemical Physics*, 111, 5482 (2007).

(142) E. Piovesan , R.A. Silva , A. Marletta, Journal of Non-Crystalline Solids, 352, 3711 (2006).

(143) J. Berdys, I. Anusiewicz, P. Skurski, J. Simons, *Journal of the American Chemical Society*, 126, 6441-6447 (2004).

(144) C. von Sonntag, *The Chemical Basis of Radiation Biology*, Taylor & Francis (1987.

(145) M. Raposo, P.J. Gomes, J.M.C. Lourenco, M. Coelho, S.V. Hoffmann, A.M. Botelho do Rego, R.W. McCullough, N.J. Mason, C. Lage, P. Limao-Vieira, P.A. Ribeiro, *AIP Conference Proceedings*, 1080, 125-131 (2008).

(146) M.J. Isaacson, *Chemical Physics*, 56, 1803-1812 (1972).

(147) D. Roca-Sanjuán, M. Rubio, M. Merchán, L. Serrano-Andrés, *Journal of Chemical Physics*, 125, 084302 (2006).

(148) M.K. Shukla, J.J. Leszczynski, *Computacional Chemistry*, 25, 768-778 (2004).

(149) A.C. Borin, L. Serrano-Andrés, M.P. Fülscher, B.O. Roos, *Journal of Chemical Physics* A, 103, 1838-1845 (1999).

(150) R. So, S. Alavi, *Journal of Chemistry*, 28, 1776-1782 (2007).

(151) K. Tasaki, X. Yang, S. Urano, S. Fetzer, P.R. LeBreton, *Journal of the American Chemical Society*, 112, 538-548 (1990).

(152) S. Brondsted-Nielsen, T. Chakraborty, S.V. Hoffmann, *ChemPhysChem*, 6, 2619-2624 (2005).

(153) N. Gault, O. Rigaud, J.L. Poncy, J.L. Lefaix, *International Journal of Radiation Biology*, 81, 767-779 (2005).

(154) M. Lindqvist, M. Sarkar, A. Winqvist, E. Rozners, R. Strömberg, A. Gräslund, *Biochemistry*, 39, 1693-1701 (2000).

(155) M. Banyay, M. Sarkar, A. Gräslund, *Biophysical Chemistry*, 104, 477-488 (2003).

(156) Y.L. Tang, Z.Y. Guo, *Acta Biochimica et Biophysica Sinica*, 37, 39-46 (2005).

(157) F. Cataldo, *International Journal of Biological Macromolecules*, 38, 248-254 (2006).

(158) F. Cataldo, *Polymer Degradation and Stability*, 89, 274-281 (2005).

(159) W.J. Schreier, T.E. Schrader, F.O. Koller, P. Gilch, C.E. Crespo-Hernández, V.N. Swaminathan, T. Carrel, W. Zinth, B. Kohler*, Science*, 315, 625-29 (2007).

(160) E. Cubero, F.J. Luque, M. Orozco, *Biophysical Journal*, 90, 1000-1008 (2004).

(161) M. Monajjemi, B. Chahkandi, *Journal of Molecular Structure: Theochem*, 714, 43-60 (2005).

(162) J. Sponer, P. Jurecka, P. Hobza, *Journal of the American Chemical Society*, 126, 10142-10151 (2004).

(163) E.S. Kryachko, J.R. Sabin, *International Journal of Quantum Chemistry*, 91, 695-710 (2003).

(164) K.I. Miyamoto, K.I. Ishibashi, R.T. Yamaguchi Y. Kimura, H. Ishii, M. Niwano*, Journal of Applied Physics*, 99, 094702 (2006).

(165) M. Sarkar, U. Dornberger, E. Rozners, H. Fritzsche, R. Strömberg, A. Gräslund, *Biochemistry*, 36, 15463-71 (1997).

(166) J. Berdys, I. Anusiewicz, P. Skurski, J. Simons, *Journal of the American Chemical Society*, 126, 6441-6447 (2004).

(167) M. Folkard, K.M. Prise, B. Brocklehurst, B.D. Michael, *Journal of Physical B: Atomic, Molecular and Optical Physics*, 32, 2753-2761 (1999).

(168) M. Folkard, K.M. Prise, *Acta Physica Polonica A*, 109, 265-271 (2006).

(169) M.A. Huels, B. Boudaiffa, P. Cloutier, D. Hunting, L. Sanche, *Journal of the American Chemical Society*, 125, 4467-4477 (2003).

(170) J.R. Sabin, *Advances in Quantum Chemistry*, Elsevier/Academic Press: Amsterdam, vol. 52, Netherlands (2007).

(171) P.J. Gomes, P.A. Ribeiro, D. Shaw, N.J. Mason, M. Raposo, *Polymer Degradation and Stability*, 94, 2134-2141 (2009).

(172) D. Almeida, F.F. da Silva, G. García, P. Limão-Vieira, *Physical Review Letters*, 110, 023201 (2013).

(173) I. Baccarellia, I. Baldc, F.A. Gianturco, E. Illenberger, J. Kopyrad, *Physics Report*, 508 (1-2), 1-44 (2011).

(174) C.R. Arumainayagam, H.-L. Lee, R.B. Nelson, D.R. Haines, R.P. Gunawardane, *Surface Science Reports*, 65,1-44 (2010).

(175) M. Raposo, M. Coelho, P.J.Gomes, P. Vieira, P.A. Ribeiro, N.J. Mason, C.A. Hunniford, R.W. Mc Cullough, *International Journal of Radiation Biology*, 90(5), 344-350 (2014).

(176) P.J. Gomes, M. Coelho, M. Dionísio, P.A. Ribeiro, M. Raposo, *Applied Physics Letters*, 101, 123702 (2012).

(177) H. Rabitz, R. de Vivie-Riedle, M. Motzkus, K. Kompa, *Science*, 288, 824-828 (2000.

(178) S. Wada, R. Sumii, K. Isari, S. Waki, E.O. Salo, T. Sekiguchi, T. Sekitani, *Surface Science*, 528, 242-248 (2003).

(179) S. Ptasinska, S. Denifl, V. Grill, T.D. Märk, E. Illenberger, P. Scheier, *Physical Review Letters*, 95, 093201 (2005).

(180) V.S. Prabhudesai, A.H. Kelkar, D. Nandi, E. Krishnakumar, *Physical Review Letters*, 95, 143202 (2005).

(181) P.A. Sloan, R.E. Palmer, *Nature*, 434, 367-371 (2005).

(182) I. Bald, J. Kopyra, E. Illenberger, *Angewandte Chemie International Edition*, 45, 4851 (2006).

(183) H.H. Fielding, M.A. Robb, *Physical Chemistry and Chemical Physics*, 12, 15569 (2010).

(184) L. Ratschbacher, C. Zipkes, C. Sias, M. Köhl, *Nature Physics*, 8, 649 (2012).

(185) S. Eden, P. Limao-Vieira, S.V. Hoffmann, N.J. Mason, *Chemistry Physics Letters*, 323, 313 (2006).

(186) Q. Ferreira, P.J. Gomes, P. A. Ribeiro, N.C. Jones, S.V. Hoffmann, N.J. Mason, O.N. Oliveira Jr., M. Raposo, *Langmuir*, 29, 448 (2013).

(187) A.M. Botelho do Rego, L.F.V. Ferreira, *Handbook of Surfaces and Interfaces of Materials*; H.S. Nalwa, Ed. Academic Press: New York, Vol.2, p. 243-313 (2001).

(188) XPSPeak 4.1, freeware.

(189) G. Beamson, D. Briggs, *High Resolution XPS of Organic Polymers*; Jonh Wiley and Sons, England (1992).

(190) C.J. May, H.E. Canavan, D. Castner, *Analytical Chemistry*, 76, 1114 (2004).

(191) N.T. Samuel, C.Y. Lee, L.J. Gamble, D.A. Fisher, D.G. Castner, *Journal of Electron Spectroscopy and Related Phenomena*, 152, 134 (2006).

(192) J. Peeling, F.E. Hruska, N.S. McIntyre, *Canadian Journal Chemistry*, 56, 1555 (1978).

(193) M. Furukawa, H. Fujisawa, S. Katano, H. Ogasawara, Y. Kim, T. Komeda, A. Nilsson, M. Kawai, *Surface Science*, 532-535, 261 (2003).

(194) A.V. Naumkin, A. Kraut-Vass, S.W. Gaarenstroom, C.J. Powell, NIST X-ray Photoelectron Spectroscopy Database, NIST Standard Reference Database 20, Version 4.1 (http://srdata.nist.gov/xps/, accessed in May 2013)

(195) M.R. Vilar, A.M. Botelho do Rego, A.M. Ferraria, Y. Jugnet, C. Nogues, D. Peled, R. Naaman, *Journal Physical Chemistry B*, 112, 6957-6964 (2008).

(196) M.R. Cohen, R.P. Merill, *Surface Science*, 245, 1 (1991).

(197) P. Löfgren, A. Krozer, J. Lausmaa, B. Kasemo, *Surface Science*, 370, 277-292 (1997.

(198) M. Nyberg, J. Hasselstrom, O. Karis, N. Wassdahl, M. Weinelt, A. Nilsson, L.G.M Pettersson, *Journal Chemical Physical*, 112, 5420 (2000).

(199) A. Haug, S. Schweizer, F. Latteyer, M.B. Casu, H. Peisert, C. Ochsenfeld T. Chassé, *ChemPhysChem*, 9, 740 (2008).

(200) L.S. Shlyakhtenko, A.A. Gall, J.J. Weimer, D.D. Hawn, Y.L. Lyubchenko, *Biophysical Journal*, 77, 568 (1999).

(201) M. Furukawa, T. Yamada, S. Katano, M. Kawai, H. Ogasawara, A. Nilsson, *Surface Science*, 601, 5433-5440 (2007).

(202) J. Hasselström, O. Karis, M. Weinelt, N. Wassdahl, A. Nilsson, M. Nyberg, L.G.M. Pettersson, M.G. Samant, J. Stöhr, *Journal of Surface Science*, 407, 221 (1998).

(203) A.V. Saprigin, C.W. Thomas, C.S. Dulcey, C.H. Patterson Jr., M.S. Spector, *Surface and Interface Analysis*, 37, 24 (2005).

(204) M. Raposo, J.M.C. Lourenço, A.M. Botelho do Rego, A.M. Ferraria, P.A. Ribeiro, *Colloids and Surfaces A*, 412, 1 (2012).

(205) O. Boulanouar, M. Fromm, C. Mavon, P.Cloutier, L. Sanche, *Journal of Chemical Physics*, 139, 055101 (2013

(206) D. Almeida, R. Antunes, G. Martins, S. Eden, F.F. da Silva, Y. Nunes, G. Garcia, P. Limão-Vieira, *Physical Chemistry and Chemical Physics*, 13, 15657-15665 (2011).

(207) S. Denifl, S. Ptasińska, M. Probst, J. Hrušák, P. Scheier, T.D. Märk, *Journal of Physical Chemistry A*, 108, 6562-6569 (2004).

(208) R. Improta, G. Scalmani, V. Barone, *International Journal of Mass Spectrometry*, 201, 321 (2000).

(209) H.-W. Jochims, M. Schwell, H. Baumgärtel, S. Leach, Chemical Physics, 314, 263 (2005).

(210) R.G. Endres, D.L. Cox, R.R.P. Singh, *Reviews of Modern Physics*, 76, 195 (2004).

(211) H.W. Fink, C. Schönenberger, *Nature*, 398, 407 (1999).

(212) Y.T. Long, C.Z. Li, H.B. Kraatz, J.S. Lee, *Biophysical Journal*, 84, 3218 (2003).

(213) S. Hleli, A. Abdelghani, A. Tlili, *Sensors*, 3, 472- 479 (2003).

(214) S. Tomic, S.D. Babić, T. Vuletić, S. Krča, D. Ivanković, L. Griparić, R. Podgornik, *Physical Review E*, 75, 021905 (2007).

(215) I. Kratochvílová, K. Král, M. Bunček, S. Nešpůrek, A. Kochalska, T. Todorciuc, M. Weiter, J. Navrátil, B. Schneider, J. Pavluch, *Central European Journal of Physics*, 6, 422-426 (2008).

(216) I. Kratochvílová, K. Král, M. Bunček, A. Víšková, S. Nešpůrek, A. Kochalska, T. Todorciuc, M. Weiter, B. Schneider, *Biophysical Chemistry*, 138, 3-10 (2008).

(217) J. Wang, *Physical Review B*, 78, 245304 (2008).

(218) F. Lisdat, D. Schäfer, *Analytical and Bioanalytical Chemistry*, 391, 1555-1567 (2008).

(219) Y.S. Liu, P.P. Banada, S. Bhattacharya, A.K. Bhunia, R. Bashir, *Applied Physics Letters*, 92, 143902 (2008).

(220) A.D. Bodadila, E.P. Bellido, N.L. Rangel, H. Zhong, M.L. Norton, A. Sinitskii J.M. Seminario, *Journal of Chemical Physics*, 130, 171101 (2009).

(221) O.A. Sadik, A.O. Aluoch, A. Zhou, *Biosensors and Bioelectronics*, 24, 2749- 2765 (2009).

(222) Y. Zheng, L. Sanche, *Reviews in Nanoscience and Nanotechnology*, Vol. 2(1), pp.1-28 (2013).

(223) A. Savelyev, G.A. Papoian, *Journal of the American Chemical Society*, 128, 14506-14518 (2006).

(224) C. Chatgilialoglu, P. O´Neill, *Experimental Gerontology*, 36, 1459-1471 (2001).

(225) I. Pshenichnov, I. Mishustin, W. Greiner, *Physics in Medicine and Biology*, 50, 5493-5507 (2005).

(226) V.Cobut, Y. Frongillo, J. P. Patau, T. Goulet, M. J. Fraser, J.P. Jay-Gerin, *Radiation Physics and Chemistry*, 51, 229-243 (1998).

(227) M.A. Huels, B. Boudaiffa, P. Cloutier, D. Hunting, L. Sanche, *Journal of the American Chemical Society*, 125, 4467-4477 (2003).

(228) T. Schlathölter, R. Hoekstra, R. Morgenstern, *International Journal of Mass Spectrometry*, 233, 173-179 (2004).

(229) C.A. Hunniford, D.J. Timson, R.J.H. Davies, R.W. McCullough, *Physics in Medicine and Biology,* 52, 3729-3740 (2007).

(230) C.A. Hunniford, D.J. Timson, R.J.H. Davies, R.W. McCullough, *Journal of Physics: Conference Series*, 101, 012012 (2008).

(231) M. Schlapp, R. Trassl, E. Salzborn, R.W. McCullough, T.K. McLaughlin, H.B. Gilbody, Nucl. Instr. and Meth. B 98, 525 (1995).

(232) A. Dawes, A. Hunniford, P. Holtom, R.J. Mukerji, R.W. McCullough, N. Mason, Physical Chemestry and Chemical Physics, 9(22), 2886-2893 (2007).

(233) A. Barth, Biochimica et Biophysica Acta, 1767(9), 1073-1101 (2007).

(234) A. Mezzetti, L. Blanchet, A. de Juan, W. Leibl, C.Ruckebusch, Analytical and Bioanalytical Chemistry, 399(6), 1999-2014 (2011).

(235) *Two-dimensional correlation spectroscopy- Applications in vibrational and optical spectroscopy*, Edited by I. Noda, Y. Ozaki, John Wiley & Sons, West Sussex (2004).

(236) G. Wang, Q. Ding, Z. How, *Trends in Analytical Chemistry*, 27 (4), 368-378 (2008).

(237) *Independent Component Analysis: Adaptive and Learning Systems for Signal Processing Communication and Control Series*, Edited by O. Erkki, H. Apo, K. Juha, John Wiley & Sons, West Sussex (2002).

(238) *Independent Component Analysis*, Edited by A. Hyvärinen, J. Karhunen, E. Oja, John Wiley & Sons, West Sussex (2001).

(239) *Infrared Spectroscopy: Fundamentals and Applications*, Edited by B. H. Stuart, John Wiley & Sons, West Sussex (2004).

(240) X. Zhou, R.G. Liberman, P.L. Skipper, Y. Margolin, S.R. Tannenbaum, P.C. Dedon, *Analytical Biochemistry*, 343, 84-92 (2005).

(241) J.R. Hwu, J.-R. Yang, S.-C. Tsay, M.-H. Hsu, Y.-C. Chen, S.-S.P. Chou, *Tetrahedron Letters*, 49, 3312-3315 (2008).

(242) V. Andrushchenko, H. Wieser, P. Bouř, *Journal of Physical Chemistry B*, 106, 12623-12634 (2002).

(243) A. Polyanichko, H. Wieser, *Biopolymers*, 78, 329-339 (2005).

(244) *Spectrometric Identification of Organic Compounds*, Edited by R. M. Silverstein, G. C. Bassler, T.M. Morrill, John Wiley & Sons, West Sussex (1991).

(245) G. Rivero, A. Vazquez, L.B. Manfredi, *Journal of Applied Polymer Science,* 117, 1667-1673 (2010).

(246) W. Chan, B. Chen, L. Wang, K. Taghizadeh, M.S. Demott, P.C. Dedon, *Journal of the American Chemical Society,* 132, 6145-6153 (2010).

(247) M. de la Fuente, A. Heranz, and R. Navarro, *Journal of Biological Inorganic Chemistry*, 9, 973-986 (2004).

(248) V.P.N. Geraldo, M.L. Moraes, V. Zucolotto, O.N. Oliveira Jr., *Journal of Nanoscience and Nanotechnology*, 11,1167-1174 (2011).

(249) M.L. Moraes, P.J. Gomes, P.A. Ribeiro, P. Vieira, A.A. Freitas, R. Kohler, O.N. Oliveira Jr., M. Raposo, *Journal of Colloid and Interface Science*, 350, 268-274 (2010).

(250) A.S. Angelatos, K. Katagiri, F. Caruso, *Soft Matter*, 2,18-23 (2006).

(251) M. Ferreira, P.A. Fiorito, O.N. Oliveira Jr., *Biosensors and Bioelectronic*, 19, 1611 (2004).

(252) M. Tanaka, E. Sackmann, *Nature*, 437, 656-663 (2005).

(253) F. Yamauchi, Y. Koyamatsu, K. Kato, H. Iwata, *Biomaterials*, 27, 3497-3504 (2006).

(254) M.L. Moraes, M.S. Baptista, R. Itri, V. Zucolotto, O.N. Oliveira Jr., *Materials Science and Engineering: C*, 28, 467-471 (2008).

(255) M. Malcher, D. Volodkin, B. Heurtault, P. André, P. Schaaf, H. Möhwald, J.-C. Voegel, A. Sokolowski, V. Ball, F. Boulmedais, B. Frisch, *Langmuir*, 24, 10209-10215 (2008).

(256) R. Richter, A. Mukhopadhyay, A. Brisson, *Biophysical Journal*, 85, 3035–3047 (2003).

(257) R.P. Richter, R. Berat, A.R. Brisson, *Langmuir*, 22, 3497-3505 (2006).

(258) S. Gromelski, A.M. Saraiva, R. Krastev, G. Brezesinski, *Colloids and Surfaces B: Biointerfaces*, 74,477-483 (2009).

(259) A.A. Duarte, S.L. Filipe, L.M.G. Abegão, P.J. Gomes, P.A. Ribeiro, M. Raposo, *Microscopy and Microanalysis*, 19, 867-875 (2013).

(260) C. Delajon, T. Gutberlet, R. Steitz, H. Mohwald, R. Krastev, *Langmuir*, 21, 8509-8514, (2005).

(261) J. Choi, M.F. Rubner, *Macromolecules*, 38,116-124 (2005).

(262) A. Baba, F. Kaneko, R.C. Advincula, *Colloids and Surfaces A: Physicochemical and Engineering Aspects*,173, 39-49 (2000).

(263) T. Ari, M. H. Güven, *Journal of Electronic Spectroscopy and Relatated Phenomena*, 106, 29-35 (2000).

(264) E.E. Barnes, W.T. Simpson, *Journal of Chemical Physics*, 39, 670-675 (1963).

(265) K. Xu, G. Amaral, J. Zhang, *Journal of Chemical Physics*, 111, 6271-6282 (1999).

(266) S. Satyapal, J. Park, R. Bersohn, B. Katz, *Journal of Chemical Physics*, 91, 6873-6879 (1989).

(267) Y. Wen, J. Segall, M. Dulligan, C. Wittig, *Journal of Chemical Physics*, 101, 5665-5671 (1994).

(268) S. Harich, J.J. Lin, Y.T. Lee, X. Yang, *Journal of Chemical Physics*, 111, 5-9 (1999).

(269) S.-H. Lee, H.-I. Lee, Y.T. Lee, *Journal of Chemical Physics*, 121, 11053-11059 (2004).

(270) Z.-J. Zhang, H.-H Chen, X.-X. Yang, J.-T. Zhao, G.-B. Zhang, C.-S. Shi, *Journal of Physics D: Applied Physics*, 41, 105503 (2008).

(271) M. Kaneyoshi, *Journal of Luminiscence*, 21, 102-108 (2006).

(272) R.P.R. Mota, A. Giuliani, M.-J. Hubin-Franskin, J.M.C. Lourenço, G. Garcia, S.V. Hoffmann, N.J. Mason, P.A. Ribeiro, M. Raposo, P. Limão-Vieira, *Chemical Physics Letters*, 416, 152-159 (2005).

(273) R.J. Thompson, A.B.F. Duncan, *Journal of Chemical Physics*, 14, 574-577 (1946).

(274) A. Osted, J. Kongsted, O. Christiansen, *Journal of Physical Chemistry A*, 109,1430-1440 (2005).

(275) W.R. Harshbarger, *Journal of Chemical Physics*, 54, 2504-2509 (1971).

(276) W.R. Harshbarger, A. Skerbele, E.N. Lassettre, *Journal of Chemical Physics*, 54, 3784-3789 (1971).

(277) E. Tannenbaum, E.M. Coffin, A.J. Harrison, *Journal of Chemical Physics*, 21, 311-318 (1953).

(278) M.-J. Hubin-Franskin, J. Delwiche, A. Giuliani, M.-P. Ska, F. Motte-Tollet, I.C. Walker, N.J. Mason, J.M. Gingell, N.C. Jones, *Journal of Chemical Physics*, 116, 9261 (2002).

(279) L. Chantranupong, G. Hirsch, R.J. Buenker, M. Kimura, M.A. Dillon, *Chemical Physics Letters*, 154, 13-21 (1991).

(280) P.H.B. Aoki, D. Volpati, A. Riul Jr., W. Caetano, C.J.L. Constantino, *Langmuir*, 25, 2331-2338 (2009).

(281) P.H.B. Aoki, P. Alessio, M.L. Rodríguez-Méndez, J.A.D.S. Saez, C.J.L. Constantino, *Langmuir*, 25, 13062-13070 (2009).

(282) T.F. Schmidt, L. Caseli, T. Viitala, O.N. Oliveira Jr., *Biochimica et Biophysica Acta*, 1778, 2291–2297 (2008).

(283) J. Pimthon, R. Willumeit, A. Lendlein, D. Hofmann*, Journal of Molecular Structure*, 921, 38-50 (2009).

(284) R.I.S. Romão, Q. Ferreira, J. Morgado, J.M.G. Martinho, A.M.P.S.G Silva, *Langmuir*, 26, 17165-17177 (2010).

(285) E. Reimhult, B. Kasemo, F. Hook, *International Journal of Molecular Science*, 10, 1683-1696 (2009).

(286) T.H. Anderson, Y.J. Min, K.L. Weirich, H.B. Zeng, D. Fygenson, J.N. Israelachvili, *Langmuir*, 25, 6997-7005 (2009).

(287) K.L. Weirich, J.N. Israelachvili, D.K. Fygenson, *Biophysical Journal*, 98, 85-92 (2010).

(288) C. Stefaniu, G. Brezesinski, H. Möhwald, Advances in Colloid and Interface Science, 208, 197–213 (2014).

(289) P.J. Gomes, A.M.P.S. Gonçalves da Silva, P.A. Ribeiro, O.N. Oliveira Jr., M.Raposo, "Interaction of DNA with Langmuir monolayers of opposite charged phospholipids", *To be submitted*

(290) M. Cardenas, T. Nylander, B. Jönsson, B. Lindman, Journal of Colloid and Interface Science, 286, 166-175 (2005).

(291) S. Gromelski, G. Brezesinski, Langmuir, 22, 6293-6301 (2006).

(292) S. Erokhina, T. Berzina, L. Cristofolini, O. Konovalov, V. Erokhin, M.P. Fontana, *Langmuir*, 23(8), 4414-4420 (2007).

(293) M.N. Antipina, I. Schulze, M. Heinze, B. Dobner, A. Langner, G. Brezesinski, ChemPhysChem, 10(14), 2471-2479 (2009).

(294) D. Grigoriev, R. Miller, R. Wustneck, N. Wustneck, U. Pison, H. Mohwald, *Journal of Physical Chemistry B*, 107(51), 14283-14288 (2003).

(295) A. Pavinatto, A.L. Souza, J.A.M. Delezuk, F.J. Pavinatto, S.P. Campana-Filho, O.N. Oliveira Jr., *Colloids and Surfaces B: Biointerfaces*, S114 , 53-59 (2014).

(296) C. Montis, S. Sostegni, S. Milani, P. Baglioni, D. Berti, *Soft Matter*, 10(24), 4287-4297 (2014).

(297) A.M. Gonçalves da Silva, M.I. Viseu, *Colloids and Surfaces A*, 144, 191 (1998).

(298) D. Vollhardt, V.B. Fainerman, S. Siegel, *Journal of Physical Chemistry*, 104, 4115 (2000).

(299) O. Albercht, H. Matsuda, K. Eguchi, T. Nakagiri, *Thin Solid Films*, 338, 252 (1999).

(300) R.D. Smith, J.C. Berg, *Journal of Colloid and Interface Science*, 74, 213 (1980).

(301) A. Giehl, T. Lemm, O. Bartelsen, K. Sandhoff, A. Blume, *European Journal of Biochemistry*, 261, 650 (1999).

(302) R.A. Demel, W.S.M. Geurts van Kessel, R.F.A. Zwaal, B. Roelofsen, L.L.M. van Deenen, *Biochimica et Biophysica Acta – Biomembranes*, 406, 97 (1975).

(303) L. Wang, J.W. Brauner, G. Mao, E. Crouch, B. Seaton, J. Head, K. Smith, C.R. Flach, R. Mendelsohn, *Biochemistry*, 47, 8103 (2008).

(304) A.P. Le Brun, L.A. Clifton, C.E. Halbert, B. Lin, M. Meron, P.J. Holden, J.H. Lakey, S.A. Holt, *Biomacromolecules*, 14, 2014−2022 (2013).

(305) A.T Neves, Master Degree thesis, New University of Lisbon, Portugal (2014).

(306) S. Morandat, M. Bortolato, G. Anker, A. Doutheau, M. Lagarde, J.-P.Chauvet, Bernard Roux, *Biochimica et Biophysica Acta*, 1616, 137 (2003).

(307) S. Ortial, S. Morandat, M. Bortolato, B. Roux, A. Polidori, B. Pucci, G.Durand, *Colloids and Surfaces B: Biointerfaces*, 113, 384 (2014).

(308) D. Markovi, *Journal of the Serbian Chemical Society*, 71, 349 (2006).

(309) I. Sigal-Batikoff, O. Konovalov, A. Singh, A. Berman, *Langmuir*, 26, 16424 (2010).

(310) C. Mestras, A. Ortiz, I. Haro, F. Reig, M. Alsina, *Langmuir*,13, 5669 (1997).

(311) S.G.Taneva, K.M.W. Keough, *Biochimica et Biophysica Acta*, 1236, 185 (1995).

(312) R.A. Demel, W.S. M.Geurts van Kessel, R.F. A.Zwaal, B.Roelofsen, L.L.M. van Deenen, *Biochimica et Biophysica Acta – Biomembranes*, 406, 97 (1975).

(313) L.Wang, J. W.Brauner, G. Mao, E.Crouch, B. Seaton, J. Head, K. Smith, C.R. Flach, R. Mendelsohn, *Biochemistry*, 47, 8103 (2008).

(314) A.A. Duarte, P.J. Gomes, J.H.F. Ribeiro, P.A. Ribeiro, S.V. Hoffmann, N.J. Mason, O.N. Oliveira Jr., M. Raposo, *The European Physical Journal E-Soft matter*, 36, 9912 (2013).

(315) A. Dicko, H. Bourque, M. Pezolet, *Chemistry and Physics of Lipids*, 96, 125 (1998).

(316) P.H.B. Aoki, D. Volpati, F.C. Cabrera, V.L. Trombini, A. Riul Jr., C.J.L. Constantino, *Materials Science and Engineering C*, 32, 862 (2012).

(317) T.E. Goto, L. Caseli, *Langmuir*, 29, 9063, (2013).

(318) A. Blume, W. Hübner, G. Messner, *Biochemistry*, 27, 8239 (1988).

(319) C. Schwieger, A. Blume, *European Biophysics Journal*, 36, 437 (2007).

(320) M. Paolorossi, G. G. Montich, Biochimica et Biophysica Acta, 1808, 2167 (2011).

(321) W.K. Surewicz, H.H. Mantsch, Biochimica et Biophysica Acta, 952, 115 (1988).

(322) R. El-Jastimi, M. Lafleur, Biochimica et Biophysica Acta, 1324, 151 (1997).

(323) B.H. Stuart, *Infrared Spectroscopy: Fundamentals and Applications*, John Wiley & Sons, Ltd (2004).

(324) J. Laudát, F. Laudát, *European Biophysics Journal,* 21, 233-239 (1992).

(325) D. Porath, A. Bezryadin, S. de Vries, C. Dekker, *Nature* (London) 403, 635-638 (2000).

(326) C. Adessi, S. Walch, M. P. Anantram, *Physical Reviews B*, 67, 081405 (2003).

(327) C. Adessi, M. P. Anantram, *Applied Physics Letters*, 82, 2353-2355 (2003).

(328) K.-H. Yoo, D. H. Ha, J.-O. Lee, J. W. Park, J. Kim, J. J. Kim,H.-Y. Lee, T. Kawai,H. Y. Choi, *Physical Reviews Letters,* 87,198102 (2001).

(329) E.M. Conwell, S.V. Rakhmanova*, Proceedings of National Academy of Science of the U.S.A.*, 97, 4556 -4560 (2000).

(330) Y.J. Ye, R.S. Chen, A. Martinez, P. Otto, J. Ladik, *Solid State Communications*, 112, 139-144 (1999).

(331) R. Bruinsma, G. Grüner, M.R. D'Orsogna, J. Rudnick, *Physical Reviews Letters,* 85, 4393-4396 (2000).

(332) Y.A. Berlin, A.L. Burin, M.A. Ratner, *Journal of Physical Chemistry* A, 104, 443-445 (2000)

(333) A.A. Voityuk, J. Jortner, M. Bixon, N. Rösch, *Journal of Chemical Physics*, 114, 5614-5620 (2001).

(334) A.A. Voityuk, N. Rösch, M. Bixon, J. Jortner, *Journal of Physical Chemistry* B, 104, 9740-9745 (2000).

(335) G.E. Pike, *Physical Review B*, 6(4), 1572-1578 (1972).

(336) R. Gangopadhyay, A. De, S. Das, *Journal of Applied Physics*, 87(5), 2363-2371 (2000).

(337) M. Pollak, *Philosophical Magazine*, 23, 519 (1971).

(338) A.R. Long, *Advances in Physics*, 31, 553-637 (1982).

(339) M. Song-Shan, X. Hui, W. Huan-You, G. Rui, Chinese Physics B, 18(8), 3591-3596 (2009).

(340) S.R. Elliot, *Philosophical Magazine*, 36, 1291 (1977).

(341) K. Iguchi, *International Journal of Modern physics B*, 18(3), 1845-1910 (2004).

(342) Y. Orimoto, F. L. Gu, A. Imamura, Y. Aoki*, Journal of Chemical Physics*, 126, 215104 (2007).

(343) H. Yamada, K. Iguchi, *Advances in Condensed Matter Physics, 2010*, 380710 (2010).